Recent Applications of Scanning Microscopy in Surface Engineering 2020

Lead Guest Editor: Guosong Wu
Guest Editors: Paul K. Chu, Gheorghe Dinescu, Ranju Jung, and Ying Zhao

Recent Applications of Scanning Microscopy in Surface Engineering 2020

Recent Applications of Scanning Microscopy in Surface Engineering 2020

Lead Guest Editor: Guosong Wu
Guest Editors: Paul K. Chu, Gheorghe Dinescu,
Ranju Jung, and Ying Zhao

Contents

WILEY | Hindawi

Research Article

Improving Corrosion Resistance of Magnesium Alloy in Cl⁻ Containing Simulated Concrete Pore Solution by Ultrasound-Assisted Chemical Deposition

Ye Wang [ID] **and Guosong Wu** [ID]

College of Mechanics and Materials, Hohai University, Nanjing 211100, China

Correspondence should be addressed to Guosong Wu; wugsjd@126.com

Coatings are playing an important role in corrosion mitigation of magnesium alloys, and in this study, a facile and eco-friendly chemical deposition process is proposed to improve the corrosion resistance of magnesium-neodymium alloys. The mixture of 1.5 mol/L KH_2PO_4 solution and 1.2 mol/L $CaCl_2$ solution is used for reaction solution, and ultrasound is introduced into the process for assisting the chemical deposition. After 40 minutes of the surface treatment, the surface and cross-sectional morphologies are observed by scanning electron microscope (SEM), which reveals that a layer of dense coating is formed on Mg alloy. Energy-dispersive X-ray spectroscopy (EDS) and X-ray Diffraction (XRD) are further combined to analyze the coating, and it is thereby confirmed that this coating mainly consists of $CaHPO_4·2H_2O$. Electrochemical tests and soaking experiments are conducted to evaluate the corrosion resistance of the treated samples in simulated concrete pore solutions. Both the untreated and treated samples have a good corrosion resistance in the Cl⁻ free simulated concrete pore solution, but their corrosion behavior is influenced by the introduction of Cl⁻ in this study. Fortunately, the coating can protect the substrate effectively in the Cl⁻ containing simulated concrete pore solution. In summary, it provides a possible way for magnesium alloys to improve their corrosion resistance when they are used in building engineering.

1. Introduction

Magnesium alloys have received much attention in the aerospace, automotive, electronic, and biomedical industries due to their low density, high specific strength, and natural biodegradability. However, poor corrosion resistance is one of their fatal disadvantages to hinder their further engineering applications [1–7]. Usually, coating is an effective means to improve the corrosion resistance of Mg alloys in aqueous solutions and many kinds of techniques have ever been attempted [8–11]. Compared to chemical methods, most physical methods such as physical vapor deposition and ion implantation are innocuous to environment [12–14]. But the related equipment is always expensive and not suitable for large-scale engineering. Therefore, it is very imperative to develop new green chemical methods for the surface treatment of magnesium alloys.

Lightweight construction has been gradually recognized in modern civil engineering, and steel is expected to be replaced with lighter structural materials. For example, aluminum alloy bars have been considered an alternative to steel rebars in concrete structures. But, their native oxide coating is not stable in acid (pH <4) or alkaline (pH >9) environments, and aluminum alloy bars are often susceptible to corrosion in the alkaline environment of concrete structures [15]. In fact, magnesium alloys are lighter and have higher specific strength than aluminum alloys. Furthermore, magnesium has good immune behavior in alkaline aqueous environments [16, 17], which may make magnesium alloys adapt the alkaline concrete environment. However, chloride ions may appear in the concrete environment and affect the corrosion behavior of magnesium alloys. Therefore, it is essential to develop a facile and eco-friendly surface treatment process to protect magnesium alloys. Ultrasound has often been
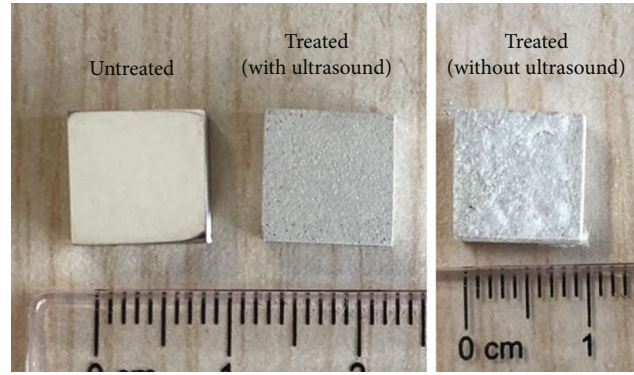
FIGURE 1: Appearance of the untreated and treated samples.

(a)

(b)

(c)

(d)

(e)
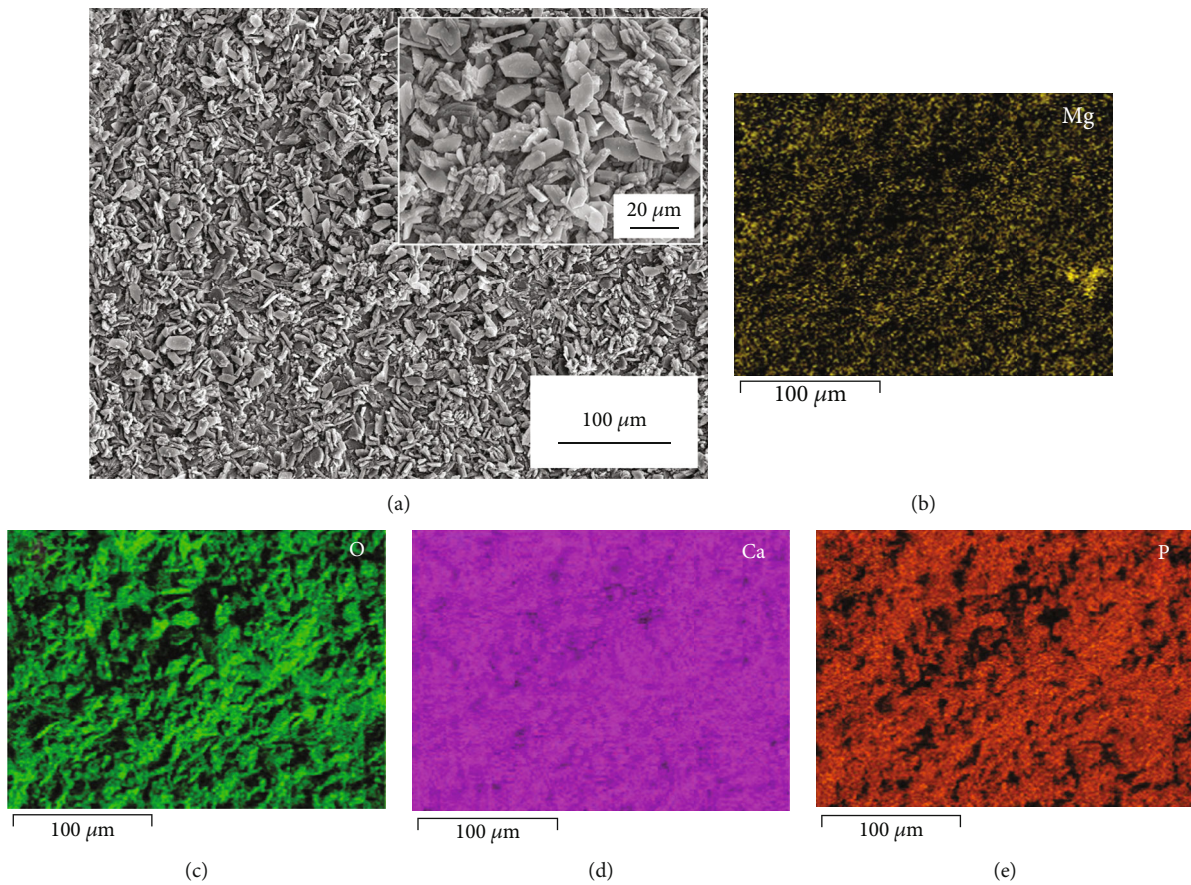
FIGURE 2: Surface morphology (a) and elemental distribution (b–e) of the treated Mg alloy. The inset in Figure 2(a) shows the surface morphology observed at higher magnification.

introduced into the chemical reaction process and can assist the formation of dense coating without using additional heating [18]. Calcium-phosphorus (Ca-P) coatings have been paid more attentions due to their excellent corrosion resistance [19]. For instance, Li et al. have applied the hydrothermal method to fabricate a glucose-induced phosphate coating on pure magnesium [20]. But most of the processes are complicated and time-consuming, which are not suitable for civil engineering. In this study, a calcium-phosphorus coating is prepared on the surface of Mg-3.3 wt. %Nd alloy by ultrasound-assisted chemical deposition, and its corrosion behavior is also investigated in simulated concrete pore solutions.

2. Materials and Methods

As-cast Mg-3.3 wt. %Nd alloys were used for substrate materials and cut into $10 \, mm \times 10 \, mm \times 5 \, mm$ pieces in this investigation. First, the samples were mechanically ground with SiC paper up to # 1200 and then polished with Al_2O_3

(a)

(b)

(c)

(d)

(e)

(f)
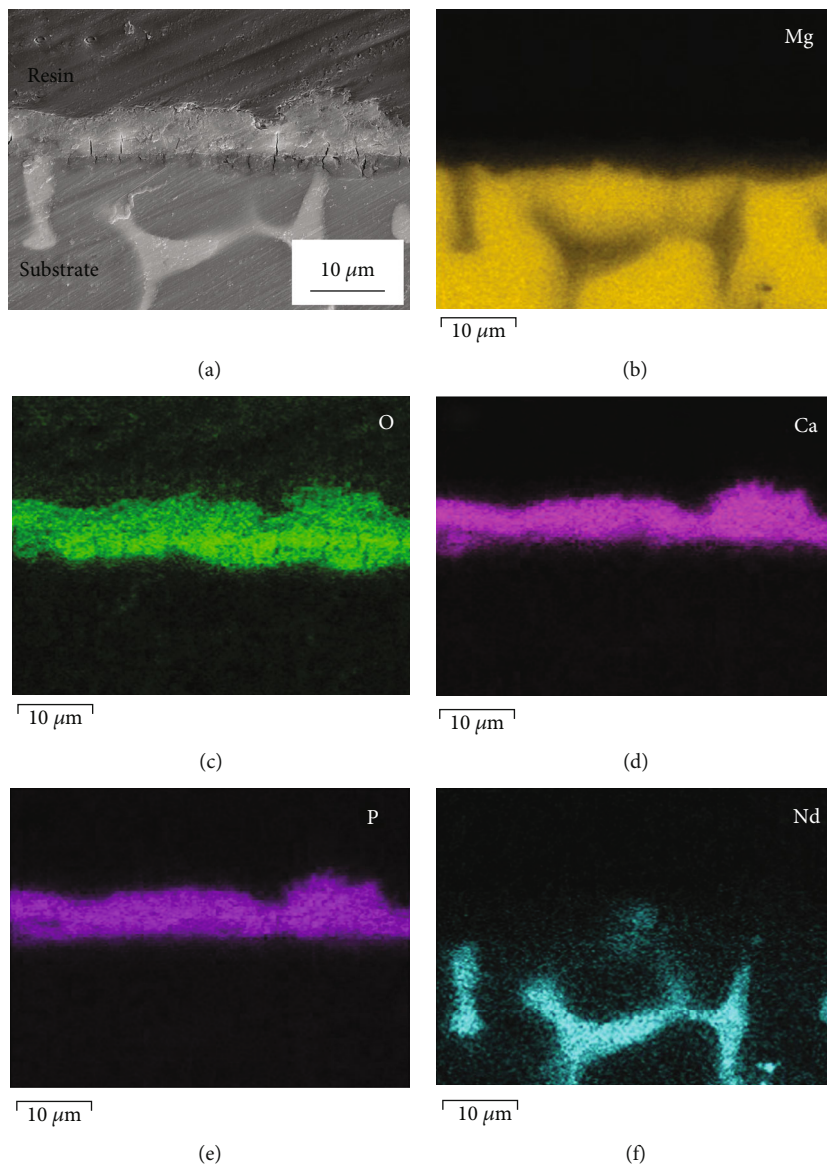
FIGURE 3: Cross-section of the treated sample: (a) SEM image and (b–f) its EDS elemental maps.
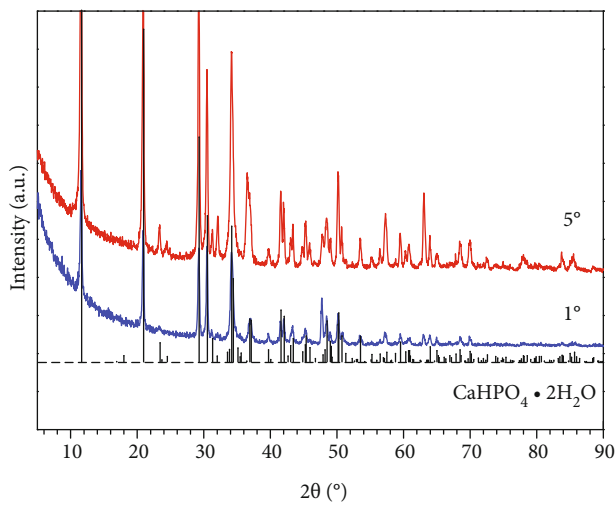
FIGURE 4: GIXRD patterns of the treated sample.

(a)

(b)

(c)

(d)
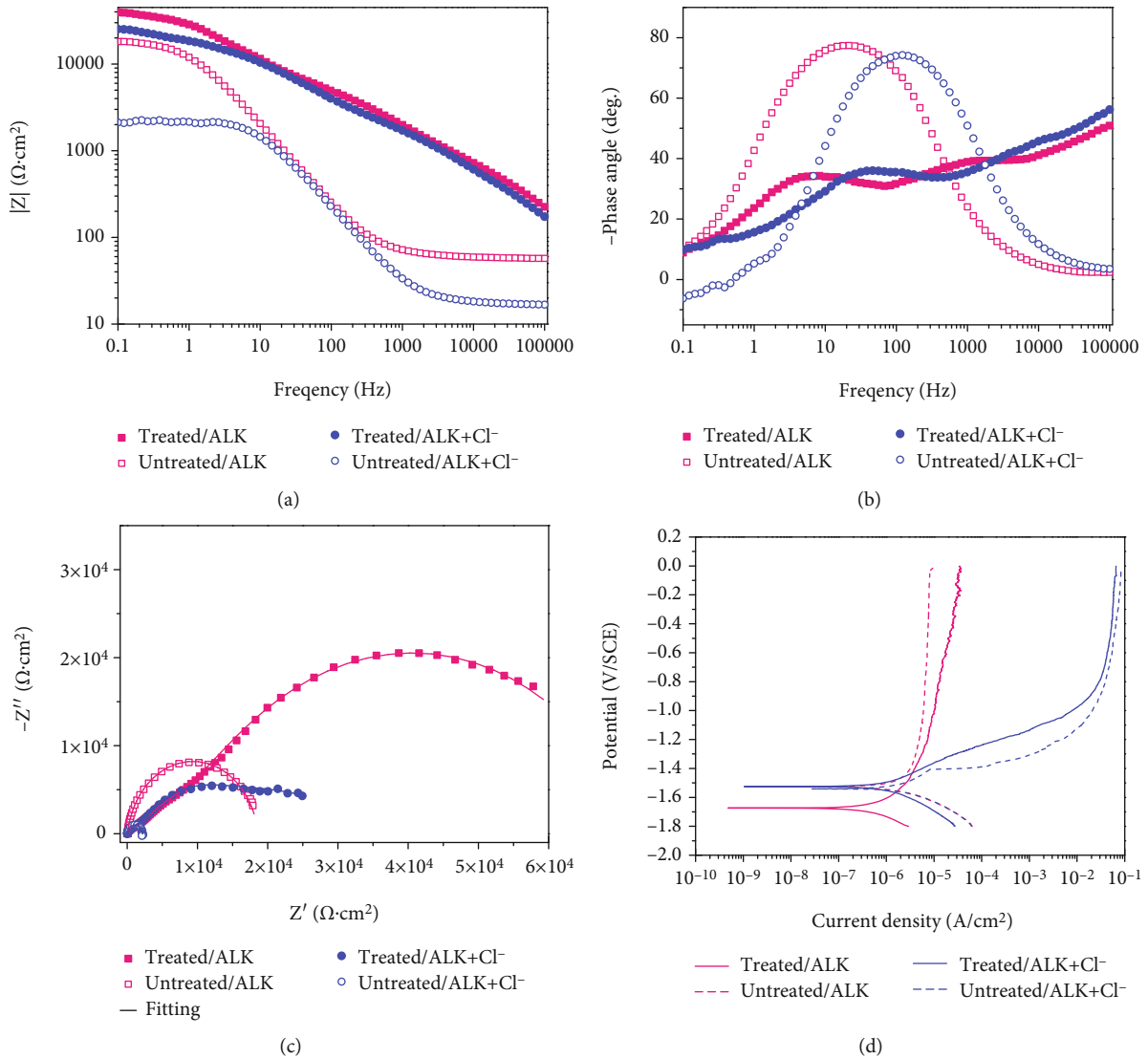
FIGURE 5: (a) Bode plots of the samples: impedance versus frequency. (b) Bode plots of the samples: phase angle versus frequency. (c) Nyquist plots of the samples. (d) Polarization curves of the samples.

(a)

(b)
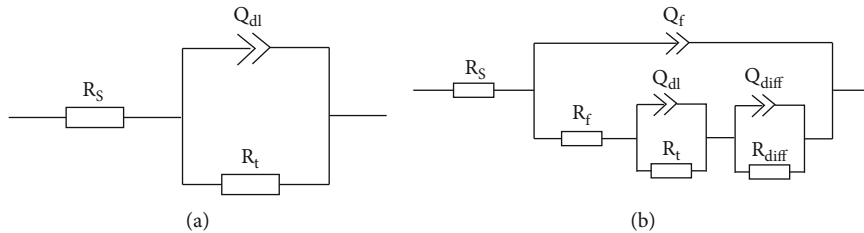
FIGURE 6: Equivalent circuit models for EIS data fitting: (a) Untreated samples [21] and (b) treated samples [22].

pastes. Second, they were rinsed with ethanol at room temperature and rapidly dried with hot air. Third, 1.5 mol/L KH_2PO_4 and 1.2 mol/L $CaCl_2$ were prepared, respectively. Here, a conventional ultrasonic cleaner was used for producing ultrasound, and a beaker with 30 mL of the mixture was placed into the ultrasonic cleaner. After the Mg alloy samples

were treated in the beaker at a frequency of 40 kHz for 40 minutes, they were taken out, washed with deionized water and ethanol in turns, and then naturally dried in air at room temperature.

Field emission scanning electron microscope (FESEM) was performed to observe the surface and cross-section

TABLE 1: Fitted results for the different samples in simulated concrete pore solution based on the corresponding equivalent circuit models.

Equivalent circuit model	Untreated/ALK R(QR)	Treated/ALK R(Q(R(QR)(QR)))	Untreated/ALK+Cl⁻ R(QR)	Treated/ALK+Cl⁻ R(Q(R(QR)(QR)))
R_S (Ω cm^2)	59.42	225.05	17.47	101.26
Y_f (Ω^{-2} cm^{-2} s^{-n})		1.473×10^{-7}		9.872×10^{-7}
n_f		0.7224		0.646
R_f (Ω cm^2)		1864		1542
Y_{dl} (Ω^{-2} cm^{-2} s^{-n})	1.069×10^{-5}	4.94×10^{-6}	1.016×10^{-5}	3.866×10^{-6}
n_{dl}	0.9228	0.7278	0.9392	0.8604
R_{ct} (Ω cm^2)	1.856×10^4	6.17×10^4	2177	5891
Y_{diff} (Ω^{-2} cm^{-2}s^{-n})		3.034×10^{-6}		2.554×10^{-5}
n_{diff}		0.5772		0.3757
R_{diff} (Ω cm^2)		9167		2.812×10^4

morphology of the treated sample, and the elemental distribution of the treated one was analyzed by energy-dispersive X-ray spectrometer (EDS). Grazing incidence X-ray diffraction (GIXRD) was performed to characterize the surface phase composition of the treated sample, and two different angles of X-ray incidence α ($\alpha = 1°$ and $5°$) were selected in this investigation.

In order to simulate the alkaline environment in the concrete construction, a saturated Ca (OH)$_2$ solution was used as the simulated concrete pore solution. In addition, the saturated Ca (OH)$_2$ solution was further diluted by 3.5 wt.% NaCl solution with a volume ratio of 1 : 1 to evaluate the effect of chloride ions. Electrochemical test and soaking experiment were applied to evaluate the corrosion behavior in the above solutions. Electrochemical corrosion tests were conducted on a CHI660E electrochemical workstation using the conventional three-electrode technique. Here, the potential was referenced to a saturated calomel electrode (SCE), and the counter electrode was a platinum sheet. The specimen with an exposed surface area of 1×1 cm^2 was immersed in 200 mL simulated concrete pore solution. After immersion for 30 min, the electrochemical impedance spectra (EIS) were collected from 100 kHz to 100 mHz with a 5 mV sinusoidal perturbing signal at the open-circuit potential. After the test of EIS, potentiodynamic polarization curves were recorded from -1.8 V to 0 V at a scanning rate of 1.0 mV·s^{-1}. All the electrochemical measurements were repeated three times to ensure reproducibility. In the immersion test, both untreated and treated samples were immersed in 20 mL Cl⁻ containing simulated concrete pore solutions for 24 h. After that, the samples were taken out, rinsed with water and ethanol, and naturally dried in air. Then, their surface morphologies after immersion were observed by scanning electron microscopy (SEM).

3. Results and Discussion

Figure 1 shows the appearance of the Mg-Nd alloy samples used in this study, indicating the surface of Mg alloy has been obviously changed after chemical deposition. By comparison, it is concluded that the ultrasound-assisted chemical deposi-

TABLE 2: Corrosion potential and corrosion current density determined from polarization curves.

	E_{corr} (V/SCE)	I_{corr} (A•cm^{-2})
Untreated/ALK	-1.481 ± 0.050	$(3.46 \pm 4.47) \times 10^{-7}$
Treated/ALK	-1.667 ± 0.039	$(3.74 \pm 0.11) \times 10^{-7}$
Untreated/ALK+Cl⁻	-1.531 ± 0.023	$(6.09 \pm 1.12) \times 10^{-6}$
Treated/ALK+Cl⁻	-1.545 ± 0.019	$(1.96 \pm 2.51) \times 10^{-6}$

tion can obtain a smoother surface than that without using ultrasound. Here, it should be pointed out that the chemical deposition without ultrasound cannot meet the requirement from the view of surface quality. Therefore, we abandon the strategy of conventional chemical deposition in this study and directly choose the process of ultrasound-assisted chemical deposition. Figure 2 exhibits the microscale surface morphologies of the treated sample observed by SEM. As shown in Figure 2(a), the treated surface is evenly covered by a layer of microflakes, and the inset acquired at high magnification shows that those microflakes pile up tightly. Figures 2(b)–2(e) further reveals the elemental distribution of elements Mg, O, Ca, and P, which means that a Ca-P coating has been formed on the surface.

Figure 3 exhibits the cross-section of the treated sample. It can be clearly seen in Figure 3(a) that a layer of dense coating is well formed on the substrate. According to the EDS elemental maps in Figures 3(b)–3(f), the layer mainly contains Ca, P, and O. GIXRD is performed to further determine the phase composition of the coating and the corresponding results are shown in Figure 4. Due to the difference of the investigated depths, those peaks on the curve of 1° (incident angle) are weaker than those on the curve of 5° (incident angle). But the positions of those peaks are the same, which also match those of standard CaHPO$_4$·2H$_2$O diffraction peaks very well. Thus, it can be easily confirmed by comparison that this coating mainly consists of CaHPO$_4$·2H$_2$O.

Figure 5 shows the results of those electrochemical tests including electrochemical impedance spectra and
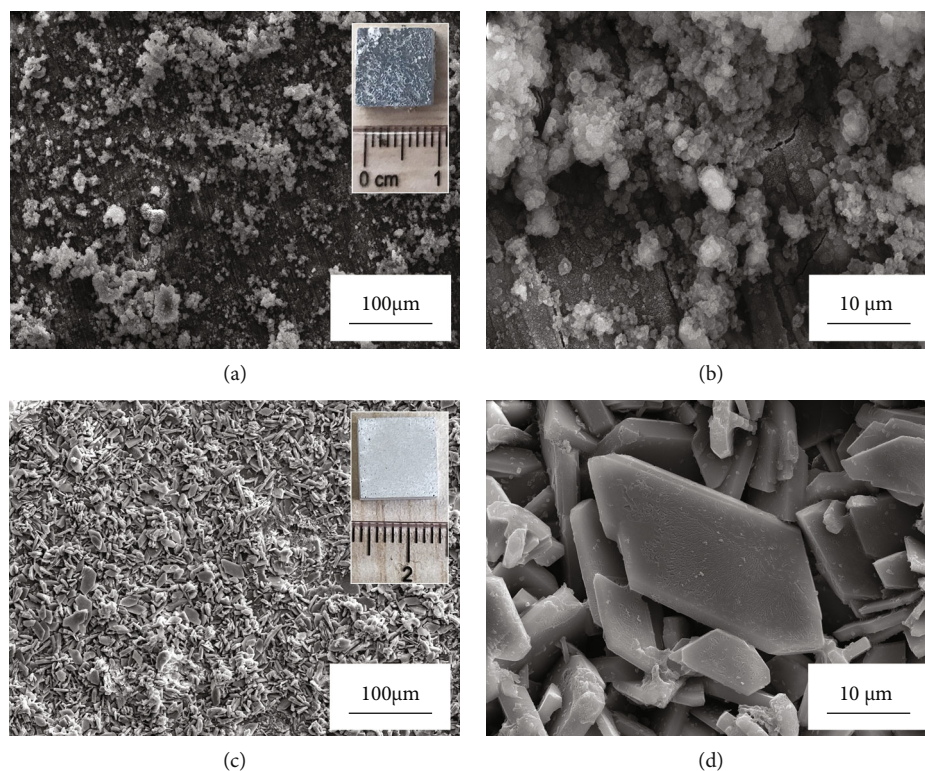
FIGURE 7: SEM images of the untreated and treated samples after immersion in Cl⁻ containing simulated concrete pore solution for 24 h: (a, b) surface morphology of the untreated sample and (c, d) surface morphology of the treated sample. The insets show the appearance of the samples after immersion for 24 h.

polarization. Figure 5(a) gives the Bode plots of impedance versus frequency, Figure 5(b) exhibits the Bode plots of phase angle versus frequency, and Figure 5(c) draws their corresponding Nyquist plots. Here, the saturated Ca $(OH)_2$ solution is denoted as ALK, and the Cl⁻ containing solution is named after ALK+Cl⁻. Both the untreated sample and treated sample have a high impedance in the saturated Ca $(OH)_2$ solution, but in the saturated Ca $(OH)_2$ solution diluted by 3.5 wt.% NaCl solution, the impedance of the untreated sample becomes very low. Fortunately, the treated sample changes this trend, and its impedance turns close to that of the untreated one in the Cl⁻ free saturated Ca $(OH)_2$ solution, indicating that the corrosion resistance is improved by ultrasound-assisted chemical deposition. Two equivalent circuits, $R_s (Q_{dl}R_t)$ [21] and $R_s(Q_f(R_f(Q_{dl}R_t)(Q_{diff}R_{diff})))$ [22] in Figure 6, are proposed to fit the impedance spectra of the untreated samples and treated samples, respectively. Here, R_s is the solution resistance. Q_{dl} and R_t represent the double-layer capacitance and charge transfer resistance, respectively. Q_{diff} represents the capacitance pertaining to the diffusion, and R_{diff} represents the relevant resistance. Q_f denotes the capacitance of the deposited film, and R_f is the total resistance of the pores in the film. The fitted data are exhibited in Table 1. The polarization curves obtained in this study are displayed in Figure 5(d), and the corrosion potential as well as corrosion current density is derived from cathodic Tafel region extrapolation (shown in Table 2). Generally, higher corrosion current density corresponds to lower

corrosion resistance. In Cl⁻ containing simulated concrete pore solutions, the corrosion current density of the treated sample has been reduced to about one-third of that of the untreated sample. Therefore, it can be found based on the data in Table 2 that the treated sample has a better corrosion resistance than the untreated one in the Cl⁻ containing simulated concrete pore solution.

Figure 7 shows the surface morphology of the samples after the immersion in Cl⁻ containing simulated concrete pore solutions for 24 h. It can be seen that the untreated sample suffers from severe aqueous corrosion whereas the treated one still keeps its surface intact. Even in SEM images, it is observed that those microflakes on the surface of the treated sample are well preserved. Finally, it is confirmed that the dense coating prepared by ultrasound-assisted chemical deposition can act as an effective barrier to mitigate the corrosion of Mg-Nd alloys in Cl⁻ containing simulated concrete pore solutions.

If metallic magnesium is immersed in aqueous solutions, the overall corrosion reaction can be described as follows: $Mg + 2H_2O \rightarrow Mg^{2+} + 2OH^- + H_2\uparrow$ [23]. Usually, the dissolution of Mg increases the OH⁻ concentration, and magnesium hydroxide will precipitate once its solubility limit is exceeded [24]. Therefore, it can be easily understood based on the above chemical reaction that magnesium owns an immune behavior in alkaline solutions. Unfortunately, OH⁻ is prone to be replaced by Cl⁻ to form soluble chloride which expedites the dissolution of magnesium hydroxide [25]. Thus, the corrosion resistance of magnesium and its alloys will decrease

significantly when Cl⁻ occurs in the simulated concrete pore solution.

A layer of dense coating is revealed in Figures 2 and 3, and here, its formation mechanism is simply discussed as follows. Firstly, $H_2PO_4^-$ ionizes in aqueous solutions to release HPO_4^{2-} and H^+ [26, 27]. Next, HPO_4^{2-} preferentially bonds with Ca^{2+} to form insoluble $CaHPO_4·2H_2O$ in this acidic phosphate solution, whose related chemical reaction is shown below: $Ca^{2+} + HPO_4^{2-} + 2\ H_2O \rightarrow CaHPO_4•2H_2O$ [28, 29]. In addition, OH^- produced from the corrosion of magnesium will react with $H_2PO_4^-$ to facilitate the formation of HPO_4^{2-} [28, 29]. Finally, when the surface is uniformly covered by $CaHPO_4·2H_2O$, the corrosion resistance of magnesium alloys can be improved due to the protective effect of $CaHPO_4·2H_2O$. Nowadays, magnesium alloys have many potential applications such as formwork and reinforcing bar in building engineering due to the urgent requirement of lightweight construction. On the heels of this trend, a facile process is successfully developed in our study to enhance the corrosion resistance of magnesium alloys in Cl⁻ containing simulated concrete pore solutions.

4. Conclusion

A layer of dense Ca-P coating is fabricated on Mg-3.3 wt. %Nd alloy by ultrasound-assisted chemical deposition, which mainly consists of $CaHPO_4·2H_2O$. Mg-Nd alloy has a good corrosion resistance in the simulated concrete pore solution because of the immune behavior of magnesium in alkaline aqueous environments. However, it cannot resist the corrosion attack when chloride ions occur in the simulated concrete pore solution. Fortunately, this Ca-P coating can protect the substrate effectively in the Cl⁻ containing simulated concrete pore solution. In summary, it offers an economical and environmentally friendly means to produce a barrier structure on Mg-Nd alloys and further paves a potential way to develop Mg alloys as civil engineering materials in the future.

Data Availability

The data used in this study are available from the corresponding author upon request.

Conflicts of Interest

The authors declare that they have no competing interests.

Acknowledgments

References

[1] B. L. Mordike and T. Ebert, "Magnesium," *Materials Science and Engineering A*, vol. 302, no. 1, pp. 37–45, 2001.

[2] W. Xu, N. Birbilis, G. Sha et al., "A high-specific-strength and corrosion-resistant magnesium alloy," *Nature Materials*, vol. 14, no. 12, pp. 1229–1235, 2015.

[3] B. Xu, J. Sun, Z. Yang et al., "Microstructure and anisotropic mechanical behavior of the high-strength and ductility AZ91 Mg alloy processed by hot extrusion and multi-pass RD-ECAP," *Materials Science and Engineering: A*, vol. 780, p. 139191, 2020.

[4] F. Cao, G. Song, and A. Atrens, "Corrosion and passivation of magnesium alloys," *Corrosion Science*, vol. 111, pp. 835–845, 2016.

[5] J. Sun, B. Xu, Z. Yang et al., "Achieving excellent ductility in high-strength Mg-10.6Gd-2 Ag alloy via equal channel angular pressing," *Journal of Alloys and Compounds*, vol. 817, p. 152688, 2020.

[6] S. Wu, X. Liu, K. W. K. Yeung, C. Liu, and X. Yang, "Biomimetic porous scaffolds for bone tissue engineering," *Materials Science and Engineering R*, vol. 80, pp. 1–36, 2014.

[7] H. Feng, G. Wang, W. Jin et al., "Systematic study of inherent antibacterial properties of magnesium-based biomaterials," *ACS Applied Materials & Interfaces*, vol. 8, no. 15, pp. 9662–9673, 2016.

[8] G. Wu, J. M. Ibrahim, and P. K. Chu, "Surface design of biodegradable magnesium alloys — a review," *Surface & Coatings Technology*, vol. 233, pp. 2–12, 2013.

[9] J. E. Gray and B. Luan, "Protective coatings on magnesium and its alloys — a critical review," *Journal of Alloys and Compounds*, vol. 336, no. 1-2, pp. 88–113, 2002.

[10] G. Y. Liu, S. Tang, D. Li, and J. Hu, "Self-adjustment of calcium phosphate coating on micro-arc oxidized magnesium and its influence on the corrosion behaviour in simulated body fluids," *Corrosion Science*, vol. 79, pp. 206–214, 2014.

[11] L. Y. Cui, G. B. Wei, R. C. Zeng, S. Q. Li, Y. H. Zou, and E. H. Han, "Corrosion resistance of a novel SnO2-doped dicalcium phosphate coating on AZ31 magnesium alloy," *Bioactive Materials*, vol. 3, no. 3, pp. 245–249, 2018.

[12] G. Wu, X. Zeng, W. Ding, X. Guo, and S. Yao, "Characterization of ceramic PVD thin films on AZ31 magnesium alloys," *Applied Surface Science*, vol. 252, no. 20, pp. 7422–7429, 2006.

[13] G. Wu, K. Ding, X. Zeng, X. Wang, and S. Yao, "Improving corrosion resistance of titanium-coated magnesium alloy by modifying surface characteristics of magnesium alloy prior to titanium coating deposition," *Scripta Materialia*, vol. 61, no. 3, pp. 269–272, 2009.

[14] Y. Zhao, G. Wu, H. Pan, K. W. K. Yeung, and P. K. Chu, "Formation and electrochemical behavior of Al and O plasma-implanted biodegradable Mg-Y-RE alloy," *Materials Chemistry and Physics*, vol. 132, no. 1, pp. 187–191, 2012.

[15] G. Xing and O. E. Ozbulut, "Flexural performance of concrete beams reinforced with aluminum alloy bars," *Engineering Structures*, vol. 126, pp. 53–65, 2016.

[16] Y. Yun, Z. Dong, N. Lee et al., "Revolutionizing biodegradable metals," *Materials Today*, vol. 12, no. 10, pp. 22–32, 2009.

[17] M. Esmaily, J. E. Svensson, S. Fajardo et al., "Fundamentals and advances in magnesium alloy corrosion," *Progress in Materials Science*, vol. 89, pp. 92–193, 2017.

[18] J. M. Costa and A. F. de Almeida Neto, "Ultrasound-assisted electrodeposition and synthesis of alloys and composite materials: A review," *Ultrasonics-Sonochemistry*, vol. 68, article 105193, 2020.

[19] K. Xia, H. Pan, T. Wang et al., "Effect of Ca/P ratio on the structural and corrosion properties of biomimetic Ca P coatings on ZK60 magnesium alloy," *Materials Science and Engineering C*, vol. 72, pp. 676–681, 2017.

[20] L. Y. Li, L. Y. Cui, L. Bin et al., "Corrosion resistance of glucose-induced hydrothermal calcium phosphate coating on pure magnesium," *Applied Surface Science*, vol. 465, pp. 1066–1077, 2019.

[21] Y. Wang, G. Wu, C. Xu, Z. Yang, and J. Sun, "Revealing anticorrosion behavior of magnesium alloy in simulated concrete pore solution," *Materials Letters*, vol. 285, pp. 10–13, 2021.

[22] H. Wu, Z. Shi, X. Zhang et al., "Achieving an acid resistant surface on magnesium alloy via bio-inspired design," *Applied Surface Science*, vol. 478, pp. 150–161, 2019.

[23] G. Wu, X. Zhang, Y. Zhao, J. M. Ibrahim, G. Yuan, and P. K. Chu, "Plasma modified Mg–Nd–Zn–Zr alloy with enhanced surface corrosion resistance," *Corrosion Science*, vol. 78, pp. 121–129, 2014.

[24] M. Taheri, R. C. Phillips, J. R. Kish, and G. A. Botton, "Analysis of the surface film formed on Mg by exposure to water using a FIB cross-section and STEM–EDS," *Corrosion Science*, vol. 59, pp. 222–228, 2012.

[25] L. Chang, F. Cao, J. Cai, W. Liu, J. Zhang, and C. Cao, "Formation and transformation of Mg(OH)2 in anodic coating using FTIR mapping," *Electrochemistry Communications*, vol. 11, no. 11, pp. 2245–2248, 2009.

[26] C. Zhang, S. Liao, B. Yu et al., "Ratio of total acidity to pH value of coating bath: A new strategy towards phosphate conversion coatings with optimized corrosion resistance for magnesium alloys," *Corrosion Science*, vol. 150, pp. 279–295, 2019.

[27] W. Zai, Y. Su, H. C. Man, J. Lian, and G. Li, "Effect of pH value and preparation temperature on the formation of magnesium phosphate conversion coatings on AZ31 magnesium alloy," *Applied Surface Science*, vol. 492, pp. 314–327, 2019.

[28] Y. W. Song, D. Y. Shan, and E. H. Han, "Electrodeposition of hydroxyapatite coating on AZ91D magnesium alloy for biomaterial application," *Materials Letters*, vol. 62, no. 17-18, pp. 3276–3279, 2008.

[29] Y. Song, D. Shan, R. Chen, F. Zhang, and E. Han, "A novel phosphate conversion film on Mg–8.8Li alloy," *Surface & Coatings Technology*, vol. 203, no. 9, pp. 1107–1113, 2009.

WILEY | Hindawi

Research Article

A Cost-Effective Method for Preparing Robust and Conductive Superhydrophobic Coatings Based on Asphalt

Wenbin Li [iD],[1,2] **Yong Wang,**[1,2] **Yanting Feng,**[1,2] **Qing Wang,**[1,2] **Xuexia Xu,**[1,2] **Guowei Li,**[1,2] **Guozhen Dong,**[1,2] **Shangqian Jing,**[1,2] **Ersong Chen,**[1] **Xiaoliang Fan,**[3] **and Peng Wang** [iD][3]

[1]*State Grid Hebei Electric Power Research Institute, Shijiazhuang 050021, China*
[2]*State Grid Hebei Energy Technology Service Co., Ltd., Shijiazhuang 050021, China*
[3]*School of Energy, Power and Mechanical Engineering, North China Electric Power University, Baoding 071003, China*

Correspondence should be addressed to Wenbin Li; wenbinli1975@126.com and Peng Wang; wang.peng.ncepu@foxmail.com

The wide application of superhydrophobic materials is mainly hindered by the poor mechanical robustness and complicated preparation method. To overcome these problems, we tried to make a combination of hierarchical and self-similar structure by the means of a simple spraying method. By adding nanofiller (carbon nanotube) and microfiller (graphite powder and expanded graphite), the hierarchical structure was constructed. By further doping the fillers in the commercial asphalt uniformly, the self-similar structure was prepared. Based on the aforementioned work, the as-prepared sample could withstand the sandpaper abrasion for 12.00 m under 4.90 kPa. Moreover, this superhydrophobic coating demonstrated good conductivity, superior self-cleaning property, and excellent corrosion resistance. The integration of conductivity with the superhydrophobicity might open new avenues for ground grid applications.

1. Introduction

The steel is widely used in our daily life and industry due to its relatively low price, excellent mechanical strength, and superior machinability [1–3]. However, most steel is prone to be corroded, which results in massive economic losses. Many methods have been developed to prohibit the corrosion [4–7]. Particularly, superhydrophobic materials, which can be fabricated by the combination of micro/nanostructure and low surface energy, are attracting more and more attention because the water droplets can maintain nearly spherical shape on them and roll off easily [8–11]. Based on this extreme repellency, many researches have tried to use the superhydrophobic materials to protect corrosion [12–14]. For instance, Cao et al. fabricated a superhydrophobic film which could protect the metal substrate for a long time [15]. Zhang et al. prepared a superhydrophobic coating by combining the epoxy resin with carbon nanotubes, which can effectively protect the Q235 carbon steel [16].

However, the Achilles' heel for superhydrophobic surfaces is the poor mechanical durability. Most superhydrophobic surfaces are prone to be damaged by a slight scratch, or even finger contact [17, 18]. To overcome this weakness, three different methods were developed. First, Lu et al. introduced a "Paint+Adhesive" method which tried bonding the hydrophobic particles using the adhesives [19]. Second, Verho et al. adapted hierarchical structure which tried to utilize the relatively robust microstructure to protect the fragile nanostructure [20]. Third, the self-similar structure is also a potential method which let the new exposed part maintain superhydrophobicity because they are similar in texture and functionality with the abrade parts [21].

The electrical conductivity is also a key consideration because it is crucial in many practical applications. For instance, Q235 steel is widely used as ground grid in the electricity substation due to its cheap price and relatively low electrical resistance. Then, the excellent electrical conductivity should be guaranteed when we tried to use superhydrophobic

coating to protect the ground grid [22]. To achieve superhydrophobicity and excellent conductivity simultaneously, scattering carbon-based fillers in the polymer matrix is the main solution. For instance, Hejazi et al. fabricated hairlike superhydrophobic carbon nanotube structure using a template method, which achieved superhydrophobicity without any modification [23]. Gu et al. prepared superhydrophobic surface by coating polystyrene onto the carbon nanotube membrane [24]. Wang et al. constructed a superhydrophobic coating by mixing the graphene with the polydimethylsiloxane [25]. Nevertheless, the aforementioned conductive/superhydrophobic materials have the weakness of mechanical robustness.

In our previous work, a superhydrophobic/conductive material based on the mixture of epoxy and carbon nanotubes has been prepared [26]. The asphalt is widely used in our daily life as the pavement due to its outstanding mechanical strength [27]. Compared with the epoxy, the asphalt has many different specialties, which lead to some special applications such as the pavement. Here, we tried to use the asphalt as the basement to enhance the mechanical strength. In order to obtain self-similar structure, the conductive fillers were uniformly dispersed in the asphalt matrix. In order to further obtain hierarchical structure, both microscale filler (graphite powder and expanded graphite) and nanoscale filler (multiwall carbon nanotube) were utilized. Thus, the hierarchical and self-similar structures were combined which endowed the superhydrophobic coating with outstanding conductivity, excellent mechanical robustness, and superior self-cleaning performance. Moreover, this superhydrophobic coating was achieved by simply spraying, which has the potential for large-scale production.

2. Materials and Methods

2.1. Materials. The 10# asphalt, 70# asphalt, Q235 steel plate, and expanded graphite (EG) were purchased from a local market. The multiwalled carbon nanotubes with a mean diameter and length of 9.5 nm and 1.5 μm were purchased from Nanocyl Co. Ltd., Belgium (NC7000). 1H,1H,2H,2H-per-fluorooctyltriethoxysilane (C$_8$F$_{13}$H$_4$Si(OCH$_2$CH$_3$)$_3$, FAS) were purchased from Aladdin Reagent Co., Ltd., Shanghai, China. All other chemicals were bought from Sinopharm Chemical Reagent Co., Ltd. (SCRC, China) and used as received.

2.2. The Pretreatment of the Q235 Plate. The Q235 steel plates with dimensions of 20 mm × 20 mm × 1.5 mm were utilized as the substrates. Before using, the Q235 substrates were abraded to be the 800# sandpaper and then ultrasonically cleaned in deionized water.

2.3. Preparation of the Superhydrophobic Coating. The schematic of the fabrication process can be found in Figure 1. First, 1.6 g 10# asphalt and 0.4 g 70 # asphalt were mixed into 7.0 g tetrahydrofuran (THF) by mechanical stirring for 4 h, which was marked as solution A. Separately, 0.6 g graphite powder, 0.15 g MWCNTs, 0.03 g EG, and 0.2 g FAS were sequentially dissolved into 8 g THF by means of mechanical
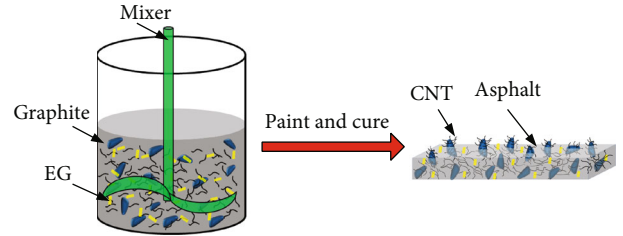
FIGURE 1: The schematic of the fabrication process.

stirring, which was defined as solution B. It should be noted that we further altered the amount of MWCNTs and EG for the purpose of improving the electrical conductivity. Then, the solution A was mixed with solution B. After stirring for 4 h, the mixture A was obtained. In the next step, the mixture A was sprayed onto the Q235 steel with the help of spray gun under the pressure of 0.4 MPa. Finally, the coating was cured at room temperature for 24 h. The thickness of the as-prepared coating was ~0.45 mm.

2.4. Characterization. The surface microstructures of the superhydrophobic coating were investigated by a scanning electron microscope (SEM, TESCAN Vega3), and the element compositions were assessed from the equipped energy-dispersive spectroscopy (EDS). Before the SEM test, a thin Au film (~2-3 nm) was sputtered onto the samples. The true color confocal microscope was employed to measure the surface roughness. The water contact angles (CAs) were evaluated by a home-made contact angle meter. A high-speed camera (Revealer 2F04) was utilized to assess the sliding angles (SAs). The 5 μL water droplets were adapted in the aforementioned CA and SA tests.

For the resistivity test, the coating was sprayed on a glass slide (76 mm × 26 mm × 2 mm). A DC bridge (QJ84, Shanghai Zhengyang Instrument Factory, China) was utilized to investigate the volume resistivity according to Chinese standard GB/T 2439-2001. The volume resistivity (ρ) was calculated as follows:

$$\rho = R \times \frac{S}{L}, \tag{1}$$

where R is the electrical resistance of the coating, S is the cross-sectional area, and L is the length of the coating. The conductivity (s) is the reciprocal of the volume resistivity.

The CHI760E electrochemical workstation (Shanghai CH Instruments) was utilized to investigate the polarization curves. We used the three-electrode system and set the scanning rate at 1 mV/s. The specimen and a platinum electrode were adapted as the working and counter electrode, respectively. A saturated calomel electrode (SCE) was employed as the reference electrode.

2.5. The Abrasion Test. In the abrasion test, the superhydrophobic coating was faced down to the rough surface of 200# SiC sandpaper. Then, a weight of 200 g (4.90 kPa) was put on the top of the Q235 substrate. With the help of
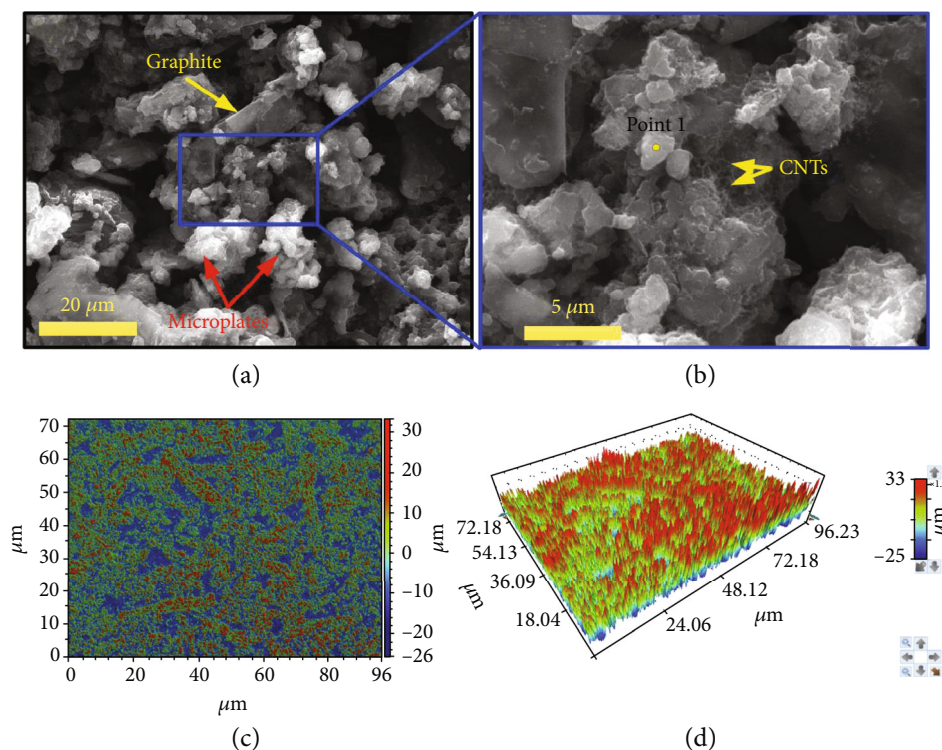
FIGURE 2: The SEM image of the as-prepared superhydrophobic sample with (a) low and (b) high magnification. (c) 2D and (d) 3D true color confocal microscope images of the as-prepared sample.

external force, the specimen was dragged along the ruler for 20 cm, which was defined as one abrasion cycle.

3. Results and Discussion

In this study, the hierarchical structure was prepared by means of adding both microscale filler and nanoscale filler. The SEM observation confirmed the existence of the hierarchical structure. Many microscale bulges (2-20 μm) could be found from Figure 2(a), which came from the EG and graphite. We further amplified the magnification of SEM observation. Then, many MWCNTs could be found which were on and between the microbulges (Figure 2(b)). We further utilized the true color confocal microscope to evaluate the surface morphology (Figures 2(c) and 2(d)). The surface roughness was calculated to be ~6.55 μm, indicating the microscale roughness of the as-prepared superhydrophobic sample.

To detect the chemical composition, the EDS measurement was carried out at the area of Figure 2(b). The C, O, F, and Si components could be detected from Figure 3(a). We attributed the F component to the FAS, which played a vital role in the low surface energy. The Au component came from the Au sputtering prior to the SEM observation. Therefore, this coating obtained superhydrophobicity by means of the combination of hierarchical structure and the low surface energy. It can be found that eight spherical shape water droplets were randomly scattered on the surface (Figure 3(b)), indicating the outstanding superhydrophobicity. We further calculated the CAs and SAs to quantitatively evaluate the

wetting state, and this coating exhibited a high CA of 163° and a low SA of 5°. Thus, it is reasonable to deduce that this coating demonstrated stable Cassie-Baxter state where the water droplets were suspended on the surface [28, 29].

XPS measurement was performed to further investigate the surface chemical composition of the as-prepared superhydrophobic surface. Figure 4 shows the survey spectra of the sample. It can be found that the Si 2p, Si 2s, C 1s, O 1s, and F 1s peaks are detected from the surface. Figure 4(b) shows curve-fitted F 1s core-level spectra of the sample. A dominant peak appearing at 689.32 eV corresponds to fluorine bonded as CF_x in the FAS chain indicating that F is present in same bonding environment as that of FAS [30]. A shoulder peak at higher binding energy of 689.75 eV could be associated with Si-F_x interaction [31]. This confirms the presence of fluoride groups on the silica particles [32]. Curve-fitted Si 2p core-level spectra of the sample are showed in Figure 4(c). Si 2p core-level spectra show a dominant peak at 104.15 eV, which corresponds to -Si-OH or Si-F_x species. Low-intense component peak around 102.64 eV could be due to SiO_2-based network. Figure 4(d) shows the multielement spectra of C 1s; observed peaks at 284.50, 284.78, 285.60, 292.00, and 294.27 eV are ascribed to C-Si, C-C, C-O, CF_2, and CF_3, respectively [30–32].

The universal utilization of superhydrophobic materials is hindered by their poor robustness. In other words, the micro/nanostructures which are indispensable for constructing the superhydrophobicity are destructed easily. To solve this problem, the asphalt was utilized as the binder which is widely used in pavement for its excellent mechanical strength

(a)

(b)
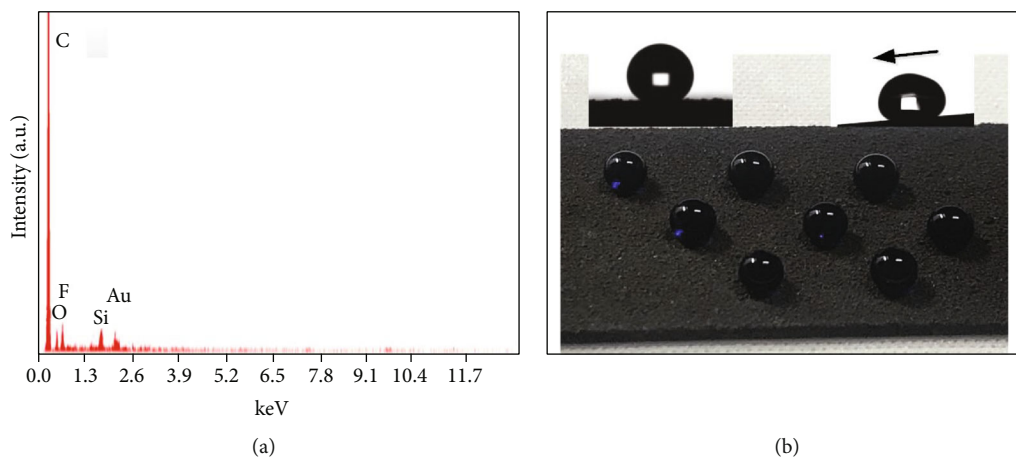
Figure 3: (a) EDS test of point 1 in Figure 2(b). (b) Photograph of water drops deposited on the superhydrophobic sample.

(a)

(b)

(c)

(d)
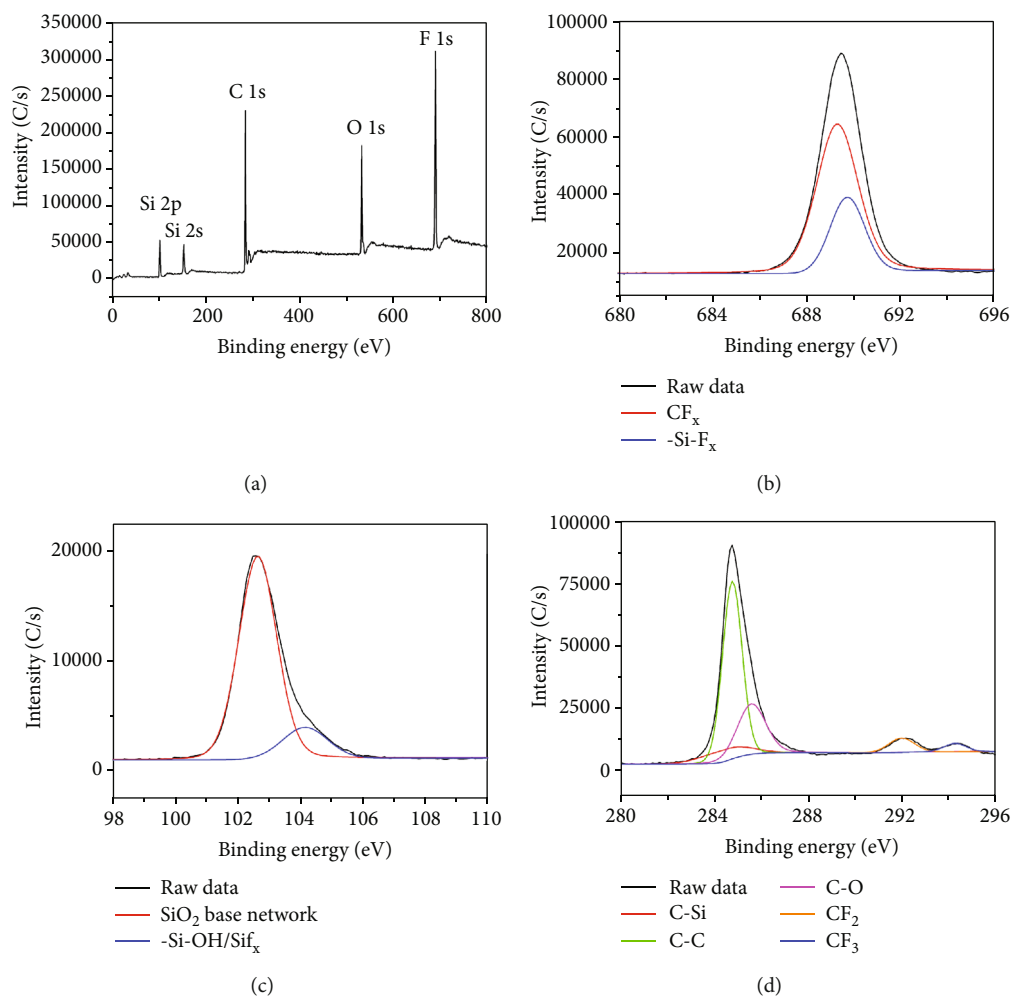
Figure 4: XPS measurement of the graphene superhydrophobic composite. (a) Survey XPS spectrum of the as-prepared superhydrophobic surface. (b) F 1s, (c) Si 2p, and (d) C 1s XPS spectrum of the sample.

and bonding force. At the same time, both micro- and nano-fillers were doped in the asphalt matrix to guarantee the formation of hierarchical structure which would enhance the mechanical durability. The sandpaper abrasion test has been widely utilized to evaluate the mechanical robustness [33–41]. Tian et al. further pointed out that the abrasion distance and applied pressure are two key factors to facilitate comparison among different researches [42].
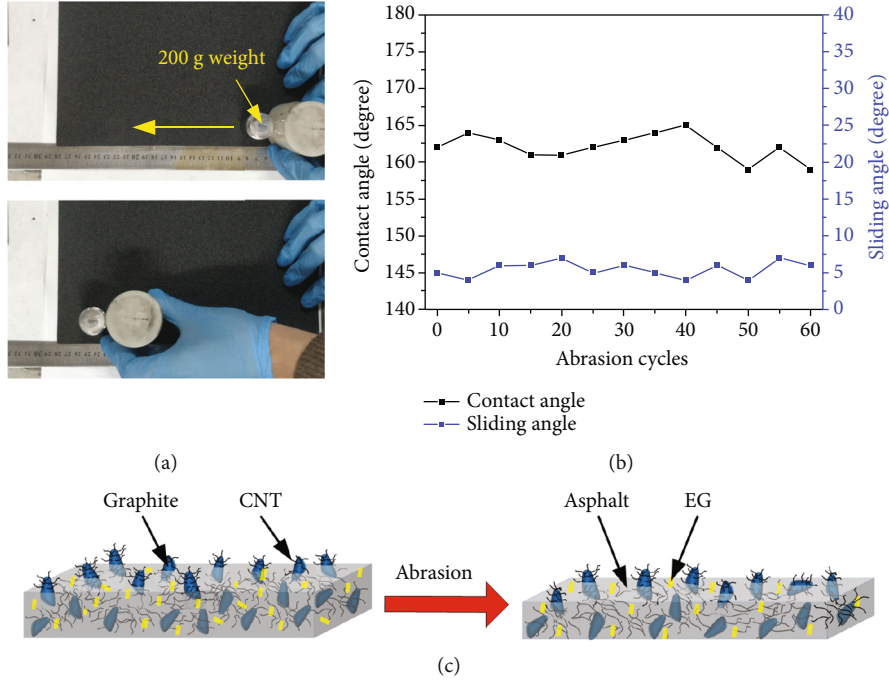
FIGURE 5: (a) Images of the processes and results of destruction by sandpaper abrasion. (b) The CAs and SAs on the as-prepared sample as a function of abrasion cycle. (c) The schematic of antiabrasion mechanism.

Thus, the sandpaper abrasion test was performed in this research. First, the sample was faced down to the rough surface of SiC sandpaper (200#). Then, a weight of 200 g (4.90 kPa) was put on the top of the sample, as shown in Figure 5(a) and Movie S1. By applying the external force, the sample moved along the ruler for 20 cm as one abrasion cycle. Although some powders could be found during the abrasion process, the superhydrophobicity was retained by watching the behavior of dropping waters. The quantitative changes in CAs and SAs during the abrasion process could be further found in Figure 5(b). Even after 60 abrasion cycles, the CA was 159° and the SA was 6°, indicating the outstanding mechanical robustness. Meanwhile, it was found that the thickness of the coating reduced from ~0.45 mm to ~0.10 mm. We ascribe the retention of superhydrophobicity to the self-similar structure (Figure 5(c)), which makes the undamaged layer of the superhydrophobic coating similar to the exposed parts in functionality and texture.

The conductivity of the materials has received more and more attention recently. On the one hand, the conductive coating could shed off the accumulated electrons and then improve the reliability of the microelectronic device. On the other hand, the excellent conductivity is indispensable for some special application such as the ground grid. In this research, we tried to optimize the electrical property by means of altering the amount of the MWCNTs and EGs. The electrical conductivity and antiabrasion ability were investigated simultaneously, and the results are summarized in Table 1. The detailed test method of the electrical conductivity and antiabrasion ability can be found in the experiment

TABLE 1: The experiment results of the superhydrophobicity with different contents of the filler.

Experiment	MWCNT (g)	EG (g)	Conductivity (S/m)	Antiabrasion (cycles)
1	0.10	0.00	1.96	600
2	0.15	0.03	4.26	300
3	0.20	0.04	8.53	80
4	0.30	0.05	42.46	60
5	0.35	0.06	138.14	5

section. With the addition of conductive fillers, the electrical conductivity is increased, but the antiabrasion property decreased simultaneously. Thus, how to make a balance between the electrical conductivity and antiabrasion property is a crucial challenge. After optimization, this coating could exhibit a conductivity of 42.46 S/m, which could maintain superhydrophobicity after 60 abrasion cycles.

Here, the soil was utilized as the model contaminant, and the glass slide was used as the substrate. As shown in Figure 6(a) and Movie S2, we first placed the superhydrophobic sample at a slope angle of ~15° and then spread a layer of soil onto the sample. In the next step, the water droplets were dribbled onto the sample. It can be found that the water droplets rolled down easily (Figures 6(b) and 6(c)). Once the water droplet contacted the soil particles, it would take the contaminant array due to the extremely low water adhesion. Finally, a completely clean sample was obtained (Figure 6(d)), suggesting the excellent self-cleaning property.

(a)

(b)

(c)

(d)
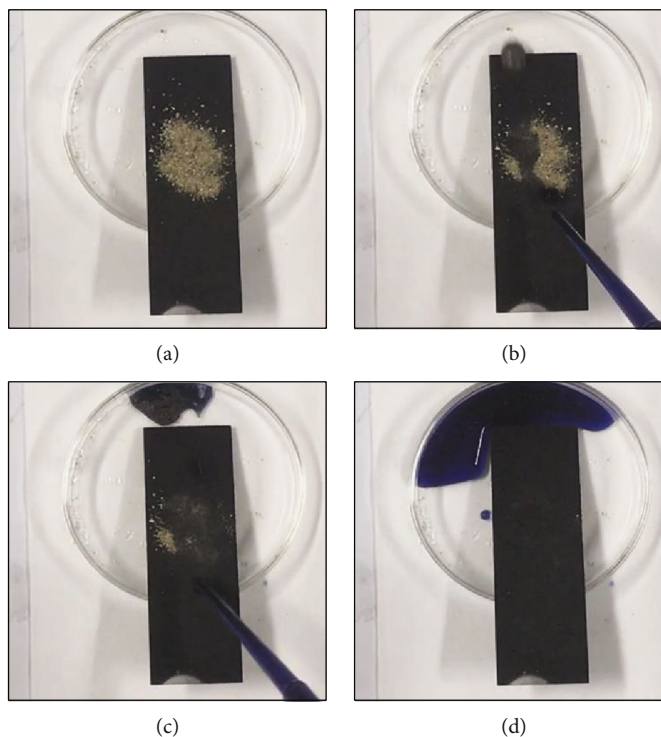
FIGURE 6: Self-cleaning process on the as-prepared superhydrophobic surface: (a) the surface contaminated by the soil powder; (b, c) the contaminated surface dropped with water droplets; (d) the contaminated surface after the water dropping process.

Moreover, this superhydrophobic coating exhibited excellent corrosion resistance [43–45]. The steel is universally utilized in our daily life due to their excellent mechanical strength, easy processing, and cost efficiency. Corrosion is regarded as the main failure mechanism for steel (especially for Q235 steel). In this research, we tried to improve the anticorrosive performance by means of superhydrophobic coating. The polarization curves were utilized to evaluate the corrosion resistance, as shown in Figure 7. Here, we employed the 3.5 wt% NaCl aqueous solutions as the electrolyte. Before the electrochemical test, we immersed the samples into the electrolyte for 3 h. Because the corrosion potential (E_{corr} vs. SCE) and the corrosion current density (i_{corr}) are two crucial for assessing the anticorrosive performance, we further deduced them from the polarization curves. The corrosion potentials for the bare Q235 steel, Q235 steel with epoxy coating, and superhydrophobic coating were calculated to be -0.198, -0.413, and -0.547 v, respectively. Furthermore, the corrosion current density for the bare Q235 steel, Q235 steel with epoxy coating, and superhydrophobic coating was calculated to be 2.41×10^{-5}, 6.24×10^{-6}, and 6.91×10^{-7} A/cm^2, respectively. Thus, the superhydrophobic coating could reduce the corrosion current density 35 folds compared with the bare sample and reduce 9 folds compared with the epoxy coating. We ascribed the outstanding corrosion resistance to superhydrophobicity. When the superhydrophobic coating was immersed in a corrosive solution, the micro/nanostructures of the coating tend to trap the air, which will serve as a cushion and hold back the electron transfer between Q235 steel substrate and the corrosive electrolyte [46, 47].
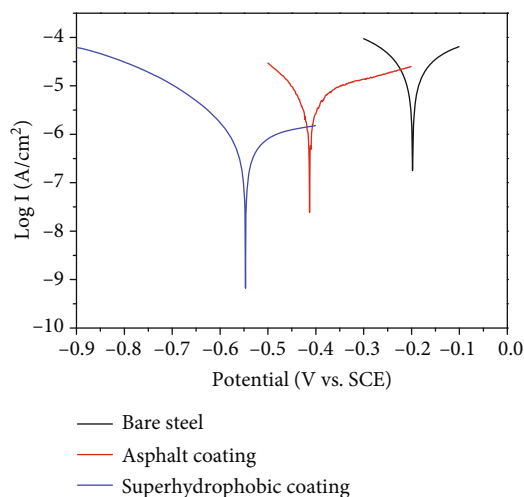
FIGURE 7: Tafel polarization curves of bare Q235 steel, epoxy coating, and superhydrophobic coating.

4. Conclusion

In summary, we reported a simple and cost-effective method to prepare superhydrophobic/conductive asphalt. The conductivity of the asphalt can be controlled by adding conductive filler. When the filler was dispersed uniformly in the asphalt matrix, the self-similar structure can be obtained. Moreover, the hierarchical structure could be constructed by adding nanoscale filler (carbon nanotube) and microscale filler (graphite powder and expanded graphite). Due to the

combination of self-similar and hierarchical structure, this superhydrophobic asphalt demonstrated mechanical robustness to the sandpaper abrasion. Moreover, this asphalt composite exhibited good conductivity, superior self-cleaning property, and excellent corrosion resistance.

Data Availability

The video data used to support the findings of this study are included within the supplementary information files.

Conflicts of Interest

The authors declare that they have no competing interests.

Acknowledgments

Supplementary Materials

The following are available online. Movie S1: the antiabrasion test. Movie S2: the self-cleaning test. (Supplementary Materials)

References

[1] G. Wu, E.-H. Choi, P. K. Chu, G. Dinescu, R. Jung, and Y. Zhao, "Recent applications of scanning microscopy in surface engineering," *Scanning*, vol. 2018, Article ID 7546310, 2 pages, 2018.

[2] P. Wang, T. Yao, B. Sun, T. Ci, X. Fan, and H. Han, "Fabrication of mechanically robust superhydrophobic steel surface with corrosion resistance property," *RSC Advances*, vol. 7, no. 63, pp. 39699–39703, 2017.

[3] Z. Wang, M. Wang, J. Jiang et al., "Atmospheric corrosion analysis and rust evolution research of Q235 carbon steel at different exposure stages in Chengdu atmospheric environment of China," *Scanning*, vol. 2020, Article ID 9591516, 8 pages, 2020.

[4] Y. Wang, G. Wu, and J. Sun, "Improved corrosion resistance of magnesium alloy in simulated concrete pore solution by hydrothermal treatment," *Scanning*, vol. 2020, article 4860256, pp. 1–7, 2020.

[5] Q. Zheng, K. Li, X. Yin et al., "Corrosion properties of 34CrMo4 steel modified by shot peening," *Scanning*, vol. 2017, Article ID 1928198, 8 pages, 2017.

[6] N. Wang, L. Tang, W. Tong, and D. Xiong, "Fabrication of robust and scalable superhydrophobic surfaces and investigation of their anti-icing properties," *Materials & Design*, vol. 156, pp. 320–328, 2018.

[7] N. Wang, L. Tang, Y. Cai, W. Tong, and D. Xiong, "Scalable superhydrophobic coating with controllable wettability and investigations of its drag reduction," *Colloids and Surfaces A: Physicochemical and Engineering*, vol. 555, pp. 290–295, 2018.

[8] X. Wang, M. Li, Y. Shen, Y. Yang, H. Feng, and J. Li, "Facile preparation of loess-coated membranes for multifunctional surfactant-stabilized oil-in-water emulsion separation," *Green Chemistry*, vol. 21, no. 11, pp. 3190–3199, 2019.

[9] X. Bai, Y. Shen, H. Tian, Y. Yang, H. Feng, and J. Li, "Facile fabrication of superhydrophobic wood slice for effective water-in-oil emulsion separation," *Separation and Purification Technology*, vol. 210, pp. 402–408, 2019.

[10] P. Wang, S. Wang, X. Zhang et al., "Rational construction of CoO/CoF$_2$ coating on burnt-pot inspired 2D CNs as the battery-like electrode for supercapacitors," *Journal of Alloys and Compounds*, vol. 819, article 153374, 2020.

[11] P. Wang, W. Wang, T. Ci, L. Li, and H. Han, "Pump-free oil droplet transfer by combining microfibre array and superoleophobic mesh," *Applied Surface Science*, vol. 455, pp. 980–986, 2018.

[12] G. Wei, Z. Wang, X. Zhao et al., "Pump-free oil droplet transfer by combining microfibre array and superoleophobic mesh," *Materials Research Express*, vol. 2, article 015501, 2015.

[13] R. Qiu, Z. Li, and Z. Wu, "Enhanced anti-icing and anti-corrosion properties of wear-resistant superhydrophobic surfaces based on Al alloys," *Materials Research Express*, vol. 6, no. 4, article 045059, 2019.

[14] N. Wang, D. Xiong, Y. Deng, Y. Shi, and K. Wang, "Mechanically robust superhydrophobic steel surface with anti-icing, UV-durability, and corrosion resistance properties," *ACS Applied Materials & Interfaces*, vol. 7, no. 11, pp. 6260–6272, 2015.

[15] Y. Cao, D. Zheng, X. Li et al., "Enhanced corrosion resistance of superhydrophobic layered double hydroxide films with long-term stability on Al substrate," *ACS Applied Materials & Interfaces*, vol. 10, no. 17, pp. 15150–15162, 2018.

[16] F. Zhang, H. Qian, L. Wang et al., "Superhydrophobic carbon nanotubes/epoxy nanocomposite coating by facile one-step spraying," *Surface and Coatings Technology*, vol. 341, pp. 15–23, 2018.

[17] M. Liu, Y. Hou, J. Li, L. Tie, Y. Peng, and Z. Guo, "Inorganic adhesives for robust, self-healing, superhydrophobic surfaces," *Journal of Materials Chemistry A*, vol. 5, no. 36, pp. 19297–19305, 2017.

[18] P. Wang, W. Wei, Z. Li, W. Duan, H. Han, and Q. Xie, "A superhydrophobic fluorinated PDMS composite as a wearable strain sensor with excellent mechanical robustness and liquid impalement resistance," *Journal of Materials Chemistry A*, vol. 8, no. 6, pp. 3509–3516, 2020.

[19] Y. Lu, S. Sathasivam, J. Song, C. R. Crick, C. J. Carmalt, and I. P. Parkin, "Repellent materials. Robust self-cleaning surfaces that function when exposed to either air or oil," *Science*, vol. 347, no. 6226, pp. 1132–1135, 2015.

[20] T. Verho, C. Bower, P. Andrew, S. Franssila, O. Ikkala, and R. H. A. Ras, "Mechanically durable superhydrophobic surfaces," *Advanced Materials*, vol. 23, no. 5, pp. 673–678, 2011.

[21] C. Peng, Z. Chen, and M. K. Tiwari, "All-organic superhydrophobic coatings with mechanochemical robustness and liquid impalement resistance," *Nature Materials*, vol. 17, no. 4, pp. 355–360, 2018.

[22] M. J. Nine, M. A. Cole, L. Johnson, D. N. H. Tran, and D. Losic, "Robust superhydrophobic graphene-based composite coatings with self-cleaning and corrosion barrier properties," *ACS Applied Materials & Interfaces*, vol. 7, no. 51, pp. 28482–28493, 2015.

[23] I. Hejazi, G. M. M. Sadeghi, S. H. Jafari et al., "Transforming an intrinsically hydrophilic polymer to a robust self-cleaning superhydrophobic coating via carbon nanotube surface embedding," *Materials & Design*, vol. 86, pp. 338–346, 2015.

[24] J. Gu, P. Xiao, J. Chen et al., "Robust preparation of superhydrophobic polymer/carbon nanotube hybrid membranes for highly effective removal of oils and separation of water-in-oil emulsions," *Journal of Materials Chemistry A*, vol. 2, no. 37, pp. 15268–15272, 2014.

[25] P. Wang, T. Yao, B. Sun et al., "A cost-effective method for preparing mechanically stable anti-corrosive superhydrophobic coating based on electrochemically exfoliated graphene," *Colloids and Surfaces A: Physicochemical and Engineering Aspects*, vol. 513, pp. 396–401, 2017.

[26] W. Li, Y. Wang, Y. Feng et al., "Fabrication of robust conductive and superhydrophobic coating based on carbon nanotubes," *Materials Research Express*, vol. 7, no. 5, article 055009, 2020.

[27] Y. Gao, L. Qu, B. He, K. Dai, Z. Fang, and R. Zhu, "Study on effectiveness of anti-icing and deicing performance of superhydrophobic asphalt concrete," *Construction and Building Materials*, vol. 191, pp. 270–280, 2018.

[28] P. Wang, M. Chen, H. Han, X. Fan, Q. Liu, and J. Wang, "Transparent and abrasion-resistant superhydrophobic coating with robust self-cleaning function in either air or oil," *Journal of Materials Chemistry A*, vol. 4, no. 20, pp. 7869–7874, 2016.

[29] N.-u.- H. Saddiqi and S. Seeger, "Chemically resistant, electric conductive, and superhydrophobic coatings," *Advanced Materials Interfaces*, vol. 6, no. 7, article 1900041, 2019.

[30] B. J. Basu, V. D. Kumar, and C. Anandan, "Surface studies on superhydrophobic and oleophobic polydimethylsiloxane-silica nanocomposite coating system," *Applied Surface Science*, vol. 261, pp. 807–814, 2012.

[31] N. Saleema, D. K. Sarkar, D. Gallant, R. W. Paynter, and X. G. Chen, "Chemical nature of superhydrophobic aluminum alloy surfaces produced via a one-step process using fluoroalkyl-silane in a base medium," *ACS Applied Materials & Interfaces*, vol. 3, no. 12, pp. 4775–4781, 2011.

[32] H. Wang, J. Fang, T. Cheng et al., "One-step coating of fluoro-containing silica nanoparticles for universal generation of surface superhydrophobicity," *Chemical Communications*, vol. 877, no. 7, pp. 877–879, 2008.

[33] P. Wang, B. Sun, Y. Liang et al., "A stretchable and super-robust graphene superhydrophobic composite for electromechanical sensor application," *Journal of Materials Chemistry A*, vol. 6, no. 22, pp. 10404–10410, 2018.

[34] X. Zhang, L. Wang, and J. D. Sørensen, "REIF: a novel active-learning function toward adaptive Kriging surrogate models for structural reliability analysis," *Reliability Engineering & System Safety*, vol. 185, pp. 440–454, 2019.

[35] X. Zhang, L. Wang, and J. D. Sørensen, "AKOIS: an adaptive Kriging oriented importance sampling method for structural system reliability analysis," *Structural Safety*, vol. 82, p. 101876, 2020.

[36] J. Wang, L. Pan, Y. Bian, and Y. Lu, "Experimental investigation of the surface roughness of finish-machined high-volume-fraction SiCp/Al composites," *Arabian Journal for Science and Engineering*, vol. 45, no. 7, pp. 5399–5406, 2020.

[37] P. Wang, B. Sun, T. Yao et al., "A novel dissolution and resolidification method for preparing robust superhydrophobic polystyrene/silica composite," *Chemical Engineering Journal*, vol. 326, pp. 1066–1073, 2017.

[38] J. Song, D. Zhao, Z. Han et al., "Super-robust superhydrophobic concrete," *Journal of Materials Chemistry A*, vol. 5, no. 28, pp. 14542–14550, 2017.

[39] J. Song, F. Guan, W. Pan et al., "Droplet-based self-propelled miniboat," *Advanced Functional Materials*, vol. 30, no. 16, p. 1910778, 2020.

[40] J. Song, L. Huang, C. Zhao et al., "Robust superhydrophobic conical pillars from syringe needle shape to straight conical pillar shape for droplet pancake bouncing," *ACS Applied Materials & Interfaces*, vol. 11, no. 48, pp. 45345–45353, 2019.

[41] J. Song, Z. Liu, X. Wang et al., "High-efficiency bubble transportation in an aqueous environment on a serial wedge-shaped wettability pattern," *Journal of Materials Chemistry A*, vol. 7, no. 22, pp. 13567–13576, 2019.

[42] X. Tian, T. Verho, and R. H. A. Ras, "Moving superhydrophobic surfaces toward real-world applications," *Science*, vol. 352, no. 6282, pp. 142-143, 2016.

[43] X. Yin, Z. Wang, Y. Shen, P. Mu, G. Zhu, and J. Li, "Facile fabrication of superhydrophobic copper hydroxide coated mesh for effective separation of water-in-oil emulsions," *Separation and Purification Technology*, vol. 230, p. 115856, 2020.

[44] J. Li, R. Kang, X. Tang, H. She, Y. Yang, and F. Zha, "Superhydrophobic meshes that can repel hot water and strong corrosive liquids used for efficient gravity-driven oil/water separation," *Nanoscale*, vol. 8, no. 14, pp. 7638–7645, 2016.

[45] J. Li, L. Yan, X. Tang, H. Feng, D. Hu, and F. Zha, "Robust superhydrophobic fabric bag filled with polyurethane sponges used for vacuum-assisted continuous and ultrafast absorption and collection of oils from water," *Advanced Materials Interfaces*, vol. 3, no. 9, p. 1500770, 2016.

[46] P. C. Uzoma, F. Liu, L. Xu et al., "Superhydrophobicity, conductivity and anticorrosion of robust siloxane-acrylic coatings modified with graphene nanosheets," *Progress in Organic Coatings*, vol. 127, pp. 239–251, 2019.

[47] M. J. Kreder, J. Alvarenga, P. Kim, and J. Aizenberg, "Design of anti-icing surfaces: smooth, textured or slippery?," *Nature Reviews Materials*, vol. 1, no. 1, pp. 1–15, 2016.

WILEY | Hindawi

Research Article

Accuracy and Precision Evaluation of International Standard Spherical Model by Digital Dental Scanners

Hong Xin Cai,[1] Qi Jia,[1] HaoYu Shi,[1] Yujie Jiang,[1] Jingnan Xue,[1] ChunXu Chen,[1] Haotian Gong,[1] Jie Liu,[1] Eui-Seok Lee [ID],[2] and Heng Bo Jiang [ID][1]

[1]*Stomatological Materials Laboratory, School of Stomatology, Shandong First Medical University & Shandong Academy of Medical Sciences, Tai'an, Shandong 271016, China*
[2]*Department of Oral and Maxillofacial Surgery, Graduate School of Clinical Dentistry, Korea University, Seoul 08308, Republic of Korea*

Correspondence should be addressed to Eui-Seok Lee; ees225@hanmail.net and Heng Bo Jiang; hengbojiang@vip.qq.com

With the popularization of digital technology and the exposure of traditional technology's defects, computer-aided design and computer-aided manufacturing (CAD/CAM) has been widely used in the field of dentistry. And the accuracy of the scanning system determines the ultimate accuracy of the prosthesis, which is a very important part of CAD/CAM, so we decided to evaluate the accuracy of the intraoral and extraoral scanners. In this study, we selected the sphere model as the scanning object and obtained the final result through data analysis and 3D fitting. In terms of trueness and precision, the scanner of SHINING was significantly different from that of others; however, there was no significant difference between TRIOS and CEREC. SHINING showed the lowest level of accuracy, with CEREC slightly lower than TRIOS. The sphere model has also been proven to be scanned successfully.

1. Introduction

With the emergence of digitalization, CAD/CAM systems [1] have found an increasingly wide utilization in the field of prosthodontics on account of its considerable strengths [2]. Given the fact that the traditional prostheses gradually fail to meet the needs of patients, the use of intraoral [3] and extraoral scanners in dentistry is becoming more and more common [4, 5].

By using the specific and intuitive model presented from intraoral and extraoral scanners [6–9], we can immediately obtain detailed information of the patient's oral cavity and its digital files. And the files will be imported into the computer to complete the design and production [10]. The extraoral scanner scans the impression model, and the intraoral scanner directly scans the patient's oral cavity [7]. Compared to the traditional technology, the scanning technology is undoubtedly time-saving and efficient [11, 12].

There are many factors that affect the scanning results and data collection. Recent studies have shown that different scanning strategies can affect the accuracy of results [13]. It has been reported that different scanning systems also contribute to different experimental results [14]. In addition, the selection of the impression materials and operation time will affect the accuracy of extraoral scanners, while the scanning range, light [15], and oral tissue will affect intraoral scanners [16, 17].

Considering the above factors, it is of clinical significance to evaluate the accuracy of intraoral and extraoral scanners [9]. The early Flügge's study claimed that the extraoral scanners performed better than intraoral scanners under the oral environment [13]. However, as the algorithms and scanning techniques evolve, Tomita et al. concluded that the intraoral scanners had higher accuracy than extraoral scanners as they were studying their self-manufactured denture model *in vitro* [18]. Further, the performance of the intraoral

(a)

(b)
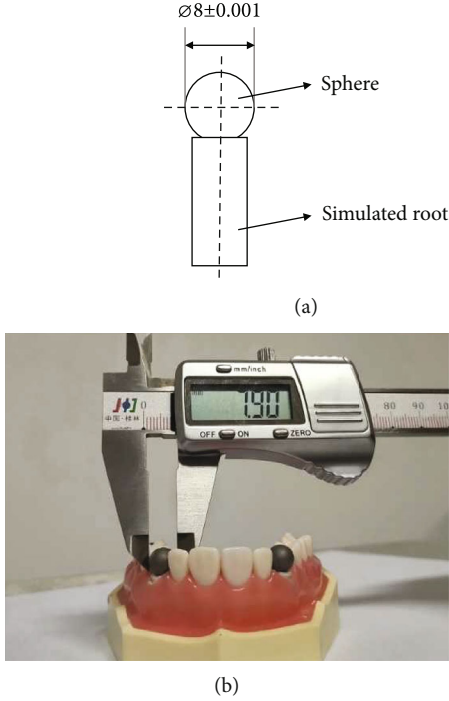
FIGURE 1: Design drawings of the (a) sphere model, and (b) optical image.

TABLE 1: Mean trueness/precision values ± standard deviation (SD).

Test group	Trueness (mm)	Precision (mm)
SHINING	0.061 ± 0.018	0.059 ± 0.023
CEREC	0.010 ± 0.010	0.014 ± 0.010
TRIOS	0.006 ± 0.003	0.006 ± 0.003
True value		7.908

scanner is significantly influenced by the geometry of the scanned object, for the fact that it accumulates the scanned image and records the scanning path of the object to obtain the complete image. Especially, the uniformity of the model will also reduce the performance of the intraoral scanner. Therefore, this study is based on an international standard model to evaluate the accuracy of intraoral and extraoral scanners [19, 20].

After looking up a lot of literature, we found that there were few papers based on the sphere model [19], so this experiment adopted the ISO standard sphere model [21]. According to the definition of accuracy regulated in ISO 5725 including trueness and precision, the trueness refers to the degree of uniformity between a measurement result and the reference value, while the latter one maintains the uniformity between independent measurement results. According to the standard in ISO 3290-2, we chose a sphere with Grade 20 to conduct the experiment. And the error of diameter and surface less than 0.001 mm can be ignored in this grade [22].

(a)

(b)
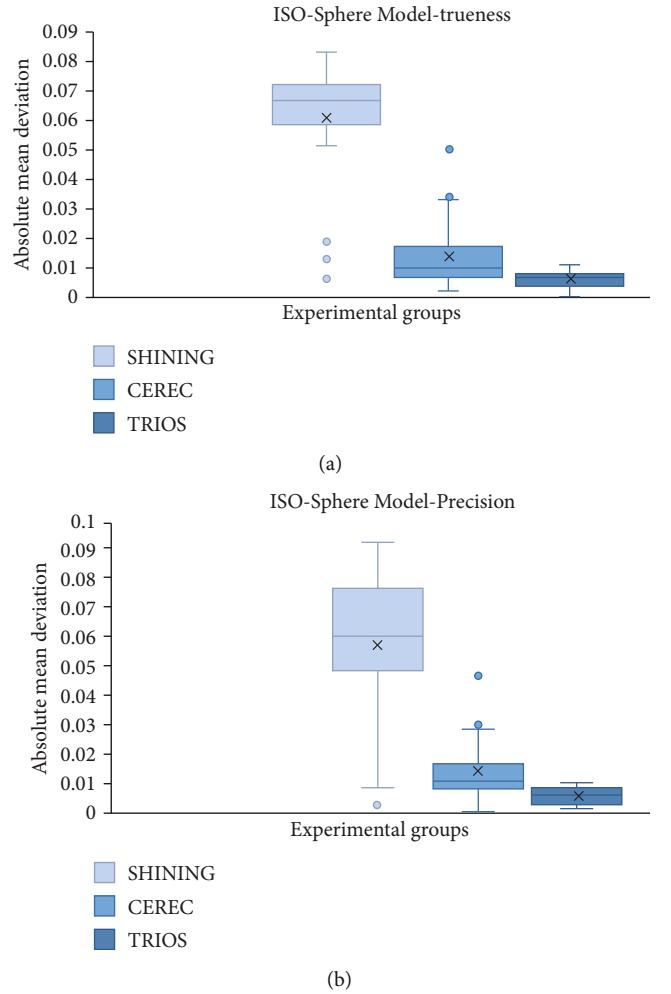
FIGURE 2: Boxplots of absolute mean trueness (a) and precision values (b) of the sphere model. The horizontal line of each Boxplot from top to bottom represents the upper edge, upper quartile, median, lower quartile, and lower edge of the value, respectively, in addition the round dots represent outliers, and the crosses represent averages.

TABLE 2: Relative errors of the trueness and precision of the sphere model (diameter).

Test group	Trueness (mm)	Precision (mm)
SHINING	0.008	0.008
CEREC	0.002	0.002
TRIOS	0.001	0.001

2. Materials and Methods

2.1. Fabrication of Models. According to the clinical practice, the theoretical value of the diameter of the sphere model based on the ISO 12836 [21] was set as 8 mm, as shown in Figure 1(a). The 3D file of the model was drawn by computer-aided design software (AutoCAD 2018, Autodesk, USA), which was exported in stereolithography (STL)
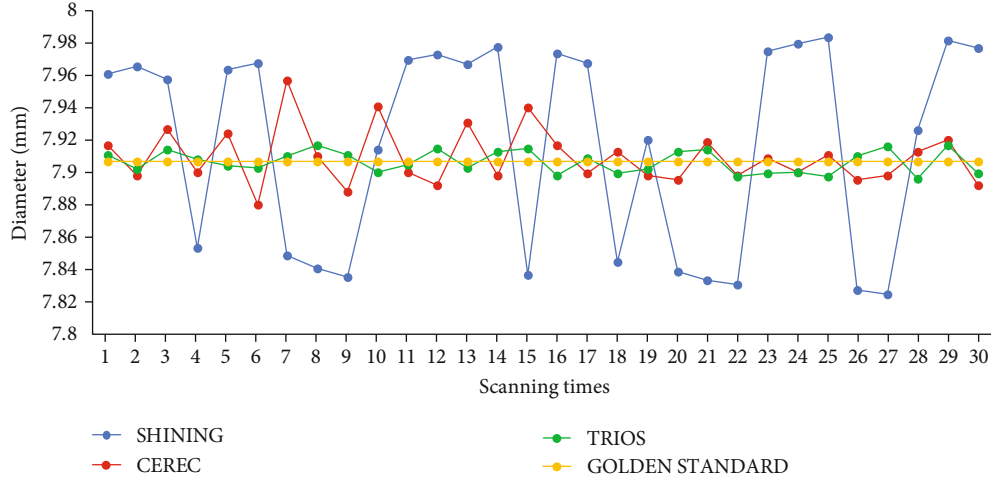
FIGURE 3: The broken line graph of the original data of the sphere model diameter measured by scanners. The fluctuation range and frequency of the tree broken lines are different and represent different meanings. (The yellow line used for comparison means the gold standard.)

TABLE 3: RMSE values for the 3D-fitting results.

Test group	RMSE
SHINING	0.064
CEREC	0.017
TRIOS	0.007

format. The test model was made of stainless steel, and we used computer numerical controlled (CNC) milling to fabricate it. Moreover, the model was sandblasted with a powder size of 80 μm as specified by the international standard.

2.2. Creation of Gold Standard Values. Thirty measurements of the sphere model's diameter were taken by Vernier Calipers, the average of which was taken as the truth value in this paper. One of the measurements was shown in Figure 1(b). The true value was set as the gold standard for evaluation, and the 3D file based on the value was created as the gold standard file for 3D fitting.

2.3. Scanning Process. One extraoral scanner (SHINING D200+, CHN) and two intraoral scanners (CEREC AC D3492, Sirona, GER and TRIOS T12A, 3Shape, DEN), respectively, performed 30 scans of the sphere model and saved them as STL files. The model was scanned by the same skilled technician who followed the scanning method recommended by the different instrument manufacturers to eliminate interference and improve feasibility [7].

2.4. Data Acquisition and Image Matching. The scanned original files were converted into STL files, which were then imported into a reverse engineering software (Geomagic Control X 2018, 3D SYSTEMS, USA). The test indicator (diameter) was measured and recorded through the software, and the 3D files of test groups were compared with the gold standard files for 3D fitting. Meanwhile, root mean square error (RMSE) values were recorded.

2.5. Mathematical Analysis. The formula for accuracy assessment is as follows [23]:

$$\text{Trueness} = |(d_R - d_M)|, \tag{1}$$

$$\text{Precision} = |(d_A - d_M)|, \tag{2}$$

$$\Delta d_M = |(d_R - d_M)/d_R|, \tag{3}$$

$$\Delta S(d_M) = |S(d_M)/d_R|,$$

d_R : The standard reference value for the
  diameter of the model,

d_M : Measured value for the diameter of the model,

d_A : Average of the measured value for
  the diameter of the model,

Δd_M : Relative error of trueness,

$\Delta S(d_M)$: Relative error of precision,

$S(d_M)$: Standard deviation of the measured
  value for the diameter of the model.

$$\tag{4}$$

Perform statistical analysis on scanned data using SPSS v.20.0 (IBM, USA). The data conform to a normal distribution, but they are not conformable in the homogeneity of the variance. The Nonparametric Kruskal-Wallis test analyzed the difference in parameters and the result of $p < 0.01$ attested statistically significant differences.

3. Results

3.1. Absolute Mean Trueness and Precision of the Sphere Model. The value of absolute mean trueness and precision of the sphere model is enumerated in Table 1. Figure 2(a) shows boxplots of the absolute mean trueness values, and Figure 2(b) shows boxplots of the absolute mean precision
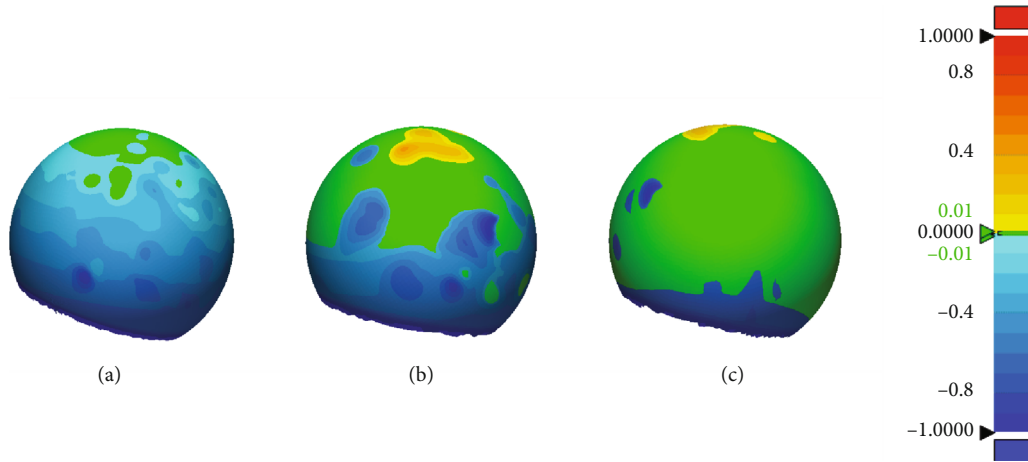
FIGURE 4: 3D-fitting comparison of digital impression files ((a) SHINING, (b) CEREC, and (c) TRIOS) with gold standard file. Within the specified accuracy range, green represents the overlap between test groups and control group, yellow represents higher than the control group, and blue represents lower than the control group. The greener areas mean the more accurate the scanned image.

values of the sphere model. Regarding diameter errors of the sphere model, the TRIOS reveals the highest trueness and precision, respectively. The comparison between the intraoral scanners and the extraoral scanners shows that compared to the CEREC and SHINING, the mean trueness value of TRIOS is much lower. The mean precision value of TRIOS is significantly lower than CEREC and SHINING.

3.2. Relative Errors of Sphere Model. Table 2 shows the relative errors of the trueness and precision of the sphere model. The relative errors of the sphere model are less than 0.008 mm, respectively. This is an ideal result that when comparing the relative errors of trueness and precision between these scanners, the trend is similar to that of the absolute mean deviation of trueness and precision.

3.3. Broken Line Graph and RMSE. The broken line graph of the original data of the sphere model diameter measured by scanners is shown in Figure 3. The yellow line is the gold standard. It is obvious that SHINING's values are not concentrated and far from the yellow line. We found that the values of CEREC and TRIOS were very close to the gold standard, also highly centralized and accurately combined with RMSE in Table 3.

3.4. 3D-Fitting Measurement. Figure 4 shows a 3D-fitting comparison of the digital impression between test groups and the control group. The difference in colors other than green represents the difference between the measured value and the gold standard. More green areas mean the scanned image more accurate. The results show that there is a larger error of SHINING compared with other scanners, and a large area is lower than the control group. The fitting result of TRIOS is the best with the largest green area.

3.5. Analysis of Significant Difference. We find that there is no significant difference between CEREC and TRIOS, but the absolute mean precision values of the CEREC are significantly lower than TRIOS through statistical analysis. And

SHINING is different from CEREC and TRIOS in terms of precision and trueness obviously.

4. Discussion

In this study, the accuracy of intraoral and extraoral scanners was evaluated by a sphere model described in ISO 12836 [21]. The sphere model is of positive geometry with a precision limited to 0.0002 mm, made of dimensionally stable stainless steel. There have been many studies evaluating the accuracy of scanners by Inlay-cavity die and Grown-and-bridge die, but few studies are based on the sphere model because it is difficult to be identified by the intraoral scanner.

Arakida et al. assessed the influence of ambient light illumination and color temperature on the authenticity and accuracy of a digital signal and proved that the conditions of 3900 k and 500 lux are the most suitable conditions for digital scanning [24]. Sun et al. compared the reproducibility of intraoral scanners *in vivo* and *in vitro*, respectively, and the results showed that the reproducibility was comparable, so different scanning environment will affect the scanning results of intraoral scanners [25].

According to the scanning standard described in ISO 12836 [21], the scanning process of each scanner was executed 30 times with room temperature of $(23 \pm 2)°C$ and the change of temperature controlled within $\pm 1°C$, which we had followed to minimize the error caused by external interference.

There are still many factors like equipment or manual operations that can affect the accuracy of the scanner [26]. Therefore, we designed some schemes aimed at these problems to minimize their impact on accuracy. The scanning principle and operation methods of intraoral and extraoral scanners in this experiment are different. And we added a base at the bottom of the sphere model for proper operation. If the operator had touched the sphere directly by hand in the experiment, the surface of the model would have changed greatly and thus the final result would have been affected.

Thus, it is necessary to add the base which can also fix the sphere model to make scanning easier.

Reproducibility and repeatability are also important components of the evaluation [27]. Reproducibility can be defined as the consistency of the measured results of the same object under different conditions, while repeatability is affected by operating, timing, equipment, etc. Therefore, this experiment was carried out by a skilled operator in strict accordance with the methods specified by the scanner manufacturers to reduce the influence of operation.

There is no significant difference between values obtained in the experiment and the standard values created from the model, so it is feasible to scan the sphere model with these three scanners.

There are limitations to our experiments as well. The long operation of the scanner may result in the degradation of the performance, which may affect the scanning results of the latter part. And the choice of a single model has some limitations in the evaluation of scanners. In terms of the clinic, due to the complex oral environment, like saliva, blood, and soft tissue, there will be deviations in the actual operation [28, 29]. Additionally, the level of analysis and measurement software used also affects the results.

According to the study of Burzynski et al., with the progress of intraoral scanning technology, the shrinking of the camera, and the acceleration of acquisition time, patients may show a greater preference for digital impression [30]. Through investigation, Ahmed et al. found that with the development of digitization and the improvement of scanner accuracy, people's acceptance of using CAD/CAM for oral disease treatment has gradually increased [31]. Alghazzawi argued that the coming trend for most practitioners would be the use of an acquisition camera attached to a computer that was equipped with appropriate software and the capability of forwarding the image to the laboratory [32].

Our experiment compared one extraoral scanner (SHINING) with two intraoral scanners (CEREC, TRIOS), whose results showed that the accuracy of CEREC was between the other two. It indicated that the intraoral scanners were better than the extraoral one. Since no controversy was shown in the results of this experiment, the results of clinical trials of the extraoral and intraoral scanners need further discussion.

5. Conclusions

The accuracy of the intraoral scanners in this experiment was greater than that of the extraoral scanner. The intraoral scanner has certain reliability in practical application and is worth to trial in clinics. The sphere model is achievable as a scanning object, but it requires further research and improvement.

Data Availability

The data used to support the findings of this study are included within the article.

Conflicts of Interest

We declare that we have no financial and personal relationships with other people or organizations that can inappropriately influence our work.

Authors' Contributions

HongXin Cai, Qi Jia, and HaoYu Shi contributed equally to this work.

Acknowledgments

References

[1] M. J. Peluso, S. D. Josell, S. W. Levine, and B. J. Lorei, "Digital models: an introduction," *Seminars in Orthodontics*, vol. 10, no. 3, pp. 226–238, 2004.

[2] M. Santoro, S. Galkin, M. Teredesai, O. F. Nicolay, and T. J. Cangialosi, "Comparison of measurements made on digital and plaster models," *American Journal of Orthodontics and Dentofacial Orthopedics*, vol. 124, no. 1, pp. 101–105, 2003.

[3] M. Imburgia, S. Logozzo, U. Hauschild, G. Veronesi, C. Mangano, and F. G. Mangano, "Accuracy of four intraoral scanners in oral implantology: a comparative in vitro study," *BMC Oral Health*, vol. 17, no. 1, p. 92, 2017.

[4] R. Nedelcu, P. Olsson, I. Nyström, J. Rydén, and A. Thor, "Accuracy and precision of 3 intraoral scanners and accuracy of conventional impressions: a novel in vivo analysis method," *Journal of Dentistry*, vol. 69, pp. 110–118, 2018.

[5] S. Shimizu, A. Shinya, S. Kuroda, and H. Gomi, "The accuracy of the cad system using intraoral and extraoral scanners for designing of fixed dental prostheses," *Dental Materials Journal*, vol. 36, no. 4, pp. 402–407, 2017.

[6] L. O. L. Bohner, G. De Luca Canto, B. S. Marció, D. C. Laganá, N. Sesma, and P. T. Neto, "Computer-aided analysis of digital dental impressions obtained from intraoral and extraoral scanners," *The Journal of Prosthetic Dentistry*, vol. 118, no. 5, pp. 617–623, 2017.

[7] G. H. Park, K. Son, and K. B. Lee, "Feasibility of using an intraoral scanner for a complete-arch digital scan," *The Journal of Prosthetic Dentistry*, vol. 121, no. 5, pp. 803–810, 2019.

[8] A. P. Keating, J. Knox, R. Bibb, and A. I. Zhurov, "A comparison of plaster, digital and reconstructed study model accuracy," *Journal of Orthodontics*, vol. 35, no. 3, pp. 191–201, 2008.

[9] S. B. Patzelt, A. Emmanouilidi, S. Stampf, J. R. Strub, and W. Att, "Accuracy of full-arch scans using intraoral scanners," *Clinical Oral Investigations*, vol. 18, no. 6, pp. 1687–1694, 2014.

[10] S. Logozzo, E. M. Zanetti, G. Franceschini, A. Kilpelä, and A. Mäkynen, "Recent advances in dental optics – part i: 3d intraoral scanners for restorative dentistry," *Optics and Lasers in Engineering*, vol. 54, pp. 203–221, 2014.

[11] S. B. Patzelt, S. Bishti, S. Stampf, and W. Att, "Accuracy of computer-aided design/computer-aided manufacturing-generated dental casts based on intraoral scanner data," *Journal of the American Dental Association*, vol. 145, no. 11, pp. 1133–1140, 2014.

[12] R. van Noort, "The future of dental devices is digital," *Dental Materials*, vol. 28, no. 1, pp. 3–12, 2012.

[13] T. V. Flugge, S. Schlager, K. Nelson, S. Nahles, and M. C. Metzger, "Precision of intraoral digital dental impressions with itero and extraoral digitization with the itero and a model scanner," *American Journal of Orthodontics and Dentofacial Orthopedics*, vol. 144, no. 3, pp. 471–478, 2013.

[14] D. T. Chandran, D. C. Jagger, R. G. Jagger, and M. E. Barbour, "Two- and three-dimensional accuracy of dental impression materials: effects of storage time and moisture contamination," *Bio-medical Materials and Engineering*, vol. 20, no. 5, pp. 243–249, 2010.

[15] B. Giménez, M. Özcan, F. Martínez-Rus, and G. Pradíes, "Accuracy of a digital impression system based on active triangulation technology with blue light for implants: effect of clinically relevant parameters," *Implant Dentistry*, vol. 24, no. 5, pp. 498–504, 2015.

[16] T. Grunheid, S. D. McCarthy, and B. E. Larson, "Clinical use of a direct chairside oral scanner: an assessment of accuracy, time, and patient acceptance," *American Journal of Orthodontics and Dentofacial Orthopedics*, vol. 146, no. 5, pp. 673–682, 2014.

[17] J. Maeng, Y. J. Lim, B. Kim, M.-J. Kim, and H.-B. Kwon, "A new approach to accuracy evaluation of single-tooth abutment using two-dimensional analysis in two intraoral scanners," *International Journal of Environmental Research and Public Health*, vol. 16, no. 6, article 1021, 2019.

[18] Y. Tomita, J. Uechi, M. Konno, S. Sasamoto, M. Iijima, and I. Mizoguchi, "Accuracy of digital models generated by conventional impression/plaster-model methods and intraoral scanning," *Dental Materials Journal*, vol. 37, no. 4, pp. 628–633, 2018.

[19] F. Emir and S. Ayyildiz, "Evaluation of the trueness and precision of eight extraoral laboratory scanners with a complete-arch model: a three-dimensional analysis," *Journal of Prosthodontic Research*, vol. 63, no. 4, pp. 434–439, 2019.

[20] J. L. Porter, C. K. Carrico, S. J. Lindauer, and E. Tüfekçi, "Comparison of intraoral and extraoral scanners on the accuracy of digital model articulation," *Journal of Orthodontics*, vol. 45, no. 4, pp. 275–282, 2018.

[21] International Standard (ISO) 12836, *Dentistry —Digitizing Devices for CAD/CAM Systems for Indirect Dental Restorations— Test Methods for Assessing Accuracy*, International Organization for Standardization, Geneva, Switzerland, 2nd edition, 2015.

[22] R. G. Nedelcu and A. S. Persson, "Scanning accuracy and precision in 4 intraoral scanners: an in vitro comparison based on 3-dimensional analysis," *The Journal of Prosthetic Dentistry*, vol. 112, no. 6, pp. 1461–1471, 2014.

[23] ADA/ANSI Standard No. 132, *Scanning Accuracy of Dental Chairside and Laboratory CAD/CAM System*, American Dental Association, Chicago, IL, USA, 2015.

[24] T. Arakida, M. Kanazawa, M. Iwaki, T. Suzuki, and S. Minakuchi, "Evaluating the influence of ambient light on scanning trueness, precision, and time of intra oral scanner," *Journal of Prosthodontic Research*, vol. 62, no. 3, pp. 324–329, 2018.

[25] L. Sun, J. S. Lee, H. H. Choo, H. S. Hwang, and K. M. Lee, "Reproducibility of an intraoral scanner: a comparison between in-vivo and ex-vivo scans," *American Journal of Orthodontics and Dentofacial Orthopedics*, vol. 154, no. 2, pp. 305–310, 2018.

[26] P. Gonzalez de Villaumbrosia, F. Martinez-Rus, A. Garcia-Orejas, M. P. Salido, and G. Pradíes, "In vitro comparison of the accuracy (trueness and precision) of six extraoral dental scanners with different scanning technologies," *The Journal of Prosthetic Dentistry*, vol. 116, no. 4, pp. 543–550.e1, 2016.

[27] H. B. Jacob, G. D. Wyatt, and P. H. Buschang, "Reliability and validity of intraoral and extraoral scanners," *Progress in Orthodontics*, vol. 16, no. 1, p. 38, 2015.

[28] J. Abduo and M. Elseyoufi, "Accuracy of intraoral scanners: a systematic review of influencing factors," *The European Journal of Prosthodontics and Restorative Dentistry*, vol. 26, no. 3, pp. 101–121, 2018.

[29] F. S. Andriessen, D. R. Rijkens, W. J. van der Meer, and D. W. Wismeijer, "Applicability and accuracy of an intraoral scanner for scanning multiple implants in edentulous mandibles: a pilot study," *The Journal of Prosthetic Dentistry*, vol. 111, no. 3, pp. 186–194, 2014.

[30] J. A. Burzynski, A. R. Firestone, F. M. Beck, H. W. Fields Jr., and T. Deguchi, "Comparison of digital intraoral scanners and alginate impressions: time and patient satisfaction," *American Journal of Orthodontics and Dentofacial Orthopedics*, vol. 153, no. 4, pp. 534–541, 2018.

[31] K. E. Ahmed, T. Wang, K. Y. Li, W. K. Luk, and M. F. Burrow, "Performance and perception of dental students using three intraoral CAD/CAM scanners for full-arch scanning," *Journal of Prosthodontic Research*, vol. 63, no. 2, pp. 167–172, 2019.

[32] T. F. Alghazzawi, "Advancements in CAD/CAM technology: options for practical implementation," *Journal of Prosthodontic Research*, vol. 60, no. 2, pp. 72–84, 2016.

WILEY | Hindawi

Research Article

Surface Characterization and Corrosion Resistance of Biomedical AZ31 Mg Alloy Treated by Microarc Fluorination

Lin Sun,[1] **Bing Cheng Zhao,**[1] **Teng Wang,**[1] **Jia Yi Cui,**[1] **ShuXin Zhang,**[1] **Feng Li,**[1] **Qianqian Zhang,**[2] **HongXin Cai,**[1] **Heng Bo Jiang** ⓘ**,**[1] **and Eui-Seok Lee** ⓘ[3]

[1]*Stomatological Materials Laboratory, School of Stomatology, Shandong First Medical University & Shandong Academy of Medical Sciences, Tai'an, Shandong 271016, China*
[2]*Shandong Liming Institute of Technology and Vocational College, Tai'an, Shandong 271000, China*
[3]*Department of Oral and Maxillofacial Surgery, Graduate School of Clinical Dentistry, Korea University, Seoul 08308, Republic of Korea*

Correspondence should be addressed to Heng Bo Jiang; hengbojiang@vip.qq.com and Eui-Seok Lee; ees225@hanmail.net

The application prospect of biodegradable materials is being studied extensively. However, the high corrosion rate and its alloys in body fluids have been major limitations of the application of pure Mg (magnesium). To improve corrosion resistance of biodegradable AZ31 Mg alloy, we adopted microarc fluorination within a voltage range of 100-300 V in 46% hydrofluoric acid. To obtain morphologies, chemical compositions, and structural characteristics, field-emission scanning electron microscopy (FE-SEM), energy-dispersive X-ray spectroscopy (EDS), and X-ray diffraction (XRD) were performed, respectively. Results showed that the coating was mainly composed of MgF_2. Electrochemical corrosion and immersion tests proved that the corrosion resistance of MAF-treated AZ31 Mg alloy was significantly improved compared with untreated AZ31 Mg alloy in HBSS (Hank's Balanced Salt Solution). Current densities of AZ31, MAF100, MAF150, MAF200, MAF250, and MAF300 were 342.4, 0.295, 0.228, 0.177, 0.199, and $0.212\,\mu A/cm^2$, respectively. The roughness test indicated that samples under MAF treatment of 200 V, 250 V, and 300 V had large surface roughness. Meanwhile, the contact angle measurement and surface free energy test suggested that those samples had smaller contact angle and higher SFE than Ti. Thus, MAF-treated AZ31 Mg alloy might have promising application in various fields.

1. Introduction

In orthodontic treatment of oral cavity, microimplant nails are often used in anchorage treatment. Screws must be removed from patients after treatment. During the removal of screws, there is a risk of screw breakage. The broken screw might remain in a patient due to an operational error [1]. Removal of the broken screw might cause secondary injury to the patient. If the screw is made of biodegradable material, the broken portion of the screw can naturally degrade in the patient. Mg has been a research focus in recent years [2, 3]. Compared to other biodegradable materials, Mg and its alloys have higher specific strength, better degradation ability, and better seismic performance [4, 5]. For example, the elastic mod-

ulus of Mg or its alloy (45 GPa) is close to that of the human bone (20 GPa), thus alleviating stress shielding effect between the bone and implant. However, the elastic modulus is about 110 GPa for titanium alloy and about 200 GPa for stainless steel, making it easier to cause the stress shielding effect. Besides, the density of metallic magnesium is $1.7\text{-}2.0\,g/cm^3$, similar to the density ($1.8\text{-}2.1\,g/cm^3$) of a natural bone. These characteristics indicate that Mg and its alloy are promising bone implant materials [6]. However, their degradation rate is too high to produce microimplant nails. Therefore, Mg and its alloys need to have an appropriate degradation rate to ensure their mechanical properties and normal metabolism of hydrogen.

Our main research direction is to slow down the degradation rate of Mg in vivo. Currently, degradable membrane

formed on the metal surface through metal passivation treatment, metal plating [7, 8], or metal surface fluorination [9] can delay the degradation of metal. These methods can maintain good mechanical properties [10, 11]. At present, electrochemical methods have been widely used for surface treatment of Mg. These methods have been proven to be extremely effective [12–14].

Microarc oxidation (MAO) is a surface treatment method carried out under high voltage. The coating prepared by MAO has advantages of short preparation time, uniform surface characteristics similar to the bone, adjustable coating thickness, and high biocompatibility. Properties of MAO coatings are mainly determined by electrolytes used, including borate [15], silicate [16], fluoride [13], potassium fluorozirconate [17], phosphate [18], and aluminate [19]. Coating surface morphology and thickness are main factors affecting MAO coatings [20]. For example, the porosity of MAO coating is decreased with an improvement of frequency, but increased with an increase of the final voltage. Through pores and microcracks in MAO coatings lead to electrochemical corrosion of Mg alloys more easily than nonthrough pores [21]. Sealing is an important method to improve the physical barrier role of MAO coating. The coating can be sealed using silicates, phosphates, sol gels, and alkaline materials with additional polymer coatings [22, 23].

Fluorine (F) is an essential trace element. A proper amount of fluorine is beneficial for the human health [24]. MgF_2 coating is formed by infiltrating Mg in hydrofluoric acid for more than 24 hours. However, the biocompatibility of the MgF_2 coating is poor [13]. That MgF_2 coating also has disadvantages of long preparation time and environmental pollution [9, 25]. A high F content in MAO coating is toxic. A recent study has shown that MAO coating containing high F content (higher than 19 at%) exhibits high toxicity [26]. One study has shown that MAO coating containing the F content of 62.12 at % can improve the proliferation of cells [13].

To improve corrosion resistance of Mg, we adopted the method of microarc fluorination (MAF), a combination of MAO and fluorination. The coating prepared by MAF overcomes disadvantages of MAO coating's easy cracking and smooth surface prepared by fluorination [13].

In this study, hydrofluoric acid was used as an electrolyte to prepare coating at a voltage range of 100-300 V. Then, the coatings were immersed in Hank's Balanced Salt Solution (HBSS) for corrosion experiment. After the corrosion experiment, surface analysis was carried out using field-emission scanning electron microscope (FE-SEM), energy-dispersive X-ray spectroscopy (EDS), and X-ray diffraction (XRD). Roughness, contact angle, and surface free energy (SFE) of the corroded sample were measured. Corrosion resistances of samples were analyzed.

Most experiments on the corrosion performance of Mg are in vitro experiments [27–29]. Few experiments have explained the corrosion behavior of Mg in vivo. We used HBSS to conduct the immersion experiment to simulate an in vivo experiment. Limited by ethical aspects and laboratory conditions, it is impossible to use animal models to simulate in vivo experiments.

TABLE 1: Elemental compositions of AZ31 Mg alloy.

Element	Weight %	Element	Weight %
Al	2.85	Fe	0.003
Zn	0.75	Cu	0.00045
Mn	0.62	Ni	0.00052
Si	0.025	Mg	In balance

2. Materials and Methods

2.1. Sample Preparations. AZ31 Mg alloy discs (diameter = 16 mm; thickness = 2 mm) were laser cut from the AZ31 sheet. Its compositions are shown in Table 1. Titanium discs (diameter = 16 mm; thickness = 2 mm) were prepared as references for surface free energy analysis. Samples were polished with a 2000# SiC sandpaper in absolute ethyl alcohol, washed with absolute ethyl alcohol, and blow-dried.

2.2. MAF Treatment. In the electrolyte of 100 mL hydrofluoric acid (Sigma-Aldrich, 46%), AZ31 Mg alloy was used as an anode, and a graphite rod was used as a cathode. After numerous experiments, it was found that a large amount of hydrofluoric acid gas was released during a violent reaction of hydrofluoric acid at a high voltage, polluting the environment and harming health. Therefore, 100, 150, 200, 250, and 300 V were chosen as experimental voltages in the present study. Five sets of different voltages (100, 150, 200, 250, and 300) were applied at a DC constant voltage with a maximum current of 2 A for 30 seconds. MAF-treated AZ31 Mg alloy was then prepared and rinsed with deionized water three times and blow-dried. A diagram of the MAF process is shown in Figure 1. The code name and the process of preparing MAF-treated samples are shown in Table 2.

2.3. Surface Characterization. Surface morphology and basic elements of samples were observed using an FE-SEM (JSM-7001F; JEOL, Ltd, Tokyo, Japan) and EDS. Surface compositions of samples were determined by XRD. At 40 kV and 30 mA, the scan rate was 1°/min using a Cu-Kα line.

Surface roughness was measured by the 3D optical profilometry (ContourGT, Bruker, Tucson, AZ, USA). The scattering angle was fixed at a smaller value of 1. According to a single diffuse scattering scan, Ra, Rp, Rq, Rt, and Rv values were measured based on ISO 4287 standard. The sampling area was $0.17 \times 0.2 \, mm^2$.

2.4. Surface Free Energy Analysis. Deionized water and diiodomethane as test liquids were used for contact angle measurements. A drop of test liquid (5 μL droplet from a syringe) was placed on the surface of each sample for 60 s. The equilibrium contact angle was then determined with an image analyzer. The contact angle was recorded for both sides. The SFE of each sample was calculated using Eq. (1) and Eq. (2).

$$\gamma = \gamma^p + \gamma^d, \tag{1}$$
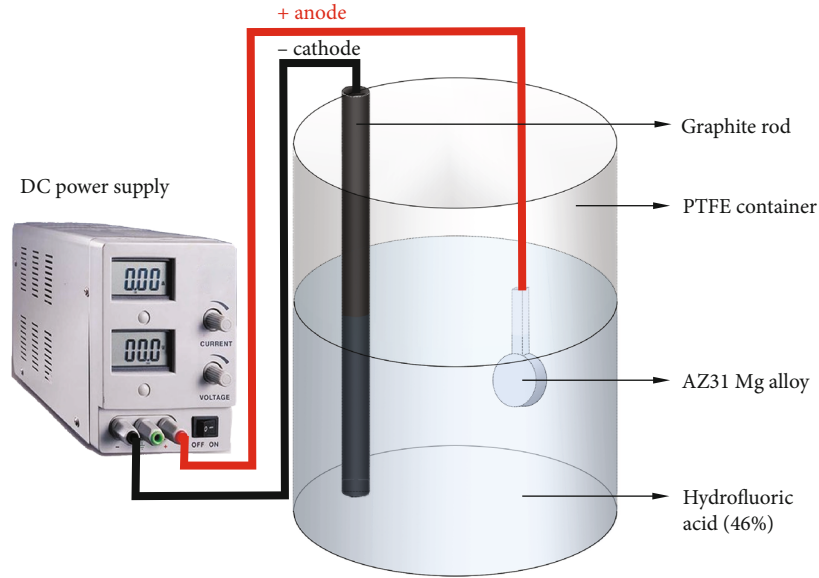
*Polytetrafluoroethylene, abbreviated as PTFE.

FIGURE 1: Diagram of the MAF treatment of AZ31 Mg alloy.

TABLE 2: Sample code name and the process of preparing MAF treatment.

Code	Surface treatment	Processing time
AZ31	None	None
MAF100	Immersed in 46% hydrofluoric acid at DC and constant voltage of 100 V	30s
MAF150	Immersed in 46% hydrofluoric acid at DC and constant voltage of 150 V	30s
MAF200	Immersed in 46% hydrofluoric acid at DC and constant voltage of 200 V	30s
MAF250	Immersed in 46% hydrofluoric acid at DC and constant voltage of 250 V	30s
MAF300	Immersed in 46% hydrofluoric acid at DC and constant voltage of 300 V	30s

$$(1 + \cos \theta)\gamma_1 = 2\left(\gamma_s{}^d \gamma_1{}^d\right)^{1/2} + 2(\gamma_s{}^p \gamma_1{}^p)^{1/2}, \qquad (2)$$

where θ is the mean equilibrium contact angle of H_2O or CH_2I_2, γ_1 is the surface free energy of water, $\gamma_1{}^d$ and $\gamma_1{}^p$ refer to the hydrogen bonding and dispersion force components of γ_1; γ_s is the surface free energy of samples, and $\gamma_s{}^d$ and $\gamma_s{}^p$ refer to the dipole-dipole interactions and dispersion force components of γ_s.

2.5. Electrochemical Corrosion Tests. Corrosion resistances of AZ31 and MAF-treated AZ31 Mg alloys were determined with the open circuit potential and potentiodynamic polarization test. An Ag/AgCl/Sat-KCl electrode was used as a reference electrode. A pure graphite rod was used as a reaction electrode. Each sample was exposed ($1 \, cm^2$) as a working electrode, and 1000 mL of HBSS (Shanghai Yuanye Bio-Technology Co, Ltd, China) was used as an electrolyte. The temperature of the electrolyte was maintained at $37 \pm 1°C$. In this test, in order to stabilize the potential of the test sample, the sample was first immersed in PBS for 1 hour to perform its open circuit potential (OCP) mode. Then, a potential dynamic polarization (PDP) test was performed. Electrochemical tests were performed using a VersaSTAT3 potentiostat (Model 300, AMETEK, Inc, Berwyn, PA, USA) coupled with a VersaStudio 2.43.3 software (AMETEK, Inc.) for electrochemical control and data analyses.

2.6. Immersion Corrosion Tests. AZ31 and MAF-treated AZ31 Mg alloys were vertically immersed in HBSS at 37°C for one week and four weeks. Each group had three parallel samples. The ratio of the HBSS volume to the sample area was $20 \, mL/cm^2$. HBSS was refreshed weekly. After immersion for one week or four weeks, samples were ultrasonically cleaned with a chromium trioxide (CrO_3) solution (Aladdin Inc. China) for 3 minutes, rinsed with deionized water three times, and blow-dried. The percentage of mass loss was calculated using Eq. [3]:

Mass loss% = $(MO - M1/M0) \times 100\%$, [3] where M_0 is the mass of samples before immersion. M_1 is the mass of the samples after the immersion. Three samples in each

(a)

(b)

(c)

(d)

(e)

(f)
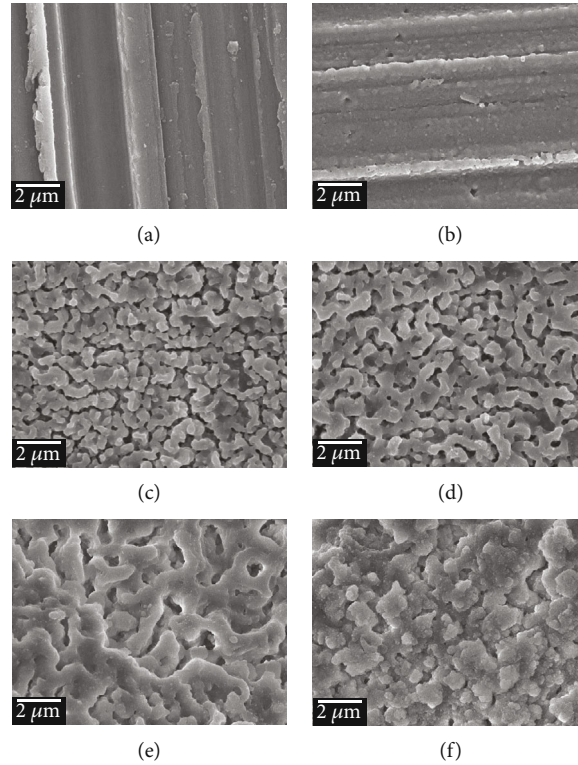
FIGURE 2: FE-SEM surface morphology of (a) AZ31, (b) MAF100, (c) MAF150, (d) MAF200, (e) MAF250, and (f) MAF300.

group were tested, and mass loss was expressed as mean standard deviation (SD).

2.7. Statistical Analysis. All data are expressed as mean ± standard deviation. Data of the materials were subjected to one-way analysis of variance (ANOVA) and post-hoc analysis using Tukey's test. Student's test was used to compare values before and after MAF treatment. All statistical analysis was performed using IBM SPSS Statistics version 23.0 for Windows (IBM Corporation, Armonk, New York, USA). Statistical significance was defined at $p < 0.01$.

3. Results and Discussion

Figure 2 displays surface topographies of AZ31 and MAF-treated AZ31 Mg alloy. The surface of MAF100 was not smooth. There were several small holes and particles. The coral-like structure appeared densely from 150 V but disappeared at 250 V. Diameters of crystal particles for MAF150, MAF200, and MAF250 were approximately 0.5, 0.6, and 0.7 μm, respectively. The coral-like structure was gradually fused, forming micropores that could promote adhesion and proliferation of osteoblasts [30]. However, MAF300 crystal particles were nonuniform in diameter.

Figure 3 demonstrates that surface elements are mainly composed of F and Mg. Thus, it could be concluded that magnesium fluoride coatings were formed on surfaces of the samples through MAF. Based on chemical element compositions on surfaces of AZ31, MAF100, MAF150, MAF200, MAF250, and MAF300 based on EDS analysis, the percentage

of fluoride increased within increasing voltage. Compared with MAF100, MAF150 exhibited a significant increase of fluoride, achieving an increase of 43.39%. Fluoride percentages on surface of MAF200, MAF250, and MAF300 were 71.11%, 71.61%, and 70.58%, respectively. At 150 V, The AZ31 Mg alloy surface appeared as an obvious spark discharge phenomenon. However, with further increase of voltage, the strong spark discharge deposition in the anodic oxidation process of AZ31 Mg alloy released a large amount of heat, resulting in overheating of the surface of the AZ31 Mg alloy and a significant increase of the temperature of local solution which accelerated the dissolution rate of the oxide film. Therefore, coating after 150 V caused little change in the fluorine content.

Figure 4 presents crystalline structures of samples by XRD analysis. Referring to the standard JCPDS card, the coating was mainly made up of tetragonal MgF_2 (JCPDS No. 411443). Compared with untreated AZ31, patterns observed for MAF-treated AZ31 Mg alloys clearly indicated the presence of tetragonal MgF_2. As shown in Figure 4, MAF150, MAF200, MAF250, and MAF300 basically displayed the same number of diffraction peaks, angular position, relative intensity order, and shape of the diffraction peak, whereas MAF100 showed a difference possibly due to its thinner coating. X-ray projection requires tested substance to have a certain thickness. Thus, there were no peaks appearing in the relative diffraction angle for MAF100. The formation of the MgF_2 phase in the coating is through microarc oxidation reaction of the AZ31 Mg alloy substrate and hydrofluoric acid solution in the discharging channel produced by sparks. During sparks, Mg^{2+} from

(a)

Element	Weight%	Atomic%
F K	0.00	0.00
Mg K	96.04	96.96
Al K	2.90	2.64
Zn K	1.06	0.40

(b)

Element	Weight%	Atomic%
F K	13.65	16.98
Mg K	83.05	80.73
Al K	2.13	1.87
Zn K	1.17	0.42

(c)

Element	Weight%	Atomic%
F K	54.30	60.37
Mg K	44.89	39.00
Al K	0.81	0.63
Zn K	0.00	0.00

Figure 3: Continued.

Element	Weight%	Atomic%
F K	65.79	71.11
Mg K	34.21	28.89
Al K	0.00	0.00
Zn K	0.00	0.00

(d)

Element	Weight%	Atomic%
F K	66.29	71.61
Mg K	32.93	27.80
Al K	0.78	0.59
Zn K	0.00	0.00

(e)

Element	Weight%	Atomic%
F K	65.19	70.58
Mg K	34.39	29.10
Al K	0.42	0.32
Zn K	0.00	0.00

(f)

FIGURE 3: EDS analysis of (a) AZ31, (b) MAF100, (c) MAF150, (d) MAF200, (e) MAF250, and (f) MAF300.

substrate migrates outward. Meanwhile, F-inward migrates into channels owing to the electrical field. MgF_2 coating forms through the following reactions:

$$Mg \rightarrow Mg^{2+} + 2e^-,$$
$$Mg^{2+} + 2F \rightarrow MgF_2. \tag{3}$$
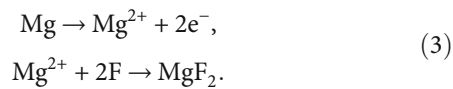
In a high-voltage electrolyte, the discharge on the AZ31 Mg alloy surface generated many electric sparks, resulting in a porous structure (Figure 2). A stable MgF_2 coating was formed on the surface. It is increased gradually, with little or no sparks at a certain thickness of coating.

Figure 5 shows surface roughness of samples by 3D optical profilometry. The image qualitatively analyzed surface roughness and visually displayed sample surface roughness. The formation of surface roughness is generally related to the processing method and other factors [31]. Due to differences in processing methods and workpiece materials, traces left on the processed surface are different in depth, density, shape, and texture [32]. The main parameter to evaluate surface roughness is contour arithmetic mean
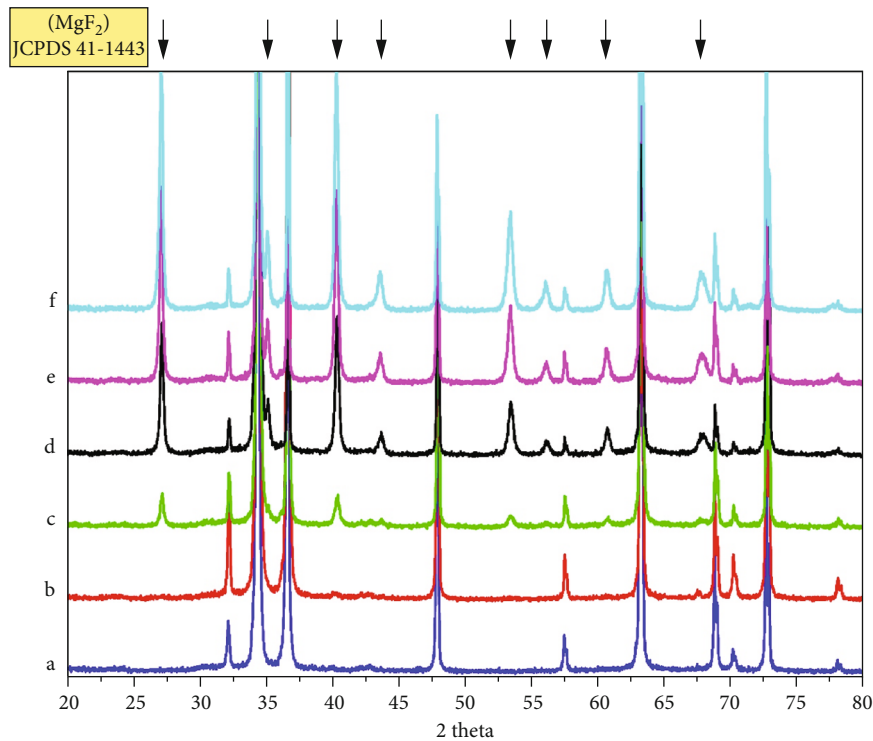
FIGURE 4: XRD patterns of (a) AZ31, (b) MAF100, (c) MAF150, (d) MAF200, (e) MAF250, and (f) MAF300.

deviation-Ra which refers to the arithmetic mean value of the distance from each point on the measured contour to the reference line within the sampling range as defined in ISO 4287. As shown in Table 3, Ra values of AZ31, MAF100, MAF150, MAF250, and MAF300 were 0.182, 0.219, 0.294, 2.010, 3.235, and 6.689, respectively. Samples under treatment of MAF200, MAF250 and MAF300 had a large surface roughness. Moreover, those treated with MAF300 had significantly increased surface roughness. At a low voltage, the film growth rate was slow. However, the resulting film was dense, and the roughness was reduced. At a high voltage, the intense spark discharge deposition in the anodic oxidation process of AZ31 Mg alloy released a large amount of heat, and the electrolyte temperature increased, resulting in an increase of the dissolution rate of the film which led to an uneven film and increased roughness. There are large troughs on the surface of rough parts. They are sensitive to stress concentration such as sharp notch and cracks. Thus, surface roughness affects fatigue strengths of parts [33]. Meanwhile, rough surface can easily cause corrosive gases or liquids to penetrate into the inner layer of metal through microscopic concave valley of the surface, resulting in surface corrosion.

Figures 6(a) and 6(b) show SFE and contact angles of Ti, AZ31, and MAF-treated AZ31 Mg alloy. In clinical practice, titanium as an emerging material has been widely used in fields of surgical instruments and implants in the world. It has achieved great success. Thus, it was selected as a reference object as in previous studies [34–36]. It was found that MAF100 and MAF150 had lower SFE than other samples. Simultaneously, it could be concluded that their hydrophilicity and lipophilicity were poor as shown in Figure 6(c).

Values of contact angles and SFE of them are showed in Table 4. One study has revealed that incremental SFE can result in a faster colonization of the surface, indicating excellent biocompatibility [37]. Therefore, we propose that biocompatibility of MAF100 and MAF150 is less than Ti and AZ31. Thus, MAF100 and MAF150 might be more suitable than Ti and AZ31 for fields such as bone plates that do not require good tissue compatibility. However, MAF200, MAF250, and MAF300 had higher SFE and better hydrophilicity and lipophilicity than other samples. Hence, they have the potential to be biocompatible and are more likely to be suitable than Ti for dental implants, anchorage nails, and so on that need materials to possess good tissue compatibility. FE-SEM revealed that microporous structures were formed on surfaces of AZ31 treated under high voltages which might result in an increase of the surface area. Due to capillary principle, liquid can easily infiltrate [38]. Thus, hydrophilicity and lipophilicity of MAF200, MAF250, and MAF300 were inferable to be good.

Figure 7(a) shows OCP curves of AZ31 and MAF-treated AZ31. At 60 min, MAF200, MAF250, and MAF300 processed higher OCP values than other samples, suggesting that they had lower corrosion potential. Overall, the OCP curve tended to plateau in 60 min. In addition, the OCP values of MAF-treated AZ31 Mg alloys were improved than those of AZ31, indicating that the prepared coating had good corrosion resistance.

Figure 7(b) shows the typical Tafel curve of AZ31 and MAF-treated AZ31 Mg alloy. It was obtained by plotting E and $\log |I|$, where I was the current density and E was the overpotential. The combination of a higher corrosion current

(a)

(b)

Figure 5: Continued.

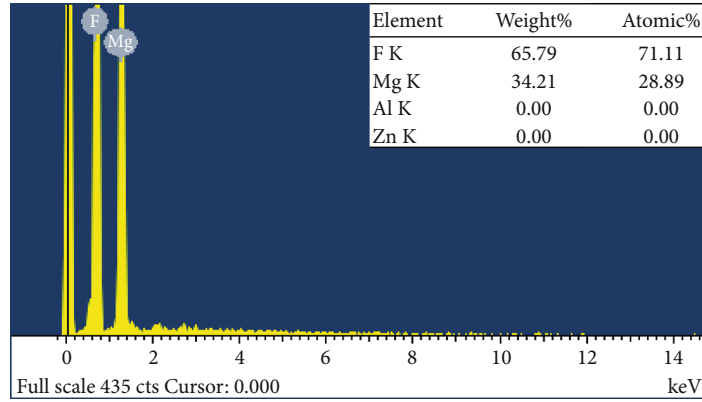(c)
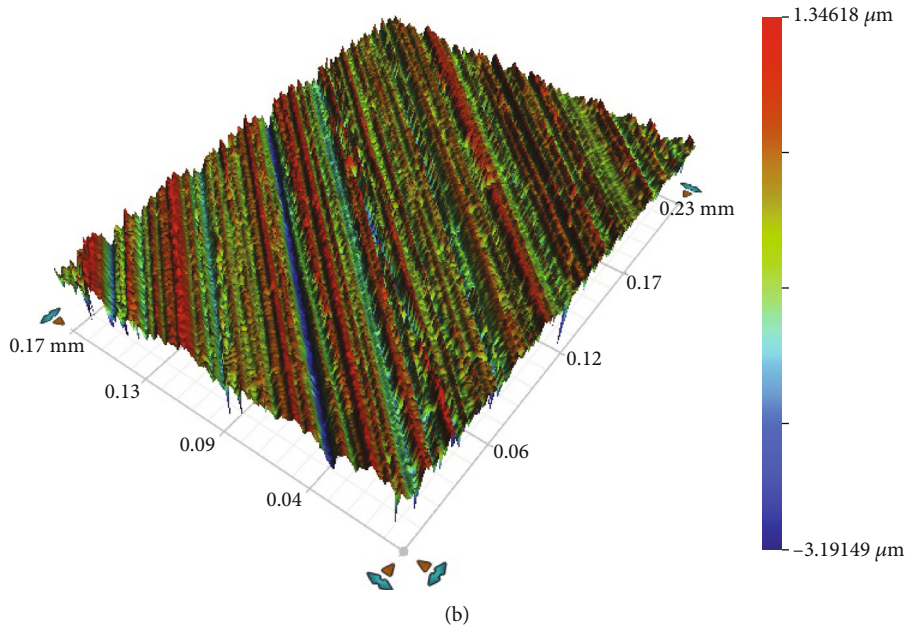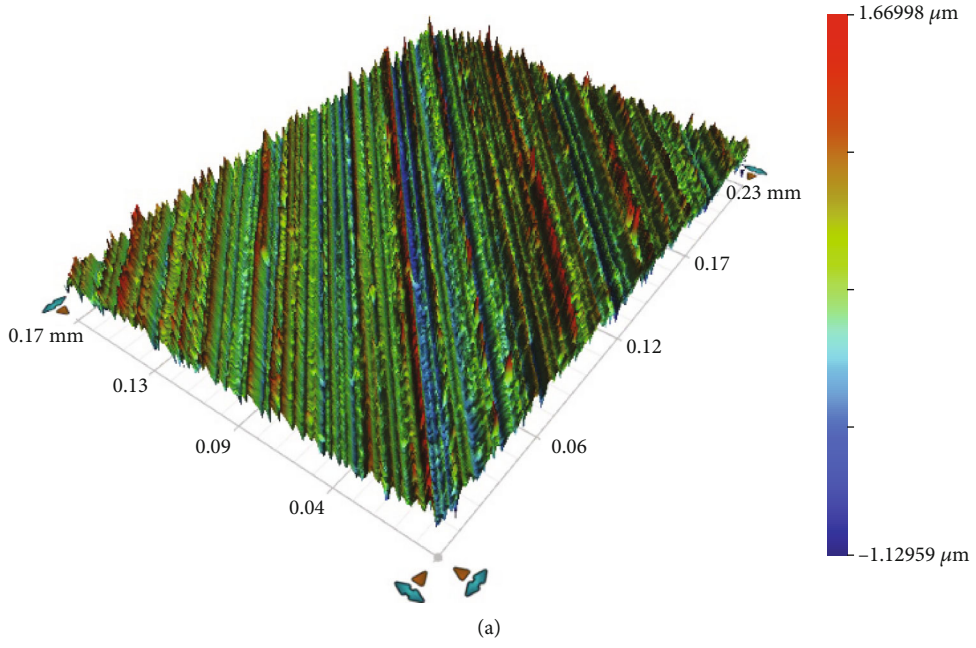
(d)

Figure 5: Continued.

(e)

(f)
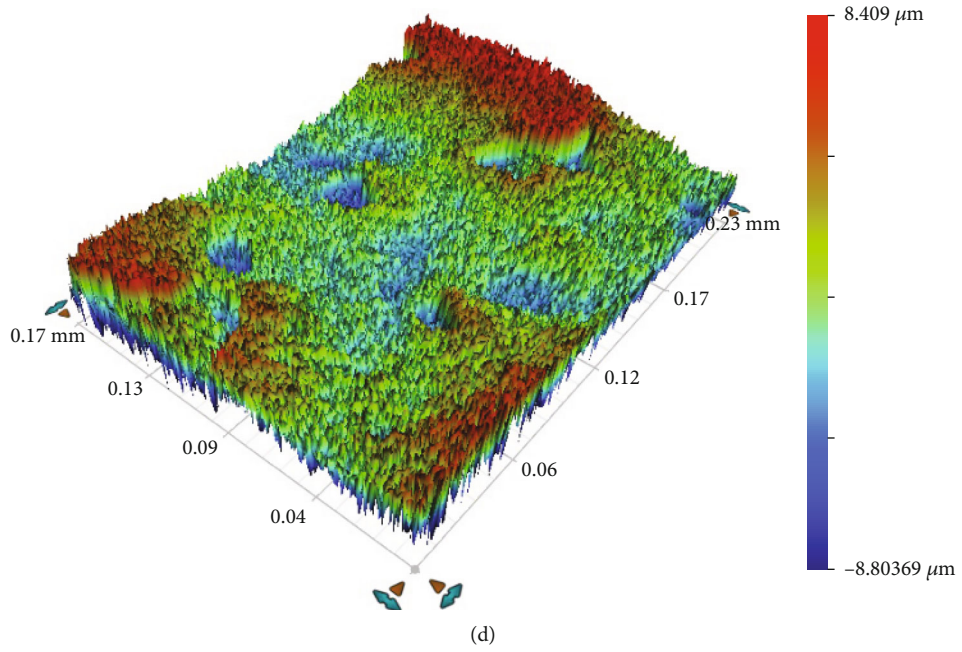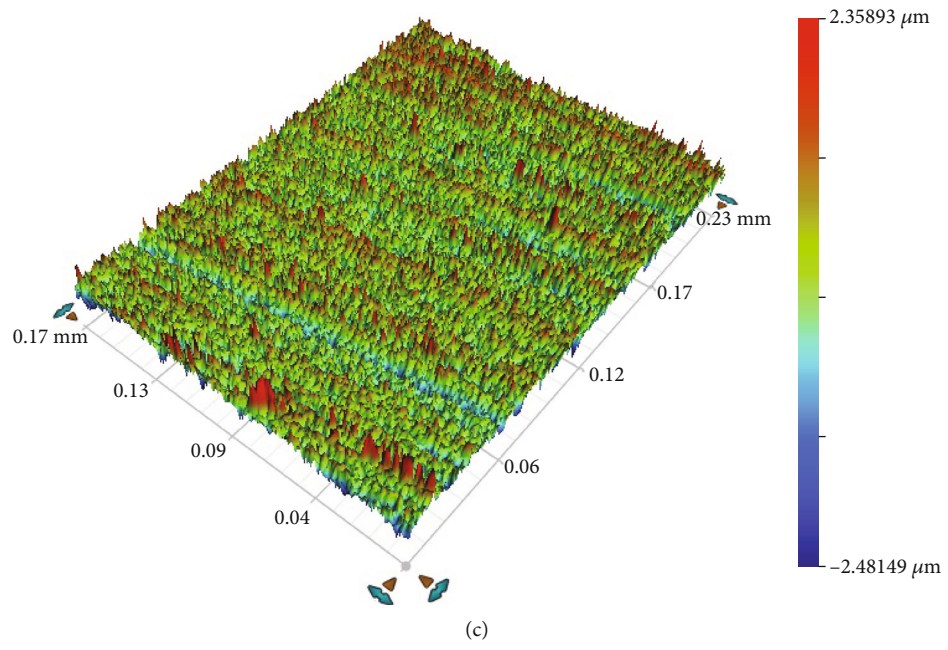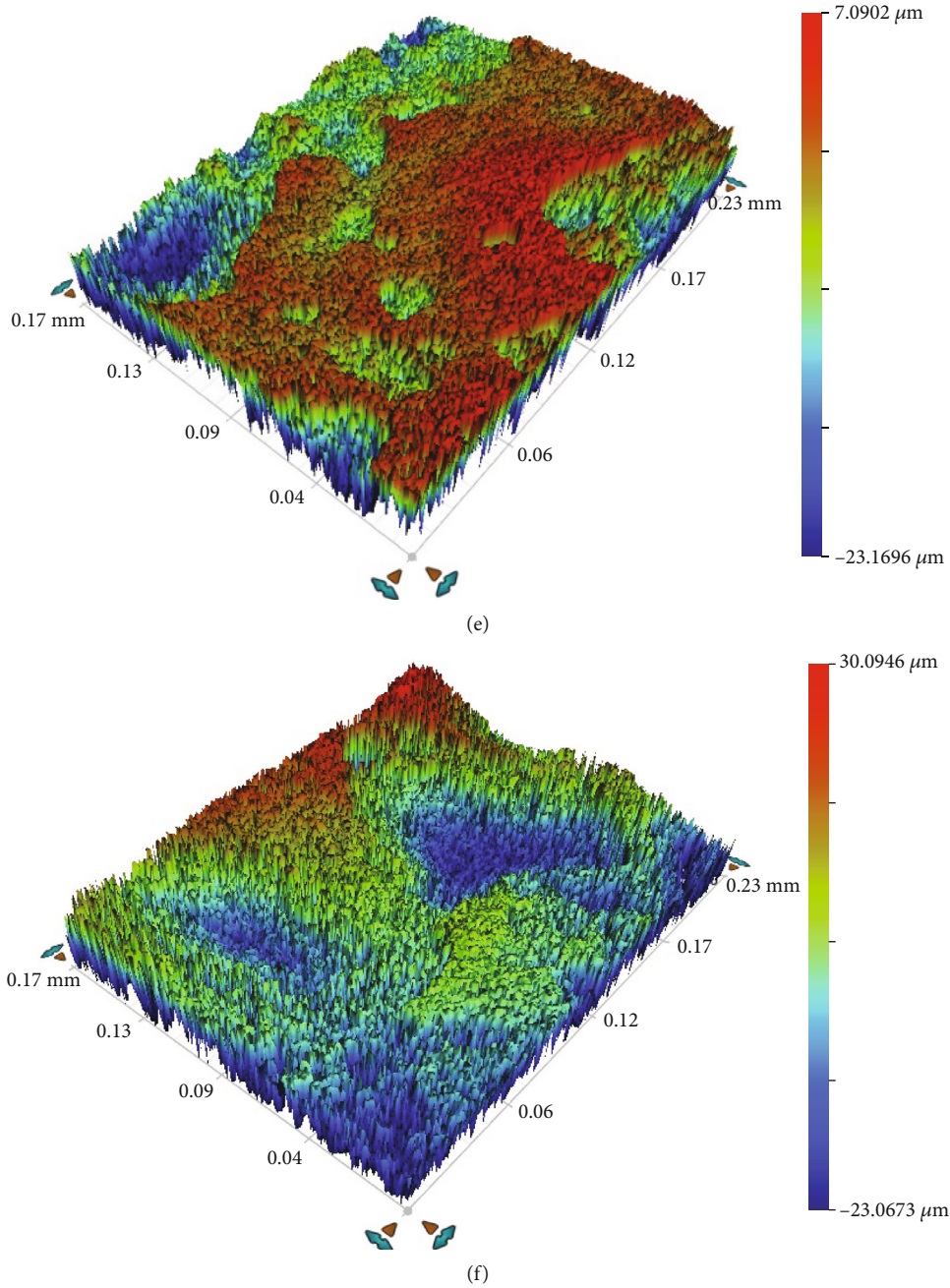
Figure 5: Surface roughness by 3D optical profilometry of (a) AZ31, (b) MAF100, (c) MAF150, (d) MAF200, (e) MAF250 and (f) MAF300.

Table 3: Surface roughness of AZ31, MAF100, MAF150, MAF200, MAF250, and MAF300.

Code	Ra (μm)	Rp (μm)	Rq (μm)	Rt (μm)	Rv (μm)
AZ31	0.182	1.670	0.229	2.800	-1.130
MAF100	0.219	1.346	0.286	4.538	-3.191
MAF150	0.294	2.359	0.381	4.840	-2.481
MAF200	2.010	8.409	2.457	17.213	-8.804
MAF250	3.235	7.090	4.490	30.260	-23.170
MAF300	6.689	30.095	8.608	53.162	-23.067

density and a lower corrosion potential means a higher corrosion rate [39]. From Figure 7, we can infer that with an increase in the treatment voltage of microarc fluorination, the polarization curve of the sample showed a shift to lower current density value. These results indicated that AZ31 Mg alloy exhibited a general corrosion behavior in electrolyte while the corrosion of MAF-treated Mg alloys was hindered. In addition, MAF200 had the highest corrosion potential (-1.262 V) and the lowest current density (0.177 μA/cm^2). Therefore, it is reasonable to assume that the corrosion resistance of MAF200 is the best. The results of the potentiodynamic corrosion test on AZ31 and MAF-treated AZ31 are showed in Table 5.
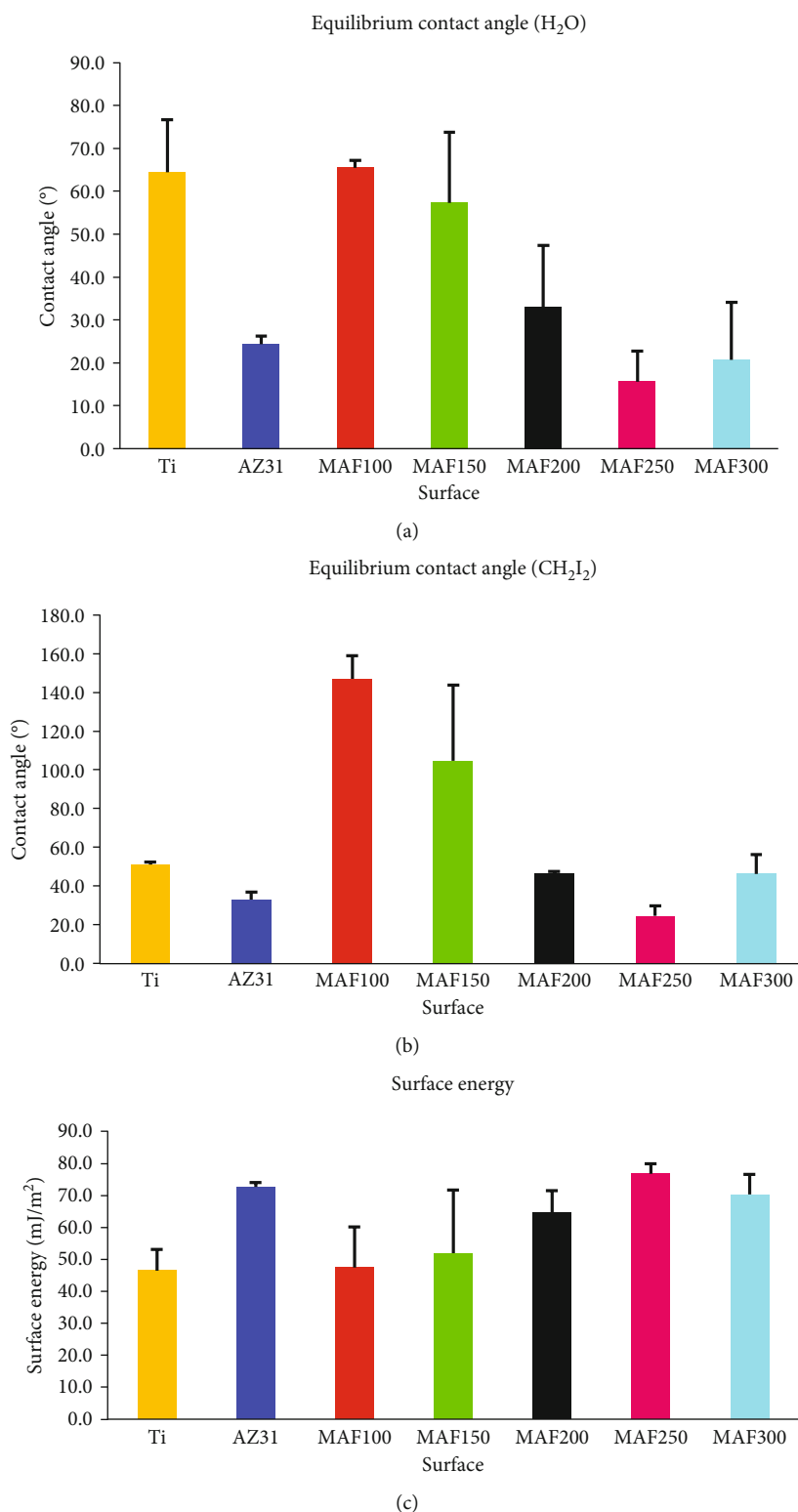
FIGURE 6: Contact angle and surface free energy of Ti, AZ31, MAF100, MAF150, MAF200, MAF250, and MAF300. Contact angle measurement with (a) H_2O, (b) CH_2I_2 as probe reagent, and (c) values of surface free energy.

Figure 8 shows weight loss percentages of AZ31 and MAF-treated AZ31 Mg alloy after immersion in HBSS. In a certain voltage of 100 V and 200 V, with an increase of the treatment voltage, the weight loss of AZ31 Mg alloy decreased. The weight loss value of MAF200 was the lowest. The weight loss value of MAF250 and MAF300 was gradually increased compared with the weight loss value of MAF200, indicating that the degradation rate increased with increasing voltage. It

TABLE 4: Values (mean ± SD) of contact angel and energy for Ti, AZ31, MAF100, MAF150, MAF200, MAF250, and MAF300.

| Code | Contact angle (°) | | E (mJ/m^2) | | |
	Deionized water	Di-iodomethane	γ^d_s *	γ^p_s *	SFE
Ti	64.5 ± 12.9	51.1 ± 3.8	33.67 ± 0.65	12.87 ± 6.09	46.55 ± 6.55
AZ31	24.4 ± 2.4	33.0 ± 4.4	42.85 ± 1.68	29.80 ± 0.55	72.65 ± 1.42
MAF100	24.4 ± 2.4	147.0 ± 15.1	0.57 ± 0.61	46.91 ± 13.18	47.48 ± 12.58
MAF150	57.4 ± 17.2	104.6 ± 44.1	12.56 ± 15.00	39.31 ± 27.14	51.87 ± 19.82
MAF200	32.9 ± 14.5	46.4 ± 1.8	36.27 ± 0.56	28.46 ± 6.60	64.73 ± 6.74
MAF250	15.6 ± 8.7	24.5 ± 6.5	46.29 ± 1.95	30.56 ± 1.13	76.86 ± 3.08
MAF300	20.7 ± 13.5	46.4 ± 10.3	36.03 ± 5.26	34.26 ± 6.74	70.29 ± 6.20

*γ^d_s and γ^p_s refer to dipole-dipole interactions and dispersion force components, respectively.
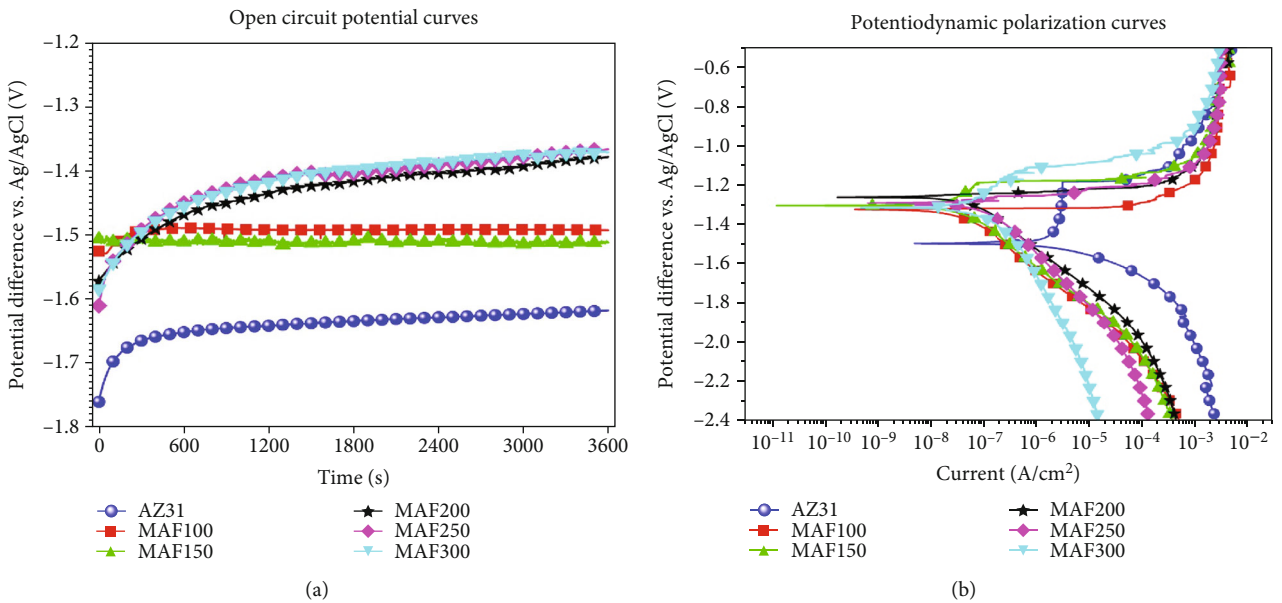
FIGURE 7: Electrochemical corrosion results. (a) OCP. (b) PDP curves of the AZ31, MAF100, MAF150, MAF200, MAF250, and MAF300.

TABLE 5: Corrosion potential and current densities of AZ31, MAF100, MAF150, MAF200, MAF250, and MAF300.

Code	E_0 (V)	I_{corr} (μA/cm^2)
AZ31	-1.501	342.4
MAF100	-1.336	0.295
MAF150	-1.318	0.228
MAF200	-1.262	0.177
MAF250	-1.293	0.199
MAF300	-1.328	0.212

might be related to the increase of surface roughness for MAF250 and MAF300. As confirmed in previous studies, surface roughness had a significant impact on the corrosion rate of AZ31 Mg alloy, leading to the accelerated corrosion rate with an increase of roughness [40]. Weight loss values of AZ31 and MAF-treated AZ31 exhibited basically identical trend after one week and four weeks. We could infer that corrosion resistance was increased with increasing surface roughness in several cases. In addition to roughness, the pore size simultaneously affects the protective ability of AZ31 substrate [21]. After microarc fluorination, coral-like fluorine coating was formed on the surface of AZ31 Mg alloy. It played a protective role on the surface [41]. Coating thickness and pore size are crucial to improve corrosion resistance of a sample.

4. Conclusions

In this study, we used MAF technology to treat and detect AZ31 in 46% hydrofluoric acid electrolyte at different voltages. We could draw the following conclusions:

(1) The coral-like structure was formed on the surface by MAF
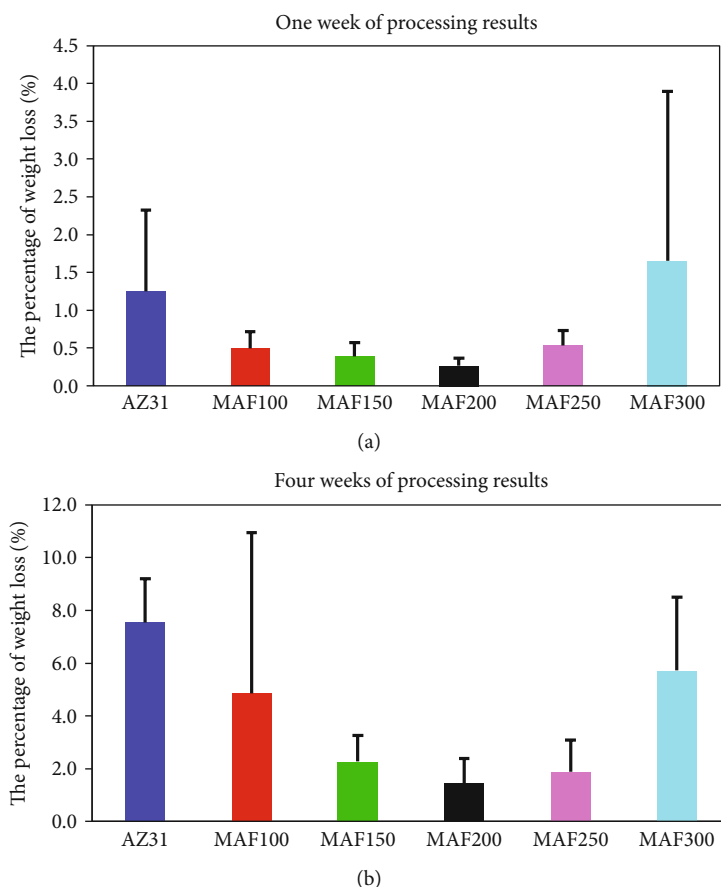
FIGURE 8: Weight loss variation over time of AZ31, MAF100, MAF150, MAF200, MAF250, and MAF300. (a) Results of one week. (b) Results of four weeks.

(2) MAF-treated AZ31, in comparison with untreated AZ31, showed significantly improved surface roughness

(3) Surface roughness increased with increasing MAF treatment voltage

(4) The corrosion resistance of a sample was determined by pore size, surface roughness of the coating, and so on

Data Availability

Data used to support findings of this study are included within the article.

Conflicts of Interest

We declare that we have no financial and personal relationships with other people or organizations that can inappropriately influence our work.

Authors' Contributions

Lin Sun, Bing Cheng Zhao, and Teng Wang contributed equally to this work. Conceptualization was performed by Heng Bo Jiang. Lin Sun and Jia Yi Cui contributed to the methodology. Bing Cheng Zhao and Jia Yi Cui performed the formal analysis. Teng Wang and Qianqian Zhang performed the investigation. Feng Li contributed to the resources. ShuXin Zhang contributed to the data curation. HongXin Cai and Bing Cheng Zhao performed the repeated test validations. Lin Sun, Bing Cheng Zhao, and Teng Wang contributed to the writing of the original draft preparation. Heng Bo Jiang and Eui-Seok Lee performed writing—review and editing. Heng Bo Jiang contributed to the supervision. Eui-Seok Lee contributed to the project administration.

Acknowledgments

References

[1] M. Desai, A. Jain, and N. Sumra, "Surgical management of fractured orthodontic mini- implant- a case report," *Journal*

of Clinical and Diagnostic Research: JCDR, vol. 9, no. 1, pp. - ZD06–ZD07, 2015.

[2] W. Xue, K. Dahlquist, A. Banerjee, A. Bandyopadhyay, and S. Bose, "Synthesis and characterization of tricalcium phosphate with Zn and mg based dopants," *Journal of Materials Science: Materials in Medicine*, vol. 19, no. 7, pp. 2669–2677, 2008.

[3] L. Yang and E. Zhang, "Biocorrosion behavior of magnesium alloy in different simulated fluids for biomedical application," *Materials Science and Engineering: C*, vol. 29, no. 5, pp. 1691–1696, 2009.

[4] M. P. Staiger, A. M. Pietak, J. Huadmai, and G. Dias, "Magnesium and its alloys as orthopedic biomaterials: a review," *Biomaterials*, vol. 27, no. 9, pp. 1728–1734, 2006.

[5] X. Li, L. Xie, F. S. Pan et al., "A feasibility study of using biodegradable magnesium alloy in glaucoma drainage device," *International Journal of Ophthalmology*, vol. 11, no. 1, pp. 135–142, 2018.

[6] N. Hort, Y. Huang, D. Fechner et al., "Magnesium alloys as implant materials – Principles of property design for mg-RE alloys☆," *Acta Biomaterialia*, vol. 6, no. 5, pp. 1714–1725, 2010.

[7] A. K. Sharma, M. R. Suresh, H. Bhojraj, H. Narayanamurthy, and R. P. Sahu, "Electroless nickel plating on magnesium alloy," *Metal Finishing*, vol. 96, no. 3, pp. 10–16, 1998.

[8] X. P. Lei, G. Yu, Y. P. Zhu et al., "Successful cyanide free plating protocols on magnesium alloys," *Transactions of the Institute of Metal Finishing*, vol. 88, no. 2, pp. 75–80, 2013.

[9] J. Y. Hu, Q. Li, X. K. Zhong, and F. Luo, "Fluoride treatment and sol film composite technology for AZ91D magnesium alloy," *Transactions of the Institute of Metal Finishing*, vol. 88, no. 1, pp. 41–46, 2013.

[10] P. Shi, W. F. Ng, M. H. Wong, and F. T. Cheng, "Improvement of corrosion resistance of pure magnesium in Hanks' solution by microarc oxidation with sol-gel TiO2 sealing," *Journal of Alloys and Compounds*, vol. 469, no. 1-2, pp. 286–292, 2009.

[11] R.-G. Hu, S. Zhang, J.-F. Bu, C.-J. Lin, and G.-L. Song, "Recent progress in corrosion protection of magnesium alloys by organic coatings," *Progress in Organic Coatings*, vol. 73, no. 2-3, pp. 129–141, 2012.

[12] A. L. Yerokhin, X. Nie, A. Leyland, A. Matthews, and S. J. Dowey, "Plasma electrolysis for surface engineering," *Surface & Coatings Technology*, vol. 122, no. 2-3, pp. 73–93, 1999.

[13] H. B. Jiang, Y. K. Kim, J. H. Ji, I. S. Park, T. S. Bae, and M. H. Lee, "Surface modification of anodized Mg in ammonium hydrogen fluoride by various voltages," *Surface & Coatings Technology*, vol. 259, pp. 310–317, 2014.

[14] J. Zhang, S. Hiromoto, T. Yamazaki et al., "Macrophage phagocytosis of biomedical Mg alloy degradation products prepared by electrochemical method," *Materials Science and Engineering: C*, vol. 75, pp. 1178–1183, 2017.

[15] R. F. Zhang, S. F. Zhang, Y. L. Shen et al., "Influence of sodium borate concentration on properties of anodic coatings obtained by micro arc oxidation on magnesium alloys," *Applied Surface Science*, vol. 258, no. 17, pp. 6602–6610, 2012.

[16] R. F. Zhang, S. F. Zhang, J. H. Xiang, L. H. Zhang, Y. Q. Zhang, and S. B. Guo, "Influence of sodium silicate concentration on properties of micro arc oxidation coatings formed on AZ91HP magnesium alloys," *Surface & Coatings Technology*, vol. 206, no. 24, pp. 5072–5079, 2012.

[17] X.-J. Cui, C.-H. Liu, R.-S. Yang, M.-T. Li, and X.-Z. Lin, "Self-sealing micro-arc oxidation coating on AZ91D Mg alloy and its formation mechanism," *Surface and Coatings Technology*, vol. 269, pp. 228–237, 2015.

[18] D. Wei, Y. Zhou, D. Jia, and Y. Wang, "Effect of heat treatment on the structure and in vitro bioactivity of microarc-oxidized (MAO) titania coatings containing Ca and P ions," *Surface & Coatings Technology*, vol. 201, no. 21, pp. 8723–8729, 2007.

[19] Y. Cheng, J. H. Cao, M. K. Mao, Z. M. Peng, P. Skeldon, and G. E. Thompson, "High growth rate, wear resistant coatings on an Al–Cu–Li alloy by plasma electrolytic oxidation in concentrated aluminate electrolytes," *Surface & Coatings Technology*, vol. 269, pp. 74–82, 2015.

[20] R. F. Zhang, D. Y. Shan, R. S. Chen, and E. H. Han, "Effects of electric parameters on properties of anodic coatings formed on magnesium alloys," *Materials Chemistry and Physics*, vol. 107, no. 2-3, pp. 356–363, 2008.

[21] L.-Y. Cui, R. C. Zeng, S. K. Guan et al., "Degradation mechanism of micro-arc oxidation coatings on biodegradable Mg-Ca alloys: the influence of porosity," *Journal of Alloys and Compounds*, vol. 695, pp. 2464–2476, 2017.

[22] X. Fan, J. Xu, Y. Wang et al., "Preparation and corrosion resistance of MAO layer/Yb2SiO5 composite coating on Mg alloy," *Surface & Coatings Technology*, vol. 240, pp. 118–127, 2014.

[23] B. M. Wilke, L. Zhang, W. Li, C. Ning, C. F. Chen, and Y. Gu, "Corrosion performance of MAO coatings on AZ31 Mg alloy in simulated body fluid vs *Earle's Balance Salt Solution*," *Applied Surface Science*, vol. 363, pp. 328–337, 2016.

[24] Y. Zheng, J. Wu, J. C. Ng, G. Wang, and W. Lian, "The absorption and excretion of fluoride and arsenic in humans," *Toxicology Letters*, vol. 133, no. 1, pp. 77–82, 2002.

[25] C. Y. Zhang, J. C. Gao, and C. L. Liu, "Effect of fluoride treatment on corrosion property of AZ31 magnesium alloy in Hank's solution," *Advanced Materials Research*, vol. 239-242, pp. 186–190, 2011.

[26] X. Shi, Y. Wang, H. Li et al., "Corrosion resistance and biocompatibility of calcium-containing coatings developed in near-neutral solutions containing phytic acid and phosphoric acid on AZ31B alloy," *Journal of Alloys and Compounds*, vol. 823, p. 153721, 2020.

[27] N. T. Kirkland, N. Birbilis, and M. P. Staiger, "Assessing the corrosion of biodegradable magnesium implants: a critical review of current methodologies and their limitations," *Acta Biomaterialia*, vol. 8, no. 3, pp. 925–936, 2012.

[28] Z. Zhen, X. I. Tingfei, and Y. Zheng, "A review on in vitro corrosion performance test of biodegradable metallic materials," *Transactions of Nonferrous Metals Society of China*, vol. 23, no. 8, pp. 2283–2293, 2013.

[29] M. Esmaily, J. E. Svensson, S. Fajardo et al., "Fundamentals and advances in magnesium alloy corrosion," *Progress in Materials Science*, vol. 89, pp. 92–193, 2017.

[30] J. S. Hwang, K. T. Oh, K. N. Kim, and K. M. Kim, "The characterization of the nano–micro hybrid structure of titanium surface and osteoblast response to the surface," *Key Engineering Materials*, vol. 342-343, pp. 589–592, 2007.

[31] P. R. Hall, "Introduction to surface roughness and scattering," *Precision Engineering*, vol. 13, no. 1, p. 62, 1991.

[32] R. P. Sekar and R. Sathishkumar, "Enhancement of wear resistance on normal contact ratio spur gear pairs through nonstandard gears," *Wear*, vol. 380-381, pp. 228–239, 2017.

[33] P. Gallo and F. Berto, "Influence of surface roughness on high temperature fatigue strength and cracks initiation in 40CrMoV13.9 notched components," *Theoretical and Applied Fracture Mechanics*, vol. 80, pp. 226–234, 2015.

[34] M. Geetha, A. K. Singh, R. Asokamani, and A. K. Gogia, "Ti based biomaterials, the ultimate choice for orthopaedic implants – a review," *Progress in Materials Science*, vol. 54, no. 3, pp. 397–425, 2009.

[35] Y. Li, C. Yang, H. Zhao, S. Qu, X. Li, and Y. Li, "New developments of Ti-based alloys for biomedical applications," *Materials*, vol. 7, no. 3, pp. 1709–1800, 2014.

[36] Ü. Cural, B. Atalay, and M. S. Yildirim, "Comparison of mechanical stabilization of the mandibular angulus fracture fixation, with titanium plates and screws, resorbable plates and screws, and bone adhesives," *Journal of Craniofacial Surgery*, vol. 29, no. 7, pp. 1780–1787, 2018.

[37] M. Quirynen and C. M. L. Bollen, "The influence of surface roughness and surface-free energy on supra- and subgingival plaque formation in man. *A review of the literature*," *Journal of Clinical Periodontology*, vol. 22, no. 1, pp. 1–14, 1995.

[38] D. S. Oh, Y. J. Kim, M. H. Hong, M. H. Han, and K. Kim, "Effect of capillary action on bone regeneration in micro-channeled ceramic scaffolds," *Ceramics International*, vol. 40, no. 7, pp. 9583–9589, 2014.

[39] T. L. Nguyen, A. Blanquet, M. P. Staiger, G. J. Dias, and T. B. F. Woodfield, "On the role of surface roughness in the corrosion of pure magnesium in vitro," *Journal of Biomedical Materials Research Part B: Applied Biomaterials*, vol. 100B, no. 5, pp. 1310–1318, 2012.

[40] B. Yoo, K. R. Shin, D. Y. Hwang, D. H. Lee, and D. H. Shin, "Effect of surface roughness on leakage current and corrosion resistance of oxide layer on AZ91 Mg alloy prepared by plasma electrolytic oxidation," *Applied Surface Science*, vol. 256, no. 22, pp. 6667–6672, 2010.

[41] Y. M. Wang, F. H. Wang, M. J. Xu, B. Zhao, L. X. Guo, and J. H. Ouyang, "Microstructure and corrosion behavior of coated AZ91 alloy by microarc oxidation for biomedical application," *Applied Surface Science*, vol. 255, no. 22, pp. 9124–9131, 2009.

WILEY | Hindawi

Research Article

Characterization of a Bioresorbable Magnesium-Reinforced PLA-Integrated GTR/GBR Membrane as Dental Applications

Xin Du,[1] Yahui Song,[1] Xinxin Xuan,[1] Shuzhen Chen,[1] Xia Wu,[2] Heng Bo Jiang ⓘ,[1] Eui-Seok Lee ⓘ,[3] and Xiaohui Wang ⓘ[1]

[1]*Stomatological Materials Laboratory, School of Stomatology, Shandong First Medical University & Shandong Academy of Medical Sciences, Tai'an, Shandong 271016, China*
[2]*Jinan Stomatological Hospital, Jinan, Shandong 250001, China*
[3]*Department of Oral and Maxillofacial Surgery, Graduate School of Clinical Dentistry, Korea University Guro Hospital, Seoul 08308, Republic of Korea*

Correspondence should be addressed to Eui-Seok Lee; ees225@hanmail.net and Xiaohui Wang; smileava1989@163.com

Inferior mechanical properties have always been a limitation of the bioresorbable membranes in GBR/GTR. This study is aimed at fabricating a bioresorbable magnesium-reinforced polylactic acid- (PLA-) integrated membrane and investigating its mechanical properties, degradation rate, and biocompatibility. The uncoated and fluoride-coated magnesium alloys, AZ91, were made into strips. Then, magnesium-reinforced PLA-integrated membrane was made through integration. PLA strips were used in the control group instead of magnesium strips. Specimens were cut into rectangular shape and immersed in Hank's Balanced Salt Solution (HBSS) at 37°C for 4, 8, and 12 d. The weight loss of the AZ91 strips was measured. Three-point bending tests were conducted before and after the immersion to determine the maximum load on specimens. Potentiodynamic polarization (PDP), electrochemical impedance spectroscopy (EIS), scanning electron microscopy (SEM), and energy-dispersive spectroscopy (EDS) were conducted on coated and uncoated AZ91 plates to examine corrosion resistance. Murine fibroblast and osteoblast cells were cultured on circular specimens and titanium disks for 1, 3, and 5 d. Thereafter, WST test was performed to examine cell proliferation. As a result, the coated and uncoated groups showed higher maximum loads than the control group at all time points. The weight loss of AZ91 strips used in the coated group was lower than that in the uncoated group. PDP, EIS, SEM, and EDS showed that the coated AZ91 had a better corrosion resistance than the uncoated AZ91. The cell proliferation test showed that the addition of AZ91 did not have an adverse effect on osteoblast cells. Conclusively, the magnesium-reinforced PLA-integrated membrane has excellent load capacity, corrosion resistance, cell affinity, and proper degradation rate. Moreover, it has great potential as a bioresorbable membrane in the GBR/GTR application.

1. Introduction

Periodontitis is a chronic inflammation of periodontal attachment tissues caused by local factors, which causes a destructive periodontal disease and alveolar bone loss [1, 2]. The regeneration of the periodontal tissue defect is a challenge for clinicians [3]. GBR/GTR is a radical treatment technique for the periodontal disease. The principle of the periodontal regeneration surgery is to use a membrane as the barrier material. The resistance of the surface to contact with the gingival connective tissue occupies a particular space. It guides the periodontal ligament cells to occupy the root surface of the tooth to form a new cementum and attachment [4].

Barrier membranes are fundamental for GTR/GBR. The ISO selects an ideal biomaterial for GTR/GBR membranes, which should fulfill the main design criteria, such as biocompatibility, space-making, cell occlusiveness, tissue integration, and clinical operability [2, 4]. These materials can be classified into nonbioresorbable and bioresorbable membranes, according to their degradation characteristics [4]. Bioresorbable membranes have the apparent advantage of

degradation. However, its strength is too low to be used for alveolar bone absorption in a large area of posterior teeth, such as polylactic (PLA), collagen membrane [5], and chitosan [6]. Collagen is currently the most popular GTR/GBR membrane material that promotes bone regeneration [7]. However, two disadvantages of collagen membrane limit its development. On the one hand, collagen membrane has low mechanical strength and fast degradation rate *in vivo*. Hence, it easily collapses and loses space support in the application process. Postlethwaite et al. [8] discussed that collagen can act as a barrier to promote cell/tissue regeneration, with an average retention time of about 6 weeks and a relatively short supporting time. On the other hand, the raw material of collagen membrane comes from animal collagen, and the extraction purity is low. Therefore, production cost is expensive. In addition, because the collagen of animals may contain infectious pathogens carried from the animals, the collagen membrane can be infectious to some extent. Chitosan, also called acetyl chitosan, is derived from crustaceans, such as crabs, shrimps, and crayfish. It is a natural polymer material that is bioresorbable [9]. However, owing to the poor mechanical strength of chitosan membrane, it can only be used to treat alveolar bone resorption and periodontal problems in small areas. Moreover, there are many methods for making chitosan membranes, most of which are in the primary stage; therefore, further research is required. Rakhmatia et al. believed that the absorption degree of bioresorbable materials was unpredictable and could affect bone regeneration. If the bioresorbable membrane material was absorbed too quickly, it would lead to the formation of an incomplete barrier membrane structure. It means that the strength of the membrane material for surgeries was not enough to support the regeneration of periodontal tissues and bones [4, 10]. Chen et al. believed that the early exposure of nonbioresorbable GTR membranes to the mouth could lead to bacterial infection, leading to a failure or the incomplete regeneration of periodontal tissues or bones [6, 11]. Nonbioresorbable membranes have prominent strength; however, they cannot be absorbed in the body because they can easily cause secondary infection, such as titanium mesh and polytetrafluoroethylene (PTFE) [4, 6, 12]. In 1984, PTFE membranes were firstly introduced into the field of oral cavity [13]. According to the structure, PTFE is divided into expanded PTFE (e-PTFE) and high-density PTFE (d-PTFE). E-PTFE has ideal mechanical properties and can better maintain the growth space of periodontal tissues. E-PTFE membranes and bioresorbable membranes are usually required to be closed with sutures during the primary surgery to prevent the growth of soft tissues, bacterial infection, membranes location migration, and exposure of implants to the mouth. Nonetheless, d-PTFE membranes have a small aperture and high density, which can prevent various bacteria from infiltrating the barrier membranes and reduce the chance of infection.

Toygar et al. [14] reported that there was no significant difference in the adhesion of dental plaque between the titanium membrane and e-PTFE membrane in the treatment of periodontal defects. The results showed that the titanium membrane was equivalent to e-PTFE membrane for peri-odontal tissue regeneration and can be used for the treatment of periodontal defects. Although the titanium mesh is excessively hard, it can increase the exposure probability of the barrier membrane and increase the stimulation to these soft tissues [15]. The barrier membrane of a single material has different defects, but a composite barrier membrane made of various materials can achieve a mutually reinforcing effect, such as Ti-PTFE [3, 12]. With the help of Ti, the strength of the barrier membrane can be enhanced; however, Ti-PTFE is not a bioresorbable membrane and requires a second operation to be removed. Therefore, it is particularly essential to seek a composite barrier membrane with high strength and bioabsorbability in the current field of GTR/GBR.

Polylactic (PLA) is an aliphatic polyester with better biological activity, deriving from fully renewable resources such as corn and sugar beets [16, 17]. It has a relatively complete manufacturing process that uses a two-step method. First, lactide is obtained by the condensation reaction of lactic acid and then prepared by ring-opening polymerization of lactide [16]. A wide range of experimental studies have found that PLA materials have superior bioabsorbability [18]. After use, PLA can be completely degraded naturally by microorganisms and eventually generate carbon dioxide and water without polluting the environment, which is relatively favorable to environmental protection. As a surgical implant material, its degradability *in vivo* and *in vitro* has also been recognized [19]. This further confirms that PLA has excellent biocompatibility, excellent processability, and controllable permeability (for the access of nutrients into the bone defect). *In vitro*, it performs well in the adhesion of epithelial connective tissues and alveolar bone regeneration, with satisfactory periodontal tissue regeneration [20]. However, considering the inferior mechanical properties of polymeric materials, the individual application of polymers in several clinical situations, especially large bone defects, is limited. Nowadays, PLA has been widely applied in GTR/GBR surgery, which still has an objective prospect in medical biology.

Magnesium alloys as biodegradable implants have distinctive preponderances over Fe-based alloys and Zn-based alloys [21]. In the human body, the degradation product of magnesium alloys is Mg^{2+}. Mg^{2+} is the coenzyme factor of many metabolisms in the body, and Mg^{2+} significantly promotes the formation of new bones [22]. Magnesium alloys produce hydrogen gas during the metabolic process, leading to a high rate of magnesium degradation, which increases the concentrations of Mg^{2+} in body fluids. However, a significant increase in the concentration of Mg^{2+} will inhibit the deposition of osteoblast mineral matrix, which in turn will reduce the osteoblast activity, thus resulting in osteomalacia-like performance [23]. The most effective way to slow down the corrosion rate of magnesium alloys is to perform surface modification, such as hydroxyapatite coating [24] and hydrofluoric acid coating [25–27]. Owing to the controlled permeability of PLA and the excellent mechanical properties of magnesium alloy AZ91, bonding the two together can complement each other. The magnesium alloy serves as the reinforcing core to support the PLA membrane and increase its strength. PLA, as a barrier, on the one hand, can prevent direct contact between magnesium alloy and the

TABLE 1: Group codes and referred composition of samples.

Group	Composition
Coated	Fluoride-coated AZ91-reinforced PLA-integrated membrane
Uncoated	Uncoated AZ91-reinforced PLA membrane
Non-Mg	Integrated membrane with PLA strip
Ti	Titanium disk

surrounding bone tissue, and on the other hand, it can reduce the leakage of Mg^{2+}.

Therefore, the preparation of a magnesium alloy (AZ91)-reinforced PLA-integrated membrane has both degradability and functional strength. Furthermore, the integrated membrane can be better applied to guided tissue regeneration, providing more and better time and space for the regeneration of periodontal tissues and bones. This study verified the feasibility of the design through mechanical experiments, degradation experiments, electrical corrosion tests, surface morphology, and elementary composition analysis for Mg and *in vitro* cell proliferation experiments, aiming to explore the effect of the application of the Mg-reinforced PLA composite membrane in GTR/GBR.

2. Materials and Methods

2.1. Fabrication. PLA granules (Goodfellow, UK) were dissolved in a glass container containing 5% acetone, heated to 50°C, and stirred vigorously for approximately 4 h. Mg alloy AZ91 (9 wt% Al, 1 wt% Zn), both coated and bare, was applied as a reinforcement core. Coated samples were made as follows: AZ91 strips with specific size were rinsed in 35% hydrochloric acid (OCI, Korea) to clean the surface and immersed in 50% hydrofluoric acid (Duksan, Korea) for 8 h to form the fluoride coating. Then, AZ91 strips were washed using deionized water and ethanol. Finally, AZ91 strips were wholly blow-dried. Bare samples (uncoated) were treated in the same way, except for being immersed in HF (Table 1).

The PLA solution was first laid in a metal mold, followed by a Mg alloy AZ91 strip, and then a layer of PLA solution was laid on the AZ91 strip. Next, the solvent was put in a drying oven at 100°C to evaporate for 6 h and produce a Mg-reinforced PLA-integrated membrane. The fabrication method of the integrated membrane in the control group is the same as above, except that the magnesium strip was replaced by a PLA strip. The average thickness of the integrated membranes was 120 μm. The integrated membranes were cut into the desired dimensions (Figure 1).

2.2. Mechanical Test. The dimension of the sample was $40 \times 20 \times 0.12$ mm^3, and the reinforcement core in the middle of the sample was $30 \times 4 \times 0.9$ mm^3. For experimental groups, the coated and uncoated AZ91 were used as the reinforcement cores. For the control group, the PLA strip with dimensions similar to that of the AZ91 strip was employed to replace the AZ91 as the reinforcement core.

Through the three-point bending test, the bending strength was determined as the maximum point of the load-displacement curve; this test was performed in a standard laboratory atmosphere with a universal testing machine (Instron, USA). The crosshead speed was set at 5 mm/min, and the support span was set at 20 mm. At least five samples in each group were tested.

2.3. Degradation Test for Membrane. The weight of magnesium strips (both coated and uncoated) used in this test was first measured as W_o. After the fabrication procedure, coated, uncoated, and non-Mg groups were placed in the closed tubes containing 45 ml of Hank's Balanced Salt Solution (HBSS, Welgene, Korea) and incubated in water baths at 37°C. At the end of each immersion period time of 4, 8, and 12 d, five samples from coated and uncoated groups were removed from the tube. Each magnesium strip was parted from the integrated membrane. It was ultrasonically washed in 20% chromium oxide (Sigma-Aldrich, USA) solution for 1 min to clean off the oxide precipitate on the surface, rinsed with absolute ethanol (Duksan, Korea), and thoroughly blow-dried. The weight was measured again as W_t. The weight loss percentage was calculated as follows:

$$\text{Weight loss (\%)} = (W_o - W_t)/W_o \times 100, \quad (1)$$

where W_o is the initial weight, and W_t is the final weight.

Five samples from each group were removed from the tube and dabbed dry with the tissue, and a three-point bending test was performed on them immediately.

2.4. Electrochemical Corrosion Test for Mg. Coated and uncoated magnesium plates were tested by PDP and EIS tests. First, PDP test was performed on these magnesium plates; thereafter, the experimental results were analyzed using a potentiostat (VersaSTAT 3 : 300) with commercial software (VersaStudio 2.44.4). The electrochemical cell composed of a classical three-electrode cell included a particular working electrode examining sample. Pure graphite was applied as the counterelectrode and Ag/AgCl/Sat-KCl (+197 mV vs. the standard hydrogen electrode) as the reference electrode. Each magnesium plate was placed in a sealed PTFE clamp with an exposed surface area of 1 cm^2 as the working electrode. HBSS (1000 ml) was put in a double-wall beaker as the electrolyte, and the temperature of the electrolyte was maintained at 37 ± 1°C by a circulating water heater. In this experiment, samples were immersed in the HBSS for 1 h to conduct their open circuit potential (OCP) mode. After the OCP, the PDP was done. They scanned the samples from the cathodic area to the anodic area at a rate of 1 mV/s, with a reference electrode value in the range of −2 V to −1 V. Thereafter, the corrosion potential (E_{corr}), current density (I_{corr}), and corrosion rate (CR) were precisely measured by the software. EIS was performed at an OCP, employing a sinusoidal potential of 5 mV in the frequency range from 10^5 to 10^{-2} Hz.

2.5. Surface Morphology and Elementary Composition Analysis. The uncoated and fluoride-coated magnesium alloy AZ91 soaked in HBSS (Welgene, Korea) were taken out; and then, the magnesium alloys were separated from the
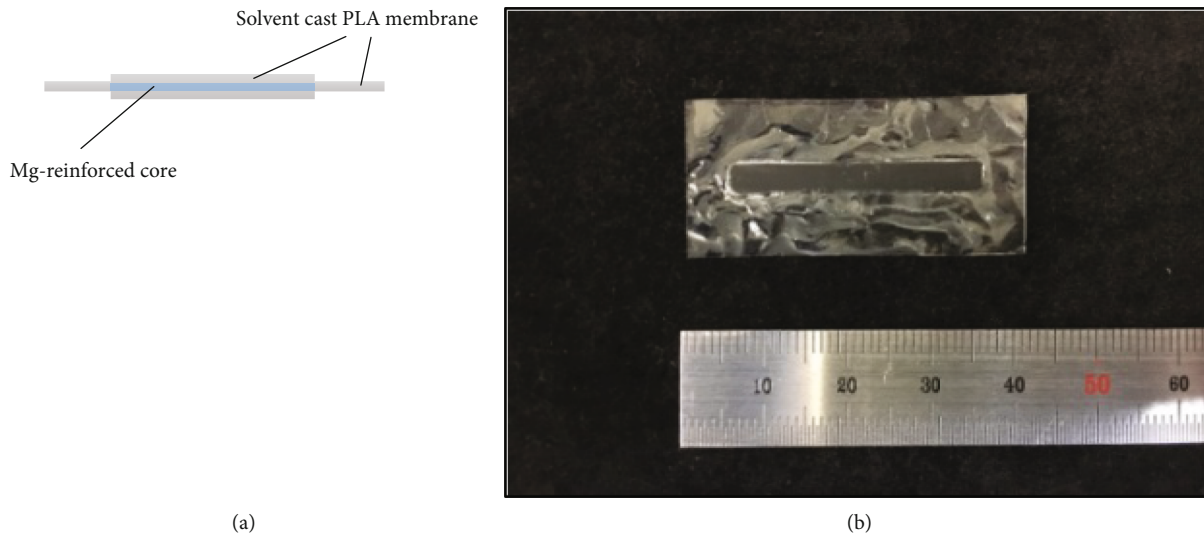
(a)

(b)

Figure 1: (a) Model diagram of magnesium-reinforced PLA-integrated membrane and (b) optical image of magnesium-reinforced PLA-integrated membrane after fabrication.

integrated membranes. Scanning electron microscopy (SEM, JSM-5600; JEOL, Japan) was applied to analyze the surface microstructure and morphology of these two alloys. The concentration analysis (quantitative analysis) of the corroded surfaces and corrosion products of these two magnesium alloys was performed using EDS (Hitachi S-4800, Hitachi, Ltd., Tokyo, Japan) connected to the scanner.

2.6. Cell Proliferation Test. The diameter of circular specimens was 16 mm. The coated magnesium alloy-reinforced PLA-integrated membrane (4×4 mm) and uncoated magnesium alloy-reinforced PLA-integrated membrane were used as experimental groups. The titanium disk and PLA-integrated membrane without Mg were used as control groups. These membranes were irradiated under UV for 1 h. Then, the membrane was individually placed in one 12-well culture plate. Murine-derived preosteoblast (MC3T3-E1) and murine-derived fibroblasts (L929) cell lines were chosen. Two types of culture medium were prepared. The MC3T3-E1 cell line was cultured in a culture media consisting of Dulbecco's modified Eagle's medium (Welgene, Korea) supplemented with 10% fetal bovine serum (FBS, Gibco, USA) and 1% antibiotic/antimycotic (Gibco, USA). The L929 cell line was cultured in a culture media consisting of RPMI 1640 medium (Welgene, Korea) supplemented with 10% FBS and 1% antibiotic/antimycotic (Gibco, USA). MC3T3-E1 and L929 cells were carefully seeded on each specimen with a concentration of 1×10^5 cells in 200 μl of the medium and incubated in 5% CO_2 at 37°C and 95% relative humidity for 1 h. Then, 2 ml of the medium was added to each well. Five samples in each group were cultured for 1, 3, and 5 d. The medium and plate were replaced on days 1, 3, and 5 before the WST test. At each time point, cells were assayed by WST test. 200 μl of the WST assay (DoGenBio, Korea) was added to each well and incubated in a 37°C environment with 5% CO_2 and 95% relative humidity for 3 h. Then, 100 μl of the solution was transferred to a 96-well plate. The absorbance values were measured at 450 nm using the

ELISA Reader. The results were expressed as the averaged absorbance levels of five replicates.

2.7. Statistical Analysis. Statistical analysis of the data was implemented by one-way analysis of variance (ANOVA) followed by Tukey's post hoc analysis, and a $p < 0.05$ was considered meaningful.

3. Results

3.1. Mechanical Test. Figure 2 shows the maximum load recorded in the three-point bending test of coated, uncoated, and non-Mg groups after each immersion time point and the linear fit of each group. Maximum loads of coated and uncoated groups were higher than those of non-Mg group at all time points. Differences between coated and uncoated groups in the whole period were not significant. The trends of decreasing maximum load were similar for all groups.

3.2. Corrosion Tests. Figure 3(a) shows the weight loss percentage of magnesium cores used in coated and uncoated groups after immersion for 4, 8, and 12 d. The weight loss percentage of the uncoated magnesium core was high, as it reached 5.7% at day 12, while that of the coated magnesium core was much lower and was only 2.0% at day 12. Figure 3(b) shows PDP curves for coated and uncoated magnesium plates in the PDP test. The curve of the samples showed an excursion to lower current density values when fluoride coating was applied. Figure 3(c) shows Nyquist plots of coated and uncoated magnesium plates in EIS test. The EIS behavior of the coated magnesium alloy was distinctly different from that of the uncoated magnesium alloy. For the coated magnesium alloy, a larger capacitive loop was shown in the figure, indicating that the corrosion resistance of the coated Mg alloy was much higher than that of the untreated one. Figure 3(d) shows EIS Bode plots obtained for the coated and uncoated magnesium plates. Under the measurement of
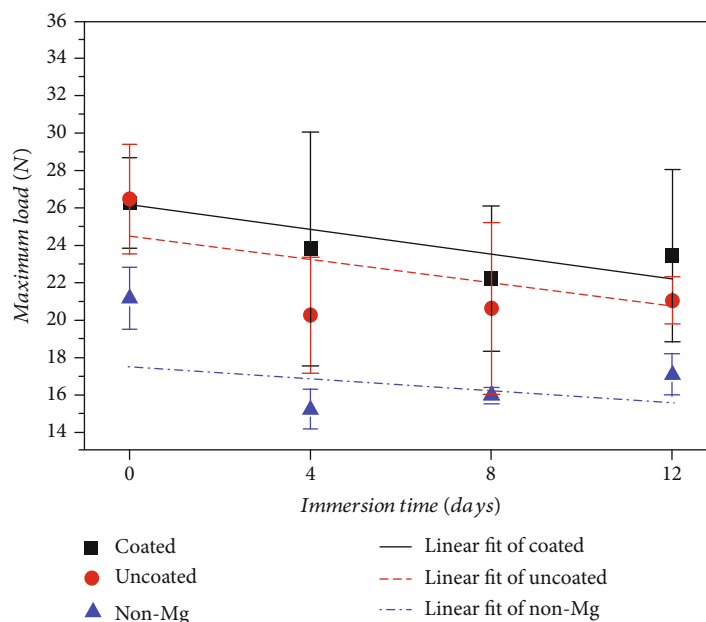
FIGURE 2: Maximum load recorded in three-point bending test after each immersion time point.

0.01 Hz, the resistance modulus value of the coated magnesium alloy is higher than that of the uncoated alloy.

3.3. Surface Morphology and Elementary Composition Analysis for Mg.

Figure 4(a) shows the corroded surface morphology and surface composition of the uncoated magnesium alloy. Through morphological scanning, it can be observed that the surface of the uncoated magnesium alloy was uneven, with prominent crevice corrosion and large-area corrosion. Moreover, a small part of the corrosion particles adheres to the surface of the alloy. From the analysis results of EDS, it can be seen that after corrosion of the uncoated magnesium alloy, from the mass fraction, $O > Mg > C$, and in terms of the atomic fraction, $O > C > Mg$. Figure 4(b) shows the corroded surface morphology and surface composition of the coated magnesium alloy. It can be seen from the picture scanned by the SEM that the corrosion surface of the fluoride-coated magnesium alloy was flatter than that of the uncoated magnesium alloy, and a small amount of hole-type corrosion occurred. Through the EDS, the element composition of the surface of the coated magnesium alloy after 12 d of immersion can be obtained. In terms of the mass fraction, $F > Mg > C > O$, and as for the atomic fraction, $F > Mg > C > O$.

3.4. In Vitro Cell Proliferation Test.

Figure 5(a) shows OD value of cell proliferation test of murine fibroblast cell L929 on membrane materials by the WST test. On day 1, non-Mg group showed significantly higher OD value than those of uncoated and Ti groups. On day 3, the uncoated group exhibited fairly lower OD value than those of coated and Ti groups. On day 5, no apparent difference was shown. Figure 5(b) shows OD value of cell proliferation test of murine osteoblast cell (MC3T3-E1) on membrane materials by the WST test. Day 1 showed no apparent difference. On day 3, the Ti group showed prominently higher OD value than that of non-Mg group. On day 5, Ti group showed relatively higher OD value than those of all other groups.

4. Discussions

Chen et al. [28] reported that the Young's modulus of Mg alloy was a lot closer to human bones than that of bioinert medical metals, such as Ti and stainless steel. Furthermore, the strength of Mg alloy is higher than that of bioabsorbable polymers, such as polylactic acid. Therefore, the magnesium alloy as a reinforcing core will enhance the mechanical properties of PLA and provide an excellent barrier for the regeneration of periodontal tissues. Coated groups and uncoated groups had a higher maximum load than non-Mg groups at all time points in Figure 2, indicating that the reinforcement of the magnesium core vastly increased the load capacity of the integrated membrane. Although coated groups showed close maximum loads as uncoated groups, the visual inspection after the immersion found that the corrosion was generally more severe on the magnesium cores of uncoated groups, indicating that the existence of the fluoride coating can slow down the CR of the magnesium core, and the fluoride coating is significantly necessary for this application. Since the experimental period was only 12 d, it may not be quite enough for the degradation to show the apparent influence on the strength reduction of the membranes. Thence, as shown in Figure 2, as the immersion time increased, the trends of the decrease of the maximum load were not drastic in all groups according to the linear fit. Yan et al. [29] investigated the differences between fluoride-coated and blank AZ31B after immersion in SBF. They found that both the bending strength and morphology of bare AZ31B changed even within two weeks, while fluoride-coated AZ31B had little effect. This result agreed with ours to a certain extent. Consequently, coating technique is vital for slowing down the
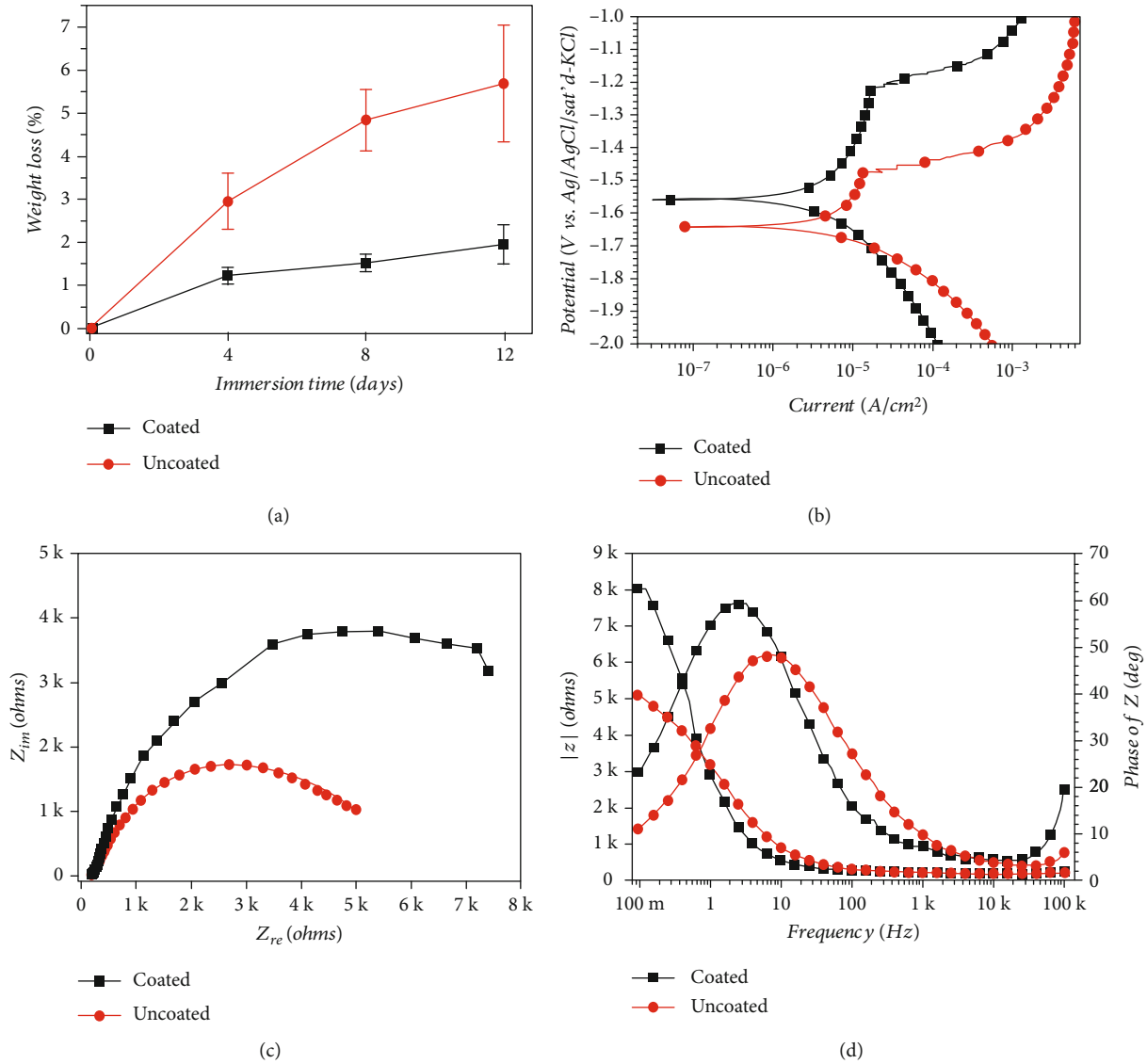
(a)

(b)

(c)

(d)

FIGURE 3: (a) Weight loss percentage of magnesium cores used in coated and uncoated groups in degradation test. (b) Potentiodynamic polarization curves for coated and uncoated magnesium plates in electrochemical corrosion test. (c) Nyquist plots of coated and uncoated magnesium plates in EIS test. (d) EIS Bode plots obtained for the coated and uncoated magnesium plates.

degradation rate and mechanical property deterioration of Mg alloys when applied *in vivo*.

Metal has unique mechanical advantages, which polymer and ceramic cannot compare to. In GBR, for treating large bone defect, Ti mesh is usually required along with the support of grafting materials. The application of polymeric membranes, especially bioabsorbable ones, is considered to result in the formation of an incomplete bone structure. The degradation process of the bioabsorbable membranes may cause the inflammation and affect the healing of bone tissues, which will destroy the integrity of the reconstructed bone [30]. In the composite material of magnesium alloy and polylactic acid, when the volume fraction of magnesium alloy reached 40%, the bending strength of the composite material reached 198 MPa. However, the bending strength of pure PLA is only 88 MPa [31]. Therefore, it is undoubted that the use of AZ91 as a reinforcement core can strengthen

the polymeric membrane. Besides AZ91, Mg and its other alloys also have the potential as reinforcement cores. Gu et al. [32] concluded that the fatigue strength of Mg alloys is in the range 20–100 MPa, whereas that of the polymer ranges from 15 to 58 MPa. The application of different Mg alloys may depend on their specific mechanical properties and biological safety.

The GTR/GBR membranes must not only have excellent mechanical properties but also have an appropriate degradation rate [30]. However, the degradation rate of the magnesium alloy is too fast [33]; hence, it is particularly vital to modify the surface of the magnesium alloy. Tian and Liu studied that hydrofluoric acid coating can reduce the CR of magnesium alloys, delaying the corrosion process in cell culture medium for at least one week [25]. As shown in Figure 3(a), since day 4, the degradation rate of uncoated magnesium cores was approximately two to three times more
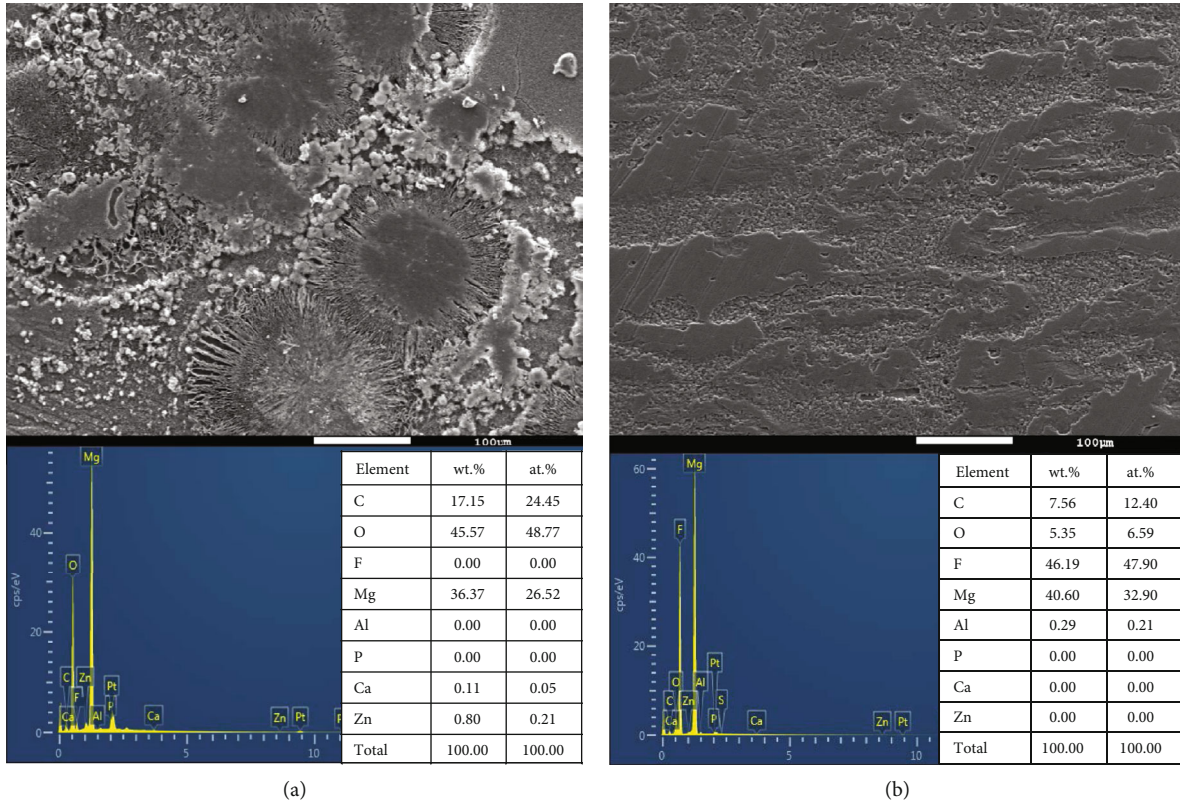
FIGURE 4: Surface morphologies (SEM) and elemental compositions (EDS) of magnesium alloys soaked for 12 days. (a) Uncoated Mg. (b) Coated Mg.
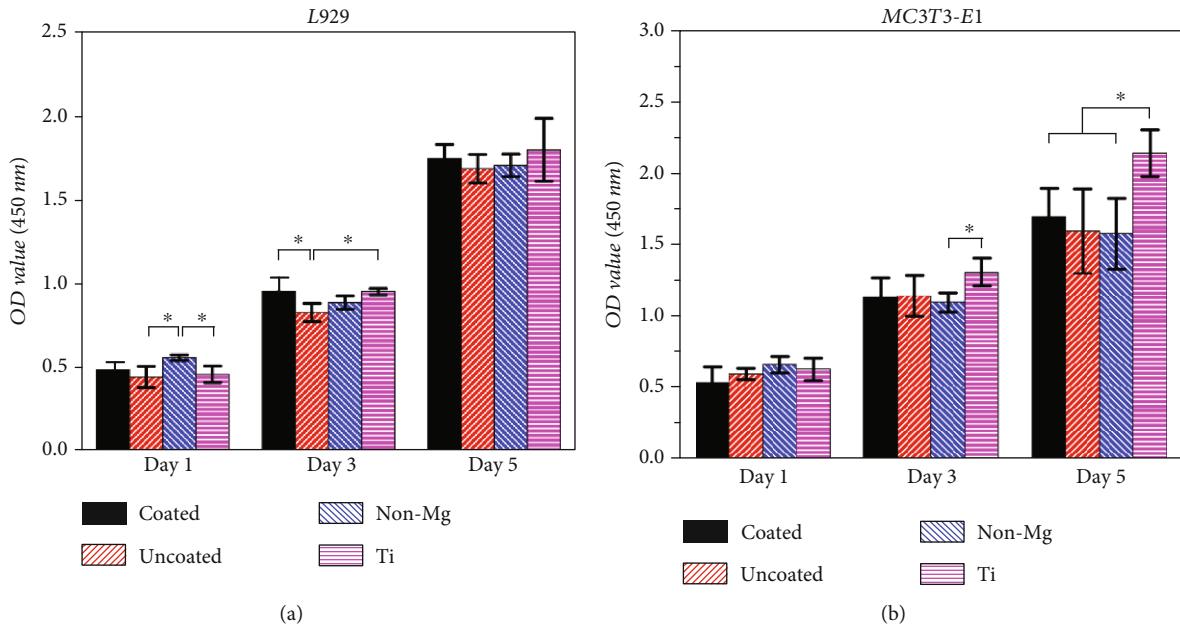
FIGURE 5: Cell proliferation on membrane materials by WST test. (a) Murine fibroblast cell L929. (b) Murine osteoblast cell MC3T3-E1. $^*p < 0.05$.

than that of the coated ones. Even with the coverage of PLA, the weight loss of the uncoated magnesium core reached approximately 6% at the end of the 12-day immersion test. Although the influence on the mechanical resistance of the membrane was not significant in this study, it can be inferred

that the degradation of the magnesium core can still be a significant issue when it is implanted in the human body. Polarization testing is the most common approach to analyze corrosion performance, detecting metal corrosion potential (E_{corr}) and the corrosion current density (I_{corr}) in SBF. I_{corr}

is closely related to CR. Its value is inversely correlated with corrosion resistance, while the value of E_{corr} is in direct proportion to the tendency of corrosion resistance. With the same potential, the coated magnesium alloy had lower current density than that of the uncoated magnesium alloy, indicating that the corrosion resistance of the magnesium alloy was enhanced by the fluoride coating in Figure 3(b). The bare Mg alloy showed weak corrosion resistance in SBF, but the corrosion was hindered after coating. The elevated corrosion resistance of coated magnesium alloy was confirmed by larger capacitive loop in Nyquist plots in Figure 3(c) and larger modulus of impedance at 0.01 Hz in EIS Bode plots in Figure 3(d). Through the comparative observation of the surface morphology shown in Figures 4(a) and 4(b), it can be found that the existence of the fluoride coating has hindered the CR of the magnesium alloy and significantly reduced the corrosion efficiency of the magnesium alloy. This experimental result proved that the fluoride coating played a crucial role in decreasing the CR of the magnesium alloy, and this result was consistent with that of previous studies [34, 35]. The energy spectrum analysis charts in Figures 4(a) and 4(b) showed that the corrosion products of magnesium alloys soaked for 12 d were mainly oxygen-containing compounds. It can be seen that the deposition of corrosion products of the coated magnesium alloy was significantly less than that of the uncoated magnesium alloy. On the surface of the uncoated magnesium alloy, the reaction acted as follows:

$$Mg + H_2O \longrightarrow Mg(OH)_2 \qquad (2)$$

$$Mg(OH)_2 \longrightarrow MgO + H_2O \qquad (3)$$
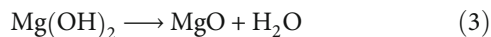
The surface of the coated magnesium alloy was mainly composed of MgF$_2$, which is not easily soluble in water due to the presence of the fluorine. Consequently, there were few corrosion products on the surface of the coated magnesium alloy AZ91, and the degree of the corrosion was lighter. These experimental results in Figures 3 and 4 demonstrated the importance of fluoride coatings for magnesium alloys as implants *in vivo*.

The superior biocompatibility was one of the vital characteristics of implants *in vivo* [36]. As shown in Figure 5(a), fibroblast cells retained steady growth on the coated groups, which can be compared to that on the Ti groups. Although there was some fluctuation in non-Mg and uncoated groups on days 1 and 3, all groups showed similar cell proliferation on day 5. The cell affinity of fibroblast cells to membrane materials can infer the materials' biocompatibility when membranes were implanted into the human body. Furthermore, the cytocompatibility of PLA and magnesium had excellent cell compatibility. In Figure 5(b), osteoblast cells grew better on the titanium, especially on day 5. As is well known, titanium has the feature of osseointegration, which can well explain its better affinity to osteoblast cells. Except for the Ti groups, osteoblast cells had similar proliferation rate on all PLA-integrated membranes with or without the reinforcement of magnesium. These results indicate that the addition of the magnesium core does not harm osteoblast cells in the early stage. Although it cannot be compared to titanium, the cell affinity of PLA has been proven to be sufficient for medical applications and as the GBR membrane. Therefore, this magnesium-reinforced PLA-integrated membrane has passed the trial on both fibroblast and osteoblast. It is going to need an *in vivo* test to confirm the integrated membrane in the future [37].

5. Conclusion

In this study, a GBR/GTR-integrated membrane made of PLA and reinforced by an Mg alloy core was fabricated. The integrated membrane had better load capacity compared to those without the Mg reinforcement. When fluoride-coated magnesium alloy was used, it showed an appropriate degradation rate and better corrosion resistance. Osteoblast and fibroblast cells both grew well on it. Consequently, this bioresorbable magnesium-reinforced PLA-integrated membrane has a potential application in the GBR/GTR technique.

Data Availability

The data used to support the findings of this study are included within the article.

Conflicts of Interest

We declare that we have no financial and personal relationships with other people or organizations that can inappropriately influence our work.

Authors' Contributions

Xin Du, Yahui Song, and Xinxin Xuan contributed equally to this work.

Acknowledgments

References

[1] M. C. Bottino, V. Thomas, G. Schmidt et al., "Recent advances in the development of GTR/GBR membranes for periodontal regeneration—a materials perspective," *Dental Materials*, vol. 28, no. 7, pp. 703–721, 2012.

[2] J. W. Seo, S. R. Shin, Y. J. Park, and H. Bae, "Hydrogel production platform with dynamic movement using photo-crosslinkable/temperature reversible chitosan polymer and stereolithography 4D printing technology," *Tissue Engineering and Regenerative Medicine*, vol. 17, no. 4, pp. 423–431, 2020.

[3] S. B. Qasim, S. Najeeb, R. M. Delaine-Smith, A. Rawlinson, and I. Ur Rehman, "Potential of electrospun chitosan fibers as a surface layer in functionally graded GTR membrane for

periodontal regeneration," *Dental Materials*, vol. 33, no. 1, pp. 71–83, 2017.

[4] Y. D. Rakhmatia, Y. Ayukawa, A. Furuhashi, and K. Koyano, "Current barrier membranes: titanium mesh and other membranes for guided bone regeneration in dental applications," *Journal of Prosthodontic Research*, vol. 57, no. 1, pp. 3–14, 2013.

[5] M. C. Bottino and V. Thomas, "Membranes for periodontal regeneration–a materials perspective," *Frontiers of Oral Biology*, vol. 17, pp. 90–100, 2015.

[6] A. Cucchi, E. Vignudelli, A. Napolitano, C. Marchetti, and G. Corinaldesi, "Evaluation of complication rates and vertical bone gain after guided bone regeneration with non-resorbable membranes versus titanium meshes and resorbable membranes. A randomized clinical trial," *Clinical Implant Dentistry and Related Research*, vol. 19, no. 5, pp. 821–832, 2017.

[7] P. Proussaefs and J. Lozada, "The use of resorbable collagen membrane in conjunction with autogenous bone graft and inorganic bovine mineral for buccal/labial alveolar ridge augmentation: a pilot study," *The Journal of Prosthetic Dentistry*, vol. 90, no. 6, pp. 530–538, 2003.

[8] A. E. Postlethwaite, J. M. Seyer, and A. H. Kang, "Chemotactic attraction of human fibroblasts to type I, II, and III collagens and collagen-derived peptides," *Proceedings of the National Academy of Sciences of the United States of America*, vol. 75, no. 2, pp. 871–875, 1978.

[9] A. Jafari Sanjari and M. Asghari, "A review on chitosan utilization in membrane synthesis," *ChemBioEng Reviews*, vol. 3, no. 3, pp. 134–158, 2016.

[10] C. M. Faggion, "Guided tissue regeneration (GTR) with bioabsorbable collagen membranes (CM) may generate more clinical attachment level gain than open flap debridement (OFD)," *Journal of Evidence Based Dental Practice*, vol. 14, no. 1, pp. 22–24, 2014.

[11] Y.-T. Chen, S. L. Hung, L. W. Lin, L. Y. Chi, and L. J. Ling, "Attachment of periodontal ligament cells to chlorhexidine-loaded guided tissue regeneration membranes," *Journal of Periodontology*, vol. 74, no. 11, pp. 1652–1659, 2003.

[12] J. M. Carbonell, I. S. Martín, A. Santos, A. Pujol, J. D. Sanz-Moliner, and J. Nart, "High-density polytetrafluoroethylene membranes in guided bone and tissue regeneration procedures: a literature review," *International Journal of Oral and Maxillofacial Surgery*, vol. 43, no. 1, pp. 75–84, 2014.

[13] Y. Zhang, X. Zhang, B. Shi, and R. J. Miron, "Membranes for guided tissue and bone regeneration," *Annals of Oral & Maxillofacial Surgery*, vol. 1, no. 1, p. 10, 2013.

[14] H. U. Toygar, E. Guzeldemir, U. Cilasun, D. Akkor, and N. Arpak, "Long-term clinical evaluation and SEM analysis of the e-PTFE and titanium membranes in guided tissue regeneration," *Journal of Biomedical Materials Research Part B: Applied Biomaterials*, vol. 91B, no. 2, pp. 772–779, 2009.

[15] F. Watzinger, J. Luksch, W. Millesi et al., "Guided bone regeneration with titanium membranes: a clinical study," *British Journal of Oral and Maxillofacial Surgery*, vol. 38, no. 4, pp. 312–315, 2000.

[16] R. E. Drumright, P. R. Gruber, and D. E. Henton, "Polylactic acid technology," *Advanced Materials*, vol. 12, no. 23, pp. 1841–1846, 2000.

[17] T. Jiang, W. I. Abdel-Fattah, and C. T. Laurencin, "In vitro evaluation of chitosan/poly(lactic acid-glycolic acid) sintered microsphere scaffolds for bone tissue engineering," *Biomaterials*, vol. 27, no. 28, pp. 4894–4903, 2006.

[18] A. Södergård and M. Stolt, "Properties of lactic acid based polymers and their correlation with composition," *Progress in Polymer Science*, vol. 27, no. 6, pp. 1123–1163, 2002.

[19] S. Ramakrishna, J. Mayer, E. Wintermantel, and K. W. Leong, "Biomedical applications of polymer-composite materials: a review," *Composites Science and Technology*, vol. 61, no. 9, pp. 1189–1224, 2001.

[20] S. G. Rudiger, B. Ehmke, A. Hommens, H. Karch, and T. F. Flemmig, "Guided tissue regeneration using a polylactic acid barrier. Part I: environmental effects on bacterial colonization," *Journal of Clinical Periodontology*, vol. 30, no. 1, pp. 19–25, 2003.

[21] Y. Chen, Z. Xu, C. Smith, and J. Sankar, "Recent advances on the development of magnesium alloys for biodegradable implants," *Acta Biomaterialia*, vol. 10, no. 11, pp. 4561–4573, 2014.

[22] F. Witte, V. Kaese, H. Haferkamp et al., "In vivo corrosion of four magnesium alloys and the associated bone response," *Biomaterials*, vol. 26, no. 17, pp. 3557–3563, 2005.

[23] S. Kamrani and C. Fleck, "Biodegradable magnesium alloys as temporary orthopaedic implants: a review," *Biometals*, vol. 32, no. 2, pp. 185–193, 2019.

[24] S.-M. Kim, J. H. Jo, S. M. Lee et al., "Hydroxyapatite-coated magnesium implants with improved in vitro and in vivo biocorrosion, biocompatibility, and bone response," *Journal of Biomedical Materials Research Part A*, vol. 102, no. 2, pp. 429–441, 2014.

[25] P. Tian and X. Liu, "Surface modification of biodegradable magnesium and its alloys for biomedical applications," *Regenerative Biomaterials*, vol. 2, no. 2, pp. 135–151, 2015.

[26] M. S. Butt, J. Bai, X. Wan et al., "Mg alloy rod reinforced biodegradable poly-lactic acid composite for load bearing bone replacement," *Surface and Coatings Technology*, vol. 309, pp. 471–479, 2017.

[27] W. Ali, A. Mehboob, M. G. Han, and S. H. Chang, "Effect of fluoride coating on degradation behaviour of unidirectional Mg/PLA biodegradable composite for load-bearing bone implant application," *Composites Part A: Applied Science and Manufacturing*, vol. 124, p. 105464, 2019.

[28] J. Chen, L. Tan, X. Yu, I. P. Etim, M. Ibrahim, and K. Yang, "Mechanical properties of magnesium alloys for medical application: a review," *Journal of the Mechanical Behavior of Biomedical Materials*, vol. 87, pp. 68–79, 2018.

[29] T. Yan, L. Tan, D. Xiong, X. Liu, B. Zhang, and K. Yang, "Fluoride treatment and in vitro corrosion behavior of an AZ31B magnesium alloy," *Materials Science and Engineering: C*, vol. 30, no. 5, pp. 740–748, 2010.

[30] W. Florjanski, S. Orzeszek, A. Olchowy et al., "Modifications of polymeric membranes used in guided tissue and bone regeneration," *Polymers*, vol. 11, no. 5, p. 782, 2019.

[31] X. Li, C. L. Chu, L. Liu et al., "Biodegradable poly-lactic acid based-composite reinforced unidirectionally with high-strength magnesium alloy wires," *Biomaterials*, vol. 49, pp. 135–144, 2015.

[32] X. N. Gu, W. R. Zhou, Y. F. Zheng et al., "Corrosion fatigue behaviors of two biomedical Mg alloys – AZ91D and WE43 – in simulated body fluid," *Acta Biomaterialia*, vol. 6, no. 12, pp. 4605–4613, 2010.

[33] X. Li, C. Qi, L. Han et al., "Influence of dynamic compressive loading on the in vitro degradation behavior of pure PLA

and Mg/PLA composite," *Acta Biomaterialia*, vol. 64, pp. 269–278, 2017.

[34] O. Saliza Azlina, M. Shafiq Ruba'ai, and D. Kurniawan, "Effect of magnesium fluoride coating on corrosion behaviour of magnesium alloy," *IOP Conference Series: Materials Science and Engineering*, vol. 694, article 012049, 2019.

[35] T. Li, Y. He, H. Zhang, and X. Wang, "Microstructure, mechanical property and in vitro biocorrosion behavior of single-phase biodegradable Mg–1.5Zn–0.6Zr alloy," *Journal of Magnesium and Alloys*, vol. 2, no. 2, pp. 181–189, 2014.

[36] J. Wang, L. Wang, Z. Zhou et al., "Biodegradable polymer membranes applied in guided bone/tissue regeneration: a review," *Polymers*, vol. 8, no. 4, p. 115, 2016.

[37] M. T. Sun, A. J. O'Connor, I. Milne et al., "Development of macroporous chitosan scaffolds for eyelid tarsus tissue engineering," *Tissue Engineering and Regenerative Medicine*, vol. 16, no. 6, pp. 595–604, 2019.

WILEY | Hindawi

Research Article

Effects of the Different Solid Deposits on the Corrosion Behavior of Pure Fe in Water Vapor at 500°C

Yanbing Tang [iD],[1,2] Xinwang Shen [iD],[3] Zhihong Liu,[3] and Ying Li [iD][1]

[1]*Institute of Metal Research, Chinese Academy of Sciences, 110016 Shenyang, China*
[2]*Marine Equipment and Technology Institute, Jiangsu University of Science and Technology, 212003 Zhenjiang, China*
[3]*School of Materials Science and Technology, Jiangsu University of Science and Technology, 212003 Zhenjiang, China*

Correspondence should be addressed to Ying Li; liying@imr.ac.cn

A comprehensive corrosion investigation of pure Fe in an environment of solid sodium salt deposit (i.e., NaCl or Na_2SO_4) with mixtures of H_2O and O_2 at 500°C was conducted by mass gain measurement, X-ray diffraction (XRD), scanning electron microscope (SEM), potentiodynamic polarization, and electrochemical impedance spectroscopy (EIS). The results showed that corrosion rates were accelerated with solid NaCl or Na_2SO_4 deposit due to their reaction with the formed protective scale of Fe_2O_3 and subsequently resulted in its breakdown. The corrosion rate of pure Fe with solid NaCl is higher than that with solid Na_2SO_4 because of the lower activation energy (E_a) for chemical reaction of Fe in solid $NaCl+H_2O+O_2$ (i.e., 140.5 kJ/mol) than that in solid $Na_2SO_4+H_2O+O_2$ (i.e., 200.9 kJ/mol). Notably, the electrochemical corrosion rate of pure Fe with solid NaCl deposit, 1.16×10^{-4} A/cm^2, was a little lower than that with solid Na_2SO_4 deposit.

1. Introduction

Corrosion of metal materials is severe in the environment with solid salt deposit and dry or wet O_2 at medium and high temperatures [1–18], especially for turbine blades in planes or ships and power boilers. Due to their excellent mechanical properties, low cost, and ease of machining, pure Fe and its alloys are the popular materials that were investigated in solid alkali chloride deposit in dry or wet O_2 [1–7]. Most researchers [2, 5, 6] thought that the solid NaCl could react with Fe_2O_3 to generate Cl_2 via the reaction, $2NaCl + Fe_2O_3 + 1/2O_2 = Na_2Fe_2O_4 + Cl_2$. Then, Cl_2 could react with Fe to form FeCl(s), i.e., $Cl_2 + Fe = FeCl_2(s)$. As such, $FeCl_2(s)$ would continuously evaporate under low vapor pressure at high temperature. The $FeCl_2$ vapor would diffuse outward through cracks and pores of the scale. Finally, the $FeCl_2$ vapor would react with O_2 to form Fe_3O_4 and/or Fe_2O_3 when they met during the process. Apparently, the solid NaCl could react with the oxidation scale that formed in dry or wet air at medium and high tempera-

tures and lead to the breakdown of the protective scale to accelerate the corrosion rate of materials. Folkenson et al. [7] proposed a new mechanism as follows. Solid KCl reacts with O_2 and H_2O to generate chloride ions (i.e., $2KCl + 1/2 O_2 + H_2O + 2e^- \longrightarrow 2KOH\,(ads) + 2Cl^-\,(ads)$) and subsequently react with iron ions to form $FeCl_2(s)$. Cao et al. [3] postulated a hypothesis of "dynamic water film" in which H_2O molecules were continuously being absorbed on and evaporated from the surface of the material. The electrochemical corrosion might occur in the dynamic water film, which accelerates the corrosion of metal [3]. Shu et al. [10] used impedance spectroscopy to investigate the corrosion mechanisms of pure Fe and pure Cr with solid NaCl deposit in water vapor at 600°C. According to the analysis of the resistance and capacitance of corrosion scale, the electrochemical corrosion was proved to occur in the corrosion environments. After that, Tang et al. [1] investigated the interaction between chemical reactions and electrochemical reactions of pure Fe in this corrosion environment. The chemical reactions and electrochemical

reactions follow "ce mechanism," in which Fe and Fe_2O_3 first react chemically with NaCl, water vapor, and oxygen to generate HCl (g). Then, the HCl (g) reacts with pure Fe electrochemically via a one-electron electrochemical reduction to form H_2.

Compared to the alkali chlorides, the corrosion mechanisms of metal/alloys with solid sulfate are lacking. However, the corrosion mechanisms are focused on molten sulfate. Recently, many studies have been carried out on the corrosion behavior of metals/alloys in a molten Na_2SO_4 environment [19–25] and many corrosion mechanisms have been proposed. One of the well-known mechanisms is the sulfidation model [19, 20], in which the formation of sulfides accelerates the corrosion. The other one is the acidic-basic fluxing [19, 21–24] mechanism, in which dissolution of the protective oxide scales, due to formation of basic Na_2O, was considered the reason for the accelerated corrosion. Moreover, based on the electrochemical mechanism [25], corrosion was considered an electrochemical reaction in which the transfer of electrons accelerated the corrosion. Tang et al. [26] investigated the corrosion behavior of pure Fe under solid Na_2SO_4 deposit in wet oxygen flow at 500°C. The results showed that the corrosion of Fe includes chemical corrosion and electrochemical corrosion. The chemical reaction and electrochemical reaction follows the "ce mechanism." Fe and Fe_2O_3 first react chemically with Na_2SO_4, water vapor, and oxygen to generate H_2SO_4 (g). And then, the H_2SO_4 (g) reacts with pure Fe electrochemically via a one-electron electrochemical reduction to form H_2. The coeffect between deposited solid Na_2SO_4 and H_2O+O_2 certainly exists and significantly accelerates the corrosion of pure Fe.

NaCl and Na_2SO_4 are normal corrosive mediums. The corrosion of materials in solid salt environment depends on the anion of the salt [18, 27]. However, the effects of the different solid deposits (NaCl and Na_2SO_4) on the corrosion behavior of pure Fe in water vapor are still unclear. In this paper, the corrosion differences of pure Fe with solid NaCl and solid Na_2SO_4 deposit in water vapor were comparatively studied to cognize the corrosion behaviors of materials in the corrosion profoundly.

2. Experimental

The pure Fe (99.9%) was used as experimental specimen. The metallography of the specimen is shown in Figure 1. The microstructure of pure Fe is ferrite. The maximum grain size is about $100\,\mu m$. Before the experiment, the sample was ground using silicon-carbide abrasive papers down to 1000 grit, degreased in acetone then ethanol, and dried in air before use. The NaCl and Na_2SO_4 are of analytical purity (≥99.5%). The solid salt was deposited on the preheated Fe sample surface by repeatedly brushing and drying a salt-saturated solution. The mass of salt was about $4\,mg/cm^2$. The temperature of the furnace was controlled at 500°C. H_2O came from an 80°C water bath. Pure O_2 was passed through the glass bubbler with a flux of 200 ml/min.

The corrosion test was carried out in a thermal balance [2]. To prevent the H_2O from condensing in the upper part of the thermal balance, a counterflow of N_2 was passed
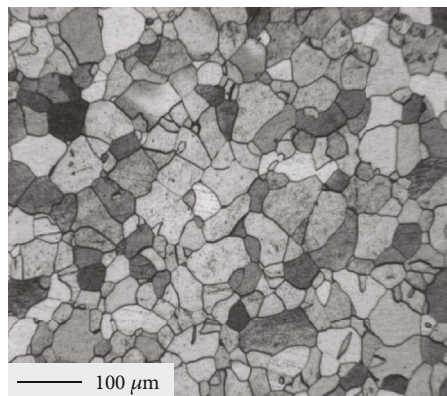

Figure 1: Metallograph of pure Fe.

through the apparatus at 150 ml/min. After the furnace was heated to the desired temperature and the gas flow was stabilized, the specimen was quickly suspended into the furnace tube, and the test was started. All the measurements were carried out at ambient pressure. After the tests, the specimens were further examined by XRD and SEM.

A special three-electrode system was built for the electrochemical measurements in this particular environment [1]. To decrease the resistance of the solution and obtain a uniform electric field, the reference electrodes consisted of four platinum wires, each with a diameter 0.4 mm, and the counter electrode was a circular strip of platinum foil about 2 mm wide. All potential values in this paper were reported versus this platinum reference electrode. The Fe working electrode was a rod 10 mm long and 5 mm diameter. The three electrodes were placed in quartz tubes, which acted as insulators. All the gaps were sealed by high-temperature inorganic glue. The three-electrode system after solid NaCl and solid Na_2SO_4 deposition was directly put into the furnace at the desired temperature and with water vapor for electrochemical measurements.

A PAR2273 Electrochemical Measurement System manufactured by EG&G was used for all electrochemical measurements, which also has the function to compensate the resistance between reference electrode and working electrode. In the galvanic corrosion measurement, the ratio of anodic area to cathodic area is 1 : 2. In the potentiodynamic polarization measurements, the measurements were carried out after 1000 s in the corrosion environment for obtaining an electrochemical stability and the scan rate was 1 mV/s. The resistance between reference and working electrodes was compensated during measurements according to the design of electrochemical system and testing work station. All measurements were repeated more than three times.

3. Results and Discussion

Figure 2 shows the mass gain of pure Fe as a function of time at 500°C with and without solid NaCl or Na_2SO_4 [26] in O_2 containing water vapor. As is seen from Figure 2, the corrosion of pure Fe is accelerated with solid NaCl or Na_2SO_4 deposit. Compared to the case with solid Na_2SO_4 deposit,
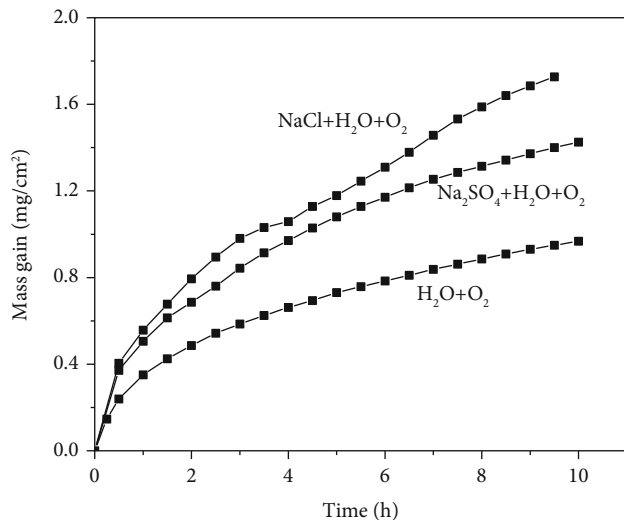
FIGURE 2: Mass gain plots of pure Fe with and without solid NaCl or Na_2SO_4 deposit in O_2 containing water vapor at 500°C.

the corrosion rate of pure Fe with solid NaCl deposit is slightly higher at all-time duration.

In our previous studies [1, 13], it is found that the corrosion of pure Fe in both corrosion environments includes a chemical corrosion process and an electrochemical corrosion process, while the overall corrosion is dominated by the chemical corrosion process with a percentage of over 90%. Herein, we investigated the differences of chemical corrosion that is influenced by NaCl and Na_2SO_4.

To affect the chemical corrosion rate, there are two aspects: (a) the protection of scale on the surface of pure Fe. The compact and integrated scale can restrain the corrosion of substrate. (b) The activity of corrosion reactants. As it is known, the corrosion rate would increase with a decreasing active energy. The details of the effects are discussed as follows.

The scale includes solid salt deposition scale (NaCl or Na_2SO_4) and corrosion scale on the surface of pure Fe. Figures 3(a) and 3(b) show the surface morphologies of solid NaCl and Na_2SO_4, respectively, before corrosion test. The results showed that both salt scales are loose and porous. However, the solid NaCl film was much looser and more porous than solid Na_2SO_4 film, which led to an easy transport of H_2O and O_2 to the interface of pure Fe and solid NaCl film, promoting the chemical corrosion process of pure Fe.

The corrosion of materials with solid salt deposit in water vapor is different with that in aqueous solution. The corrosion scale would stay on the surface of substrate, which should restrain the corrosion of substrate. Figure 4 shows the cross-sectional morphologies of pure Fe after 10 h corrosion at 500°C in $NaCl + H_2O + O_2$ (Figure 4(a)) and $Na_2SO_4 + H_2O + O_2$ (Figure 4(b)) [26]. It indicated that the corrosion scale formed on the surface of pure Fe was loose and porous in both corrosion environments. A number of volatile species are formed in the corrosion process, which could contribute to the formation of the

loose and porous corrosion scale [6]. As a matter of fact, some green deposits were observed on the tube inner surface of the furnace after many hours of experiments, confirming the formation of volatile species. However, the scale formed in solid $NaCl + H_2O + O_2$ is looser and higher porosity than that formed in solid $Na_2SO_4 + H_2O + O_2$ [26]. This indicated that the reactants (H_2O and O_2) could be easier to transport through the corrosion scale formed in the environment with NaCl. Eventually, it promotes the chemical corrosion process of pure Fe.

The components of the corrosion scale formed on the surface of pure Fe in solid $NaCl + H_2O + O_2$ or $Na_2SO_4 + H_2O + O_2$ [26] after 10 h corrosion are shown in Figure 5. The components of the scales in the two corrosion environments are remarkably different. The component of the scale on the surface of pure Fe formed in solid $NaCl + H_2O + O_2$ is hematite that mainly consists of Fe_2O_3, while the component of the scale on the surface of pure Fe formed in solid $Na_2SO_4 + H_2O + O_2$ mainly consists of Fe_3O_4 with a little of Fe_2O_3. According to the published research [27], the generation of Fe_2O_3 or Fe_3O_4 is closely relative to oxygen pressure. Fe_2O_3 would be generated at a relatively high oxygen pressure, while Fe_3O_4 would be generated at a relatively low oxygen pressure. From Figures 3 and 4, the NaCl scale is looser with higher porosity than Na_2SO_4 scale; meanwhile, the corrosion scale formed in the case of $NaCl + H_2O + O_2$ was also looser with higher porosity than that formed in the case of $Na_2SO_4 + H_2O + O_2$. The oxygen could transport inward through the corrosion scale and solid NaCl scale easily. The oxygen pressure in the corrosion scale that formed in $NaCl + H_2O + O_2$ is higher than that formed in $Na_2SO_4 + H_2O + O_2$. This is the reason why the components of the corrosion scales in the two corrosion environments were different.

The corrosion mechanism of pure Fe in the two corrosion environments could be understood on the basis of the components, morphologies of the corrosion scales, and published research.

For the case of solid NaCl, firstly, NaCl reacts with Fe_2O_3 and H_2O to generate $Na_2Fe_2O_4$ and HCl [4].

$$2NaCl(s) + Fe_2O_3 + H_2O = Na_2Fe_2O_4 + HCl. \quad (1)$$
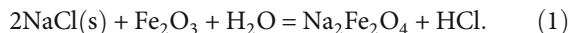
The generated HCl could react with Fe to form $FeCl_2$ [4], meanwhile, HCl could also react with O_2 to form Cl_2 [27].

$$2HCl + Fe = FeCl_2(s) + H_2$$
$$4HCl + O_2 = 2Cl_2 + 2H_2O \quad (2)$$
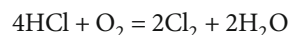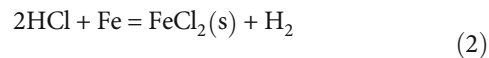
The Cl_2 could react with Fe to form $FeCl_2$ [28].

$$Fe + Cl_2 = FeCl_2(s) \quad (3)$$
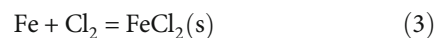
The vapor pressure for $FeCl_2(s)$ is 4×10^{-5} Pa at 500°C. A continuous evaporation will take place [6].

$$FeCl_2(s) = FeCl_2(g) \quad (4)$$

(a)

(b)
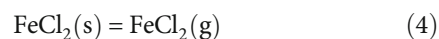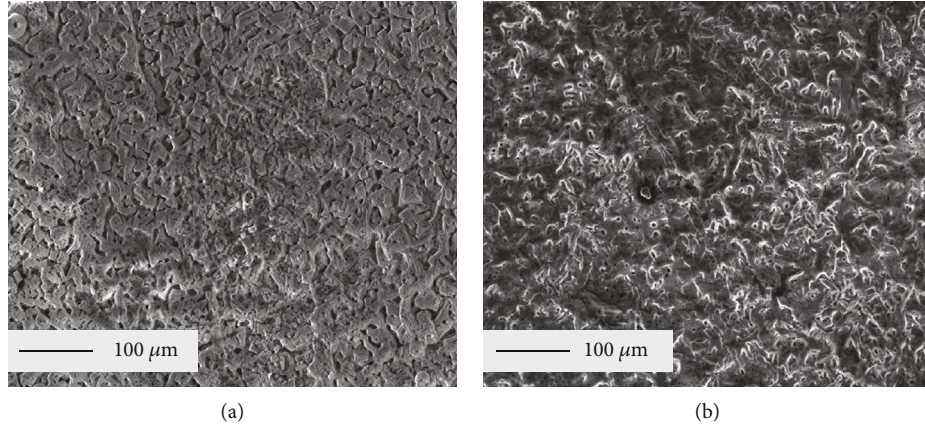
FIGURE 3: Surface morphologies of solid salt scale on pure Fe before experiment: (a) solid NaCl; (b) solid Na_2SO_4.

(a)

(b)
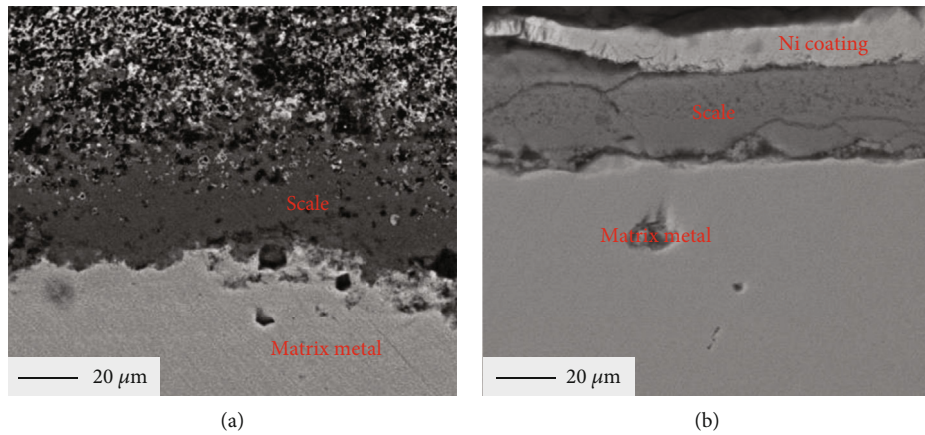
FIGURE 4: Cross-sectional morphologies of pure Fe with NaCl or Na_2SO_4 deposit in O_2 flow with water vapor for 10 h: (a) solid NaCl and (b) solid Na_2SO_4.

Δ-Hematite
O-Magnetite
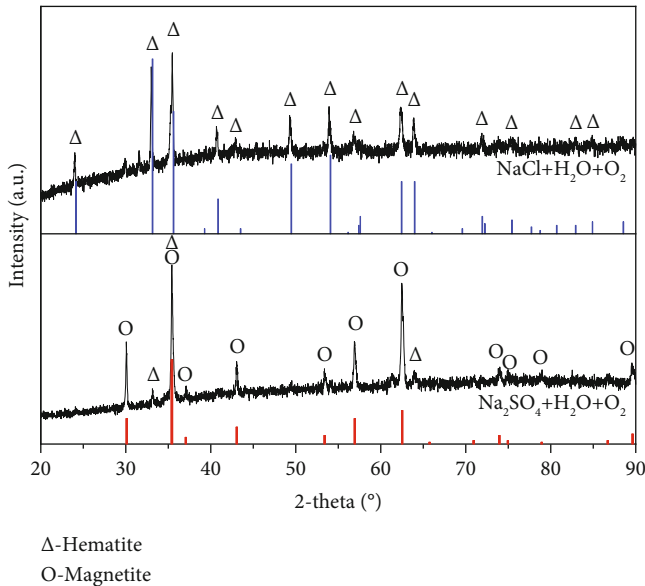
FIGURE 5: XRD results of the corrosion scale of pure Fe in water vapor with solid NaCl or Na_2SO_4 deposits at 500°C.

The $FeCl_2(g)$ diffuse outward through the scale and react with O_2 and H_2O to form a loose and porous Fe_2O_3 scale (see Figure 4(a)) [4].

$$2FeCl_2 + 1/2\,O_2 + 2H_2O = Fe_2O_3 + 4HCl \qquad (5)$$
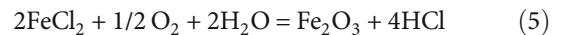
For the case of solid Na_2SO_4, firstly, Na_2SO_4 reacts with Fe_2O_3 and H_2O to generate $Na_2Fe_2O_4$ and H_2SO_4 [26].

$$Na_2SO_4 + Fe_2O_3 + H_2O = Na_2Fe_2O_4 + H_2SO_4 \qquad (6)$$
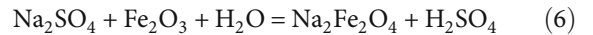
The generated H_2SO_4 could react with Fe to form $FeSO_4$.

$$H_2SO_4 + Fe = FeSO_4 + H_2 \qquad (7)$$
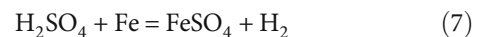
According to the XRD results, the $FeSO_4$ could react with O_2 and H_2O to form Fe_3O_4 and Fe_2O_3.

$$5FeSO_4 + 5H_2O + O_2 = Fe_3O_4 + Fe_2O_3 + 5H_2SO_4 \qquad (8)$$
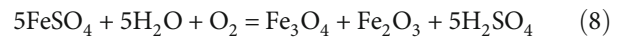
The generation of H_2SO_4 and H_2 led to the formation of many holes and cracks in the scale (see Figure 4(b)).

According to the morphologies shown in Figures 3 and 4, the more porous NaCl scale and corrosion scale formed in
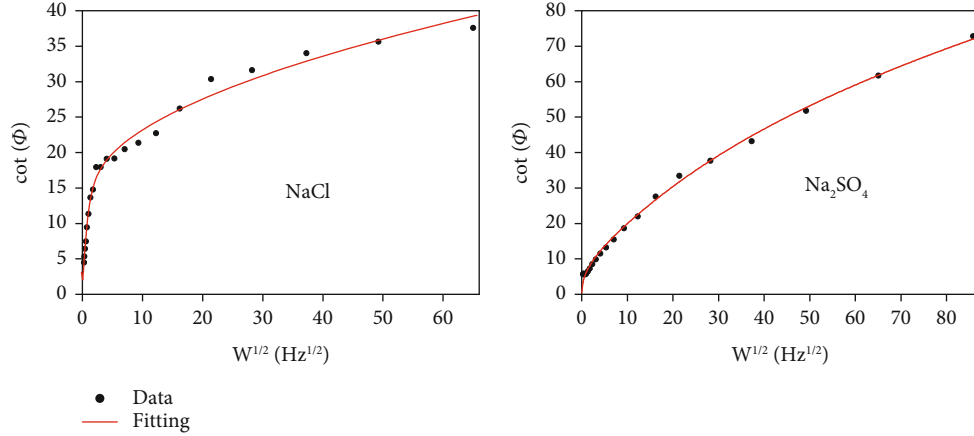
FIGURE 6: Frequency dependence of the phase angle of Fe in water vapor with NaCl or Na_2SO_4 deposits at 500°C at open circuit potential.

the $NaCl + H_2O + O_2$ promoted the chemical corrosion process. However, this did not fully explain why the corrosion rate of pure Fe in $NaCl + H_2O + O_2$ was higher than that in $Na_2SO_4 + H_2O + O_2$. The activation energy is a key parameter to estimate the chemical reaction rate. The lower the activation energy, the more atoms, ions, or molecules of substances are activated to transition state. Therefore, the rate of chemical reaction increases with decreases in chemical reaction activation energy.

Both corrosion mechanisms of pure Fe in solid $NaCl + H_2O + O_2$ and solid $Na_2SO_4 + H_2O + O_2$ corrosion environments follow the ce mechanism [1, 26]. For the ce mechanism, the relationship between phase angle and frequency could be given as Equation (9) [28].

$$\cot \phi = \frac{((2\omega)^{1/2}/\lambda) + (1/(1+e^i))\{(1/(1+K))\left[\left((1+g^2)^{1/2}+g\right)/(1+g^2)\right]^{1/2} + (K/(1+K)) + e^i\}}{(1/(1+e^i))\{(1/(1+K))\left[\left((1+g^2)^{1/2}-g\right)/(1+g^2)\right]^{1/2} + (K/(1+K)) + e^i\}},$$

(9)

$$g = \frac{k_1 + k_2}{\omega},$$ (10)

$$\lambda = \frac{k_h f}{D^{1/2}} \left(e^{-\alpha j} + e^{\beta j}\right),$$ (11)

$$K = \frac{k_1}{k_2},$$ (12)

$$\beta = 1 - \alpha,$$ (13)

$$j = \frac{nF}{RT}(E_{d.c.} - E_{1/2}^r),$$ (14)

where Φ is used for representing for phase angle, k_1 and k_2 for chemical reaction rate constants, ω for angular frequency, D for diffusion coefficient, k_h for apparent heterogeneous rate constant, f for activity coefficient, α for charge transfer coefficient, n for number of electrons transferred, $E_{d.c.}$ for applied d. c. potential, $E_{1/2}^r$ for reversible half-wave potential, and F, R, and T for their conventional electrochemical meanings. The value of k_1 can be calculated using Equation (9). Figure 6 shows the relationship between frequency and phase angles of pure Fe

in solid $NaCl + H_2O + O_2$ at 500°C. The plots have a maximum. It suggests that the corrosion mechanism of pure Fe in the two corrosion environments involves the interaction of the chemical and the electrochemical reactions, which is similar with pure Fe in solid $Na_2SO_4 + H_2O + O_2$ [26]. The calculated values of k_1 for pure Fe in solid $NaCl + H_2O + O_2$ and solid $Na_2SO_4 + H_2O + O_2$ corrosion environments are 0.230 sec^{-1} and 0.031 sec^{-1}, respectively. Therefore, the chemical corrosion rate of pure Fe in solid $NaCl + H_2O + O_2$ is higher than that in solid $Na_2SO_4 + H_2O + O_2$ because of its higher chemical reaction rate constant in the case with solid NaCl.

Chemical reaction rate is closely related with the activation energy. The lower the activation energy is, the higher the chemical reaction rate is. According to the logarithmic Arrhenius equation, the rate constant (k) dependence of temperature (T) is given by the relationship (g) [29]:

$$\ln k = \ln A - \frac{E_a}{RT},$$ (15)

where k is used for representing for the rate constant, A for a temperature-independent constant (often called the frequency factor), T for the absolute temperature, R for the universal gas constant, and E_a for the activation energy. According to Equation (15), a plot of $\ln k$ vs. $1/T$ gives a straight line with slope of - E_a/R. The values of E_a for Fe in solid $Na_2SO_4 + H_2O + O_2$ corrosion environments can be obtained from the slope of Figures 7. The value is 200.9 kJ/mol. The value of E_a for Fe in solid $NaCl + H_2O + O_2$ corrosion environments is 140.5 kJ/mol [13]. The lower activation energy of Fe in solid $NaCl + H_2O + O_2$ accounts for its higher chemical reaction and the higher overall corrosion rate.

The electrochemical corrosion of pure Fe in solid $Na_2SO_4 + H_2O + O_2$ corrosion environments has been shown in our earlier studies [1, 26]. The potentiodynamic polarization plot of pure Fe in solid $NaCl + H_2O + O_2$ at 500°C is shown in Figure 8. The anodic current densities of pure Fe in both two corrosion environments increase linearly with anodic potential increasing in the active polarization zone, which can be attributed to active dissolution in the aqueous environment, because the loose and porous corrosion scale could
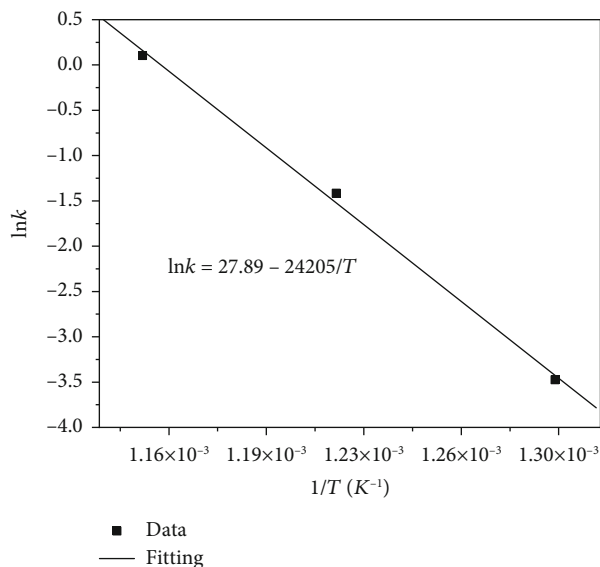
FIGURE 7: Temperature dependence of chemical reaction rate constant of pure Fe with solid Na_2SO_4 deposit in O_2 flow with water vapor.
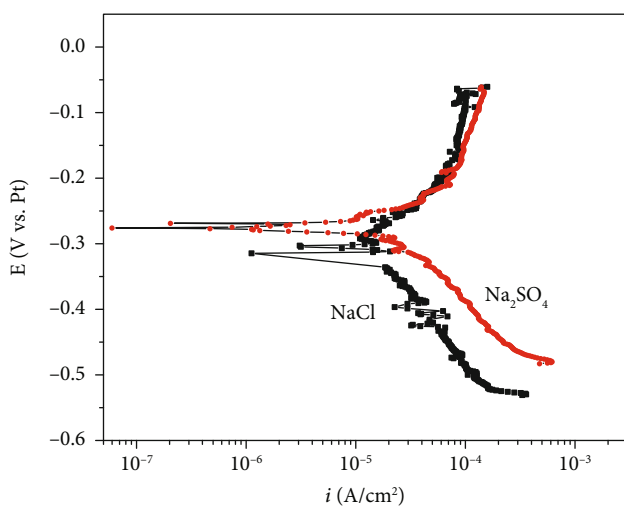

FIGURE 8: Potentiodynamic polarization plots of pure Fe in water vapor with solid NaCl or Na_2SO_4 deposits at 500°C.

not inhibit the electrochemical corrosion. The cathodic reaction rate of pure Fe in solid $Na_2SO + H_2O + O_2$ is higher than that in $NaCl + H_2O + O_2$. The electrochemical corrosion rates (i_{corr}) were calculated by fitting the potentiodynamic polarization curves in the active polarization zones. The electrochemical corrosion current density (i_{corr}) obtained was 1.16×10^{-4} A/cm^2 and 1.30×10^{-4} A/cm^2 for pure Fe in solid $NaCl + H_2O + O_2$ and solid $Na_2SO_4 + H_2O + O_2$ [26], respectively. The amount of Fe corroded by electrochemical reaction was obtained using Faraday's rule. After the calculation, the chemical reaction rates of pure Fe in the two corrosion environments within 1 h are 0.036 g/h/cm^2 and 0.041 g/h/cm^2, respectively. It must illustrate that the calculation time herein is in one hour, because the potentiodynamic polarization measurements were carried out within one hour,

and there is no significantly variety of the electrochemical corrosion rate in one hour. This was proved by presented authors used an electrochemical instrument named CMB 1510B (based on weak polarization theory) manufactured by State Key Laboratory for Corrosion and Protection, to measure the electrochemical corrosion rate every 4 minutes during the whole corrosion reaction. The electrochemical corrosion rate of pure Fe in solid $NaCl + H_2O + O_2$ is slightly lower than that in solid $Na_2SO_4 + H_2O + O_2$.

As is well-known, charge transfer is the fundamental characteristic of the electrochemical reaction [30, 31]. The corrosion scale and solid salt scale are the key influence factors for electrochemical reaction rate. The corrosion scale of pure Fe formed in solid $NaCl + H_2O + O_2$ is looser and more porous than those formed in solid $Na_2SO_4 + H_2O + O_2$ (see Figure 4), and the solid NaCl scale is also looser and more porous than solid Na_2SO_4 scale (see Figure 3). The HCl could volatilize and diffuse through the looser and more porous corrosion scale and NaCl scale easily. Thus, the cathodic reaction rate of pure Fe in solid $Na_2SO_4 + H_2O + O_2$ is higher than that in solid $NaCl + H_2O + O_2$. As a consequence, the electrochemical corrosion rate of pure Fe in solid $Na_2SO_4 + H_2O + O_2$ is higher than that in solid $NaCl + H_2O + O_2$.

As a consequence, the electrochemical corrosion rate of pure Fe in solid $Na_2SO_4 + H_2O + O_2$ is higher than that of it in solid $NaCl + H_2O + O_2$. In addition, the components of the corrosion scales formed on the surface of pure Fe in solid $NaCl + H_2O + O_2$ and solid $Na_2SO_4 + H_2O + O_2$ after 10 h corrosion are shown in Figure 5. The component of the scales on the surface of pure Fe formed in solid $NaCl + H_2O + O_2$ is hematite that mainly consists of Fe_2O_3, while the component of the scales on the surface of pure Fe formed in solid $Na_2SO_4 + H_2O + O_2$ is Magnetite that mainly consists of Fe_3O_4. The protection of Fe_2O_3 is well than that of Fe_3O_4 [32], which also inhibit the electrochemical corrosion rate of pure Fe in solid $NaCl + H_2O + O_2$ corrosion environment.

4. Conclusion

The corrosion rate of the pure Fe is significantly accelerated under a NaCl or Na_2SO_4 deposit in an atmosphere of $H_2O + O_2$ at 500°C. Both the salts of NaCl and Na_2SO_4 could react with Fe_2O_3 to result in a breakdown of the protective scale and subsequently accelerate the corrosion rate of pure Fe.

Compared to the case in solid $Na_2SO_4 + H_2O + O_2$, the corrosion rate of pure Fe is much higher in solid $NaCl + H_2O + O_2$. The activation energy (E_a) for chemical reaction of pure Fe in solid $Na_2SO_4 + H_2O + O_2$ is 200.9 kJ/mol, which is higher than that of pure Fe in solid $NaCl + H_2O + O_2$.

The percentage contribution of the electrochemical reactions in total corrosion is insignificant. It was also found that the electrochemical corrosion rate of pure Fe with solid NaCl deposit was 1.16×10^{-4} A/cm^2, which was a little lower than that with solid Na_2SO_4 deposit.

Data Availability

The data used to support the findings of this study are available from the corresponding author upon request.

Conflicts of Interest

The authors declare that they have no conflicts of interest.

Acknowledgments

References

[1] Y. B. Tang, L. Liu, Y. Li, and F. H. Wang, "Evidence for the occurrence of electrochemical reactions and their interaction with chemical reactions during the corrosion of pure Fe with solid NaCl deposit in water vapor at 600 °C," *Electrochemistry Communications*, vol. 12, no. 2, pp. 191–193, 2010.

[2] Y. H. Shu, F. H. Wang, and W. T. Wu, "Synergistic Effect of NaCl and Water Vapor on the Corrosion of $_1$Cr-11Ni-$_2$W-$_2$Mo-V Steel at 500-700°C," *Oxidation of Metals*, vol. 51, no. 1/2, pp. 97–110, 1999.

[3] M. Cao, L. Liu, Z. F. Yu, L. Fan, L. Ying, and F. H. Wang, "Studies on the corrosion behavior of Fe-20Cr alloy in NaCl solution spray at 600 °C," *Corrosion Science*, vol. 133, pp. 165–177, 2018.

[4] F. H. Wang and Y. H. Shu, "Influence of Cr content on the corrosion of Fe-Cr alloys: the synergistic effect of NaCl and water vapor," *Oxidation of Metals*, vol. 59, no. 3/4, pp. 201–214, 2003.

[5] L. Liu, Y. Li, C. L. Zeng, and F. H. Wang, "Electrochemical impedance spectroscopy (EIS) studies of the corrosion of pure Fe and Cr at 600 °C under solid NaCl deposit in H_2O," *Electrochimca Acta*, vol. 51, no. 22, pp. 4736–4743, 2006.

[6] H. J. Grabke, E. Reese, and M. Spiegel, "The effects of chlorides, hydrogen chloride, and sulfur dioxide in the oxidation of steels below deposits," *Corrosion Science.*, vol. 37, no. 7, pp. 1023–1043, 1995.

[7] N. Folkeson, T. Jonsson, M. Halvarsson, L. G. Johansson, and J. E. Svensson, "The influence of small amounts of KCl(s) on the high temperature corrosion of a Fe-2.25Cr-1Mo steel at 400 and 500°C," *Materials and Corrosion*, vol. 62, no. 7, pp. 606–615, 2011.

[8] Y. H. Shu, F. H. Wang, and W. T. Wu, "Corrosion behavior of Ti60 alloy coated with a solid NaCl deposit in O_2 plus water vapor at 500–700 °C," *Oxidation of Metals*, vol. 52, no. 5/6, pp. 463–473, 1999.

[9] L. Fan, L. Liu, Z. F. Yu, M. Cao, Y. Li, and F. H. Wang, "Corrosion behavior of Ti60 alloy under a solid NaCl deposit in wet oxygen flow at 600 °C," *Scientific Reports*, vol. 6, no. 1, pp. 1–12, 2016.

[10] Y. H. Shu, F. H. Wang, and W. T. Wu, "Corrosion behavior of pure Cr with a solid NaCl deposit in O_2 plus water vapor," *Oxidation of Metals*, vol. 54, no. 5/6, pp. 457–471, 2000.

[11] F. H. Wang, S. J. Geng, and S. L. Zhu, "Corrosion behavior of a sputtered K38G nanocrystalline coating with a solid NaCl deposit in wet oxygen at 600 to 700 °C," *Oxidation of Metals*, vol. 58, no. 1/2, pp. 185–195, 2002.

[12] C. Wang, F. Jiang, and F. H. Wang, "Corrosion inhibition of 304 stainless steel by nano-sized Ti/silicone coatings in an environment containing NaCl and water vapor at 400–600°C," *Oxidation of Metals*, vol. 62, no. 1/2, pp. 1–13, 2004.

[13] Y. B. Tang, L. Liu, Y. Li, and F. H. Wang, "The electrochemical corrosion mechanisms of pure Cr with NaCl deposit in water vapor at 600 °C," *Journal of The Electrochemical Society*, vol. 158, no. 8, pp. C237–C241, 2011.

[14] L. Fan, L. Liu, M. Cao et al., "Corrosion behavior of pure Ti under a solid NaCl deposit in a wet oxygen flow at 600 °C," *Metals*, vol. 6, no. 4, pp. 72–82, 2016.

[15] L. Fan, L. Liu, Y. Cui et al., "Effect of streaming water vapor on the corrosion behavior of Ti60 alloy under a solid NaCl deposit in water vapor at 600 degrees C," *Corrosion Scencei*, vol. 160, article 108177, pp. 165–178, 2019.

[16] E. Reese and H. J. Grabke, "Einfluß von Natriumchlorid auf die oxidation von hochlegierten Chrom- und Chrom-Nickel-Stählen," *Materials and Corrosion*, vol. 44, no. 2, pp. 41–47, 1993.

[17] P. Kofstad, *High Temperature Corrosion*, Elsevier Applied Science, London, British, 1998.

[18] Y. Shinata and Y. Nishi, "NaCl-induced accelerated oxidation of chromium," *Oxidation of Metals*, vol. 26, no. 3-4, pp. 201–212, 1986.

[19] R. A. Rapp, "*Whitney Award Lecture—1986:*Chemistry and electrochemistry of the hot corrosion of metals," *Corrosion*, vol. 42, no. 10, pp. 568–577, 1986.

[20] E. L. Simons, G. V. Browning, and H. A. Liebhafsky, "Sodium sulfate in gas turbines," *Corrosion*, vol. 11, no. 12, pp. 17–26, 1955.

[21] N. S. Bornstein and M. A. Decrescente, "The role of sodium and sulfur in the accelerated oxidation phenomena-sulfidation," *Corrosion*, vol. 26, no. 7, pp. 309–314, 1970.

[22] N. S. Bornstein and M. A. Decrescente, "The role of sodium in the accelerated oxidation phenomenon termed sulfidation," *Metallurgical and Materials Transactions*, vol. 2, no. 10, pp. 2875–2883, 1971.

[23] J. A. Goebel and F. S. Pettit, "The influence of sulfides on the oxidation behavior of nickel-base alloys," *Metallurgical and Materials Transactions*, vol. 1, no. 12, pp. 3421–3429, 1970.

[24] J. A. Goebel and F. S. Pettit, "Na_2SO_4-induced accelerated oxidation (hot corrosion) of nickel," *Metallurgical and Materials Transactions*, vol. 1, no. 7, pp. 1943–1954, 1970.

[25] M. Li, *High Temperature Corrosion of Metals*, Metallurgical Industry Press, Beijing, China, 2001.

[26] Y. B. Tang, L. Liu, L. Fan, Y. Li, and F. H. Wang, "The corrosion behavior of pure iron under solid Na_2SO_4 deposit in wet oxygen flow at 500 °C," *Materials*, vol. 7, no. 9, pp. 6144–6157, 2014.

[27] A. Zahs, M. Spiegel, and H. J. Grabke, "Chloridation and oxidation of iron, chromium, nickel and their alloys in chloridizing and oxidizing at mospheres at 400-700°C," *Corrosion Science*, vol. 42, no. 6, pp. 1093–1122, 2000.

[28] D. E. Smith, "Alternating current polarography of electrode processes wih coupled homogeneous chemical Reactions. I. Theory for systems with first-order preceding, following, and catalytic chemical reactions," *Analytical Chemistry.*, vol. 35, no. 6, pp. 602–609, 1963.

[29] L. Z. Chen and Y. H. Zhang, *Physical Chemistry*, Shanghai Science and Technology, Shanghai, 2005.

[30] Y. X. Qiao, D. K. Xu, S. Wang et al., "Effect of hydrogen charging on microstructural evolution and corrosion behavior of Ti-4Al-2V-1Mo-1Fe alloy," *Journal of Materials Science & Technology*, vol. 60, pp. 168–176, 2021.

[31] Y. X. Qiao, Z. H. Tian, X. Cai et al., "Cavitation erosion behaviors of a nickel-free high-nitrogen stainless steel," *Tribology Letters*, vol. 67, no. 1, pp. 1–9, 2019.

[32] C. Gleitzer, "Electrical properties of anhydrous iron Oxides," *Key Engineering Materials*, vol. 125-126, pp. 355–418, 1996.

Research Article

Improved Corrosion Resistance of Magnesium Alloy in Simulated Concrete Pore Solution by Hydrothermal Treatment

Ye Wang, Guosong Wu [ID], and Jiapeng Sun

College of Mechanics and Materials, Hohai University, Nanjing 211100, China

Correspondence should be addressed to Guosong Wu; wugsjd@126.com

Magnesium alloys are considered for building materials in this study due to their natural immunity to corrosion in alkaline concrete pore solution. But, chloride ions attack often hinders the application of most metals. Therefore, it is necessary to conduct a preliminary corrosion evaluation and attempt to find an effective way to resist the attack of chloride ions in concrete pore solution. In our study, hydrothermal treatment is carried out to modify Mg-9.3 wt. % Al alloy. After the treatment in NaOH solution for 10 h, scanning electron microscopy (SEM) reveals that a layer of dense coating with a thickness of about $5\,\mu m$ is formed on Mg alloy. Energy dispersive X-ray spectroscopy (EDS), X-ray photoelectron spectroscopy (XPS), and X-ray Diffraction (XRD) are combined to analyze the coating, and it is thereby confirmed that the coating is mainly composed of $Mg(OH)_2$. As expected, both immersion test and electrochemical corrosion test show that the coated magnesium alloy has a better corrosion resistance than the uncoated one in simulated concrete pore solution with and without chloride ions. In summary, it indicates that hydrothermal treatment is a feasible method to improve the corrosion resistance of Mg alloys used for building engineering from the perspective of corrosion science.

1. Introduction

Rapid corrosion in aqueous solutions always hampers the applications of magnesium alloys in the automotive, aerospace, electronics industry, and biomedical field [1–6]. Nowadays, the concept of lightweight construction and equipment has been proposed for overcoming the energy and resources shortage in the development of our society [7–9]. Therefore, magnesium alloys as one of the lightest structural materials are still very promising in the future industries. Concrete is one of the most important building materials in civil engineering, and usually, it is always strengthened by steel bars for improving its poor tensile strength [10]. Although steel has many advantages over other metals, it is always anticipated based on the consideration of energy-saving that there will be a lighter reinforcement bar for fully or partly replacing steel bars. Bamboo has

a much lower density than steel, which has already been attempted in civil engineering in recent years. But, insect and fungus attacks, shrinking, and swelling are big disadvantages [11, 12]. Aluminum alloys are also regarded as an alternative to steels in reinforced concretes due to their low density and noncorrosive characteristics, but their native oxide coating will become unstable at acid or alkaline environments, inducing aluminum alloy bars susceptible to corrosion in the alkaline environment of concrete constructions [13]. The density of magnesium is only two-thirds that of aluminum and one-fourth that of iron and the specific strength of magnesium is higher than that of iron or aluminum [14]. Obviously, it may attempt to select magnesium alloys for reinforcement bars in some low-load bearing constructions according to the strengthening rule of reinforced concrete. Furthermore, Mg-H_2O diagram tells that magnesium has a good immune behavior in alkaline

aqueous environments [15, 16]. Thus, it may predict that magnesium and its alloys can survive in those alkaline concrete pore solutions. In addition, magnesium is one of the most abundant elements in the earth's crust and oceans [17, 18]. Therefore, it seems significant to conduct a preliminary investigation on the corrosion behavior of magnesium alloys in construction environments.

It is well known that the chloride-induced corrosion of reinforcing steel is one of the most common damage phenomena of steel-reinforced concrete structures, particularly in the coastal marine environment [19, 20]. Therefore, it must be carefully considered when magnesium alloys are proposed for these new applications in building engineering. Now, alloying and surface treatment are two main ways to improve the corrosion resistance of magnesium alloys, and the latter is more economical [14, 21]. Usually, a surface barrier layer can isolate the bulk materials from the external environment to avoid corrosion. However, magnesium is a very active metal in the galvanic series inducing galvanic corrosion when it is in electrical contact with many other conductive materials in the same electrolyte [22, 23]. According to the theory of galvanic corrosion, if defects such as pores and cracks occur in those electroconductive coatings, galvanic corrosion will happen when the electrolyte reaches the interface between the coating and substrate *via* these defects [22, 23]. In general, insulating materials are favorite in those coatings on Mg alloys from the perspective of corrosion protection.

In recent years, hydrothermal treatment has been attempted to prepare $Mg(OH)_2$ or layered double hydroxide (LDH) coatings on Mg alloys for improving the corrosion resistance in sodium chloride solutions [24–27]. In our study, this method was selected for the surface treatment of Mg-Al alloys, and the corrosion behavior after the treatment was investigated in simulated concrete pore solutions with chloride ions.

2. Materials and Methods

As-cast Mg-9.3 wt. % alloys were used for substrate materials in this investigation, and the samples were cut into 10 mm × 10 mm × 5 mm pieces. The samples were mechanically ground by up to #1200 emery paper and then polished with Al_2O_3 paste. Next, they were ultrasonically washed in ethanol for 5 min and dried prior to hydrothermal treatment. Each sample was laid at the bottom of 25 ml Teflon-lined autoclave that had 10 ml of 1 M NaOH solution. After the autoclaves were sealed, they were heated to 120°C for 10 h in an oven. Finally, the samples were taken out, washed with deionized water and ethanol in turns, and then naturally dried in air at room temperature.

Field emission scanning electron microscope (FESEM, MAIA 3 GMU, TESCAN, Czech) was performed to observe the microstructure of the alloy, the surface morphology, and the cross-section morphology of the treated samples. Energy dispersive X-ray spectrometer (EDS, Oxford Instruments, UK) was used to analyze the elemental distribution of the treated samples. X-ray photoelectron spectroscopy (XPS, PHI-5000 Versa Probe III, ULVAC-PHI, Japan) was
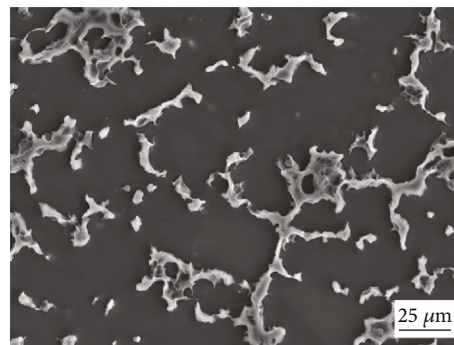

FIGURE 1: Microstructure of Mg alloys used in this study.

also conducted to obtain the chemical composition of the samples after surface treatment. X-ray diffraction (XRD, D8 ADVANCE, Bruker, Germany) was performed to characterize the phase composition of the treated and untreated samples. Here, an incident angle of 1° was adopted in the XRD experiment for the treated sample.

A saturated $Ca(OH)_2$ solution was used to simulate the concrete pore solution in this study, and in order to investigate the effect of chloride ions on the corrosion resistance, the saturated $Ca(OH)_2$ solution was further diluted by 3.5 wt.% NaCl solution with a volume ratio of 1 : 1. Electrochemical corrosion tests were conducted on a CHI660E electrochemical workstation, and the specimen with a surface area of $1 \times 1 \, cm^2$ was exposed to 200 ml of simulated concrete pore solution. Here, the potential was referenced to a saturated calomel electrode (SCE) and the counter electrode was a platinum sheet. After immersion for 30 min, the electrochemical impedance spectra (EIS) were collected from 100 kHz to 100 mHz with a 5 mV sinusoidal perturbing signal at the open-circuit potential. Potentiodynamic polarization curves following the EIS test were recorded from -1.8 V to 0 V at a scanning rate of $1.0 \, mV \cdot s^{-1}$. All the electrochemical measurements were repeated three times to ensure reproducibility. In addition, an immersion test was also carried out to further evaluate the corrosion behavior in the simulated concrete pore solution. After immersion for 24 h, the samples were taken out, rinsed with water and ethanol, and naturally dried in air. Then, their surface morphologies were observed by scanning electron microscopy (SEM).

3. Results and Discussion

Mg-9.3 wt. % alloy consists of the Mg matrix and second phase, and Figure 1 shows its microstructure. Figure 2 exhibits the macroscale and microscale surface morphologies of the treated sample. The inset in Figure 2(a) tells the appearance difference between the untreated and treated Mg alloys. It is noted that the surface of the sample turns brown after the treatment, which means that the hydrothermal process has already changed the surface of Mg alloy. As shown in Figure 2(a), the surface seems smooth when it is observed by SEM under lower magnification. Interestingly, it is further revealed under higher magnification that the

(a)

(b)
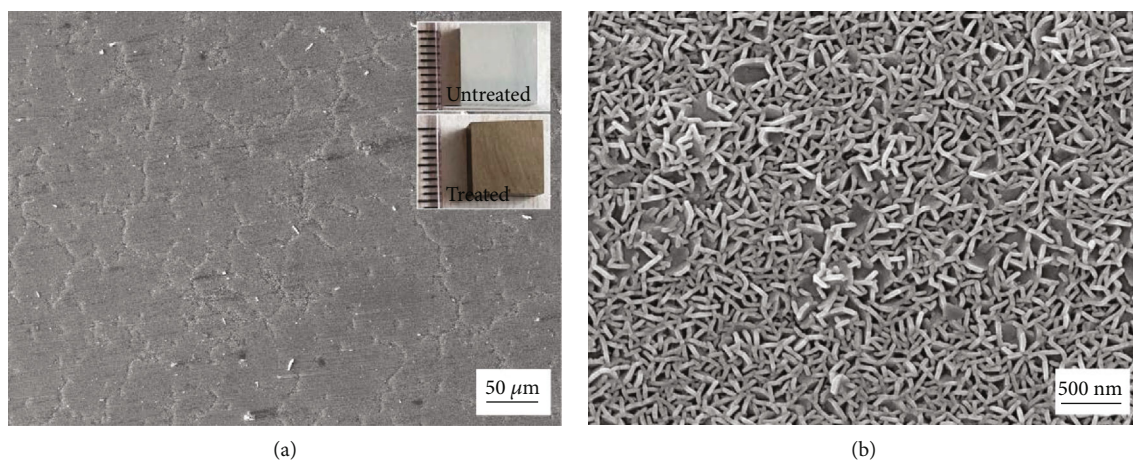
FIGURE 2: Surface morphologies of the treated Mg alloy: (a) lower magnification and (b) higher magnification. The inset shows the appearance difference between the untreated and treated sample.

(a)

(b)

(c)

(d)
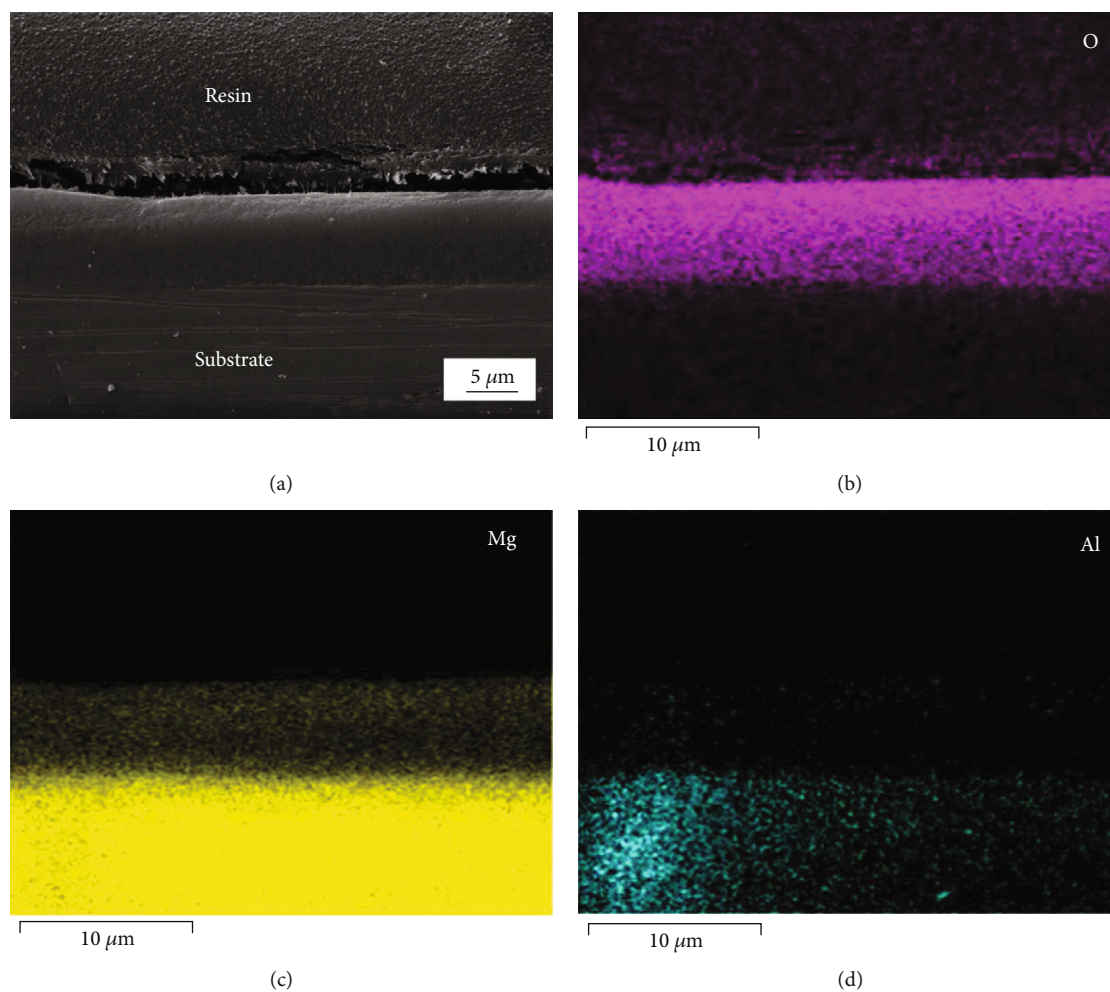
FIGURE 3: Cross-section of the hydrothermally-treated sample: (a) SEM image and (b–d) corresponding EDS elemental maps.

hydrothermally-modified surface is covered by microsheets, which is clearly shown in Figure 2(b). Figure 3 shows the cross-section of the treated sample. A layer of dense coating is clearly shown in Figure 3(a), whose thickness is about 5μm. Figures 3(b)–3(d) gives the EDS elemental maps of the corresponding site in the cross-section. Combined the
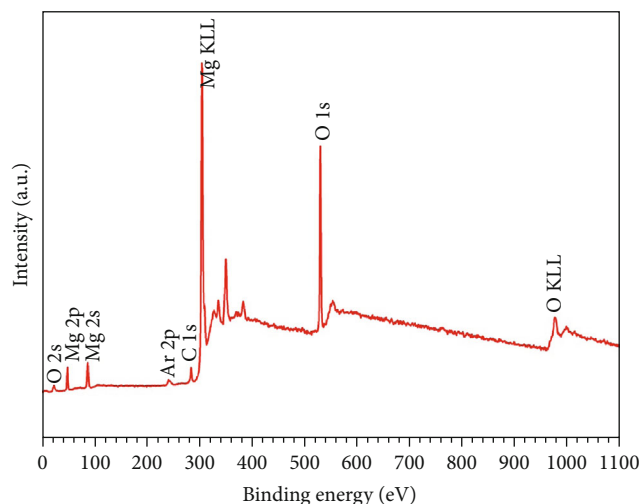
Figure 4: XPS survey spectra of the hydrothermal coating.

Figure 5: XRD patterns of the samples.

SEM image and its EDS elemental maps, it is identified that the coating is mainly composed of element O and Mg.

Figure 4 shows the XPS survey spectra of the top of the hydrothermal coating. In the spectra, it can be found that it is mainly composed of elements Mg and O, which is consistent with the result of EDS analysis. According to the spectra, it can be further obtained that the atomic ratio of O to Mg is about 2.58. Here, the presence of the oxygen on metals and alloys may be due to the surface oxidation and the unavoidable presence of adventitious contamination [28, 29]. Figure 5 presents the XRD pattern of the hydrothermally-treated Mg alloy, and the pattern of the untreated sample is provided here for reference. On the curve of the untreated sample, it exhibits the peaks corresponding to the Mg matrix and the second phase ($Al_{12}Mg_{17}$). Thus, it can be easily confirmed by comparison that the coating mainly consists of $Mg(OH)_2$.

Figure 6 shows the Nyquist plots of the samples in different solutions, and the inset gives the enlarged curves of the samples immersed in Cl^--containing solutions. Based on the EIS theory, the polarization resistance can be derived from the following formula: $R_p = R_{\omega \to 0} - R_s$. Here, R_p is the polarization resistance, $R_{\omega \to 0}$ denotes the zero-frequency impedance, and R_s represents the solution resistance [30]. In order to perform a rapid evaluation of corrosion resistance, a simplified way is adopted that the resistance at the lowest frequency in our investigation is used to substitute the polarization resistance. As shown in Figure 6, it can be found that the corrosion resistance in the saturated $Ca(OH)_2$ solution is higher than that in the $Ca(OH)_2$ solution diluted by 3.5 wt.% NaCl solution. After the hydrothermal treatment, the corrosion resistance is significantly improved in both kinds of test solutions. Figure 7 presents the polarization curves of the samples in their corresponding solutions. The corrosion potential and corrosion current density are derived from cathodic Tafel region extrapolation, and their data are as shown in Table 1. For the uncoated Mg alloy, it has a higher corrosion current density in the simulated concrete pore solution with Cl^- than that in the simulated concrete pore
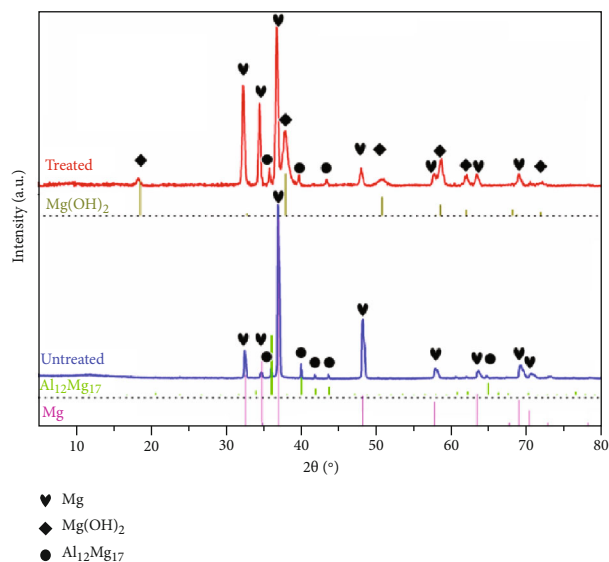
solution without Cl^-. It is known that higher corrosion current density means lower corrosion resistance. After coating, the corrosion resistance of Mg alloy has been significantly improved in either the solution with Cl^- or the one without Cl^-. In the solution with Cl^-, the coated alloy's corrosion resistance is close to that of the uncoated one in the simulated concrete pore solution without Cl^-. In addition, compared to the uncoated sample, the coated one does not have an obvious transition potential in the investigated anodic polarization region in the solution with Cl^-. In all, the results show that the hydrothermal coating on magnesium alloy has a protective effect as manifested by the lower corrosion current density and higher transition potential.

Figure 8 shows the surface morphologies of the samples after the immersion in simulated concrete pore solutions with the addition of sodium chlorides for 24 h. As mentioned above, the solution is prepared by the mixture of saturated $Ca(OH)_2$ solution and 3.5 wt. % NaCl solution with a volume ratio of 1 : 1. From the SEM images, it can be clearly seen that the surface of the uncoated sample is corroded, whereas that of the coated one still keeps intact even under the observation of higher magnification. Obviously, the result of the immersion test is in accordance with that of the electrochemical corrosion test, indicating that the hydrothermal coating can protect the Mg alloy substrate well in Cl^- containing simulated concrete pore solutions.

Magnesium alloys are considered for building materials in this study, and the corrosion resistance in simulated concrete pore solutions has been investigated preliminarily. To the best of our knowledge, there have been few studies on the corrosion behavior of magnesium alloys in simulated concrete pore solutions. As expected, Mg alloys used in this study have a good corrosion resistance in simulated concrete pore solutions due to the alkalinity of the solutions. But, when chloride ions are added into the simulated concrete pore solutions, the corrosion behavior of Mg alloys is significantly altered. Fortunately, the hydrothermal process can
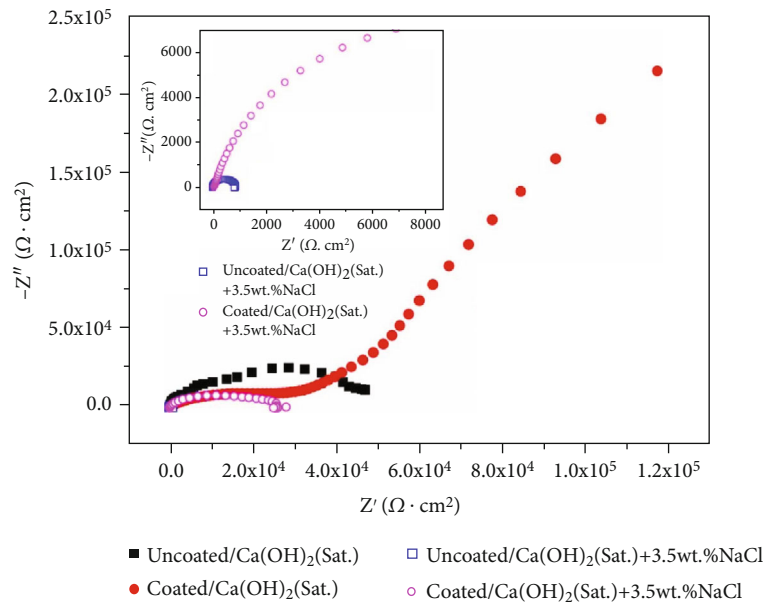
FIGURE 6: Nyquist plots of the samples in different solutions.
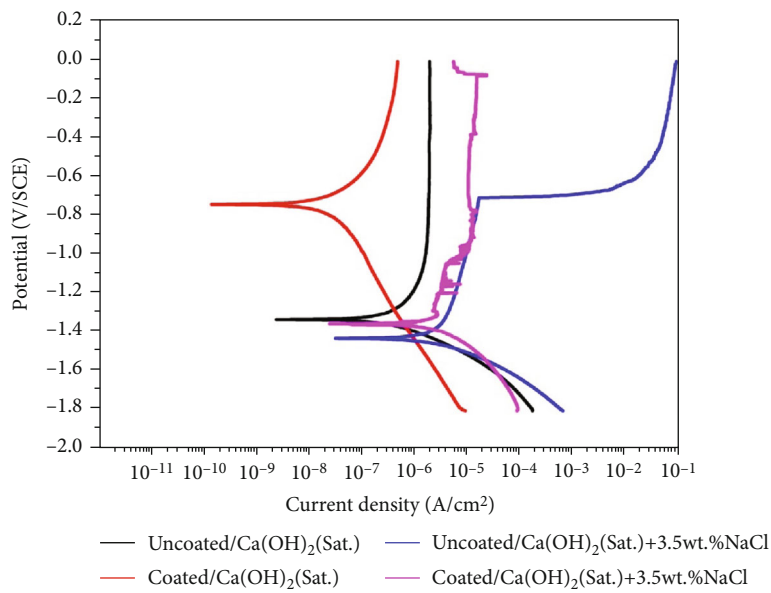
FIGURE 7: Potentiodynamic polarization curves of the samples in different solutions.

TABLE 1: Corrosion potential and corrosion current density determined from polarization curves.

	E_{corr} (V/SCE)	I_{corr} $\left(A \bullet cm^{-2}\right)$
Uncoated/[Ca(OH)$_2$ (Sat.)]	-1.343 ± 0.021	$(4.06 \pm 0.24) \times 10^{-6}$
Coated/[Ca(OH)$_2$ (Sat.)]	-0.839 ± 0.131	$(2.71 \pm 1.23) \times 10^{-8}$
Uncoated/[Ca(OH)$_2$ (Sat.)+3.5 wt.% NaCl]	-1.417 ± 0.009	$(1.01 \pm 0.16) \times 10^{-5}$
Coated/[Ca(OH)$_2$ (Sat.)+3.5 wt.% NaCl]	-1.371 ± 0.015	$(3.95 \pm 3.79) \times 10^{-6}$

(a)

(b)
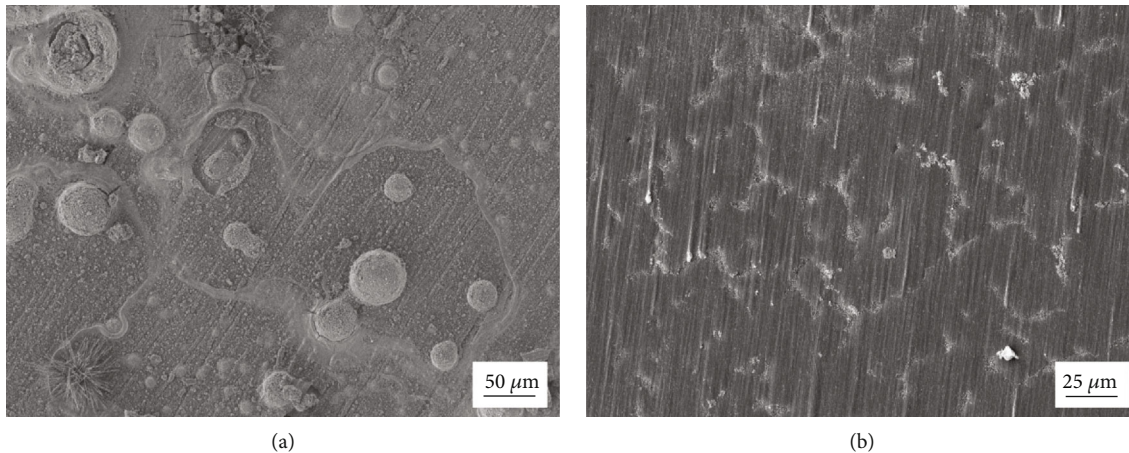
FIGURE 8: (a) SEM image of the uncoated sample after immersion for 24 h. (b) SEM image of the coated sample after immersion for 24 h.

produce a layer of dense coating on Mg alloys for the retardation of the attack of chloride ions. It is known that defects will be formed more or less in the coatings at the stage of coating preparation or service, and the occurrence of galvanic corrosion will be fatal to the coating/substrate system if the coating is electroconductive. Here, the hydrothermal coating is mainly composed of $Mg(OH)_2$, and compared to other metallic or conductive ceramic coatings, it can avoid the galvanic corrosion effectively. Furthermore, the hydrothermal solution used in this study is very simple, which make it a facile and economical processing for the applications of magnesium alloys in building engineering.

4. Conclusion

In this study, a layer of dense coating is successfully prepared on Mg-9.3 wt. % Al alloy by hydrothermal treatment. SEM discloses that the coating has a thickness of about $5\,\mu m$, and the top of the coating is covered by microsheets. It is determined by the results of XRD, EDS, and XPS that the coating is mainly composed of $Mg(OH)_2$. Due to the compact microstructure of the hydrothermal coating, the corrosion resistance of Mg alloy after the hydrothermal treatment is significantly improved in simulated concrete pore solution with and without the addition of chloride ions. In summary, this facile method provides a feasible way to improve the corrosion resistance of magnesium alloys for building engineering in the future.

Data Availability

Answer: Yes. Comment: The data used in this study are available from the corresponding author upon request.

Conflicts of Interest

The authors declare that they have no competing interests.

Acknowledgments

References

[1] W. Xu, N. Birbilis, G. Sha et al., "A high-specific-strength and corrosion-resistant magnesium alloy," *Nature Materials*, vol. 14, no. 12, pp. 1229–1235, 2015.

[2] F. Cao, G. Song, and A. Atrens, "Corrosion and passivation of magnesium alloys," *Corrosion Science*, vol. 111, pp. 835–845, 2016.

[3] G. Wu, P. Li, H. Feng, X. Zhang, and P. K. Chu, "Engineering and functionalization of biomaterials *via* surface modification," *Journal of Materials Chemistry B*, vol. 3, no. 10, pp. 2024–2042, 2015.

[4] S. Wu, X. Liu, K. W. K. Yeung, C. Liu, and X. Yang, "Biomimetic porous scaffolds for bone tissue engineering," *Materials Science and Engineering: R: Reports*, vol. 80, pp. 1–36, 2014.

[5] H. Feng, G. Wang, W. Jin et al., "Systematic study of inherent antibacterial properties of magnesium-based biomaterials," *ACS Applied Materials & Interfaces*, vol. 8, no. 15, pp. 9662–9673, 2016.

[6] G. Wang, W. Jiang, S. Mo et al., "Nonleaching antibacterial concept demonstrated by in situ construction of 2D nanoflakes on magnesium," *Advanced Science*, vol. 7, article 1902089, 2020.

[7] B. L. Mordike and T. Ebert, "Magnesium," *Materials Science and Engineering A*, vol. 302, no. 1, pp. 37–45, 2001.

[8] J. F. Nie, Y. M. Zhu, J. Z. Liu, and X. Y. Fang, "Periodic segregation of solute atoms in fully coherent twin boundaries," *Science*, vol. 340, no. 6135, pp. 957–960, 2013.

[9] Z. Wu, R. Ahmad, B. Yin, S. Sandlöbes, and W. A. Curtin, "Mechanistic origin and prediction of enhanced ductility in magnesium alloys," *Science*, vol. 359, no. 6374, pp. 447–452, 2018.

[10] D. Asprone, C. Menna, F. P. Bos, T. A. M. Salet, J. Mata-Falcón, and W. Kaufmann, "Rethinking reinforcement for digital fabrication with concrete," *Cement and Concrete Research*, vol. 112, pp. 111–121, 2018.

[11] A. Javadian, M. Wielopolski, I. F. C. Smith, and D. E. Hebel, "Bond-behavior study of newly developed bamboo-composite reinforcement in concrete," *Construction and Building Materials*, vol. 122, pp. 110–117, 2016.

[12] A. Dey and N. Chetia, "Experimental study of bamboo reinforced concrete beams having various frictional properties," *Materials Today: Proceedings*, vol. 5, pp. 436–444, 2018.

[13] G. Xing and O. E. Ozbulut, "Flexural performance of concrete beams reinforced with aluminum alloy bars," *Engineering Structures*, vol. 126, pp. 53–65, 2016.

[14] J. E. Gray and B. Luan, "Protective coatings on magnesium and its alloys — a critical review," *Journal of Alloys and Compounds*, vol. 336, no. 1-2, pp. 88–113, 2002.

[15] H. Wu, Z. Shi, X. Zhang et al., "Achieving an acid resistant surface on magnesium alloy *via* bio-inspired design," *Applied Surface Science*, vol. 478, pp. 150–161, 2019.

[16] Y. Yun, Z. Dong, N. Lee et al., "Revolutionizing biodegradable metals," *Materials Today*, vol. 12, no. 10, pp. 22–32, 2009.

[17] M. Esmaily, J. E. Svensson, S. Fajardo et al., "Fundamentals and advances in magnesium alloy corrosion," *Progress in Materials Science*, vol. 89, pp. 92–193, 2017.

[18] G. Zhang, A. Tang, L. Wu et al., "In-situ grown super- or hydrophobic Mg-Al layered double hydroxides films on the anodized magnesium alloy to improve corrosion properties," *Surface & Coatings Technology*, vol. 366, pp. 238–247, 2019.

[19] D. Song, A. Ma, W. Sun et al., "Improved corrosion resistance in simulated concrete pore solution of surface nanocrystallized rebar fabricated by wire-brushing," *Corrosion Science*, vol. 82, pp. 437–441, 2014.

[20] M. Balonis, G. Sant, and O. Burkan Isgor, "Mitigating steel corrosion in reinforced concrete using functional coatings, corrosion inhibitors, and atomistic simulations," *Cement and Concrete Composites*, vol. 101, pp. 15–23, 2019.

[21] M. I. Jamesh, G. Wu, Y. Zhao, D. R. McKenzie, M. M. M. Bilek, and P. K. Chu, "Electrochemical corrosion behavior of biodegradable Mg-Y-RE and Mg-Zn-Zr alloys in Ringer's solution and simulated body fluid," *Corrosion Science*, vol. 91, pp. 160–184, 2015.

[22] G. Wu, X. Zhang, Y. Zhao, J. M. Ibrahim, G. Yuan, and P. K. Chu, "Plasma modified Mg-Nd-Zn-Zr alloy with enhanced surface corrosion resistance," *Corrosion Science*, vol. 78, pp. 121–129, 2014.

[23] G. Wu, J. M. Ibrahim, and P. K. Chu, "Surface design of biodegradable magnesium alloys — a review," *Surface & Coatings Technology*, vol. 233, pp. 2–12, 2013.

[24] Y. Zhu, G. Wu, Y. H. Zhang, and Q. Zhao, "Growth and characterization of $Mg(OH)_2$ film on magnesium alloy AZ31," *Applied Surface Science*, vol. 257, no. 14, pp. 6129–6137, 2011.

[25] X. Zhang, G. Wu, X. Peng et al., "Mitigation of corrosion on magnesium alloy by predesigned surface corrosion," *Scientific Reports*, vol. 5, no. 1, 2015.

[26] J. Zhang, C. Gu, and J. Tu, "Robust slippery coating with superior corrosion resistance and anti-icing performance for AZ31B Mg alloy protection," *ACS Applied Materials & Interfaces*, vol. 9, no. 12, pp. 11247–11257, 2017.

[27] F. Zhang, Z. Liu, R. C. Zeng et al., "Corrosion resistance of Mg–Al-LDH coating on magnesium alloy AZ31," *Surface & Coatings Technology*, vol. 258, pp. 1152–1158, 2014.

[28] R. Kohli and K. L. Mittal, Eds., *Developments in Surface Contamination and Cleaning*, William Andrew, Norwich, NY, USA, 2008.

[29] J. Landoulsi, M. J. Genet, S. Fleith et al., "Organic adlayer on inorganic materials: XPS analysis selectivity to cope with adventitious contamination," *Applied Surface Science*, vol. 383, pp. 71–83, 2016.

[30] C. N. Cao, *Principles of Electrochemistry of Corrosion*, Chemical Industry Press, Beijing, China, 2008.

WILEY | Hindawi

Research Article
Effect of Heat Treatment on Microstructure and Tribocorrosion Performance of Laser Cladding Ni-65 WC Coating

Ze Liu,[1] **Eryong Liu** [ID],[1] **Shuangming Du,**[1] **Congwei Li,**[1] **Huiling Du,**[1] **and Yaping Bai** [ID][2]

[1]School of Materials Science and Engineering, Xi'an University of Science and Technology, Xi'an 710054, China
[2]School of Materials Science and Chemical Engineering, Xi'an Technological University, Xi'an 710021, China

Correspondence should be addressed to Eryong Liu; ley401@163.com

The Ni-65wt%WC cladding layers were prepared on the surface of Q235 using laser cladding technology, in which the effect of heat treatment on microstructure and tribocorrosion performance was investigated. The results showed that the coating is mainly consisted of Ni, WC, and W_2C, and a significant diffusion phenomenon is formed between the interfaces of WC/Ni matrix, benefited for the improvement of bonding layer between WC/Ni-based matrixes. Meanwhile, the crystallization of WC particles after heat treatment was more obvious than untreatment; the Ni matrix grain size was also grown remarkable, leading to the lower hardness and weaker plastic deformation resistance of Ni-65wt%WC coating. And the erosion results showed that the wear rate of coating gradually decreased with heat treatment temperature increasing, while brittle WC was not suitable for high impact wear conditions. Furthermore, with the increase of heat treatment temperature, the reciprocating wear performance showed that the friction coefficient and wear rate of Ni-65wt%WC coating decreased. And the friction coefficient and wear rate of the coating (700°C) in 3.5% NaCl solution were 0.15 and 4.82×10^{-8} mm$^3 \cdot$N$^{-1} \cdot$m^{-1}, respectively. Therefore, the comprehensive comparison showed that Ni-65WC coating had better performance in low impact reciprocating testing under corrosion environment, and heat treatment was helpful to further improve the tribocorrosion performance of laser cladding Ni-65wt%WC coating.

1. Introduction

Q235 steel is the most commonly used metal material, which is widely used in the automobile industry, machinery manufacturing, and chemical industry [1–3]. However, low hardness and poor wear resistance limit its application in key friction movement parts. To solve these problems, researchers have prepared high hardness, antiwear, and corrosion-resistant coating on the surface of Q235 steel by laser cladding technology. And the composite coating has better development potential in the future due to saving a lot of precious metal materials and reducing production cost and energy consumption [4–7].

Laser cladding is a rapid melting and solidification process. Therefore, cracks caused by high thermal stress and microstructure stress in the preparation of the coating limit the application of the coating in engineering [8–11]. Heat treatment after cladding can not only effectively

reduce the residual stress of the coating but also improve its mechanical properties [1, 12]. Lu et al. prepared a Ni60/H-BN coating on the surface of 304 stainless steel and heat-treated the coating at 600°C. The results show that the formation of carbides can effectively increase the hardness and wear resistance of the coating [13]. Li reported that the Ni-65WC coating heat-treated at 500°C could reduce the friction coefficient and improve the fracture toughness and wear resistance of the coating, obviously [14]. However, studying on the effect of postheat treatment to the microstructure, friction and wear properties of laser cladding composite coatings were less. Nickel-based alloys have been widely used in surface engineering because of their excellent corrosion resistance, good wettability, and relatively moderate price. Tungsten carbide has attracted much attention due to good chemical stability, thermal stability, and high hardness in the laser cladding wear-resistant composite coating in recent years.
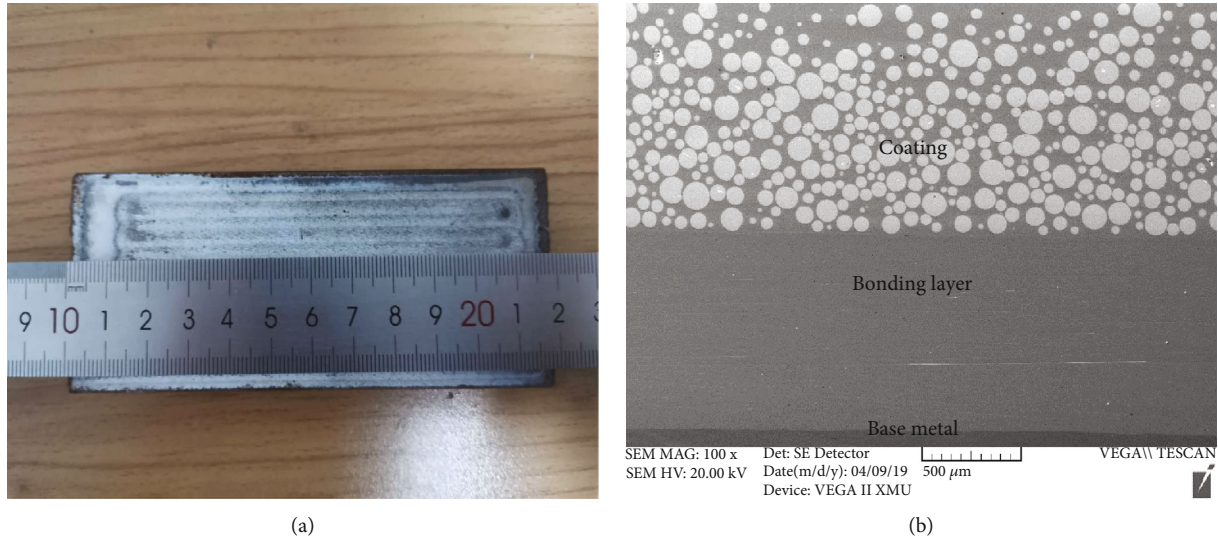
(a)

(b)

FIGURE 1: Macroscopic morphology (a) and cross-section microstructure (b) of Ni-65wt%WC coating.

In this paper, laser cladding technology is used to prepare Ni-65WC composite wear-resistant coating on the surface of Q235 steel, and the coating is postheat treated to reduce residual stress. The microstructure, friction and wear, and erosion-corrosion performance of the composite under the state of heat treatment are studied. This study provides a reference for improving the practical application of laser cladding to prepare composite wear-resistant coatings.

2. Experimental

2.1. Materials and Processing. In this study, the origin material was Q235 steel with dimensions of 100 mm × 60 mm × 20 mm. The raw Ni-based alloy powder had 10 wt% Cu, 0.95 wt% Si, 0.5 wt% B, 0.2 wt% Fe, and 88.35 wt% Ni. Then, the mixed powders (Ni-65 wt% WC) of Ni-based alloy powders (50-100 μm) and WC powders (45-105 μm) were used as the cladding material. The transition layer (Ni-Cr-B-Si) with a thickness of 1 mm was first evenly coated on the Q235 steel substrate. Then, the Ni-65WC powders were evenly spread through a preset powder process, and the thickness was approximately 1.5 mm. And they were next dried at 150°C for 6 h.

The multitrack-joined laser cladding processing was carried out by LSC-3000 laser heat treatment equipment. The optimum processing parameters are as follows: power—2500 W, spot diameter—6 mm, scanning speed—9 mm/s, and overlapping rate—50%. Next, the samples were cut into the size of 20 mm ×10 mm ×5 mm and treatment was at 500°C, 700°C, and 900°C (destress annealing, nitrogen protection) for 1 h, followed by furnace cooling.

2.2. Testing Detection Equipment and Methods. The microstructures of the cladding layers are observed by a scanning electron microscope (FE-SEM, JSM-6390A), and the crystal structure of the as-synthesized samples was detected by X-ray diffraction (XRD, Bruker) using Cu-Kα radiation

($\lambda = 1.54178$ A) in the range of 20-90° with a scanning rate of 4°·min^{-1}. The hardness of the cladding layers is tested by Vickers hardness tester (HV-1000) with a loading force about 1000 g for 15 s.

Furthermore, erosion performance of Ni-65wt%WC coating was tested by a self-assembled jet erosion testing machine. Quartz sand particles with a size of 400 mesh were mixed with water in a weight ratio of 1 : 4, and the erosion velocity, angle, and time were 5 m/s, 90°, and 30 min, respectively. The erosion-corrosion mass loss rate was calculated by the changes in weight.

The friction and wear performance of the cladding layers are detected by the friction and wear experiment (MFT-R4000) using Si$_3$N$_4$ ball (diameter 6 mm) as grinding materials. The testing parameters are as follows: wear time—120 min, load—50 N, the reciprocating frequency—20 mm/s, wear scar length—10 mm, and condition—3.5% NaCl solution. The wear rate was calculated by Equation (1), where V is the wear volume, measured by a 3D laser confocal microscope, F represents the load, and S represents the sliding distance. All tests were performed at least three times, and the average values of the friction coefficient and wear rate were recorded.

$$W_{loss} = \frac{V}{F \times S}.\tag{1}$$

3. Results and Discussions

3.1. Microstructure and Mechanical Properties of Ni-65wt%WC Coating. The macroscopic morphology and cross-sectional morphology of Ni-65WC coating are shown in Figure 1. Figure 1(a) shows that the cladding coating had no defects such as porosity and the white spherical WC particles which were relatively uniformly distributed in gray Ni base (Figure 1(b)). Furthermore, it also can be seen that the content of WC particles was higher under the cladding coating, which was attributed to the fact that the density of WC
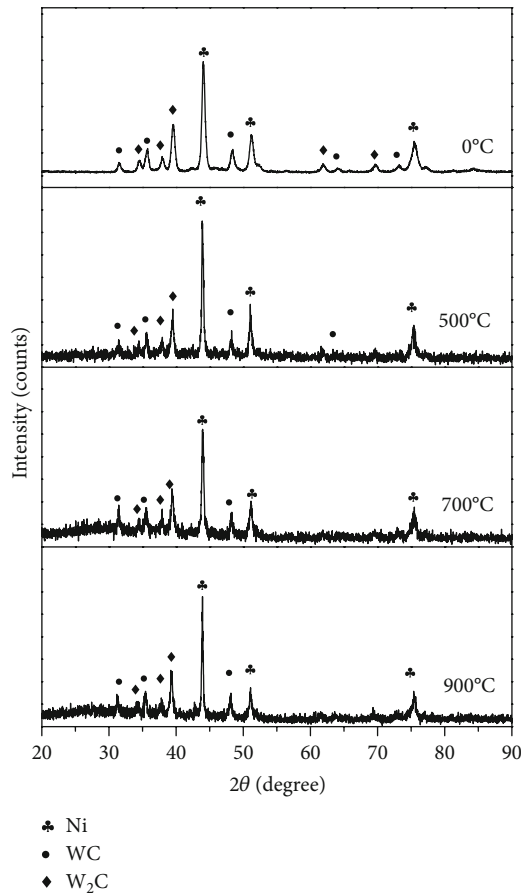
FIGURE 2: XRD pattern of Ni-65wt%WC coating after heat treatment at different temperatures.

was much higher than that of Ni matrix. Meanwhile, the buckling or delamination was not observed on both the interface of the coating/bonding layer and the bonding layer/matrix. And the interface with a smooth sharp can be attributed to the low dilution or dissolution of alloying elements into the different layers.

XRD spectra of the Ni-65WC coating after heat treatment at different temperatures are shown in Figure 2. It can be seen that the sharp diffraction peaks in Ni-65wt%WC coating were found to be for Ni (04-0850), WC (51-0939), and W_2C (20-1315). Due to the high-energy density laser and high cooling rate of laser cladding, the formation of intermetallic phases was beneficial to improve microhardness of the coating. Furthermore, XRD results of Ni-65wt%WC coating indicated that there were no new phases formed after heat treatment; only the diffraction peaks became narrower with the increase of temperature.

SEM images of Ni-65wt%WC coating after heat treatment at different temperatures are shown in Figure 3. The average grain size of Ni matrix and the width of the diffusion layer between WC particles and Ni alloy were calculated by image measure software, as shown in Figure 3(e). First, Figure 3(a) shows that the irregular globular grains of cladding Ni matrix were fine, dense, and uniform, and the average grain size of Ni-based coating was 5.64 μm. After heat

treatment, it can be seen that the average grain size of Ni matrix coating increased from 7.12 μm (700°C) to 9.66 μm (900°C). Meanwhile, the grain boundary of the spherical particles (Ni matrix) was fused during the heat treatment, which became almost oval particles. It was well known that the presence of Ni element will promote the decomposition of WC at high temperature. EDS results confirmed that the edge of WC particles dissolve, and the Ni content in the Ni/W interface diffusion layer continued to increase with the temperature increasing, indicating that the W and Ni elements at the Ni/W interface can diffuse with each other to form a bone-like diffusion layer during the heat treatment process.

Figure 4 shows the microhardness of Ni-65WC coating after heat treatment. The hardness of the Q235 substrate was about 200 HV, and the average hardness of Ni-65wt%WC coating was 700 HV, which was attributed to the higher WC contents and the dissolved of WC particles in Ni-based alloy matrix. However, the average microhardness of Ni-65wt%WC coating after heat treatment significantly decreased from 600 HV at 500°C to 450 HV at 700°C. It can be seen that with the increased heat treatment temperature, the Ni-based grains of the coating grown (Figure 3(e)), and the resistance to dislocation motion decreased, resistance to deformation by external forces appeared to be reduced. Thus, the decrease of surface hardness was attributed to microstructure variation and the decomposition of WC particles.

3.2. Erosion Performance of Ni-65wt%WC Coating. Figure 5 shows the erosion performance of Ni-65wt%WC coating. With the increase of heat treatment temperature, the results showed that the erosion-corrosion mass loss rate of the untreatment coating decreased from 0.35 mg·g^{-1} to 0.15 mg·g^{-1} (900°C). However, the erosion-corrosion mass loss rate of Ni-65wt%WC coating was higher than that of the Q235 matrix, indicating that the coating had poor erosion resistance.

SEM images of the coating after erosion testing are shown in Figure 6. It could be seen that the surface of the Q235 matrix mainly consisted of chisel pit, confirming that the toughness Q235 was hard to resist the destructive effect of quartz sand particles. However, the damage of Ni-65wt%WC coating was more serious than that of the Q235 matrix, and the SEM image showed that almost all the spherical WC particles turn into irregular spherical particles. Meanwhile, many cracks, breaking, and peeling appeared on the surface of tungsten carbide, resulting in a large number of WC particles being broken [15–17]. Combined with the microstructure and erosion performance of Ni-65wt%WC coating, it could be concluded that the toughness phase was easier to resist the erosion of quartz sand particles by plastic deformation, while the brittle ceramic phase was smashed by quartz sand particles. After heat treatment, the width of the diffusion layer between WC/Ni-based alloys increased, which benefited from the combination of the coating. In this situation, the partially dissolved WC and Ni matrix formed a dense diffusion layer, which made it hard to be spall from the surface, and the residual WC particles played a role of erosion resistance with a metal matrix. Therefore, the erosion resistance of Ni-65wt%WC coating
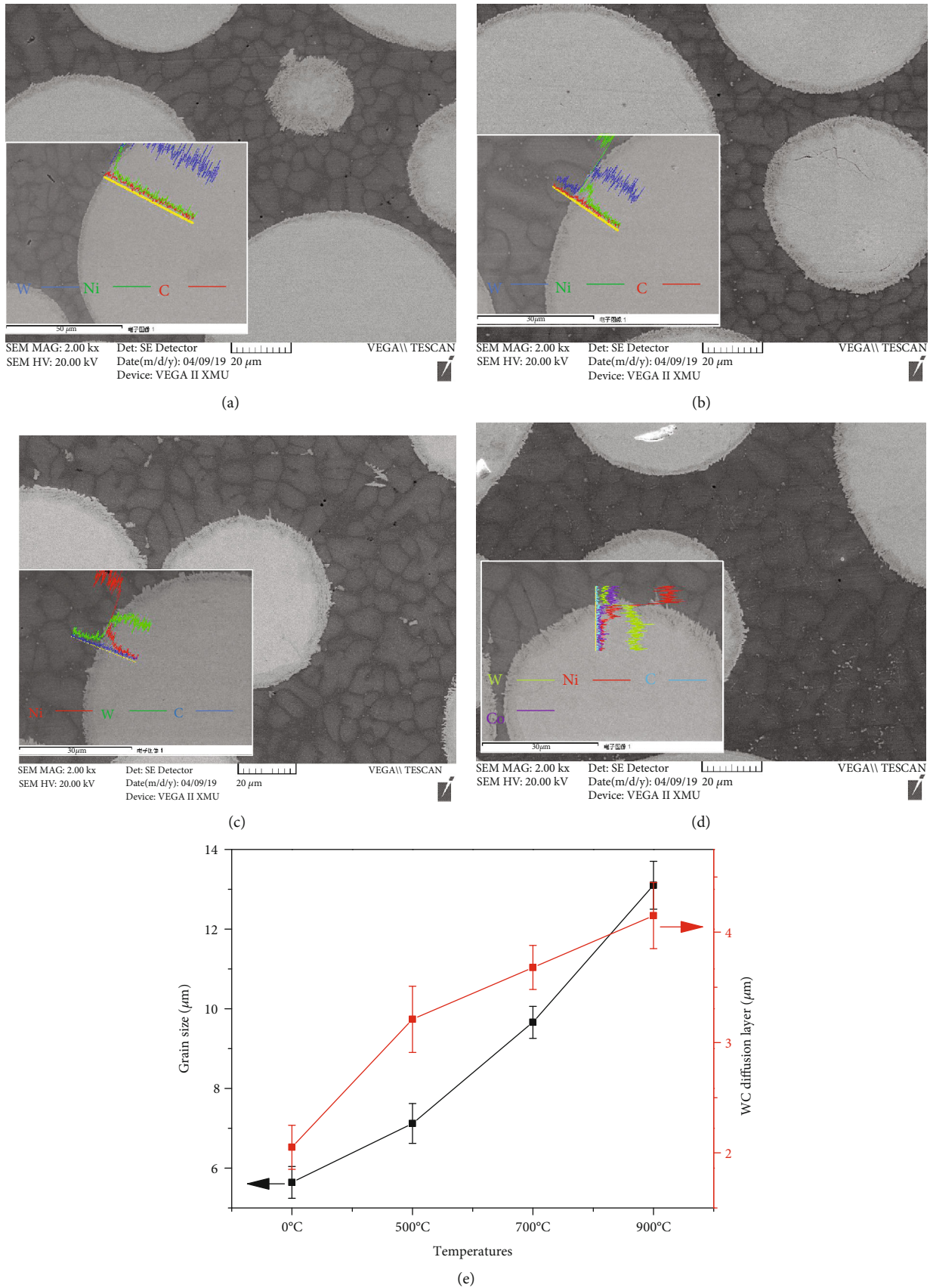
(a)

(b)

(c)

(d)

(e)

Figure 3: Cross-section microstructure and scanning of Ni/W interface of Ni-65wt%WC coating after heat treatment at different temperatures: (a) cladding coating, (b) 500°C, (c) 700°C, (d) 900°C, and (e) variation of grain size and the diffusion layer.
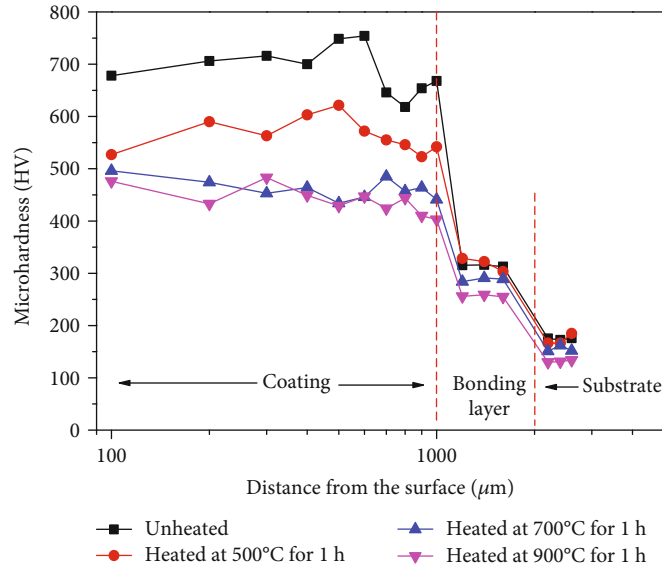
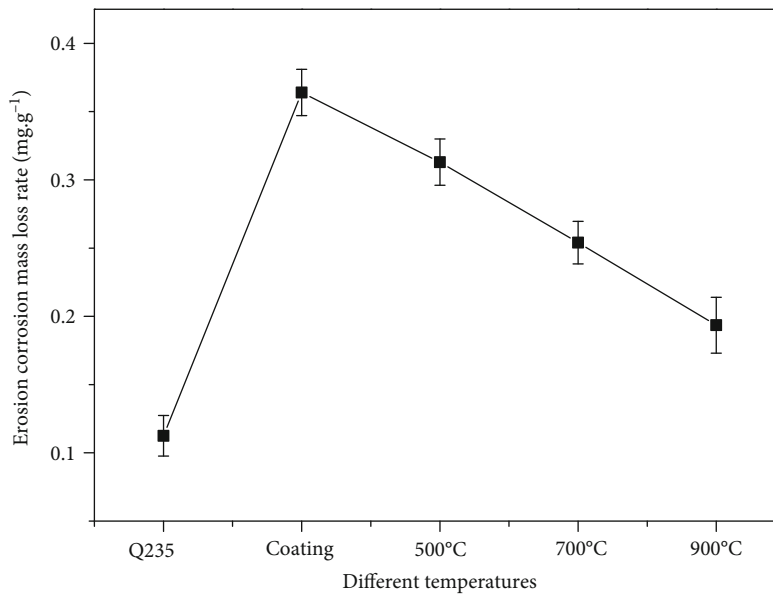Figure 4: Microhardness of Ni-65wt%WC coating.

Figure 5: Erosion corrosion mass loss rate of Ni-65wt%WC coating.

improved by heat treatment, especially at high temperatures with the width diffusion layer between WC/Ni matrixes. Furthermore, to further study the erosion mechanism of Ni-65wt%WC coating, EDS analysis was carried out on the erosion area of coating, as shown in Figure 6(f). The results showed that the erosion induced the decreases of W and C contents and increase of Ni, Si, and Cu on the erosion area of coating with the heat temperature, which can be owned by the strong combination between WC and Ni matrixes.

The damage mechanism of Ni-65wt%WC composite coating under erosion is shown in Figure 7. Although WC particles and nickel matrix formed a good metallurgical combination in Ni-65wt%WC coating, the hard coating also

showed poor erosion resistance under the high-speed erosion on 90°. During the erosion process, the cracks were easier to initiate and expand on brittle WC particles, and then, severe brittle fracture and spall appeared on WC particles, as shown in Figures 7(a) and 7(b). The Ni matrix damaged rapidly in the form of ductile fracture and then induced the lack of support of WC particles (Figure 7(c)). Figure 7(d) indicates the schematic image of the damage mechanism of Ni-65wt%WC composite coating during the erosion process. It is well known that the interface of the WC/matrix was weaker than that of the Ni matrix; thus, crack initiation and propagation were easier to appear between the interfaces of WC particles and WC/matrix. Surface fatigue occurred on WC particles during erosion when a high-energy quartz sand
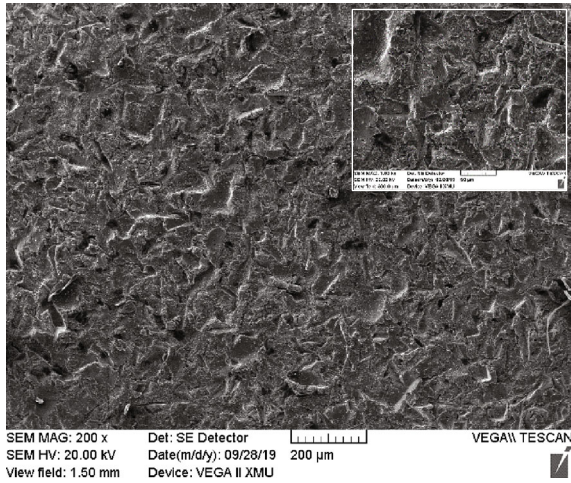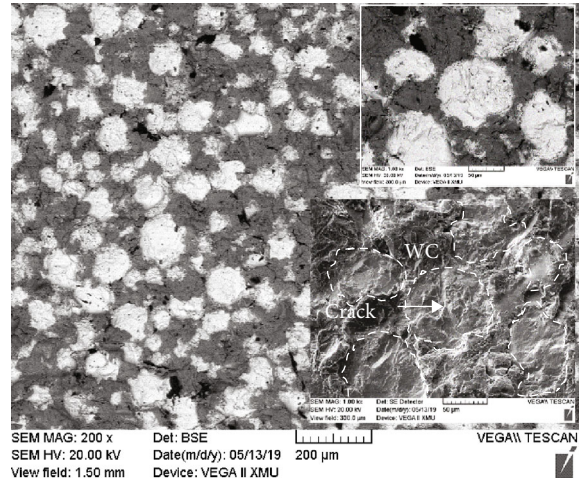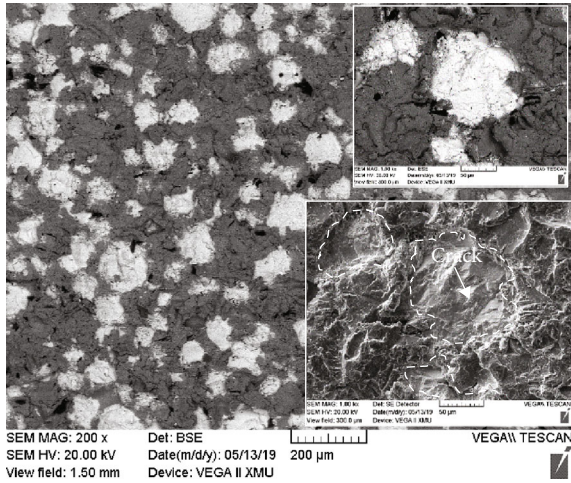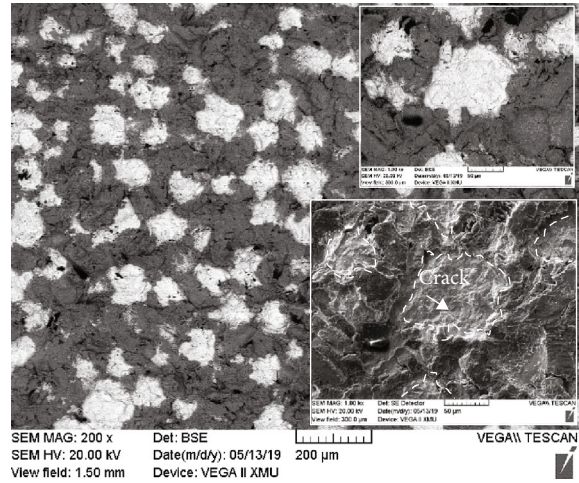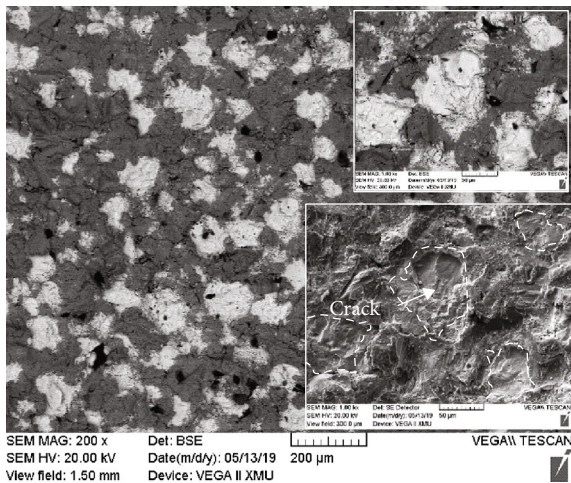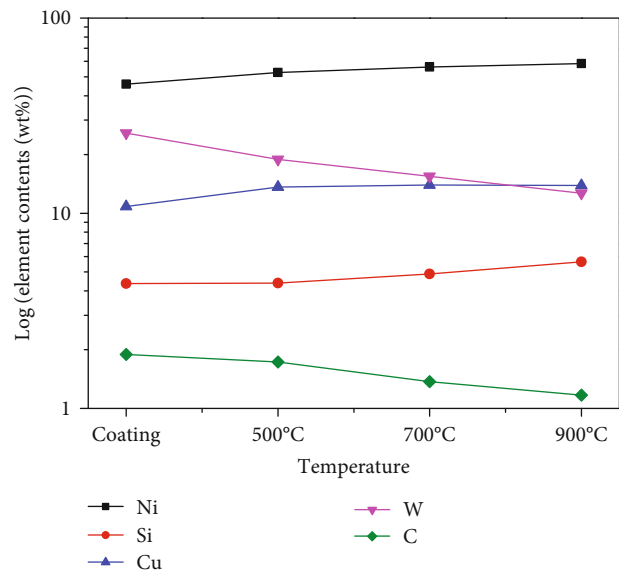
FIGURE 6: Erosion morphology of Ni-65wt%WC coating at different heat treatment temperatures: (a) Q235, (b) cladding coating, (c) 500°C, (d) 700°C, (e) 900°C, and (f) element distribution in erosion topography.

(a)

(b)

(c)

(d)
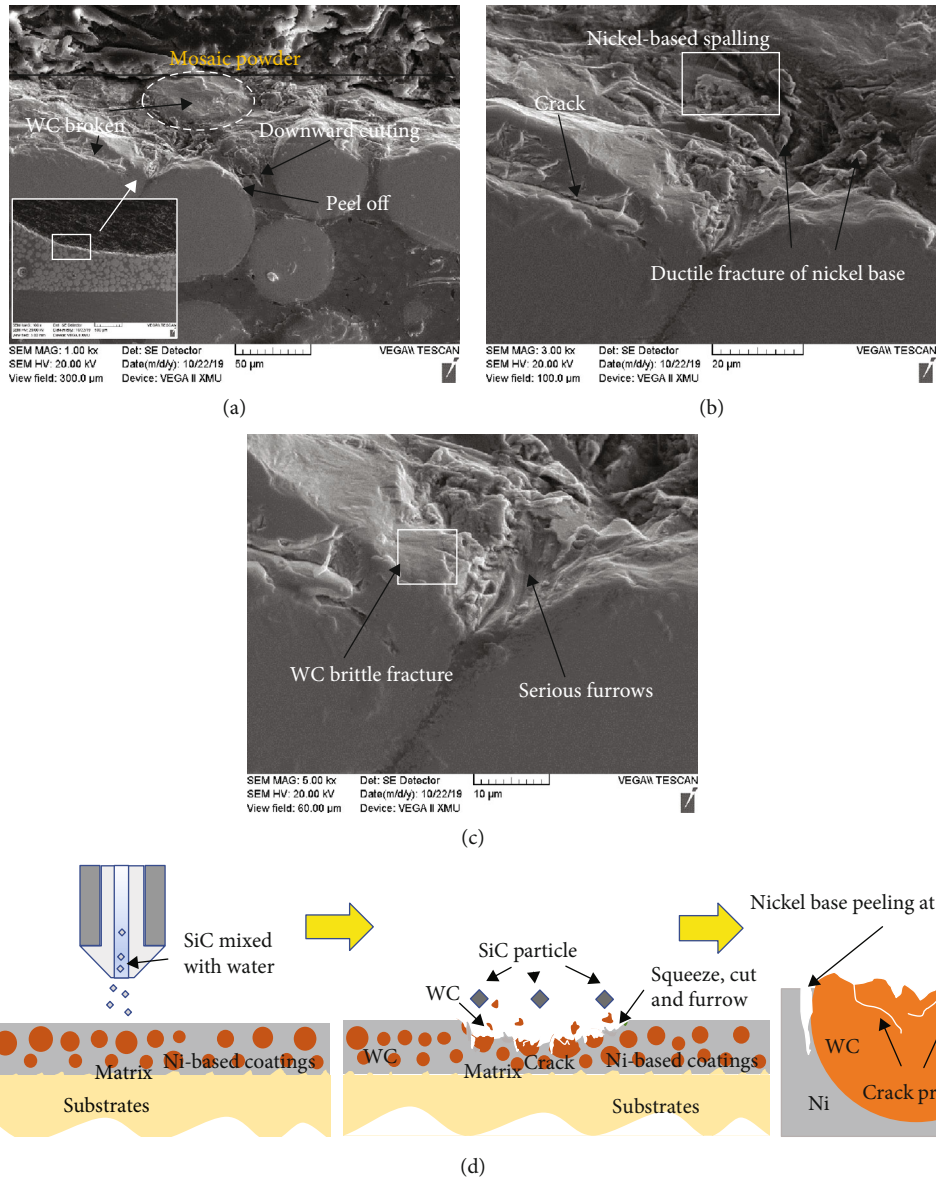
FIGURE 7: Section morphology (a–c) and schematic image of erosion mechanism (d) of Ni-65wt%WC coating under erosion wear condition.

particles were impacted on the surface, which was the first step under erosion. Subsequently, a crack initiated on the interfaces of WC particles or WC/matrix, and then, the crack gradually propagated with continuous erosion, resulting in serious spalling. Finally, it can be deduced that this kind of fatigue was likely to occur on Ni-65wt%WC coating with a weaker interface of WC/matrix and WC particles, such as cladding coating without heat treatment. Therefore, as the current results demonstrate, Ni-65wt%WC coating with brittle WC particles was hard to use in erosion resistance at 90° impact. In the future, it will be important to design application special functional materials integrated of strength and toughness in this condition.

3.3. Friction and Wear Performance of Ni-65 WC Coating under Reciprocating Tribocorrosion. After reciprocating

tribocorrosion testing, Figure 8 shows the friction coefficient and wear rate of Ni-65wt%WC coating under the atmospheric environment and 3.5% NaCl environment, respectively. It can be seen that the friction coefficient of Ni-65wt%WC coating (0.436) was about 50% lower than Q235 steel substrate (0.804) under an atmospheric environment. Meanwhile, the wear rate of Ni-65WC coating (5.04×10^{-8} mm$^3 \cdot$N$^{-1} \cdot$m^{-1}) was about 60% lower than Q235 steel substrate (12.6×10^{-8} mm$^3 \cdot$N$^{-1} \cdot$m^{-1}). After heat treatment, the friction coefficient Ni-65wt%WC coating gradually decreased and the lowest wear rate was obtained for Ni-65wt%WC coating (4.82×10^{-8} mm$^3 \cdot$N$^{-1} \cdot$m^{-1}) at 700°C. Additionally, the friction coefficients and wear rates of Ni-65wt%WC coating at the 3.5% NaCl environment were significantly lower than the atmospheric environment. It can be seen that the Ni-65wt%WC coating after heat treatment
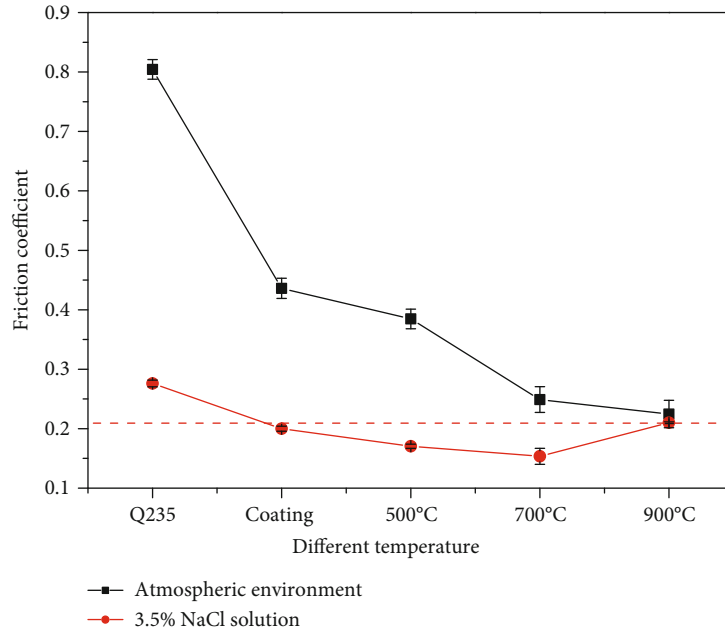
(a)
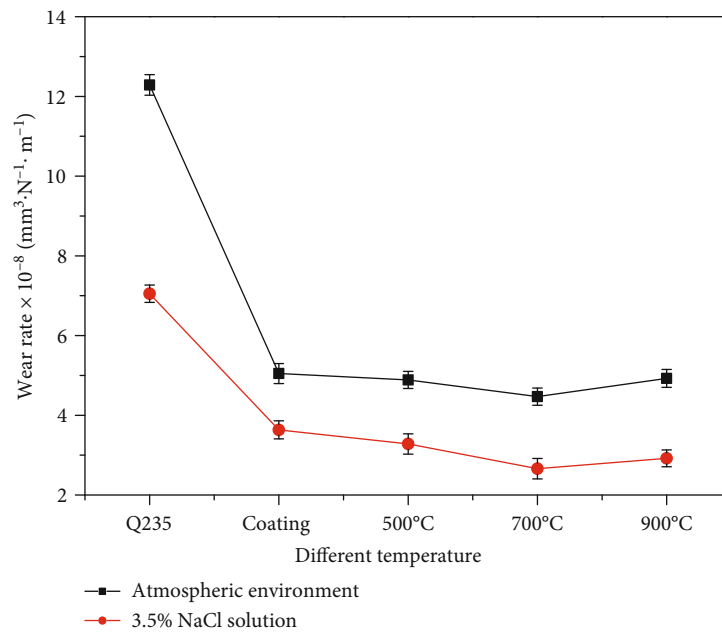
(b)

FIGURE 8: Friction coefficient (a) and wear rate (b) of Ni-65wt%WC coating under different environments.

at 700°C showed the lowest friction coefficient and wear rate; therefore, the results suggested that heat treatment reduces the friction coefficient and wear rate of Ni-65wt%WC coating under the atmospheric environment and 3.5% NaCl environment.

Worn surface morphologies of Q235 steel and Ni-65wt%WC coating tested under the atmospheric environment are shown in Figure 9. The wear scar width (1220 μm) of Ni-65wt%WC coating was significantly lower than that of the substrate (1527 μm), and the wear scar width decreased with increasing temperature, and the minimum

value (960 μm) was obtained at 700°C. To study the wear mechanism of Q235 substrate and Ni-65wt%WC coating, the wear scar depth after wear testing under the atmospheric environment is also shown in Figure 9. According to the graph, the wear depth of the substrate (60.328 μm) was about 5 times the coating (11.632 μm), which proved that the Ni-65wt%WC coating had good wear resistance. Meanwhile, the wear depth of the coating was inversely proportional to the heat treatment temperature and the lowest was 6.679 μm at 700°C. And it was found that the worn surface Q235 substrate was covered with tearing, microgroove,
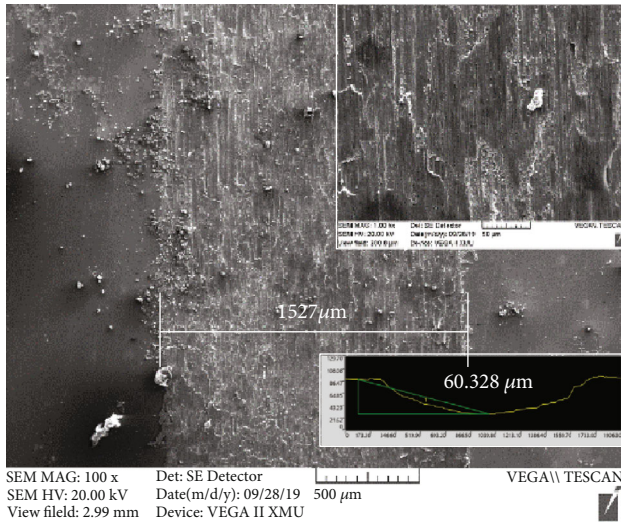
(a)
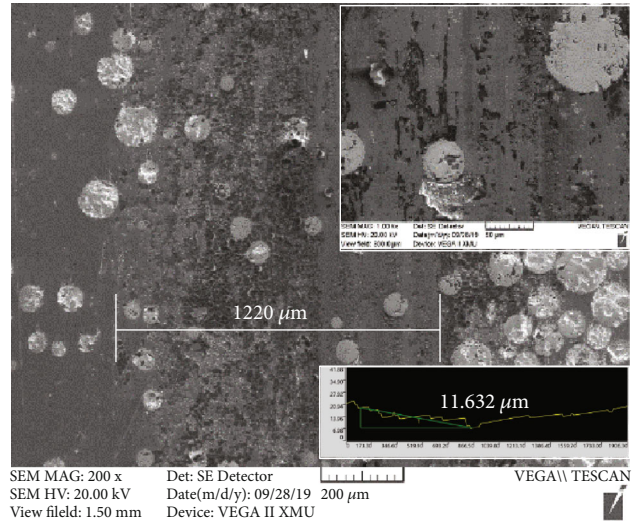
(b)
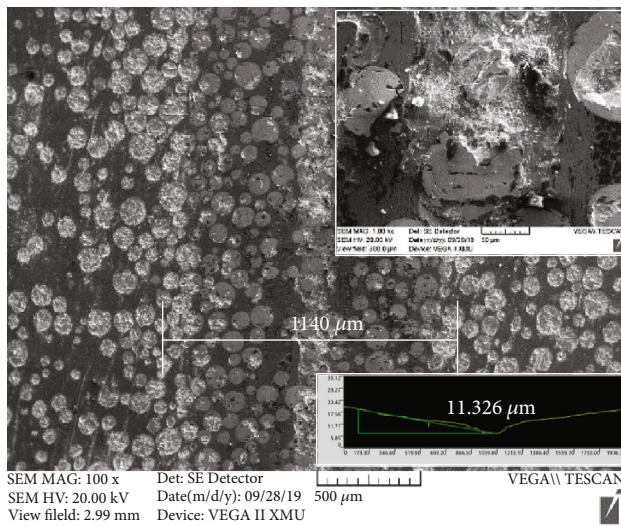
(c)
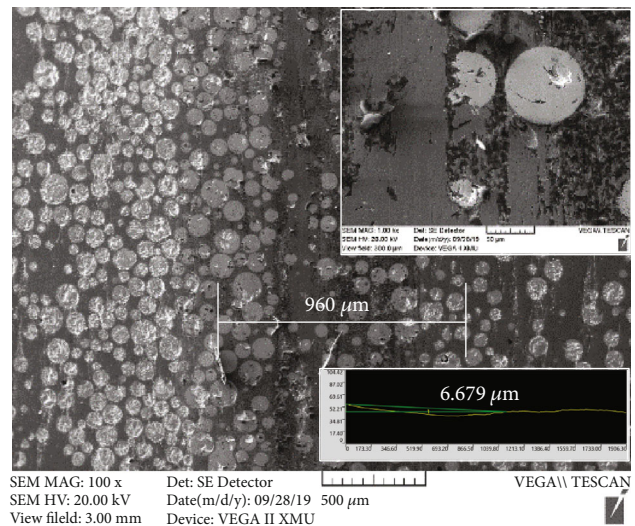
(d)
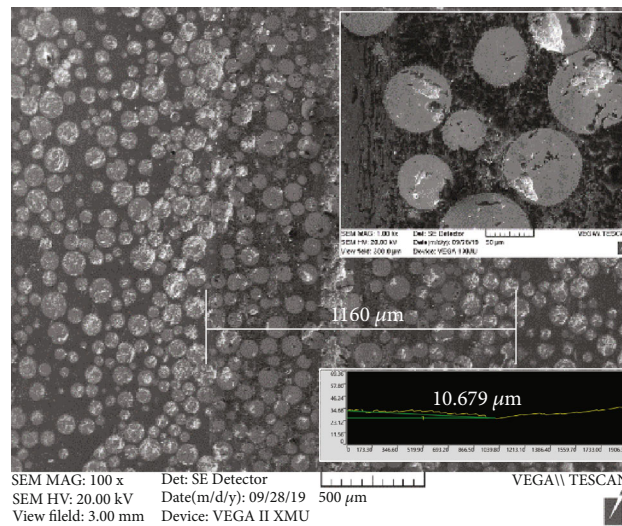
(e)

FIGURE 9: Wear scar morphology and depth of Ni-65wt%WC coating under air environments: (a) Q235, (b) cladding coating, (c) 500˚C, (d) 700˚C, and (e) 900˚C.
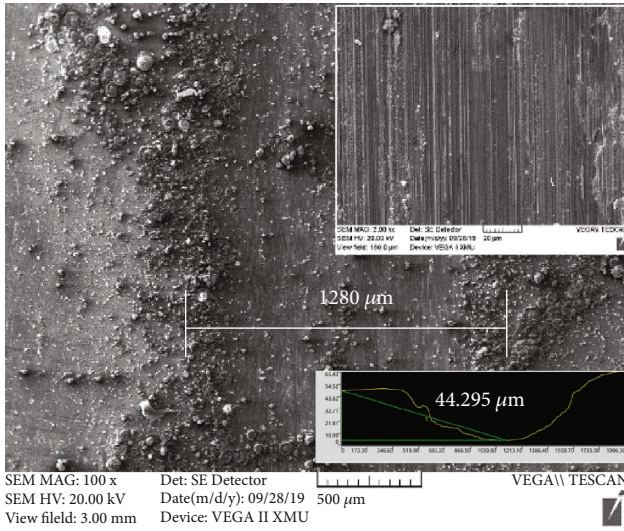
(a)
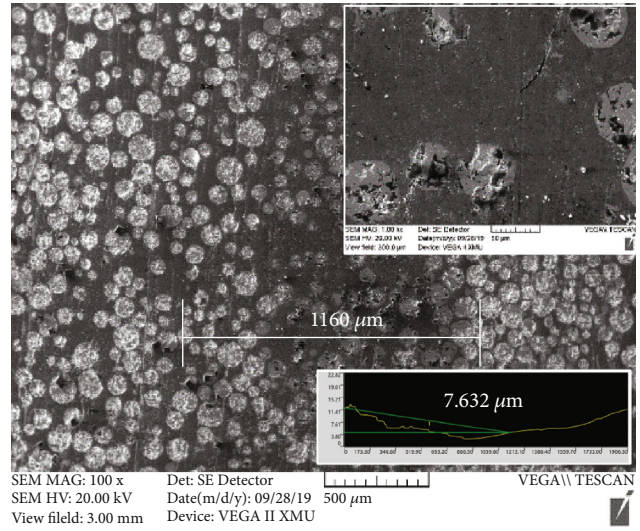
(b)
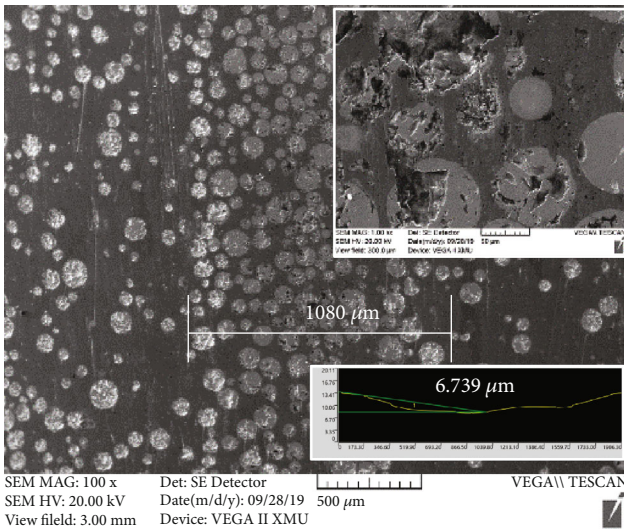
(c)
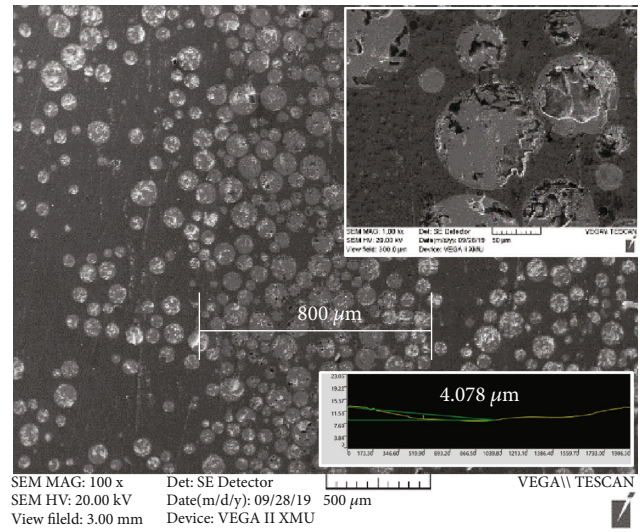
(d)
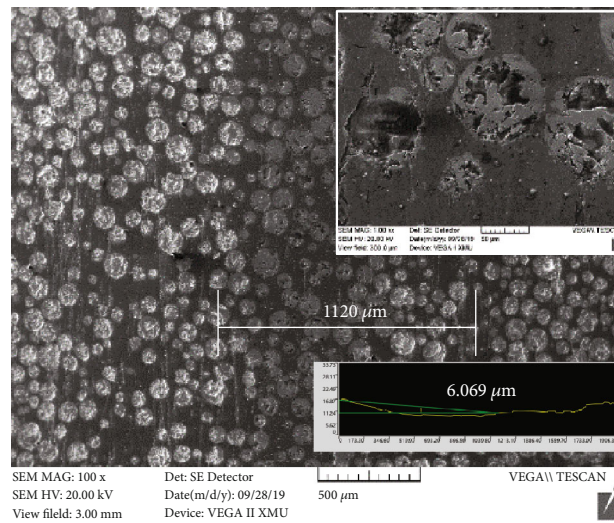
(e)

FIGURE 10: Wear scar morphology and depth of Ni-65wt%WC coating under 3.5% NaCl environments: (a) Q235, (b) cladding coating, (c) 500°C, (d) 700°C, and (e) 900°C.
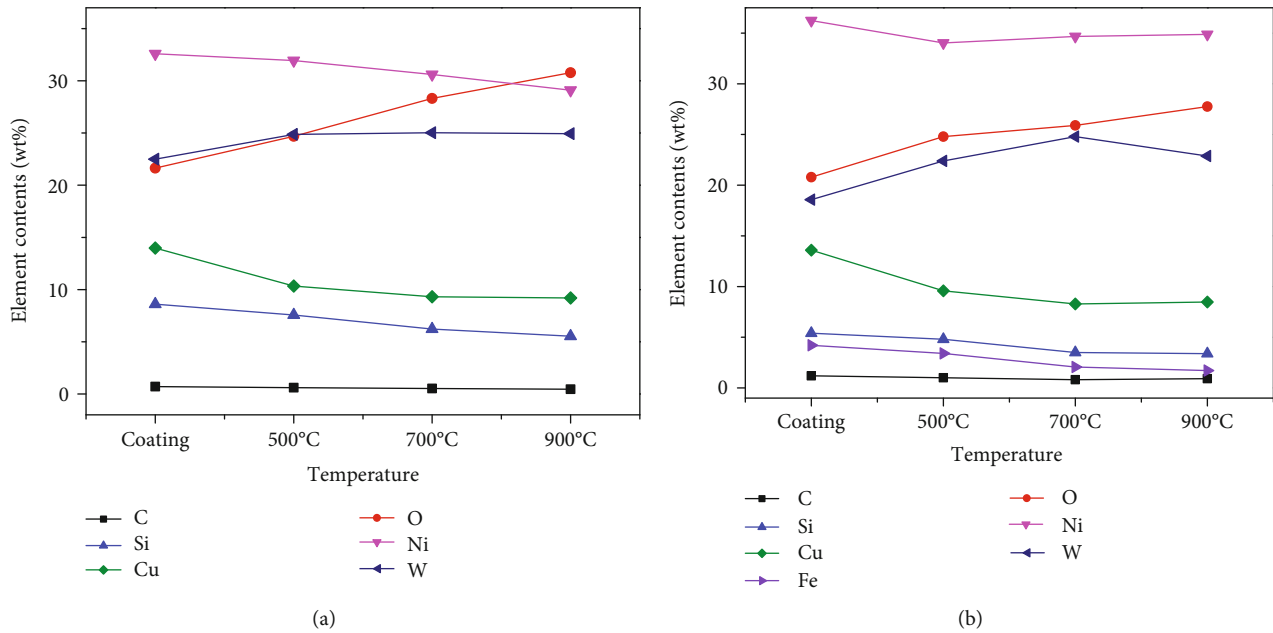
FIGURE 11: Chemical composition of wear scar of Ni-65wt%WC coating under different conditions: (a) air environments and (b) 3.5% NaCl environments.

fracture, and spalling, proving the wear mechanism was dominated by abrasive and adhesive wear. Then, the worn surface of Ni-65wt%WC coating was covered with a microgroove, proving that the wear mechanism was dominated by abrasive wear. Additionally, it can be seen that the worn surface of Ni-65wt%WC coating consisted of gray Ni matrix and white WC particles, and the existence of WC was benefited for the wear resistance of Ni-based composition coating. Furthermore, the worn surface of Ni-65WC coating after heat treatment was different from cladding coating, it can be seen that the contents of WC particles on a worn surface were much higher than the cladding coating. Therefore, the wear resistance of the coating was improved by the increase of WC content, which was owing to the improvement of interface force between WC/Ni bases.

Worn surface morphologies of Q235 steel and Ni-65wt%WC coating tested under a 3.5% NaCl environment are shown in Figure 10. The relationship between the width and depth of the wear scars with the increased heat treatment temperature was the same as the atmospheric environment. Meanwhile, the worn surface Q235 substrate was covered with microgroove and wear debris, indicating that the wear mechanism was abrasive wear. And the worn surface of the coating was smooth and accompanied by microgroove, confirming that the main wear mechanism was also dominated by abrasive wear. The width of the worn surface became narrower with heat treatment temperature, while being the lowest (800 μm) at 700°C. Therefore, it can be concluded that heat treatment was benefited for improving the wear resistance of the Ni-65wt%WC coating.

The chemical composition of wear scar of Ni-65wt%WC coating under the atmospheric environment and 3.5% NaCl environment was tested by EDS, as shown in Figure 11. Under the atmospheric environment, the results indicated that the contents of Ni, Cu, and Si decreased and the contents of the W and O element increased on the worn surface of Ni-65wt%WC coating before and after heat treatment. Thus, it can be deduced that the contents of WC and oxide were higher on the worn surface of Ni-65wt%WC coating after heat treatment, which was beneficial for antifriction and wears resistance. Under the 3.5% NaCl environment, the contents of the W element on the worn surface of Ni-65wt%WC coating after heat treatment were significantly higher than those of the cladding state. Meanwhile, the contents of the W element on Ni-65wt%WC coating after heat treatment increased first and then decreased at the higher temperature, confirming that the contents of Ni and O elements increased continuously with temperature. According to the results of Wang Xiang [18], it can be deduced that Ni and O meant the existence of Nickel hydroxide. Hence, the increase of Nickel hydroxide and the decrease of WC deteriorated the tribological properties of Ni-65wt%WC coating.

To study the wear mechanism of Ni-65wt%WC coating under reciprocating tribocorrosion condition, the cross-section morphology and schematic diagram of worn surface of Ni-65wt%WC coating after heat treatment at 700°C are shown in Figures 12(a)–12(c). During the reciprocating wear process, the coating surface was continuously removed by applying a repeated load, resulting in partial spalling of tungsten carbide. Secondly, the soft nickel base was adhered to the surface of tungsten carbide under the repeated driving of grinding ball, preventing the spalling of WC. Therefore, WC particles remained in the subsurface had a significant antiwear effect. Compared with erosion Ni-65wt%WC coating, the damage of WC was much higher during erosion wear, indicating that brittle WC particles were suitable for antiwear under

(a)

(b)

(c)
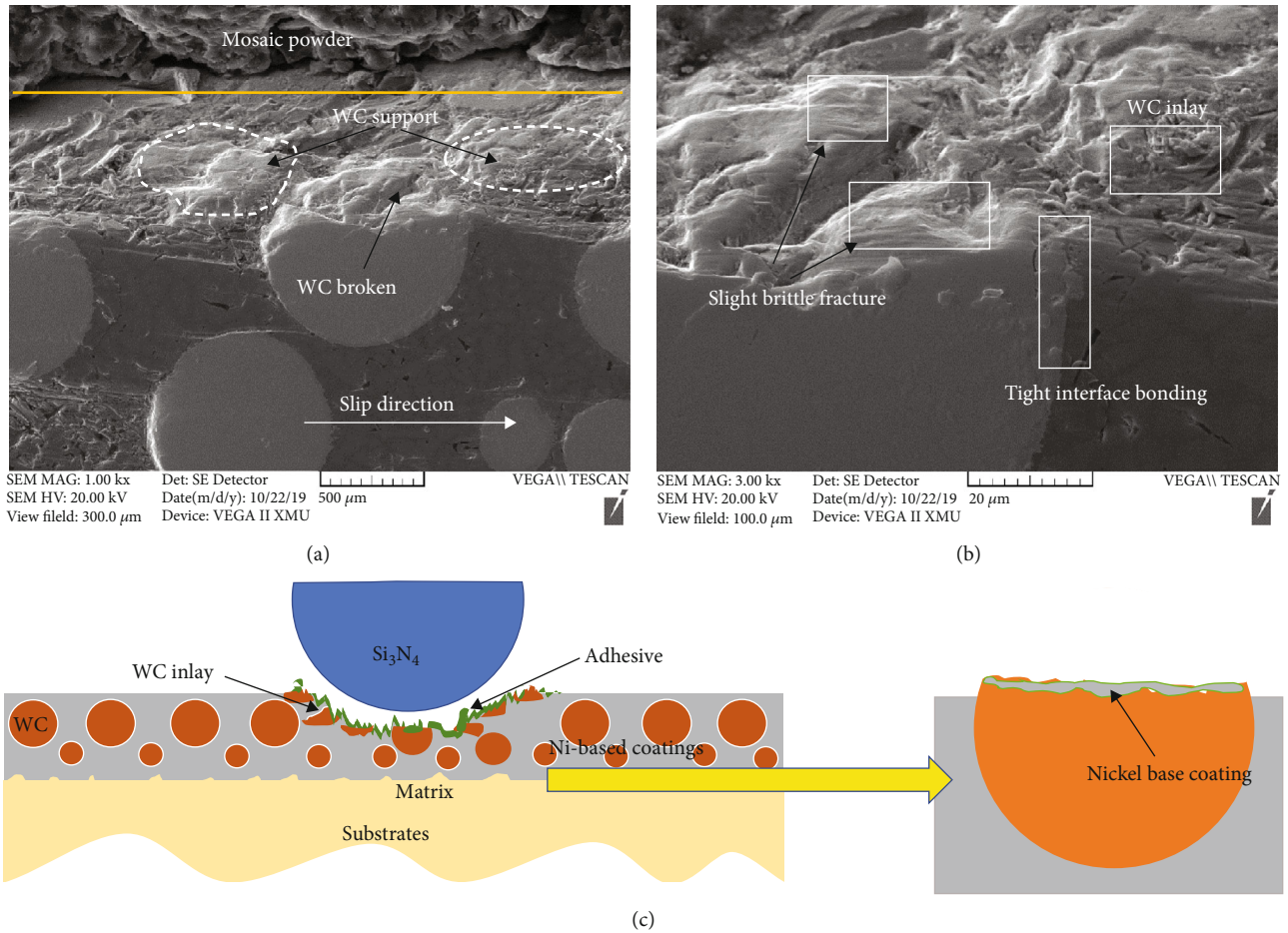
FIGURE 12: Section morphology (a, b) and schematic image of wear mechanism (c) of Ni-65wt%WC coating under reciprocating tribocorrosion condition.

low impact conditions. Therefore, it can be deduced that WC particles only play effectively supporting and strengthening the role of Ni-based compositions coating under reciprocating wear conditions, and the performance of Ni-based composition coating under severe erosion condition was deteriorated.

4. Conclusions

(1) The Ni-65wt%WC coating is prepared on Q235 steel by laser cladding technology, which mainly consisted of Ni, WC, and W_2C. After heat treatment, the interaction dendrite structure is formed between the interfaces of WC/Ni matrix. Meanwhile, the grain size of Ni matrix grown leads to the lower hardness and weaker plastic deformation resistance of Ni-65wt%WC coating

(2) With the increase of heat treatment temperature, the erosion rate of Ni-65wt%WC coating tested with quartz sand particle is lower at a higher temperature, which is enhanced by the stronger interface adhesion between WC/Ni matrixes

(3) The Ni-65wt%WC coating shows excellent performance on reciprocating tribocorrosion under 3.5% sodium chloride condition, owning to the higher antiwear effect of hard WC under low impact condition

Data Availability

The [DATA TYPE] data used to support the findings of this study are included in the article.

Conflicts of Interest

The authors declare that they have no conflicts of interest.

Acknowledgments

References

[1] H. H. Chen, C. Y. Xu, J. Chen, H. Zhao, L. Zhang, and Z. Wang, "Microstructure and phase transformation of WC/Ni60B laser cladding coatings during dry sliding wear," *Wear*, vol. 264, no. 7-8, pp. 487–493, 2008.

[2] T. Han, Y. Shen, and X. Feng, "Microstructure and phase transformations of Fe-Ni-Cr mixed powder by laser cladding on Q235 mild steel," *International Bhurban Conference on Applied Sciences and Technology*, vol. 15, pp. 63–69, 2018.

[3] S. M. Zhu and Y. D. Zhang, "The microstructure and wear-resistant properties of laser cladding Ni-based WC alloy on Q345 steel surface," in *Applied Mechanics and Materials*, vol. 556, pp. 189–192, Trans Tech Publications Ltd, 2014.

[4] R. R. Shi, S. Y. Chen, Y. G. Peng, and Z. Zhang, "Effect of pre-heating temperature on microstructure of Fe based alloy coating by laser direct metal deposition," *Engineering Materials*, vol. 703, pp. 94–99, 2016.

[5] Y. Wu and Y. Niu, "Microstructure and hardness of laser cladding nickel based alloy doped with WC on Q235 steel," *Materials Protection*, vol. 2, pp. 18–22, 2005.

[6] Y. X. Guo, Q. B. Liu, and F. Zhou, "Microstructure and properties of Fe5Cr5SiTiCoNbMoW coating by laser cladding," *Surface Engineering*, vol. 34, no. 4, pp. 283–288, 2018.

[7] Z. T. Wang, S. K. Zhu, F. Feng et al., "Microstructure and wear resistance of nanostructure WC composite coatings prepared by argon arc cladding injection," *Advanced Materials Research*, vol. 1082, pp. 480–483, 2014.

[8] S. F. Zhou, Y. B. Xu, B. Q. Liao et al., "Effect of laser remelting on microstructure and properties of WC reinforced Fe-based amorphous composite coatings by laser cladding," *Optics Laser Technology*, vol. 103, pp. 8–16, 2018.

[9] P. Farahmand and R. Kovacevic, "Laser cladding assisted with an induction heater (LCAIH) of Ni–60% WC coating," *Journal of Materials Processing Technology*, vol. 222, pp. 244–258, 2015.

[10] M. Qunshuang, L. Yajiang, W. Juan, and L. Kun, "Microstructure evolution and growth control of ceramic particles in wide-band laser clad Ni60/WC composite coatings," *Materials Design*, vol. 92, pp. 897–905, 2016.

[11] H. Zhang, K. Chong, G. C. Xiao, Z. Sun, and W. Zhao, "TIG cladding in-situ nano vanadium carbide reinforced Fe-based ultra-fine grain layers under water cooling condition," *Surface Coatings Technology*, vol. 352, pp. 222–230, 2018.

[12] T. Yu, Q. L. Deng, G. Dong, and J. Yang, "Effects of Ta on microstructure and microhardness of Ni based laser clad coating," *Applied Surface Science*, vol. 257, no. 11, pp. 5098–5103, 2011.

[13] X. L. Lu, X. B. Liu, P. C. Yu et al., "Effects of post heat-treatment on microstructure and tribological properties of Ni60/H-BN self-lubricating anti-wear composite coating on 304 stainless steel by laser cladding," *Tribology*, vol. 36, no. 1, pp. 48–54, 2016.

[14] G. J. Li, J. Li, and X. Luo, "Effects of post-heat treatment on microstructure and properties of laser cladded composite coatings on titanium alloy substrate," *Optics Laser Technology*, vol. 65, pp. 66–75, 2015.

[15] I. Kleis and P. Kulu, "Erosion resistance of powder materials and coatings," in *Solid Particle Erosion*, pp. 129–168, Springer, London, 2008.

[16] P. Kulu and T. Pihl, "Selection criteria for wear resistant powder coatings under extreme erosive wear conditions," *Journal of Thermal Spray Technology*, vol. 11, no. 4, pp. 517–522, 2002.

[17] M. R. Ramesh, S. Prakash, S. K. Nath, P. K. Sapra, and B. Venkataraman, "Solid particle erosion of HVOF sprayed WC-Co/NiCrFeSiB coatings," *Wear*, vol. 269, no. 3-4, pp. 197–205, 2010.

[18] X. Wang, L. F. Zhu, Z. M. Zhou et al., "Tribological properties of WC-reinforced Ni-based coatings under different lubricating conditions," *Journal of Thermal Spray Technology*, vol. 24, no. 7, pp. 1323–1332, 2015.

WILEY | Hindawi

Research Article

Effect of Diamond Surface Pretreatment and Content on the Microstructure and Mechanical and Oxidation Behaviour of NiAl/Fe-Based Alloys

Yaping Bai [ID], Jianping Li [ID], Jiajia Luo [ID], and Yongchun Guo [ID]

School of Materials and Chemical Engineering, Xi'an Technological University, Xi'an, 710021 Shaanxi Province, China

Correspondence should be addressed to Yaping Bai; jingpingxue2004@163.com and Jianping Li; jpli_0416@163.com

The effect of diamond surface pretreatment and content on the microstructure and mechanical properties of NiAl/Fe–x diamond ($x = 0$, 5, 10, 15, and 20 wt.%) alloys was investigated after mechanical alloying with subsequent hot-pressing sintering. The results showed that after the surface pretreatment, a complete transition layer containing W existed on the outer surface of the diamond grains, which improved the interfacial bonding strength of the diamond grains and NiAl/Fe matrix to an excellent level. As the diamond content increased, the compressive strength of the NiAl/Fe-based alloys declined, but the alloy with 10 wt.% diamond had a higher value than that of the other NiAl/Fe-based alloys. Short cracks and transgranular fracture were observed in the fracture surface of all materials. For the material with 20 wt.% diamond, intergranular fracture was obvious, and many diamond particles appeared along the fracture direction, which caused the compressive strength to be the lowest of the samples considered in this study. After the addition of diamond, the oxidation resistance of NiAl/Fe-based alloys decreased due to a loose oxidation layer and diamond graphitization. The thermal conductivity of the alloy first increased and then decreased with increasing diamond content. A NiAl/Fe-based alloy with 15 wt.% diamond demonstrated the maximum thermal conductivity of 53.2 W/(m·k) at 600°C among the samples in this study.

1. Introduction

It is generally known that the cylinder head of a diesel engine often contacts high-temperature and high-pressure gas, and it therefore bears substantial heat and mechanical loads [1–4]. Materials in severe working conditions must possess not only high strength and creep resistance but also excellent thermal conductivity and corrosion resistance [5–9]. Cast iron (7.6 g/cm^3), as the present cylinder head material, is not readily fulfilling the requirements of engines with increasing power. In particular, the mechanical properties of cast iron deteriorate sharply when the environment temperature increases to 400°C [10, 11]. Therefore, iron-based materials with low density, excellent mechanical properties, and thermal conductivity should be developed.

In 2015, scientists at the Pohang University of Science and Technology in South Korea found that during the annealing process, nickel can react with aluminium to pro-

duce nanoscale B2-ordered NiAl crystals. The B2 crystals have excellent shear resistance, so steel containing B2-ordered NiAl crystals can demonstrate high strength and high ductility [12]. Thus, the B2-ordered NiAl phase, as a particle reinforcement, is a good choice for improving the mechanical properties of iron-based alloys. In addition, it is known that the cost of synthetic diamond is low. It has not only high hardness and chemical stability but also excellent thermal conductivity (600-2000 W/m·K) and thermal stability, so it is now widely used for polishing, as a particle reinforcement and as a composite coating, for example [13–15]. The interface bonding strength between the matrix and diamond may be primarily due to mechanical mixing without a transition layer [16]. The interface between the Fe matrix and diamond particles is the major determinant of the Fe/diamond composite properties. Therefore, pretreatment of the diamond powders is very important for ensuring adhesion between the diamond and matrix. In recent years,
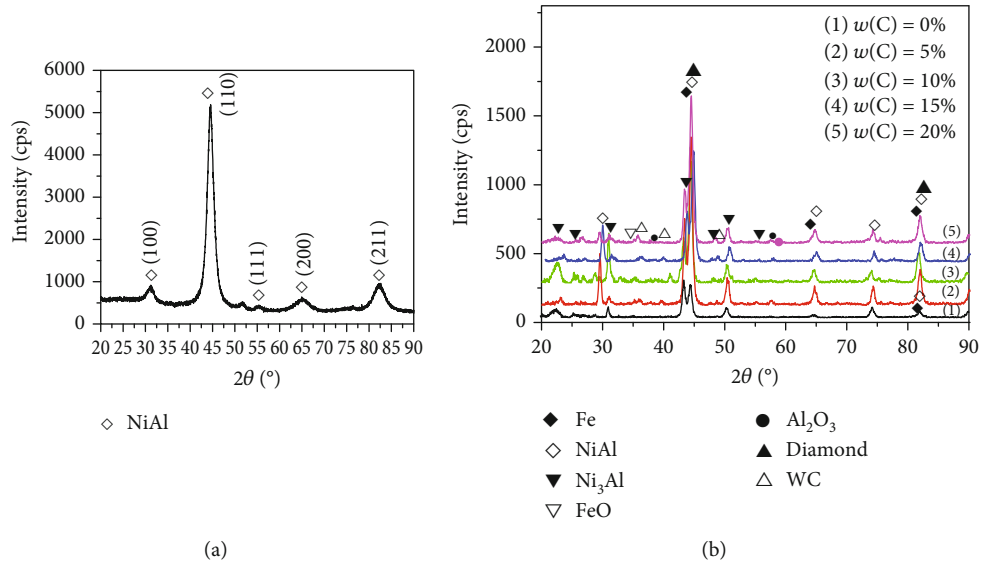
FIGURE 1: XRD patterns of NiAl powders and NiAl/Fe-based alloys with different diamond contents: (a) as-milled NiAl powders; (b) sintered NiAl/Fe-based alloys.
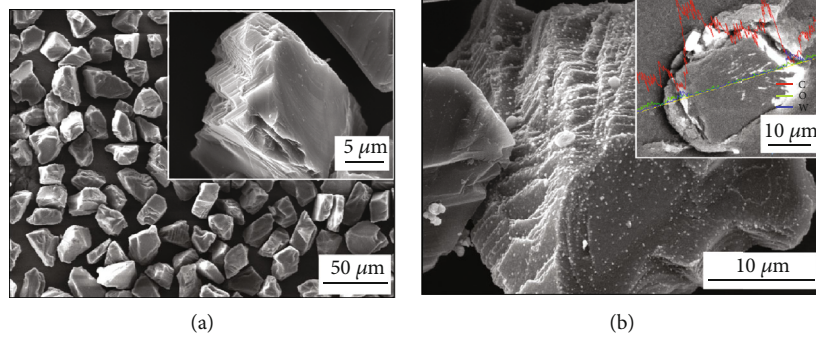
FIGURE 2: Micromorphology and line scanning results of diamond before and after pretreatment: (a) before pretreatment; (b) after pretreatment.

research has focused on surface pretreatments of the diamond to solve such problems [16–18]. Scholars found that tungsten layers can be coated on diamond by a microvacuum evaporation diffusion method and then, diamond/copper composites can be prepared by vacuum pressureless infiltration. The resulting full uniform plating layer on the diamond/copper interface has high thermal conductivity [16].

Therefore, B2-ordered NiAl/Fe-based alloys with different contents of diamond powders before/after pickling treatment are prepared by mechanical alloying with subsequent hot-pressing sintering based on previous research in our laboratory and are discussed herein. Then, the microstructure, mechanical properties, oxidation resistance, and thermal conductivity at RT ~600°C are studied. The study results can provide theoretical and technical support for future cylinder head materials.

2. Experimental Procedures

2.1. Material Preparation. The B2-ordered NiAl powders were prepared by the following ball milling process. The Ni powder and Al powder with a 1 : 1 atomic ratio were homogenized by ball milling under an argon gas protective atmosphere by a Pulverisette P5-type (Germany) variable-frequency planetary ball mill. The test parameters were as follows: the ball material ratio was 10 : 1, the speed was 250 r/min, and the process was on for 30 min and then stopped for 30 min for a total of 70 h.

Diamond-/NiAl-reinforced iron-based alloys were prepared by hot-pressing sintering after the surface pretreatment of the diamond powders. The diamond exhibited excellent properties, such as high hardness, low density, and high thermal conductivity, but it had poor interface bonding with the Fe-based alloys. Therefore, surface pretreatment of the diamond powders must be carried out first. The surface pretreatment of the diamond powders was as follows. The diamond powder, Cu powder, and W powder were mixed according to a mass ratio of 75% : 20% : 5%. Due to the good thermal conductivity of copper powder, the heat in the alloy powder can be evenly diffused without heat accumulation at high temperature. Then, the powders were treated as follows. They were pickled in acid (in 10 wt.% hydrochloric acid at
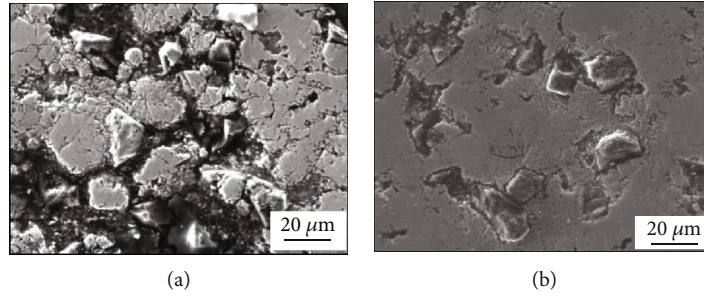
FIGURE 3: SEM images of NiAl/Fe-based alloys with 20 wt.% diamond: (a) before pretreatment; (b) after pretreatment.
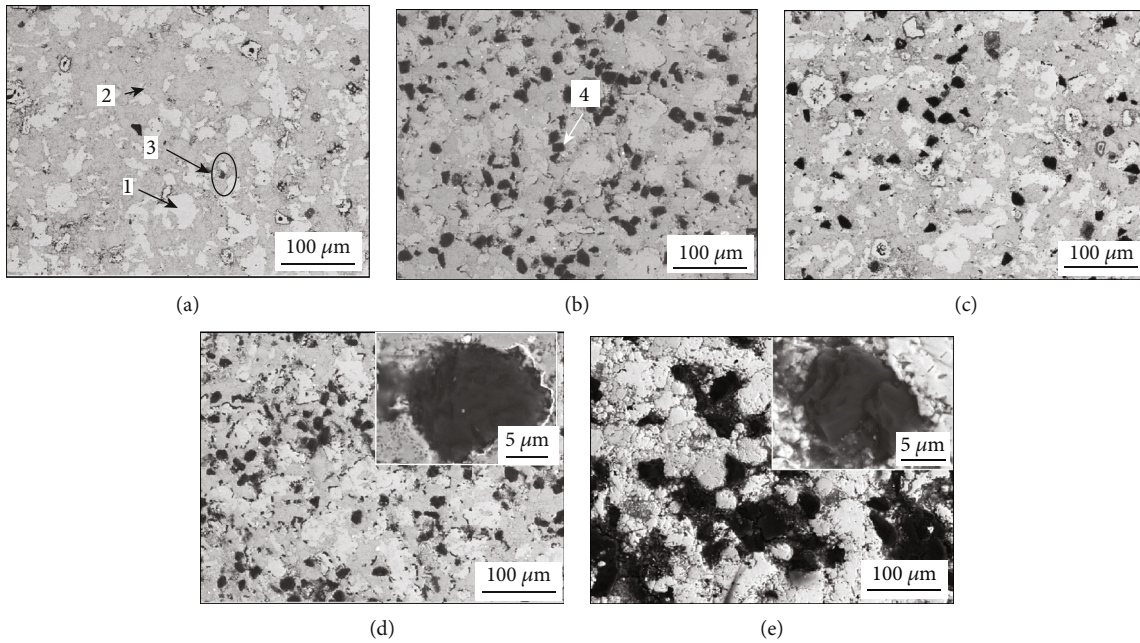
FIGURE 4: SEM images of NiAl/Fe-based alloys with different diamond contents: (a) 0 wt.%; (b) 5 wt.%; (c) 10 wt.%; (d) 15 wt.%; (e) 20 wt.%.

TABLE 1: EDS results of the points marked in Figures 4(a) and 4(b).

Points	Fe (wt.%)	Ni (wt.%)	Al (wt.%)	C (wt.%)	O (wt.%)
1	96.73	0.86	1.58	0.83	—
2	6.47	68.66	23.79	1.08	—
3	58.74	—	—	3.64	37.62
4	1.92	2.11	2.50	89.66	3.81

60°C for 30 min) → cleaned with acetone for 20 min → cleaned with alcohol for 20 min → cleaned with acetone for 20 min → dried. Then, the mixed powders were vacuum heat treated at 1000°C for 60 min. The redundant tungsten powders were removed by sieving the powder in 300-mesh, 400-mesh, and then 600-mesh sieves successively. Finally, the tungsten-coated diamond powder was obtained.

The NiAl powders and iron powders with 0 wt.%, 5 wt.%, 10 wt.%, 15 wt.%, and 20 wt.% diamond powder were mixed with a YXQM-type planetary mill at a ball : material ratio of 3 : 1 at a speed of 100 r/min for 5 h.

Thirty grams of the milled powders was packed in a graphite mould (inner size Ø30 mm × 50 mm) under a continuous pressure of 20 MPa using a hot-pressing sintering apparatus (ZT-40-20Y, Shanghai Chen Hua Electric Furnace Co., Ltd., China) that operated under a vacuum of 7×10^{-2} Pa, heated at a rate of 10°C/min, and then consolidated the material at 1050°C for 60 min.

2.2. Microstructure and Performance Test. The densities were measured by the Archimedes method. The phase analysis was evaluated by X-ray diffraction (XRD) using an X-ray diffractometer (Rigaku D/Max-RB) with Cu Kα radiation (wavelength = 0.15418 nm) at 40 kV and 100 mA. The microstructure and interface bonding were characterized by scanning electron microscopy (SEM) on an instrument equipped with an energy dispersive spectroscopy (EDS) and also transmission electron microscopy (TEM). Samples with a size of 5 mm × 5 mm were cut from the alloys by an electrical discharge wire-cutting machine for hardness testing. The bulk hardness was measured on an HRS-150 Digital Rockwell Hardness Machine with an
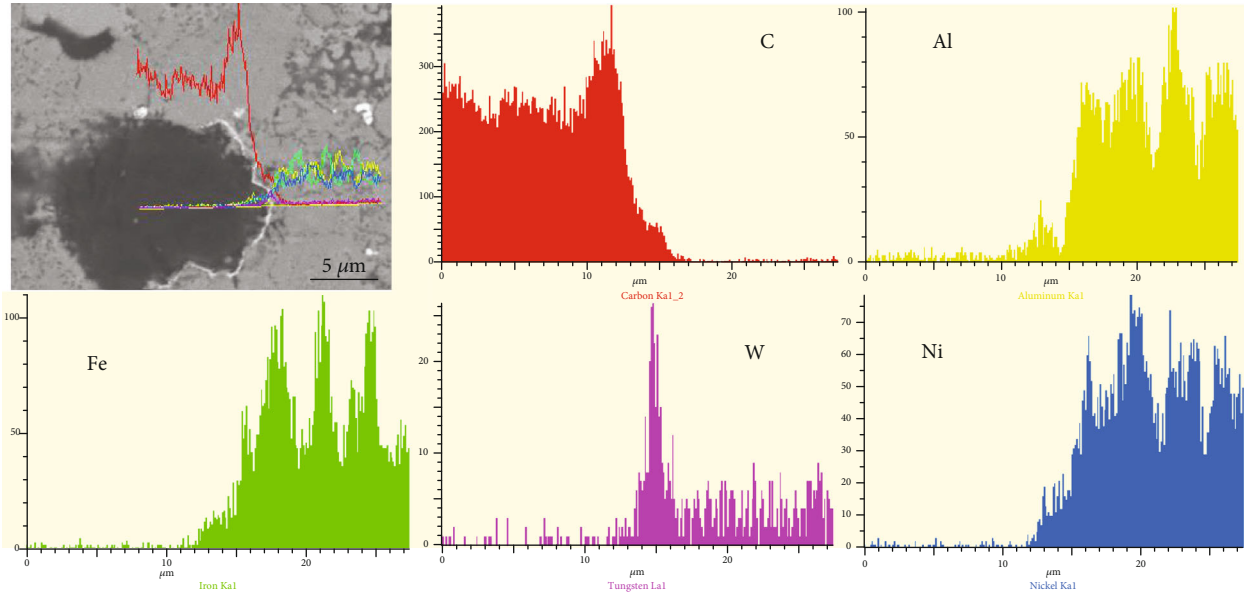
FIGURE 5: Line scanning results of NiAl/Fe-based alloys with 15 wt.% diamond shown in Figure 4(d).

(a)

(b)
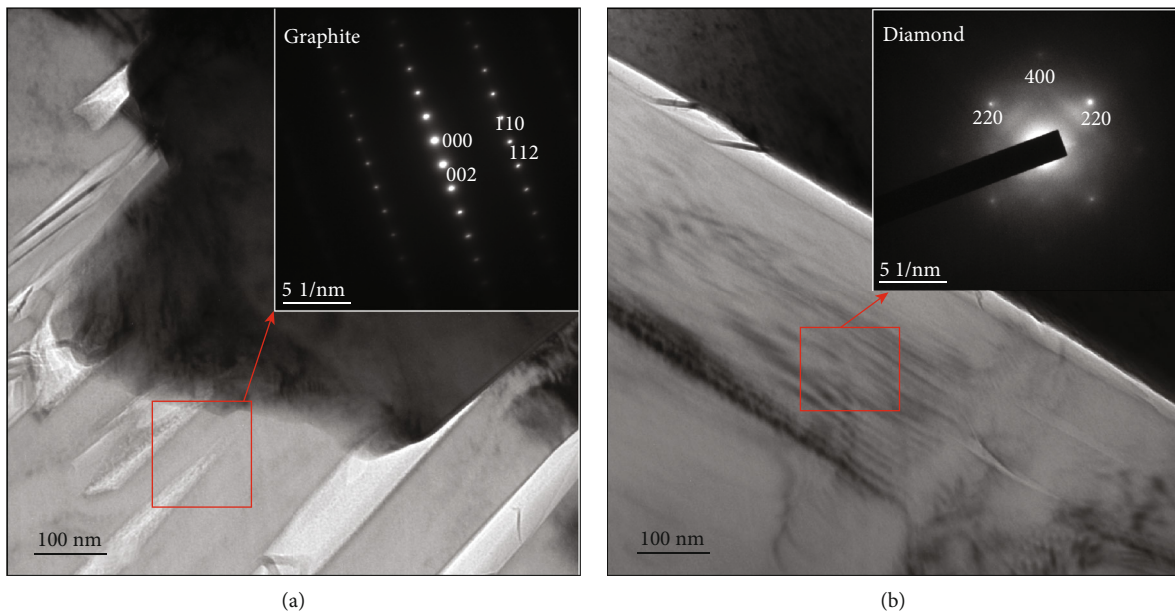
FIGURE 6: Transmission electron micrographs and selected area electron diffraction patterns of NiAl/Fe-based alloys with 10 wt.% diamond: (a) graphite structure; (b) diamond structure.

applied load of 1470 N. Specimens with a size of 4 mm × 4 mm × 7 mm were cut from the sintered bulk samples by electrodischarge machining for compression tests. Before the compression tests, the six surfaces of the specimens were polished first. The room temperature compression performance was tested with an electronic universal tensile test machine (D2-0200-1) with a strain rate of 5 × 10^{-3}/s. The oxidation behaviour of the composites was tested on a HENVEN-HJ integrated thermal analyser at 600°C for 25 h and 250 h. The nominal sample dimension was 20 mm × 20 mm × 1.5 mm, and the introduced air flo-

wed at 50 ml per minute during the oxidation experiment. Before the oxidation test, the specimens were predried to a constant weight. The thermal conductivity of the alloy with $\Phi 12.5 \times 2.5$ mm was measured by a NETZSCH-LFA457 laser thermal conductor at room temperature, 100°C, 200°C, 300°C, 400°C, 500°C, and 600°C.

3. Results and Discussion

3.1. Phase Composition and Microstructure. The XRD diffraction patterns of the as-milled NiAl powder and NiAl/Fe-

(a)

(b)
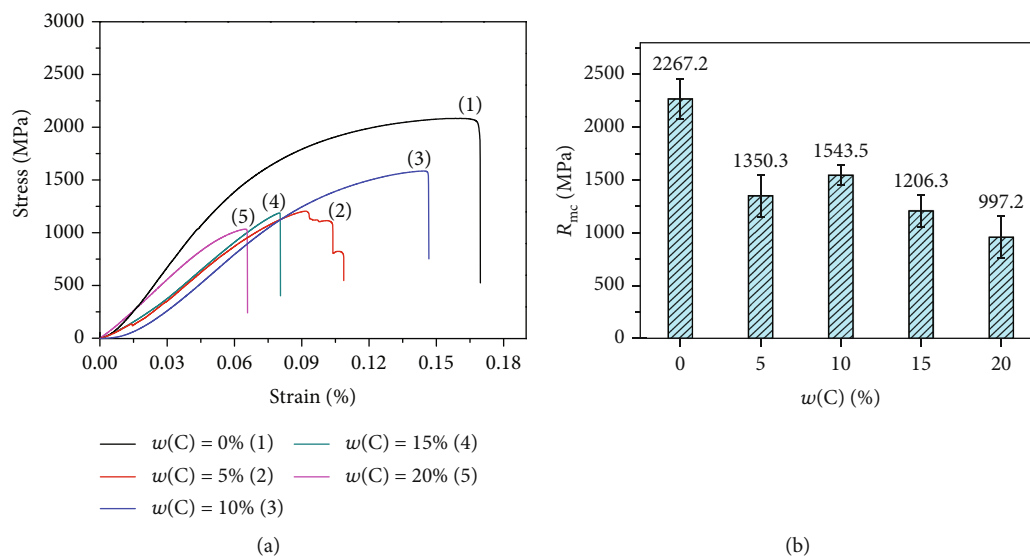
FIGURE 7: Compressive stress-strain curve and compressive strength of NiAl/Fe-based alloys with different diamond contents: (a) stress-strain curve; (b) compressive strength.

(a)

(b)

(c)

(d)
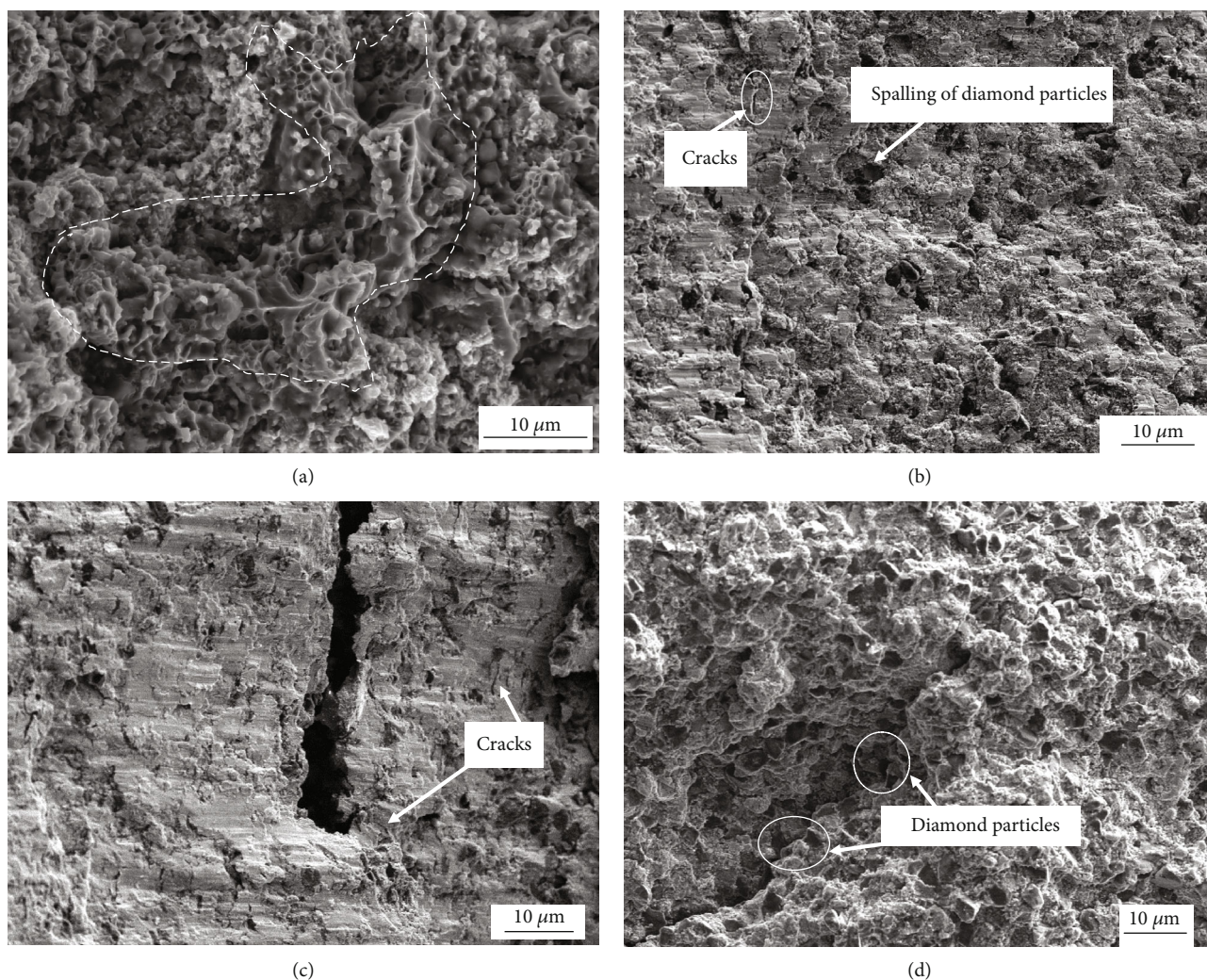
FIGURE 8: Fracture surfaces of NiAl/Fe-based alloys with different diamond contents: (a) 0 wt.% (b) 5 wt.%; (c) 10 wt.%; (d) 20 wt.%.
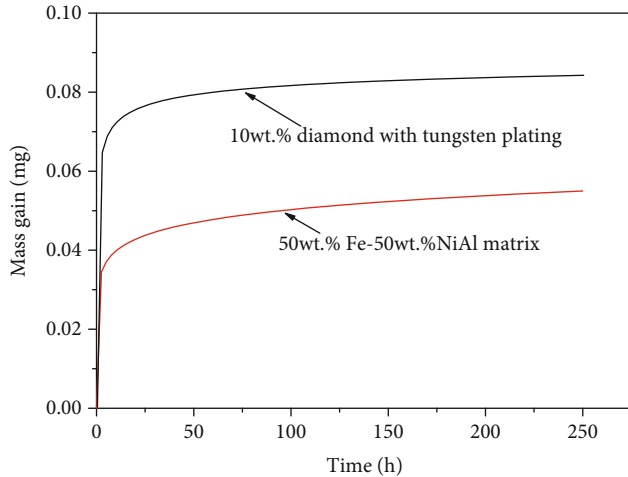
FIGURE 9: Oxidation weight gain-oxidation time curve of NiAl/Fe-based alloys with 0 wt.% and 10 wt.% diamond.

based alloys with different diamond contents after the sintering process are presented in Figures 1(a) and 1(b), respectively. From Figure 1(a), it can be observed that the diffraction peaks from the (100), (110), and (211) planes are present in the XRD pattern of the NiAl powders, especially the (110) diffraction peak, which is the strongest. It can be concluded from the XRD data that NiAl powder with a B2 structure is successfully obtained. Figure 1(b) indicates that superlattice reflection peaks of NiAl are still present in all the sintered samples. In addition, a small amount of B2-ordered NiAl phase transforms to Ni_3Al at the high temperature during the sintering process, so the Ni_3Al phase diffraction peak also appears in the XRD pattern of the bulk sample. The WC diffraction peaks obviously increase with increasing diamond content, which infers that a WC coating layer is formed on the diamond surface. In addition, during the sintering process under a low-vacuum environment, some Fe and Al elements are oxidized to FeO and Al_2O_3, respectively.

Figure 2 shows the micromorphology and line scanning results of the diamond before and after the surface pretreatment. After the pretreatment, the diamond surface becomes rough, and the results of the line scanning analysis show that there is a WC layer on the surface, which is in accordance with the results of the XRD test shown in Figure 1(b). The increased surface roughness and WC formation are beneficial to the bonding with the matrix phase during the sintering process.

Figure 3 shows SEM images (secondary electron images) of NiAl/Fe-based alloys with 20 wt.% diamond before and after pretreatment. From the secondary electron images (SE) of NiAl/Fe-based alloys with untreated/pretreated 20 wt.% diamond, there is an obvious gap between the untreated diamond and the NiAl/Fe matrix material shown in Figure 3(a); however, the interface between the pretreated diamond powder and the matrix is very close shown as the Figure 3(b), which indicates that the bonding strength of the pretreated diamond and the matrix is

improved. All these indicate that the addition of tungsten can prevent the graphitization of diamond at high temperature and can improve the bonding strength between diamond and alloy matrix.

Figure 4 shows SEM images (backscattered electron images) of the NiAl/Fe-based alloys with 0 wt.%, 5 wt.%, 10 wt.%, 15 wt.%, and 20 wt.% diamond. The corresponding point EDS analysis is shown in Table 1. The line scan result in Figure 4(d) is shown in Figure 5. Combined with Figure 4(a) and the EDS results, it can be concluded that the white areas (point 1) are iron matrix, the grey areas (point 2) are mainly NiAl phase, and the black particles (point 3) are FeO phase with a grain size of approximately $10 \mu m$. With the addition of diamond particles, homogeneous granular black particles appear in the microstructure, but when the diamond content increased to 20%, the diamond forms a substantial amount of agglomerates. From Figure 5, a relatively complete WC transition layer can be seen between the diamond and matrix. These data are enough to prove that after the diamond surface pretreatment, a complete WC layer forms on its outer surface. All the analyses are consistent with the XRD results shown in Figure 1.

The bonded area between the diamond and matrix was further magnified by transmission electron microscopy (TEM), as shown in the micrograph of the NiAl/Fe alloy with 10 wt.% diamond in Figure 6. In Figures 6(a) and 6(b), it can be seen that the diamond and matrix forms a good interface bond with no obvious gap. Further analysis proves that there are two forms of C present: a strip-like grey-white phase in Figure 6(a) and pure grey plate-like phase in Figure 6(b). The calibration results of the diffraction patterns indicate that the grey-white strip-like material is a graphite phase and that the pure grey plate-like material is a diamond phase. All these results indicate that diamond graphitization occurs during hot-pressing sintering, which also confirms that the black worm-like substance in the scanning photograph of Figure 4(d) is graphite.

3.2. Mechanical and Thermal Physical Properties. Figure 7 shows the compressive stress-strain curve of the NiAl/Fe-based alloys with different diamond contents at room temperature. Figure 8 shows the fracture surfaces of the NiAl/Fe-based alloys with different diamond contents. From Figure 7, it can be seen that the compression ratio of the NiAl/Fe-based alloys is larger than that of the NiAl/Fe-based alloys with the diamond addition at the same temperature. These results are due to the second phase addition acting as a crack source, as shown in Figure 8(b). From Figure 8(d), it is clear that cracks extend along the diamond boundary, and intergranular fracture is obvious, and many diamond particles appear along the crack. However, the fracture is nearly smooth without obvious diamond particle spalling, as shown in Figure 8(c). Therefore, NiAl/Fe-based alloys with 10 wt.% diamond have high compressive strength and excellent compression deformation.

(a)

(b)

(c)

(d)
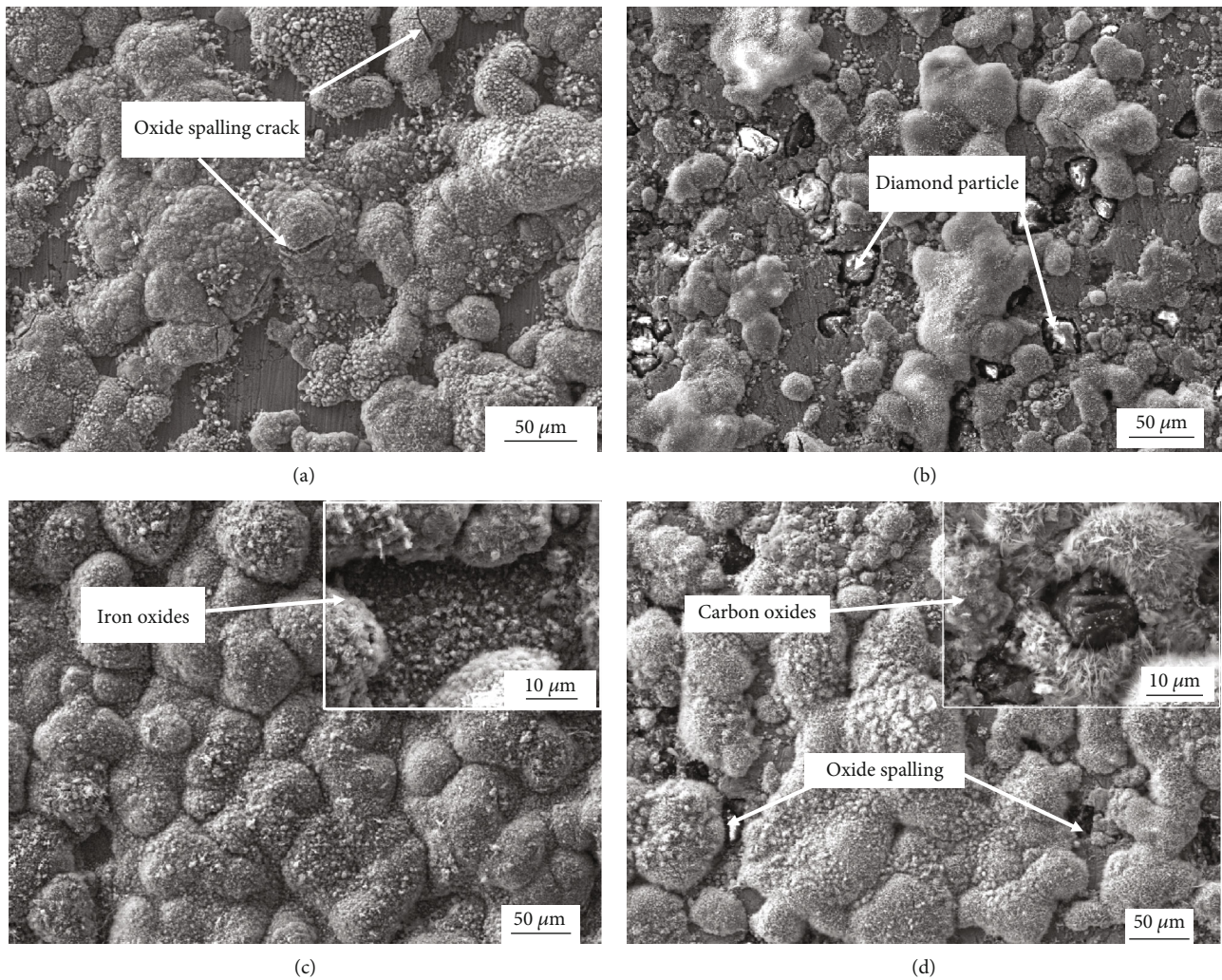
FIGURE 10: SEM images of NiAl/Fe-based alloy surface morphologies after oxidation for 25 h and 250 h: (a) NiAl/Fe-based alloys with 0 wt.% diamond—25 h; (b) NiAl/Fe-based alloys with 10 wt.% diamond—25 h; (c) NiAl/Fe-based alloys with 0 wt.% diamond—250 h; (d) NiAl/Fe-based alloys with 10 wt.% diamond—250 h.

Figure 9 shows the oxidation weight gain-oxidation time curve of NiAl/Fe-based alloys with 0 wt.% and 10 wt.% diamond after treatment at 600°C for 250 h. The oxidative weight gain of the NiAl/Fe-based alloys with 10 wt.% diamond becomes steady during the last oxidation stage (after 25 h). It can also be seen that the oxidation weight gain of NiAl/Fe-based alloys increases after 10 wt.% diamond addition. This is because graphitization of the diamond surface occurs during the oxidation test. According to the research results by Guo et al., both the shell of the iron atoms and the electrons of the diamond atoms can attract diamond atoms and gradually form graphite structures; therefore, it is concluded that iron accelerates the process of diamond graphitization [19]. This explanation is consistent with the XRD results shown in Figure 1.

Figure 10 shows SEM images of NiAl/Fe-based alloy surface morphologies after oxidation for 25 h and 250 h. From Figure 10(a), it is clear that the NiAl/Fe alloy surface oxide layer is basically formed after oxidation for 25 h, and cracks from oxidation spalling occurred in the area where the oxide layer is thick. During oxidation for 250 h, the nonoxidized areas are continuously oxidized, and the thicker areas continuously peel off, so a uniform oxide film on the sample surface is formed. The oxidation areas on the surface of the NiAl/Fe alloy are reduced with a 10 wt.% diamond addition, and a thick oxidation film around the diamond particles cannot be seen (as shown in Figure 10(b)). Obviously, the diamond addition reduces the oxidation degree of the alloy surface. From Figure 10(d), it can be seen that oxide spalling is present on the surface of the NiAl/Fe-based alloy with 10 wt.% diamond after the 250 h oxidation test. Compared with that of the NiAl/Fe-based alloy shown in Figure 10(c), the surface oxide layer of the NiAl/Fe-based alloy with 10 wt.% diamond is clearly looser.

Figure 11 shows the SEM image of the cross section of the iron-based alloys after the 25 h oxidation test. The

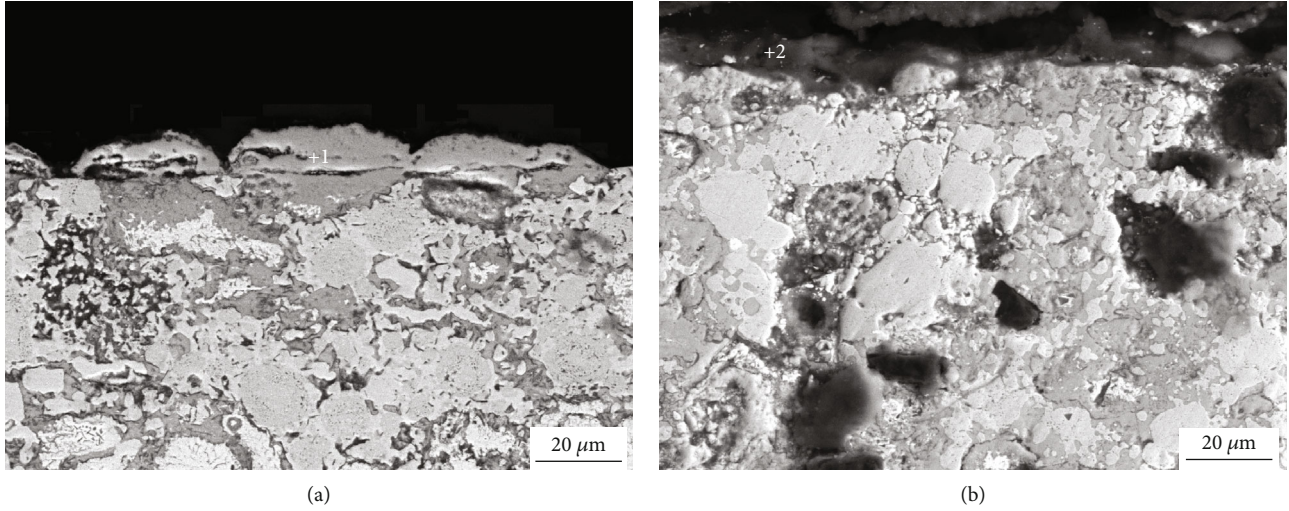Figure 11: Cross-section image of the oxide film of the NiAl/Fe-based alloy after oxidation for 25 h: (a) NiAl/Fe-based alloys with 0 wt.% diamond; (b) NiAl/Fe-based alloys with 10 wt.% diamond.

Table 2: Point analysis of the cross section of the oxide film of the NiAl/Fe-based alloy shown in Figure 11.

Points	Fe (wt.%)	Ni (wt.%)	Al (wt.%)	O (wt.%)
1	23.87	4.14	9.57	64.42
2	33.55	—	0.52	65.93

oxidation of the NiAl/Fe-based alloys with 0 wt.% diamond mainly occurs on the sample surface, while the internal oxidation of the sample is slight. When 10% diamond is added, both the sample surface and interior parts have different oxidation degrees, but the internal oxidation of the sample is particularly substantial. EDS analysis of the surface oxidation region was completed, and the results are shown in Table 2. The oxide film contains Fe, Ni, Al, and O when diamond addition is 0 wt.%. However, after adding 10 wt.% diamond, the Al content in the oxide layer is only 0.52%, the Ni element completely disappears, and the oxide film is almost entirely Fe oxides. The Ni-based oxides and Al-based oxides on the surface of NiAl/Fe-based alloys with 0 wt.% diamond can densify the oxide film on the surface of the alloy, which can hinder further oxidation. However, the oxidation of Al and Ni in the alloy is reduced or even eliminated after diamond is added. In addition, diamond also destroys the integrity of the oxide layer on the alloy surface. All these factors increase the oxidation inside the alloy.

Figures 12 and 13 show the element distribution of the cross section of the oxide film of the NiAl/Fe-based alloy with 0 wt.% diamond after oxidation for 250 h. Figure 12 shows that the oxides are mainly iron oxides. Further observation indicates that there is a small amount of alumina and iron oxides exist in alloy matrix. For the oxide film on the NiAl/Fe-based alloy with 10 wt.% diamond, the surface oxide layer is somewhat loose. It can be inferred from the element distribution in the cross section of the oxide film shown in Figure 13 that a substantial amount of Si is distributed in the oxide film because silicone phenolic plastics are the metallographic mosaic powder. It also shows a minor amount of iron oxides, and aluminium oxides appear in the surface layer. These results indicate that the oxide layer is relatively loose. This can explain why the NiAl/Fe-based alloy with 10 wt.% diamond has a higher oxidation weight gain.

The thermal conductivity of the NiAl/Fe alloy with different diamond contents with increasing temperature is shown in Figure 14. The thermal conductivity of the material increases substantially after diamond is added. As the diamond amount increases, the thermal conductivity of the material first increases and then decreases. When the content of diamond is 15 wt.%, the thermal conductivity of the material reaches its peak at each temperature, and the thermal conductivity is 53.2 W/(m·K) at 600℃. It is generally known that diamond is a natural material with the highest thermal conductivity among known materials (600-2200 W/m·K). Adding diamond to the matrix material can effectively improve the overall thermal conductivity of the material. However, with an increasing amount of diamond, the number of interface and sintering voids increases, so the electronic movement between crystals is hindered and the thermal conductivity of the material is reduced.

The addition of surface-pretreated diamond to NiAl/Fe-based alloys reduces the density and improves the thermal conductivity, but it slightly degrades the mechanical properties. Therefore, the densification of the material is further improved by hot isostatic pressing (HIP), and the overall mechanical properties and oxidation resistance of the material are further improved. Thus, low-density iron-based alloys with excellent mechanical properties, oxidation revsistance, and thermophysical properties can be obtained with this approach.
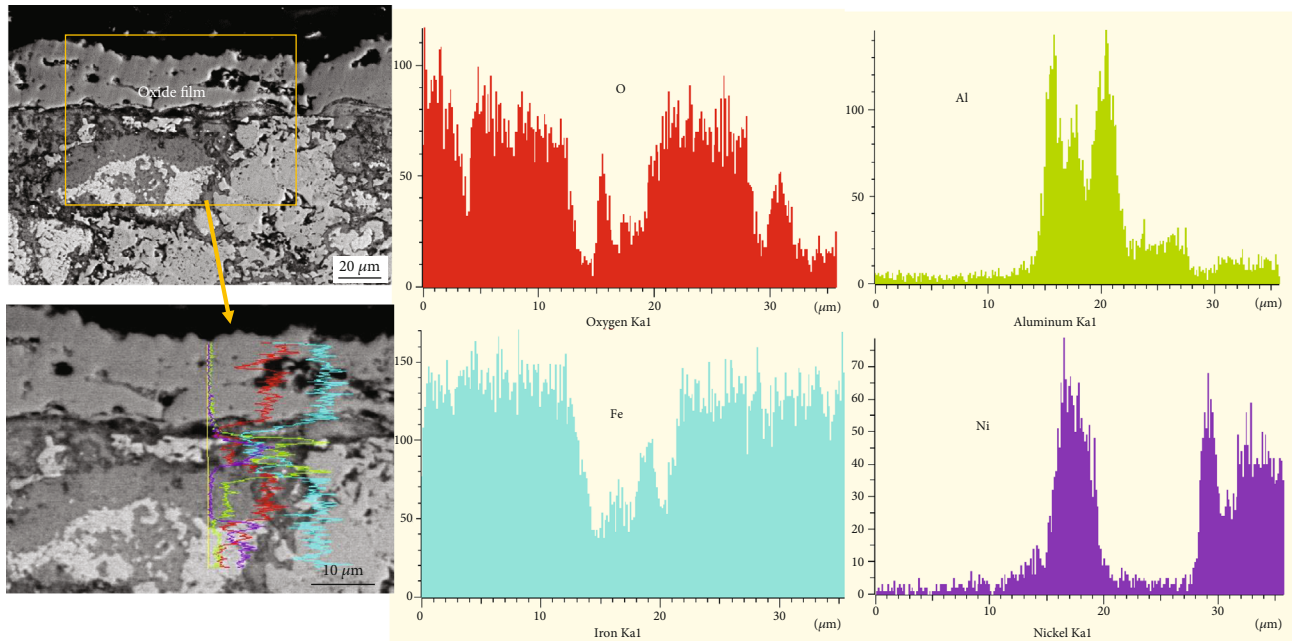
FIGURE 12: Element distribution in the cross section of the oxide film of the NiAl/Fe-based alloy with 0 wt.% diamond after oxidation for 250 h.
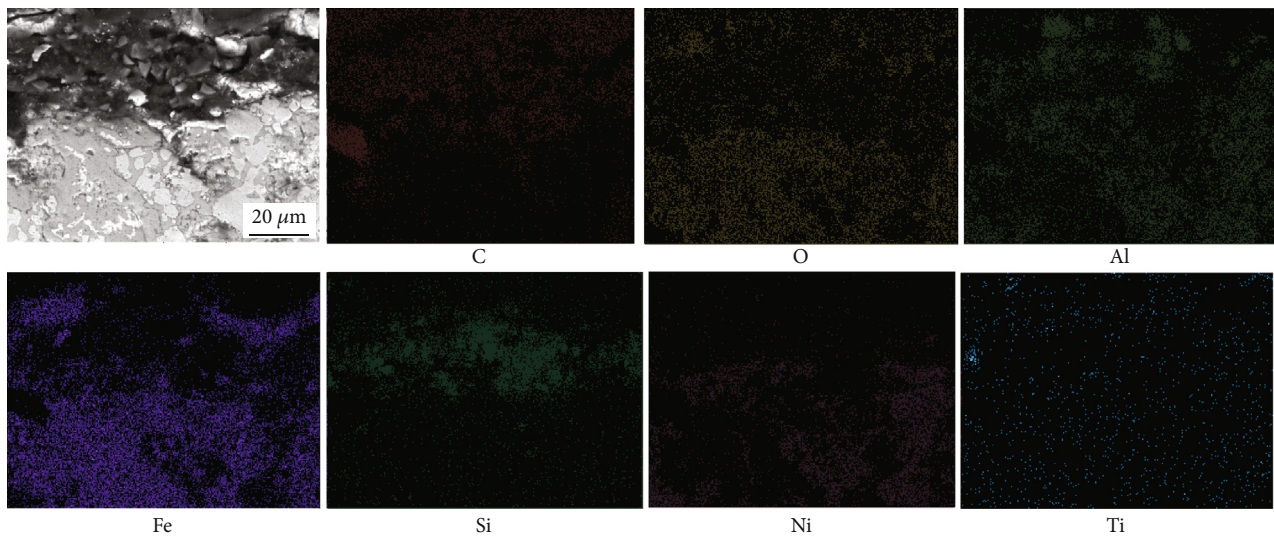
FIGURE 13: Element distribution in the cross section of the oxide film of the NiAl/Fe-based alloy with 10 wt.% diamond after oxidation for 250 h.

4. Conclusions

NiAl/Fe-based alloys with 0, 5, 10, 15, and 20 wt.% diamond-reinforced particles were prepared by hot-pressing sintering after the surface pretreatment of the diamond powders. From the microstructure, mechanical properties, oxidation resistance, and thermal conductivity analysis, the following conclusions can be summarized:

(1) A complete transition layer containing W existing outside diamond was gained after surface pretreat-ment of the diamond powders, which improved the interface bonding of the diamond grains and NiAl/Fe matrix to an acceptable level

(2) The compressive strength of NiAl/Fe-based alloys decreased after adding the pretreated diamond, but as the diamond addition increased, the alloy with 10 wt.% diamond obtained a higher compressive strength than that of other diamond contents

(3) After diamond addition, the corresponding oxidation resistance decreased because of the loose oxide layer
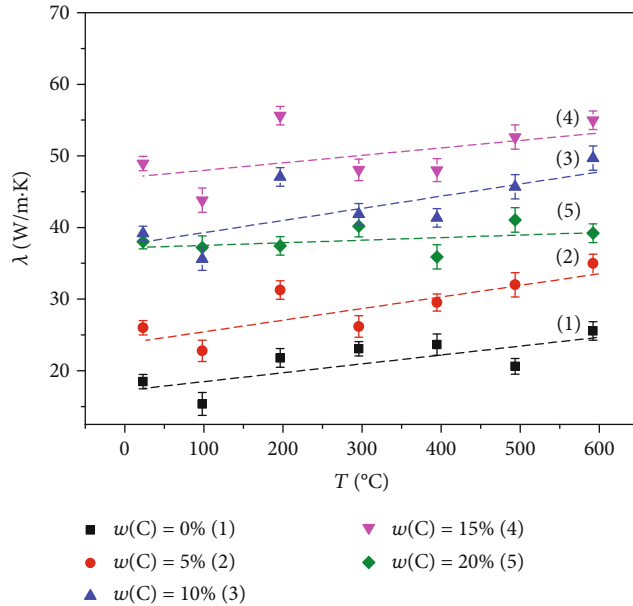
FIGURE 14: Thermal conductivity of NiAl/Fe alloy at different temperatures with diamond addition.

and diamond graphitization of the NiAl/Fe-based alloys

(4) The thermal conductivity of the alloy increased first and then decreased as the diamond content increased. When the diamond content was 15 wt.%, the thermal conductivity of the alloy reached the maximum value of 53.2 W/m·K at 600°C obtained in this study

Data Availability

The data used to support the findings of this study are included within the article.

Conflicts of Interest

The authors declare that they have no conflicts of interest.

Acknowledgments

References

[1] B. X. Zhao, D. W. Gao, J. Q. Shen et al., "Experiment and numerical analysis of temperature field of cylinder head based on a GW4D20 diesel engine," *SAE-China, FISITA (eds) Proceedings of the FISITA 2012 World Automotive Congress. Lec-*

ture Notes in Electrical Engineering, vol 190, , pp. 965–976, Springer, Berlin, Heidelberg, 2013.

[2] J. Y. Zhu, "Detection of cylinder pressure in diesel engines using cylinder head vibration and time series methods," *Journal of Marine Science and Application*, vol. 6, no. 4, pp. 8–12, 2007.

[3] M. Azadi, A. Mafi, M. Roozban, and F. Moghaddam, "Failure analysis of a cracked gasoline engine cylinder head," *Journal of Failure Analysis and Prevention*, vol. 12, no. 3, pp. 286–294, 2012.

[4] C. Barbosa, I. de Cerqueira Abud, T. S. Barros, and S. S. de Carvalho, "Microstructural analysis of the failure of a cast iron cylinder head of a thermoelectrical plant motor," *Journal of Failure Analysis and Prevention*, vol. 15, no. 3, pp. 424–429, 2015.

[5] S. Trampert, T. Göcmez, and F. J. Quadflieg, "Thermomechanical fatigue life prediction of cast iron cylinder heads," in *ASME Internal Combustion Engine Division Spring Technical Conference*, Aachen, Germany, May 2006.

[6] N. S. Prasad, N. Ganesh, and A. Kumarasamy, "Technologies for high power density diesel engines," *Defence Science Journal*, vol. 67, no. 4, p. 370, 2017.

[7] V. F. Bondareva, T. I. Kazantseva, and R. O. Krasnovskii, "Stress-strain state of a cylinder head of an internal combustion engine," *Strength of Materials*, vol. 13, no. 3, pp. 379–381, 1981.

[8] H. W. Song, G. Yu, J. S. Tan, and J. B. Di, "Intensity field design for pistons and cylinder heads in the laser induced thermal loading system," in *Computational Mechanics*, Springer Berlin Heidelberg, 2007.

[9] S. Knirsch, E. Ambos, and M. Todte, "Material and process development for cylinder heads of high-performance combustion engines," *MTZ Worldwide*, vol. 65, no. 4, pp. 14–16, 2004.

[10] M. Li, S. B. Qi, X. M. Chen, and C. H. Guo, "Experimental study on high temperature tensile properties of cast iron," *Modern Cast Iron*, vol. 3, pp. 84–88, 2017.

[11] M. X. Zhang, J. C. Pang, Y. Qiu, S. X. Li, M. Wang, and Z. F. Zhang, "Thermo-mechanical fatigue property and life prediction of vermicular graphite iron," *Materials Science & Engineering*, vol. 698, pp. 63–72, 2017.

[12] S. H. Kim, H. Kim, and N. J. Kim, "Brittle intermetallic compound makes ultrastrong low-density steel with large ductility," *Nature*, vol. 518, no. 7537, pp. 77–79, 2015.

[13] H. J. Cho, D. Yan, J. Tam, and U. Erb, "Effects of diamond particle size on the formation of copper matrix and the thermal transport properties in electrodeposited copper-diamond composite materials," *Journal of Alloys and Compounds*, vol. 791, pp. 1128–1137, 2019.

[14] J. M. Molina-Jordá, "Nano- and micro-/meso-scale engineered magnesium/diamond composites: novel materials for emerging challenges in thermal management," *Acta Materialia*, vol. 96, pp. 101–110, 2015.

[15] Y. Zhang, J. Li, L. Zhao, and X. Wang, "Optimisation of high thermal conductivity Al/diamond composites produced by gas pressure infiltration by controlling infiltration temperature and pressure," *Journal of Materials Science*, vol. 50, no. 2, pp. 688–696, 2015.

[16] J. Jia, S. Bai, D. Xiong, J. Wang, and J. Chang, "Effect of tungsten based coating characteristics on microstructure and thermal conductivity of diamond/Cu composites prepared by pressueless infiltration," *Ceramics International*, vol. 45, no. 8, pp. 10810–10818, 2019.

[17] A. V. Ukhina, D. V. Dudina, D. A. Samoshkin, E. N. Galashov, I. N. Skovorodin, and B. B. Bokhonov, "Effect of the surface modification of synthetic diamond with nickel or tungsten on the properties of copper–diamond composites," *Inorganic Materials*, vol. 54, no. 5, pp. 426–433, 2018.

[18] V. Buck, F. Deuerler, H. Kluwe, and B. Schmiler, "Influence of chemical pretreatment of hardmetal substrates for diamond deposition," *International Journal of Refractory Metals and Hard Materials*, vol. 20, no. 2, pp. 101–105, 2002.

[19] X. Guo, C. Zhai, Z. Jin, and D. Guo, "The study of diamond graphitization under the action of iron-based catalyst," *Journal of Mechanical Engineering*, vol. 51, no. 17, pp. 162–168, 2015.

WILEY | Hindawi

Research Article

Deposition and Properties of Amorphous TiBN/AlCrYN Multilayer Coatings with Various Modulation Periods

Wei Dai [ID]**, Fan Liu, and Qimin Wang** [ID]

School of Electromechanical Engineering, Guangdong University of Technology, Guangzhou 510006, China

Correspondence should be addressed to Wei Dai; popdw@126.com and Qimin Wang; qmwang@gdut.edu.cn

In this paper, multilayer coatings consisted of amorphous AlCrYN layers and TiBN layers were deposited by the cosputtering technique. The influence of the modulation period of the multilayer coatings on the structure, mechanical properties, and oxidation behavior of the coatings was studied carefully by using scanning electron microscope, X-ray diffraction, nanoindentation, scratch tester, and thermogravimetric analyzer. The results show that the TiBN/AlCrYN multilayer coatings exhibit an amorphous structure without any feature. Decreasing the modulation period could significantly improve the coating hardness and elastic modulus. In addition, the adhesion of the multilayer coatings could be enhanced as the modulation period decreases. At relative low oxidation temperature ($\leq 900°C$), a dense aluminum oxide layer formed on the coating surface can effectively hinder the inward diffusion of O and the outward diffusion of metal elements. The oxidation behaviors of the TiBN/AlCrYN multilayer coatings obeyed the diffusion control law. The oxidation resistance of the coatings was increasing with decreasing the modulation period since the interfaces of multilayer structures would block the diffusion of elements. At relative high oxidation temperature ($1000°C$), however, the coating surface was rapidly oxidized into the porous TiO_2 whiskers rather than the dense Al_2O_3 layer, resulting in the inward diffusion of O and thus causing the serious oxidation of the coatings.

1. Introduction

Hard nitride coatings deposited by physical vapor deposition (PVD) are widely used as protective coatings in many applications, such as the protection of cutting tools and molds due to their high hardness and wear resistance [1–3]. However, the thermal stability, toughness, and adhesion of the hard nitride coatings are still strong challenges for the increasing industrial applications especially under extreme conditions, e.g., high temperature [4]. Unfortunately, the PVD hard nitride coatings usually present columnar growth structures where oxygen is able to diffuse into the coatings while metal elements diffuse towards the coating surface through the columnar grain boundary, resulting in serious oxidation of the PVD coatings [5]. In addition, some unavoidable "through-thickness defects" like micropits and micropores in the PVD coatings can also provide channel for the diffusion of oxygen and thus enhance the oxidation of the coatings [5]. On the other hand, the hard coatings prepared by PVD process usually have high residual stress, causing

the poor adhesion to the substrate. Now, therefore, it is highly desirable to improve the oxidation resistance and adhesion of the PVD coatings.

Amorphous phase usually possesses the smooth dense structure without grain boundaries, which would effectively avoid boundary diffusion. On the other hand, multilayered architectural structures have been demonstrated to significantly enhance the mechanical properties and oxidation resistance of the PVD coatings [6, 7]. The interfaces among heterolayers can effectively restrain the crack growth and block the diffusion of oxygen and other media corrosion across the PVD coatings and thus improve the oxidation resistance, corrosion resistance, and mechanical properties of PVD coatings [7]. Accordingly, it is supposed that combining the multilayered architectural structure with the amorphous phase structure can significantly improve the oxidation resistance of the hard PVD coatings.

Previous literature reports that AlCrYN coatings exhibit high oxidation resistance at high temperature due to the formation of compact oxide layer on the surface [8]. In this

paper, multilayer coatings consisted of amorphous AlCrYN layers and TiBN layers were deposited by the cosputtering technique. The influence of the modulation period of the multilayer coatings on the structure, mechanical properties, and oxidation behavior was studied carefully. Furthermore, the relationships between the deposition process, microstructure, and properties of the coatings were discussed carefully.

2. Experimental Details

A direct current magnetron cosputtering deposition system composed of two independent magnetron sputtering units was employed to prepare the TiBN/AlCrYN multilayer coatings. Pure TiB_2 (99.95%, Ti : B = 33 : 67 at.%) and AlCrY (99.97%, Al : Cr : Y = 67 : 30 : 3 at.%) rectangular planar with the length of 50 mm and width of 480 mm were used as the sputtering targets. Polished cemented carbide (WC with 6 wt.% Co, mirror polish) and polycrystalline alumina wafers were used as the substrates for the characterization of mechanical properties and the high temperature oxidation test, respectively. All the substrates were cleaned each sequentially by using ultrasonic baths of acetone and alcohol for 20 minutes. The based pressure in the vacuum chamber was below 5×10^{-3} Pa. Ar glow discharge cleaning with -650 V applied on the substrate holder was taken for 3 minutes to remove the impurities and oxide on the substrate surface before deposition. During coating process, a gas mixture of Ar and N_2 (Ar/N_2 = 1 : 1) with 100 sccm was input into the chamber. The deposition pressure was kept around 0.6 Pa. The sputtering powers of the TiB_2 target and AlCrY target were maintained at 2 kW. The bias voltage of -100 V was applied on the substrate. The deposition temperature was about 350°C. The total deposition duration was 4 hours, and the thicknesses of all coatings were kept around 1.2 μm. The distances are approximately 50 mm between the sputtering targets and the substrate holder. The substrate holders were placed on a central rotary table. The modulation period of the multilayered TiBN/AlCrYN coatings was adjusted by varying the rotation speed of the central rotary table from 0.5 rpm to 3 rpm.

The growth morphologies of the coatings were observed by scanning electron microscopy (SEM, FEI, Nano430) with an operating voltage of 10 kV. The phase structure of the as-deposited coatings was characterized by X-ray diffraction (XRD, Bruker D8 Advance diffractometer, CuKα). The scanning angle of the 2θ ranged from 20° to 80° with a step width 0.02° at a speed of 2°/min. The coating hardness and elastic modulus were measured using a nanoindentation tester (CSM, TTX-NHT) with a Berkovich diamond indenter under the constant load of 5 mN. The indentation depth was controlled to about 10% of the coating thickness to minimize the effect of the substrate. The scratch test was performed by a Nano Scratch Tester (CSM, Revetest scratch tester) using Rockwell C diamond styli with a radius 200 μm to evaluate the adhesion strength of the coatings. The scratch length was 3 mm, along with the normal load increased from 1 N to 100 N with a scratch speed of 6 mm/min. The scratch morphologies of the scratch tracks were performed by an optical microscope. A thermal gravi-

metric (TG) analyzer (Setsys TMA, France) was used to investigate the oxidation behavior of the as-deposited coatings which were heated up to 800°C, 900°C, and 1000°C in oxygen atmosphere with a heating rate of 10°C/min for two hours. The samples for the TG test were deposited on the polycrystalline alumina substrates. The surface morphology and composition of the coatings after the oxidation test were investigated by SEM and energy-dispersive X-ray detector (EDS, FEI, Nano430) with an operating voltage of 20 kV and emission current of 10 μA.

3. Results and Discussion

Figure 1(a) shows the typical cross-sectional morphology of the TiBN/AlCrYN multilayer coating deposited with the rotation speed of 2 rpm. It can be seen that the coating shows dense and smooth glass-like morphology without any feature. The corresponding XRD diffractogram (Figure 1(b)) illustrates that there are no diffraction peaks attributed to the coating, which also confirm the amorphous structure of the coating. The formation of the amorphous structure might be related to the low modulation period of the coatings. The coating modulation period calculated through dividing the total coating thickness by the rotation numbers of the central rotary table decreases from 12 nm to 2 nm as the rotation speed of table increases from 0.5 rpm to 3 rpm. This means that the individual layers (both TiBN layers and AlCrYN layers) are very thin and hard to crystallize since the multilayered structure would inhibit the growth of the crystalline grains.

Figure 2 exhibits the hardness and elastic modulus of the coatings deposited with various the rotation speeds of the substrate holder table. It can be seen that the hardness of the coatings increases from 16 GPa to 22 GPa as the rotation speed of table increases from 0.5 rpm to 3 rpm. It is reported that decreasing the thicknesses of the individual layers in the multilayered structure system would enhance the coating hardness due to the complex effects of interface structures among heterolayers [9]. Additionally, decreasing the modulation period could effectively refine the microstructure of the coating components and thus improve significantly the coating mechanical properties.

Figure 3 exhibits the typical scratch morphologies of the TiBN/AlCrYN multilayer coating deposited with different rotation speeds of table. The coating deposited with 0.5 rpm shows a relatively low critical load of about 31.4 N. It should be noted that cracking and fragmentation occur prior to the onset of substrate exposure. The appearances of cracking and fragmentation might be attributed to the severe plastic deformation of the substrate under high load. The brittle hard coating cannot adapt to the deformation and thus tends to crack when being depressed into the substrate. Meanwhile, the fragmentations would peel off due to low adhesive strength of the coating/substrate. As the modulation period of the coatings decreases (the rotation speed of table increases), however, the critical load increases significantly. The critical load of the TiBN/AlCrYN multilayer coating increases to 72.1 N when the rotation speed of table increases to 3 rpm. Although the cracks also appeared before the onset
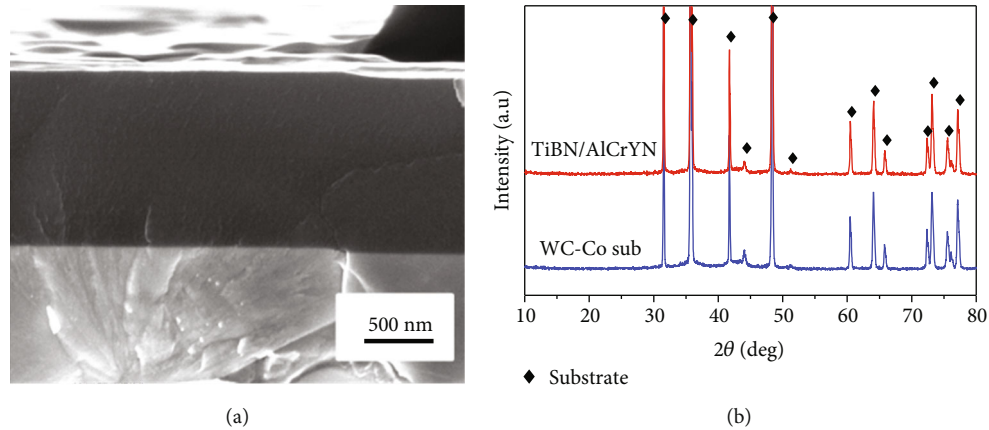
(a)

(b)

FIGURE 1: (a) Typical cross-sectional SEM image and (b) XRD pattern of the coating deposited with the rotation speed of 2 rpm.
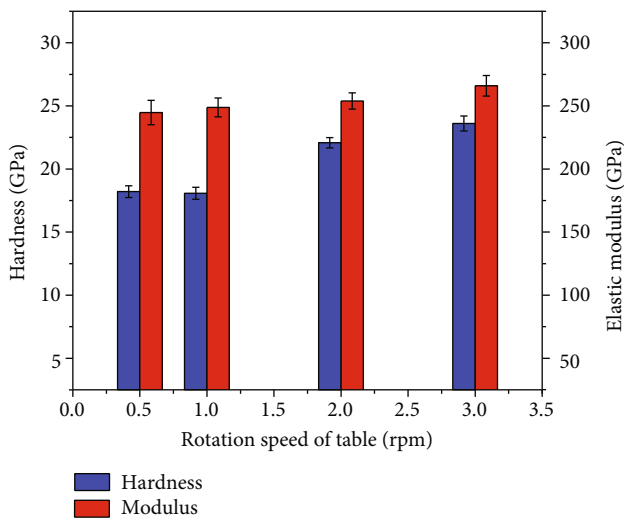

FIGURE 2: Hardness and elastic modulus of the TiBN/AlCrYN multilayer coatings with various rotation speeds of table.

of substrate exposure, they became very small and no fragmentation was observed to peel from the substrate, implying the good scratch resistance and high adhesion strength of the coatings.

The enhancement of the scratch resistance of the coatings might be ascribed to the multilayered structure where the interfaces between TiBN/AlCrYN layers can effectively prevent the propagation and extension of cracks and thus greatly improve the toughness of the TiBN/AlCrYN multilayer coatings [10]. Additionally, according to the results of nanoindention (Figure 2), the hardness/elastic modulus ratio (H/E) of the coatings increases from 0.07 to 0.09 as the rotation speed of table increases from 0.5 rpm to 3 rpm. Usually, the H/E is expected to correlate with the elastic resilience and a high H/E implies that the coating has a high elastic strain prior to the plastic deformation [11]. It is clear that the high H/E value is beneficial to the scratch resistance. As a result, the scratch resistance of the TiBN/AlCrYN multilayer coatings increases as the modulation period decreases (the rotation speed of table increases). Furthermore, the multilay-

ered structure is also believed to effectively reduce residual stress and then enhance the coating adhesion.

The oxidation behaviors of the coatings were performed by TG as shown in Figure 4. Figure 4(a) presents the typical TG curve of the coating deposited with 0.5 rpm. The mass gain of the coating increases slightly with the temperature at initial stage of heating (200°C~800°C), followed by a significant increase of the mass gain at the temperatures of about 800°C. However, the mass gain of the coating shows a significant decrease when the temperature exceeds 1000°C. In order to insight into the oxidation behaviors of the coatings, isothermal TG of the TiBN/AlCrYN multilayer coatings with different modulation periods was taken at temperatures of 800°C, 900°C, and 1000°C. Figures 4(b)–4(d) exhibit the mass grains of the coatings as a function of the oxidation time. It can be seen that the mass grains of all the samples increase with the oxidation time at all temperatures, but the shapes of the curves are different. Under the oxidation temperatures of 800°C (Figure 4(b)) and 900°C (Figure 4(c)), the mass gains of the coatings increase slowly and exhibit parabolic oxidation curves. However, the mass gain curves of the coatings could be divided into two different parts when the oxidation temperature increases to 1000°C (Figure 4(d)). At initial stage (<20 min), the mass gain of the coating increases rapidly and occurs linearly. Subsequently, the mass gains of the coatings exhibit parabolic rate. It should be noted that the mass gains of the coatings decrease as the modulation period of the coatings decreases (the rotation speed of table increases) at certain oxidation time.

The parabolic oxidation rate has been expected to follow diffusion control law which can be expressed by the equation of $(\Delta m/A)^2 = kt + c$, where the Δm is the mass change, t is time, A is the surface area of the sample, and k and c are the parabolic rate constant and constant, respectively [12]. Figure 5 presents the curves of $(\Delta m/A)^2$ versus t and the fitted straight lines for the date points. The coefficient values of determination (R^2) which indicate the goodness of fit and k values are also included in the figures. It can be seen that the R^2 values of all the samples are almost higher than 0.99 at 800°C and 900°C, indicating that all curves accord with the parabolic law. This illustrates that the oxidation reaction of
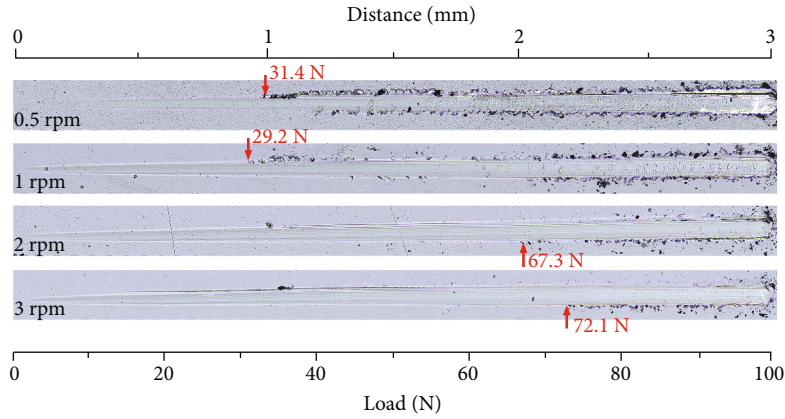
FIGURE 3: Scratch morphologies of the TiBN/AlCrYN multilayer coatings deposited with different the rotation speeds of table.

(a)

(b)

(c)

(d)
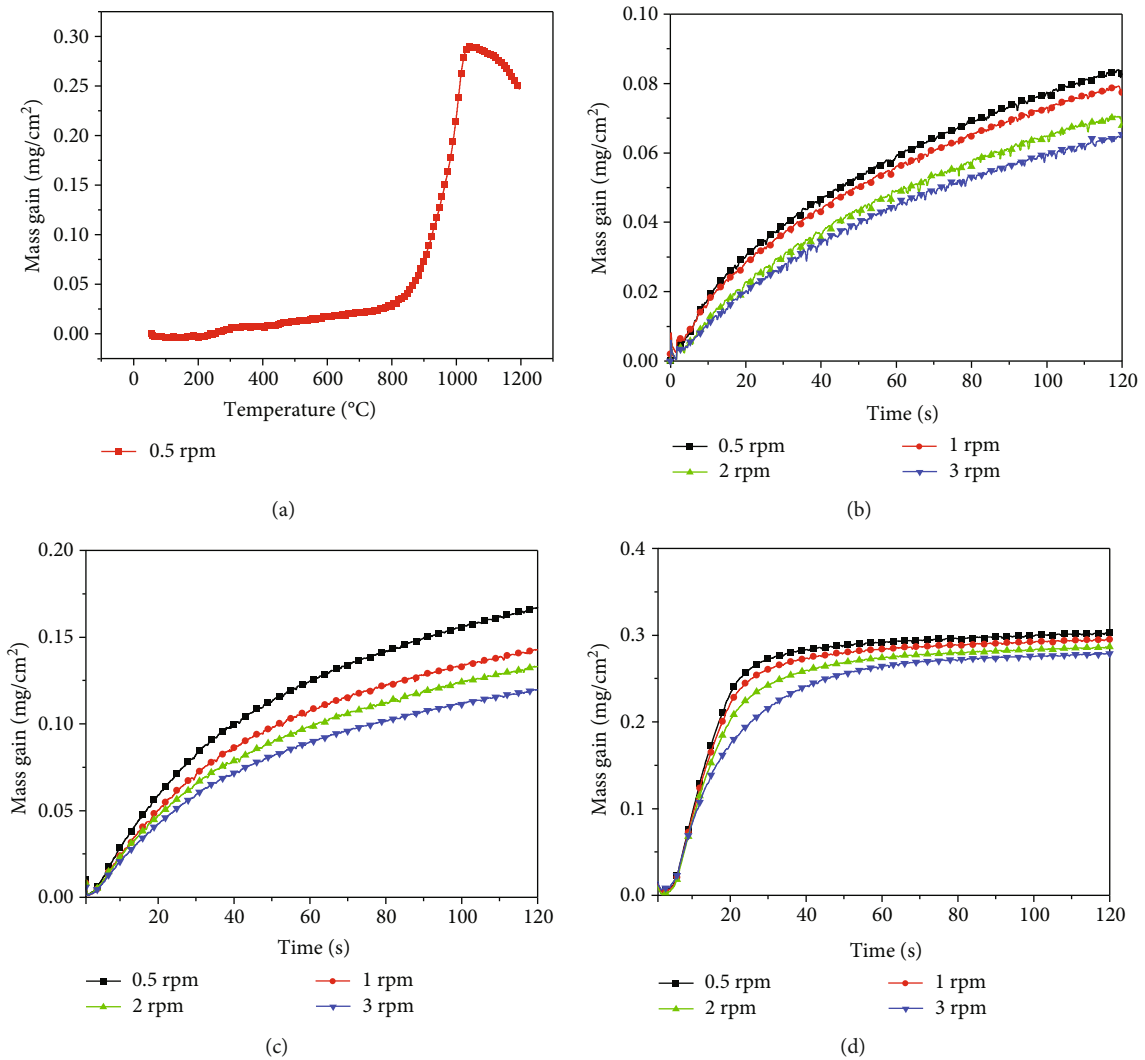
FIGURE 4: (a) Typical thermogravimetric (TG) curve of the coating deposited with 0.5 rpm and TG curves of the coatings during isothermal oxidation at (b) 800°C, (c) 900°C, and (d) 1000°C.

the TiBN/AlCrYN multilayer coatings was controlled by diffusion process at relatively low temperature (≤900°C). It should be noted that k values at 900°C are higher than that at 800°C, since the oxidation rate increases with temperature. Furthermore, the k value decreases significantly as the rotation speed of table increases. In addition, the activation
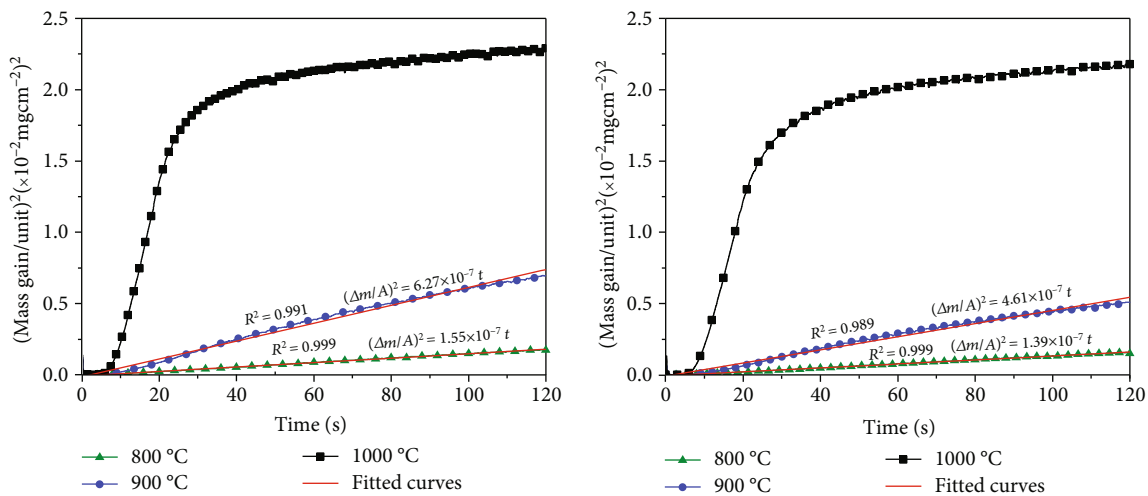
(a)

(b)
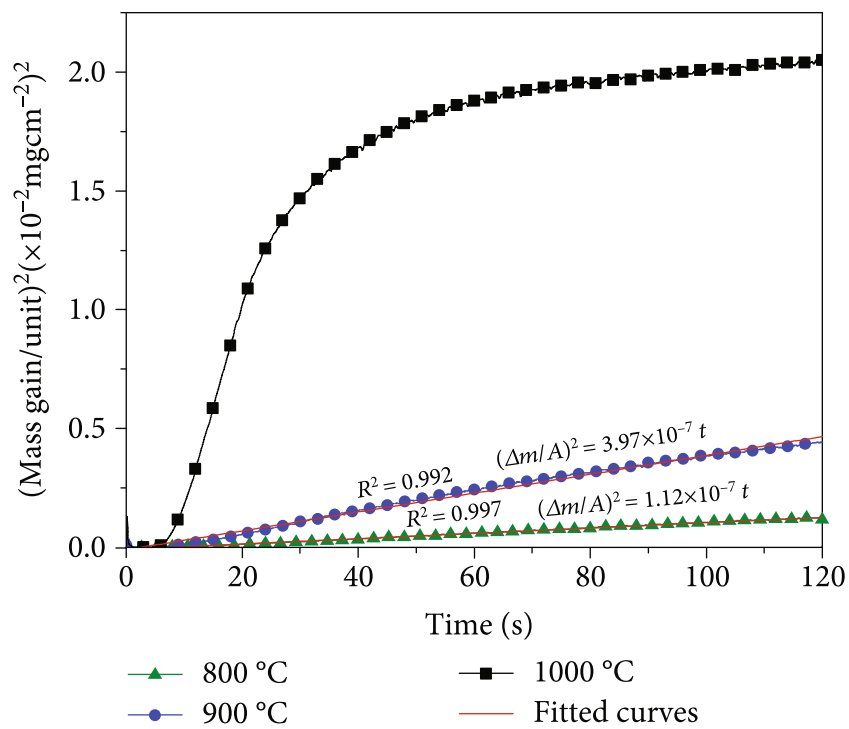
(c)

FIGURE 5: Continued.

(d)
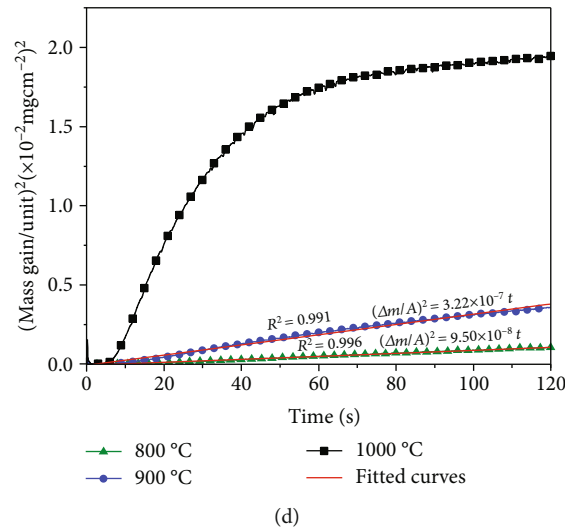
FIGURE 5: Plots of $(\Delta m/A)^2$ versus time for the TiBN/AlCrYN coatings with different rotation speeds of (a) 0.5 rpm, (b) 1 rpm, (c) 2 rpm, and (d) 3 rpm between 800°C and 1000°C. The best-fitting straight lines are given with the coefficient of determination R^2 in the plots.

(a)

(b)

(c)

(d)
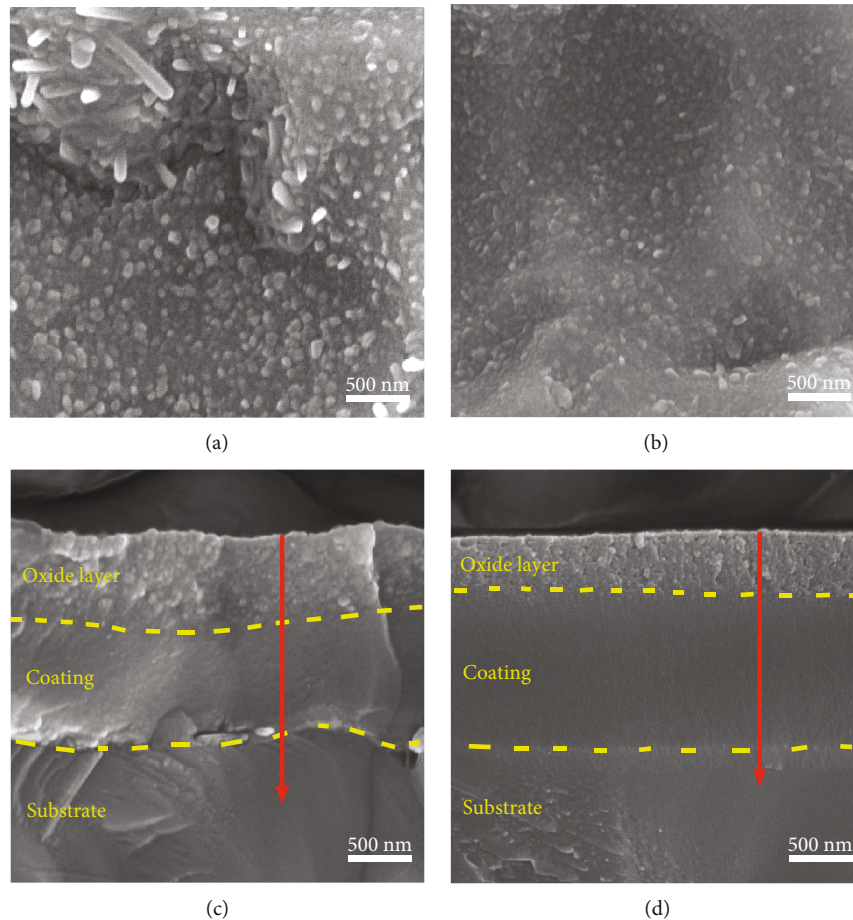
FIGURE 6: Typical surface and cross-sectional morphologies for the TiBN/AlCrYN multilayer coatings deposited with the rotation speeds of 0.5 rpm (a, c) and 2 rpm (b, d) after oxidation at 900°C.

energy for oxidation of the coatings calculated according to the Arrhenius equation increases from about $125\,kJ\,mol^{-1}$ to $185\,kJ\,mol^{-1}$ [12]. This indicates that decreasing the mod-

ulation period of the coatings would enhance the coating oxidation resistance. However, it can be seen that the oxidation behavior does not follow the parabolic law and the
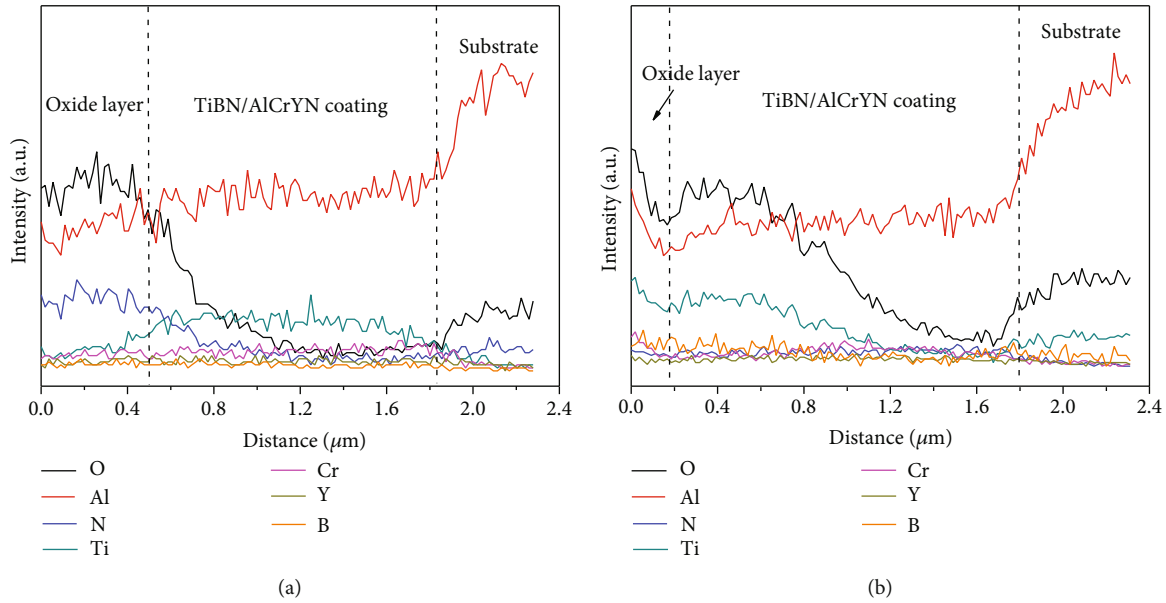
FIGURE 7: (a, b) The corresponding EDS line-scanning profiles along the red arrows shown in Figures 6(c) and 6(d), respectively.

coating exhibits the high oxidation rate when the oxidation temperature is 1000°C.

The typical surface topographies and cross-sectional morphologies of the coatings deposited with 0.5 rpm and 2 rpm after oxidation at 900°C are shown in Figure 6. It can be seen that the coating deposited with 0.5 rpm (Figure 6(a)) shows numerous granular and rod-like features on the surface. The corresponding cross-sectional SEM image reveals that a dense oxidation layer with a thickness of about 500 nm appears on the surface of the coating. As the rotation speed of table increases to 2 rpm, the coating shows a significant decrease on the size and quantity of the granular features on the surface. And the thickness of the oxidation layer decreases to about 200 nm. This also proves that the coating with the relative low modulation period shows a high oxidation resistance. It is supposed that the interfaces of multilayer structure would block the diffusions and thus enhance the oxidation resistance of the coatings. The EDS line-scanning profiles along with the coating thickness (red arrows in Figures 6(c) and 6(d)) are presented in Figure 7. It can be seen that the oxide layers on the coating surfaces mainly contain Al and O, implying that the oxide layer is consisted of aluminum oxides. The dense aluminum oxide layer could effectively hinder the inward diffusion of O and the outward diffusion of metal elements [13]. Accordingly, the oxidation behavior of coatings obeys the diffusion control law at the oxidation temperature of 900°C.

Figure 8 gives the oxidation morphologies of the coating deposited with 0.5 rpm at the oxidation temperature of 1000°C. It can be seen that numerous sharp whiskers that can be ascribed to TiO_2 are observed on the coating surface, implying oxidizing quickly of the coating in the initial stage of oxidation. The EDS line-scanning profiles (Figure 8(d)) along with the coating thickness (red arrow in Figure 8(c)) illustrate that oxygen exists throughout the coating, indicating that the coating was almost completely oxidized. The

coating thickness after oxidation also increased greatly due to the volume expansion of oxide. The cross-sectional image of the coating reveals that the oxide layer is consisted of two layers (Figure 8(c)). The layer on the top is the porous whiskers, followed by a dense oxide layer. According to the results above, the mass gain curve of the coating at the oxidation temperature of 1000°C (Figure 4(d)) can be divided into two different parts. In the initial stage of oxidation, the surface layer was oxidized rapidly into the porous TiO_2 whiskers due to the high oxidation temperature (1000°C). The TiO_2 porous whiskers hinder the formation of the dense oxide layer and allow the inward diffusion of O. As a result, the coatings showed a high oxidation rate at initial stage (<20 min) of the isothermal oxidation test (as shown in Figure 4(d)). Subsequently, the dense oxide layer was formed in the coatings, which could act as a barrier layer and block the element diffusion. Accordingly, the mass gains of the coatings exhibit parabolic rate after the initial stage.

4. Conclusions

Amorphous TiBN/AlCrYN multilayer coatings with different modulation periods were deposited by the cosputtering technique through varying the rotation speed of table. The effect of the modulation period on the structure, mechanical properties, and oxidation behavior of the coatings was studied carefully. It is found that the amorphous TiBN/AlCrYN multilayer coatings exhibit the glass-like morphology without any feature. The hardness and adhesion of the coatings could be greatly improved via decreasing the modulation period. The multilayer coatings show the high oxidation resistances at relative low oxidation temperature (≤900°C). The enhancement of the oxidation resistance could be attributed to the formation of the dense aluminum oxide layer which can effectively hinder the diffusion of elements, causing the oxidation behavior of coatings to follow the diffusion

(a)

(b)

(d)

(c)
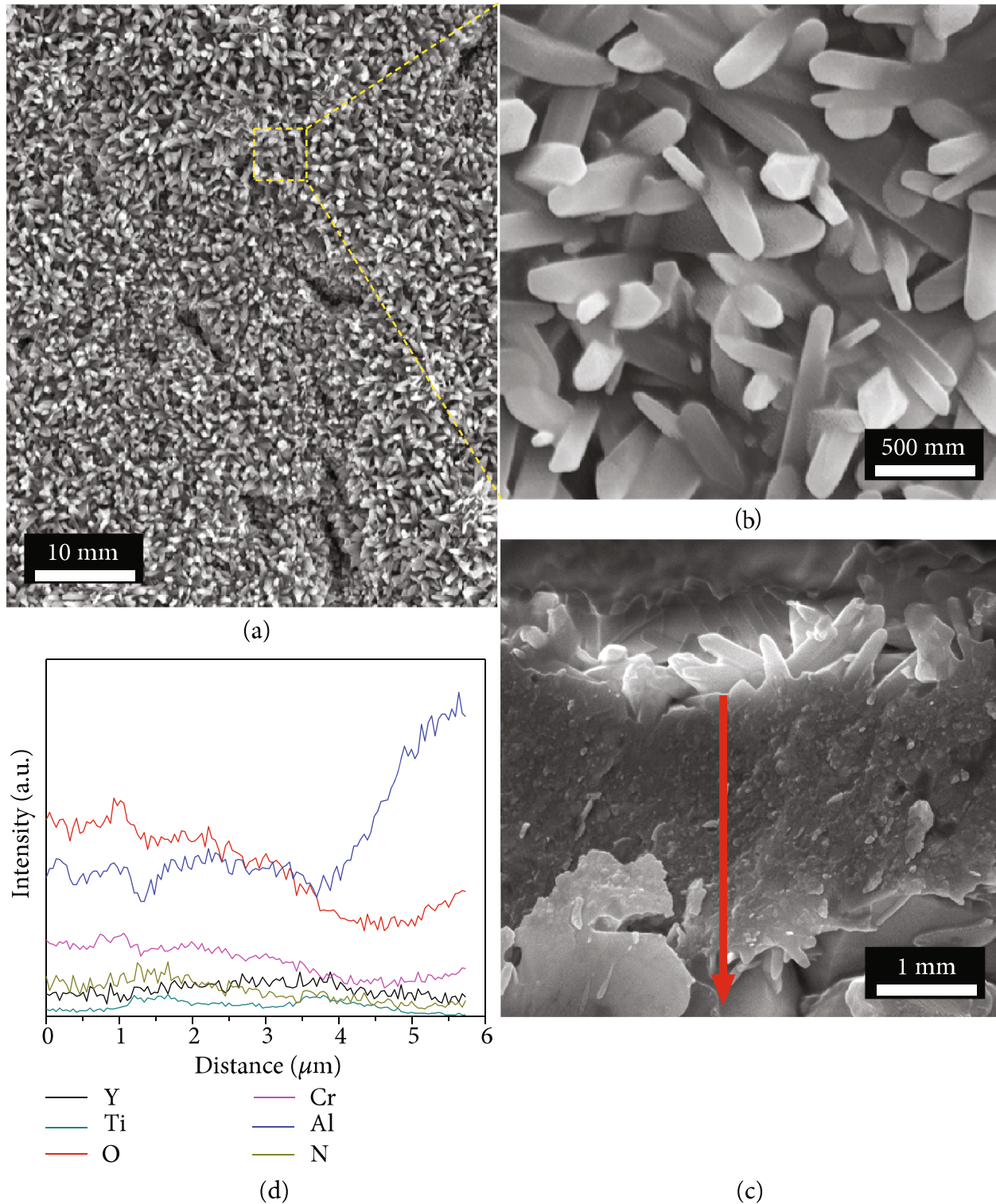
FIGURE 8: (a) Surface morphology, (b) enlarged view of (a), (c) cross-sectional morphology, and (d) the corresponding EDS line-scanning profiles along the red arrow shown in (c) of the TiBN/AlCrYN multilayer coating deposited with the rotation speeds of 0.5 rpm after oxidation at 1000°C.

control law. However, as the oxidation temperature increases further (1000°C), the coating surface would be rapidly oxidized into the porous TiO_2 whiskers, which prevented the formation of the dense oxide layer and allowed the inward

diffusion of O, resulting in a serious oxidation of the coatings. Decreasing the modulation period could be conducive to improving the coating oxidation resistance since the interfaces of multilayer structure would block the diffusions.

Data Availability

Conflicts of Interest

The authors declare that they have no conflicts of interest.

Acknowledgments

References

[1] K. Bobzin, "High-performance coatings for cutting tools," *CIRP Journal of Manufacturing Science and Technology*, vol. 18, pp. 1–9, 2017.

[2] A. Inspektor and P. A. Salvador, "Architecture of PVD coatings for metalcutting applications: a review," *Surface and Coating Technology*, vol. 257, pp. 138–153, 2014.

[3] M. Tkadletz, N. Schalk, R. Daniel, J. Keckes, C. Czettl, and C. Mitterer, "Advanced characterization methods for wear resistant hard coatings: a review on recent progress," *Surface and Coating Technology*, vol. 285, pp. 31–46, 2016.

[4] J. Musil, "Hard nanocomposite coatings: Thermal stability, oxidation resistance and toughness," *Surface and Coatings Technology*, vol. 207, pp. 50–65, 2012.

[5] P. Panjan, M. Cekada, M. Panjan et al., "Surface density of growth defects in different PVD hard coatings prepared by sputtering," *Vacuum*, vol. 86, p. 794, 2012.

[6] B. Xiao, H. Li, H. Mei et al., "A study of oxidation behavior of AlTiN- and AlCrN-based multilayer coatings," *Surface and Coating Technology*, vol. 333, pp. 229–237, 2018.

[7] W. Dai, Q. Wang, K. H. Kim, and S. H. Kwon, "Al_2O_3/CrAlSiN multilayer coating deposited using hybrid magnetron sputtering and atomic layer deposition," *Ceramics International*, vol. 45, no. 9, pp. 11335–11341, 2019.

[8] T. C. Rojas, S. Dominguez-Meister, M. Brizuela, and J. C. Sanchez-Lopez, "Influence of Al and Y content on the oxidation resistance of CrAlYN protective coatings for high temperature applications: new insights about the Y role," *Journal of Alloys and Compounds*, vol. 773, pp. 1172–1181, 2019.

[9] Y. X. Wang and S. Zhang, "Toward hard yet tough ceramic coatings," *Surface and Coating Technology*, vol. 258, pp. 1–16, 2014.

[10] N. J. M. Carvalho and J. T. M. De Hosson, "Deformation mechanisms in TiN/(Ti,Al)N multilayers under depth-sensing indentation," *Acta Materialia*, vol. 54, no. 7, pp. 1857–1862, 2006.

[11] C. A. Charitidis, "Nanomechanical and nanotribological properties of carbon-based thin films: a review," *International Journal of Refractory Metals and Hard Materials*, vol. 28, no. 1, pp. 51–70, 2010.

[12] Y. Ding, T. Hussain, and D. G. McCartney, "High-temperature oxidation of HVOF thermally sprayed NiCr-Cr_3C_2 coatings: microstructure and kinetics," *Journal of Materials Science*, vol. 50, no. 20, pp. 6808–6821, 2015.

[13] X. Y. Xu, H. Riedl, D. Holec, L. Chen, Y. Du, and P. H. Mayrhofer, "Thermal stability and oxidation resistance of sputtered Ti Al Cr N hard coatings," *Surface and Coatings Technology*, vol. 324, pp. 48–56, 2017.

WILEY | Hindawi

Research Article

Wear Behavior of the Multiheterostructured AZ91 Mg Alloy Prepared by ECAP and Aging

Bingqian Xu,[1] Jiapeng Sun ⬤,[1] Zhenquan Yang,[1] Jing Han,[2] Dan Song,[1] Jinghua Jiang,[1] and Aibin Ma ⬤[1]

[1]*College of Mechanics and Materials, Hohai University, Nanjing 210098, China*
[2]*School of Mechanical and Electrical Engineering, China University of Mining and Technology, Xuzhou, 221116 Jiangsu Province, China*

Correspondence should be addressed to Jiapeng Sun; sunpengp@hhu.edu.cn and Aibin Ma; aibin-ma@hhu.edu.cn

The microstructure design based on the development of heterostructure provides a new way for high strength and ductility Mg alloys. However, the wear property, as an important service performance, of Mg alloys with heterostructure is scarcely investigated. In this work, a high strength and ductility AZ91 Mg alloy with multiheterostructure was prepared *via* a processing route combined industrial-scale equal channel angular pressing (ECAP) and aging. The multiheterostructure consists of the heterogeneous grain structure and heterogeneous precipitates. The dry sliding wear behavior of this multiheterostructured (MH) alloy is investigated compared to the as-cast alloy. The impacts of the applied load and duration time on the wear volume and coefficient of friction (COF) are analyzed, and the wear mechanism is further discussed. The result indicates that although the MH alloy exhibits high-desirable strength-ductility synergy, it shows a poorer wear resistance but a relatively lower COF compared to the as-cast alloy at the present condition. The wear mechanism of both alloys mainly involves abrasive wear, as well as mild adhesion, delamination, and oxidation. In comparison, the MH alloy shows relatively severe adhesion, delamination, and oxidation. The poor wear resistance of the MH alloy at the present dry sliding wear condition is linked to the abundant grain boundaries and fine precipitates. Therefore, one should reasonably use the MH Mg alloy considering the service conditions to seek advantages and avoid disadvantages.

1. Introduction

According to the need for lightweight of the structural materials, magnesium (Mg) alloys, as the lightest structural metallic materials, are widely applied in the automobile, aerospace, biomedicine application, and electronics industries [1–5]. Moreover, profiting from all kinds of processing methods, numerous high strength Mg alloys have been produced in the laboratory and even some Mg alloys have been commercialized, such as Mg-Al-Zn (AZ)-typed alloys and Mg-Zn-Zr (ZK)-typed alloys [6–9]. However, the absolute strength and ductility of Mg alloys at room temperature are still much lower than that of Al alloys, Ti alloys, and steels, which restrict their widespread commercial applications. Therefore, great effort has been made to enhance the mechanical properties of the Mg alloys in the last few decades [10–13].

Due to the well-known Hall-Petch law, the ultrafine/nano-grained Mg alloys are intensely pursued to address the issues of poor strength and ductility [14–19]. In recent years, the microstructure design based on the development of the heterostructure provides a new way for the high-performance materials [20–23]. Many studies indicate that the heterostructure brings into much higher strength and ductility in several Mg alloys than the generally developed ultrafine grain structure [24, 25]. For example, Ramezani et al. [26] developed a GWZ Mg-8.1Gd-4.3Y-1.6Zn-0.4Zr (wt. %) alloy with fine-grained bimodal microstructures *via* multiaxial forging. The forged alloy exhibited an excellent ultimate tensile strength

(UTS) and ductility of 581 MPa and 15.9%, respectively. Jiang et al. [27] processed a heterogeneous Mg–1Gd/Mg–13Gd alloy laminate *via* accumulative extrusion bonding (AEB), whose strength and ductility were much superior to that of the individual component material. Wu et al. [28] demonstrated that the bimodal structure brought into high strength in the Mg-15Gd-1Zn-0.4Zr (wt. %) alloys. Xu et al. [29] prepared a bimodal-structured Mg-8.2Gd-3.8Y-1Zn-0.4Zr (wt. %) alloy using hot extrusion and aging, which had a superior strength–ductility balance. In our previous work, the laboratory scale and industrial-scale multiheterostructured AZ91 alloys were prepared *via* the combined processing route of ECAP and aging [30–32]. The multiheterostructured AZ91 alloy exceeded the known strength and ductility limits of the AZ91 alloy.

Compared to the abundant investigation on the mechanical properties, the wear behavior of Mg alloys is scarcely investigated, so that we still cannot confirm whether these high-performance Mg alloys with heterostructure have excellent wear resistance. The present work aims to investigate the dry sliding wear behavior of a multiheterostructured AZ91 alloy produced by a processing route combined industrial-scale ECAP with aging. The impacts of the applied load and duration time on the wear volume and coefficient of friction (COF) were investigated, and the wear mechanism was further discussed.

2. Experimental Procedure

A commercial as-cast AZ91 alloy ingot with a nominal chemical composition of 9 wt. % Al, 1 wt. % Zn, and 0.5 wt. % Mn was used in this work. A combined processing route of industrial-scale ECAP with aging was used to prepare the multiheterostructure AZ91 alloy. The received AZ91 alloy was referred to as "AC alloy." The AC alloy was firstly homogenized at 420°C for 24 h followed by water quenching. Next, a homemade upscaled rotary die equal channel angular pressing (RD-ECAP) with four equal square channels (50 mm × 50 mm × 100 mm) was continually performed for 16 passes with a ram speed of 3.5 mm/s at a constant temperature of 350°C, followed by rapidly water cooling. Finally, the ECAPed samples were isothermally aged at 200°C for 15 h, where the peak hardness was obtained. More details on the processing route can be found in our previous work [30], and the resultant sample was designated as "MH alloy."

The wear test was performed by a ball-on-disc facility (MFT-3001 type-Lanzhou Huahui Instrument Technology Co., LTD., China), as illustrated in Figure 1. Before wear testing, the samples were ground to 800 grit SiC sandpapers and cleaned with ethanol. The roughness of the samples is *Ra* 0.31 μm. The Si_3N_4 ball with a diameter of 6 mm was used. All the tests were performed at a velocity of 300 r/min with a revolution radius of 2.5 cm. Since duration time (T) and applied load (L) have a great influence on wear behavior, different duration times ($T = 10 \text{ min}, 30 \text{ min}, \text{and } 90 \text{ min}$) and applied loads ($L = 4.9 \text{ N}, 9.8 \text{ N}, \text{and } 14.7 \text{ N}$) were chosen to reveal their effect on the wear behavior of the AC and MH alloys. When the duration time was varied, the constant applied load was 4.9 N. When the applied load was varied,
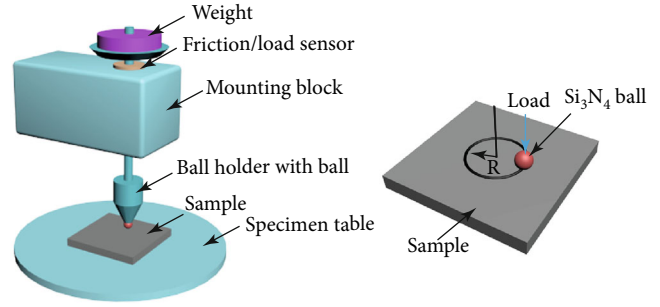
Figure 1: Schematic illustration of the ball-on-disc facility for the wear test.

the constant duration time was 30 min. For each state, at least two specimens were tested. After wear testing, the samples were ultrasonically cleaned with ethanol for 5-10 min and then stored in kerosene. The wear track was characterized by the surface profile meter (TIME3222 Beijing Time High Technology LTD, China). The wear volume was calculated according to the measured cross-section profiles, which was expressed as the product of the cross-sectional area and the length of the wear track. The micro-hardness of the samples was measured by an HXD-1000TC microhardness-testing instrument with a load of 4.9 N and a dwelling time of 15 s.

The microstructures were characterized by scanning electron microscopy with the secondary electron detector (SEM) equipped with an energy dispersive spectrometer (EDS) and electron backscattered diffraction (EBSD). For SEM observation, the samples were ground to 2000 grit SiC sandpaper successively, mechanically polished by a 1.5 μm diamond suspension, and then etched by a mixture solution of acetic acid, picric acid, ethanol, and distilled water. Whereas, the EBSD samples were ground, polished, and then ion milled.

3. Results and Discussions

3.1. Microstructure and Mechanical Properties. Figure 2 shows the SEM micrographs of the AC alloy. This alloy is featured with a typical dendritic structure which consists of a coarse α-Mg matrix with an average grain size of 180 μm, γ-phase precipitates ($Mg_{17}Al_{12}$), and interdendritic eutectic phase.

The present used combined processing route brings into a multiheterostructured (MH) AZ91 alloy, which was investigated in detail in our previous work [30]. The microstructure of the MH alloy is characterized by a heterogeneous grain structure and a heterogeneous precipitate structure, as shown in Figure 3. The SEM indicates that the fine lamellar γ-phase precipitates cover most of the grains, but some grains are still precipitate-sparse/free, indicating a heterogeneous precipitate structure, as shown in Figures 3(a) and 3(b). Here, the lamellar precipitates are formed during aging in a discontinuous mode. Besides, some cobblestone-like γ-phase particles can be found on the grain boundaries, which are dynamically precipitated during ECAP processing. The EBSD observation shows that the heterogeneous grain structure is comprised of coarse grains with an average size of 44.2 μm and fine grains with an average size of 18.7 μm,

(a)

(b)
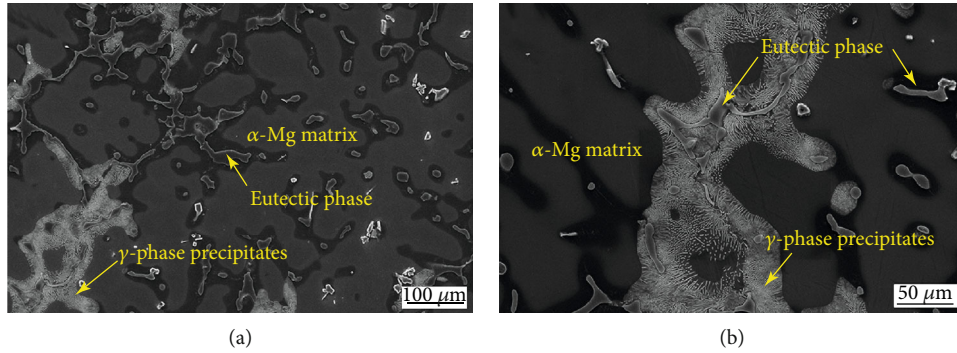
FIGURE 2: SEM micrographs of the AC alloy. The low-magnification (a) and high-magnification (b) images.

(a)

(b)

(c)

(d)
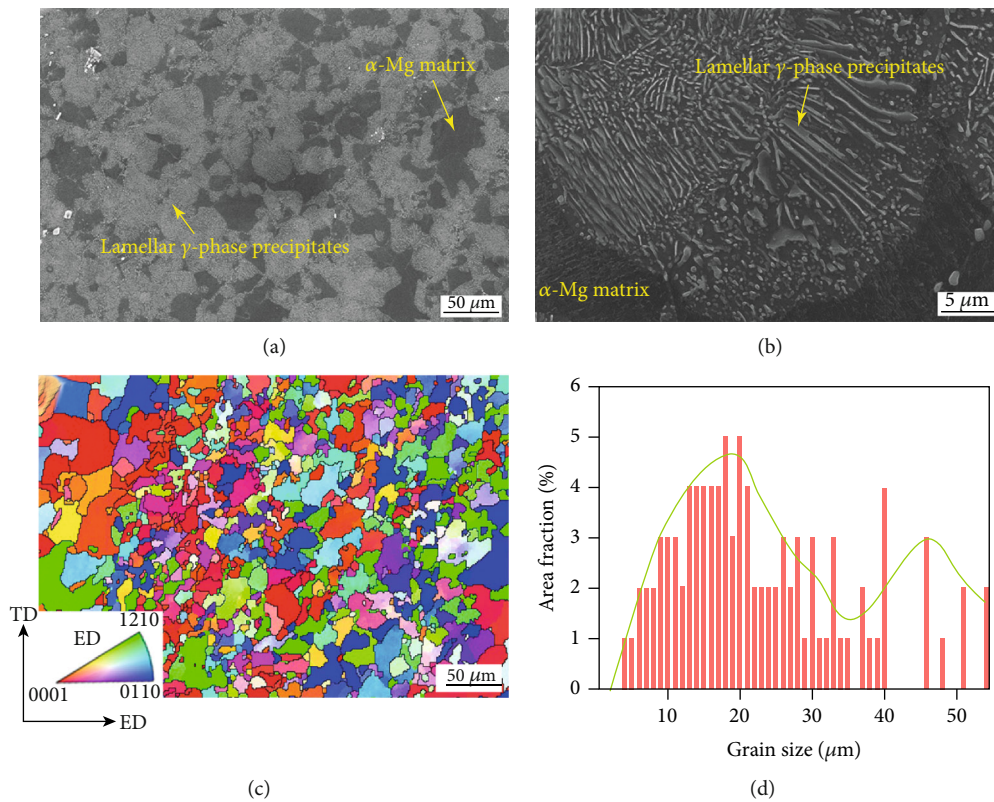
FIGURE 3: SEM micrographs (a, b), EBSD inverse pole figure mapping (c), and grain size statistics (d) of the MH alloy.

as artificial critical grain size of 35 μm is chosen, as shown in Figures 3(c) and 3(d). The volume fraction of the fine grains reaches 84.8%.

The AC alloy has poor mechanical properties, as shown in Figure 4(a). The multiheterostructure brings a superior combination of high strength and good ductility to the AZ91 alloy. The tensile yield strength (TYS), ultimate tensile strength (UTS), and elongation (EL) of the MH alloy are improved by 240.5%, 175.0%, and 80.3%, respectively, compared to the AC alloy (Figure 4(a)). Moreover, the microhardness increment of the MH alloy is over 40%, as shown in Figure 4(b).

3.2. Wear Behavior. Figure 5(a) shows the time evolution of the wear volume. The wear volume almost linearly increases with increasing duration time both for the AC alloy (from 0.234 mm^3 to 1.915 mm^3) and the MH alloy (from 0.247 mm^3 to 2.622 mm^3). The MH alloy exhibits a more rapidly increasing trend of the wear volume than the AC alloy, indicating a larger wear rate. Therefore, the MH alloy has a larger wear volume than the AC alloy under all duration time, although the difference is hard to be perceived under a short duration time. Figure 5(b) presents the wear volume as a function of the applied load. The wear volume of both alloys increases gradually with increasing the applied load and its growth trend of both alloys is similar. Apparently, the wear volume of the MH alloy (from 0.826 mm^3 to 1.908 mm^3) is larger than that of the AC alloy (from 0.701 mm^3 to 1.690 mm^3) at all the applied loads. The present

(a)

(b)
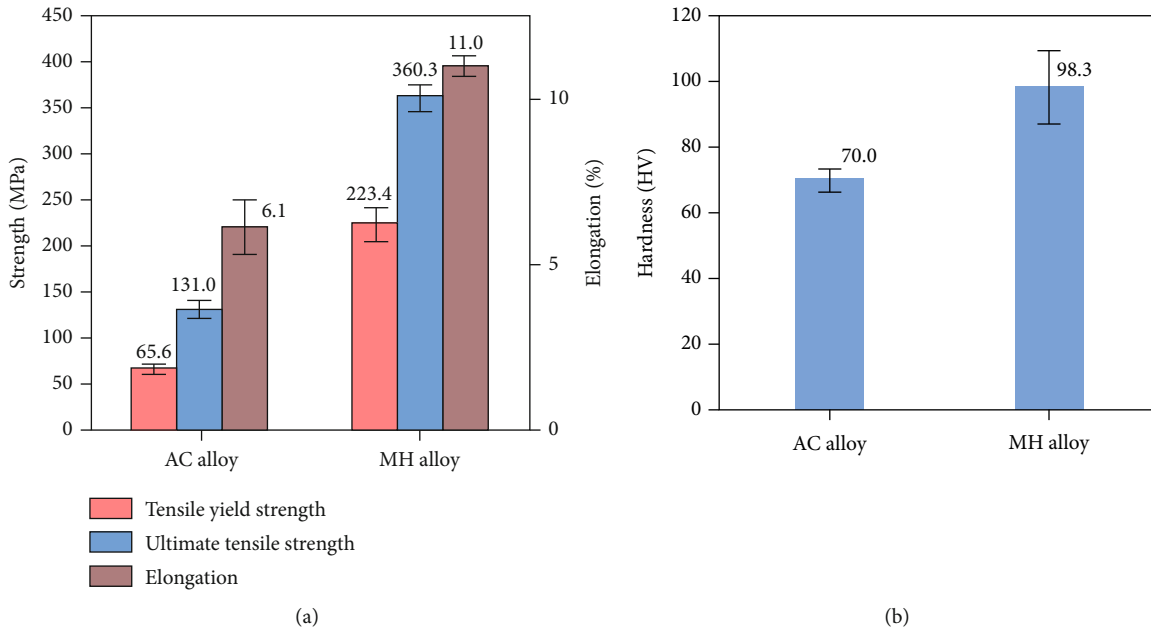
FIGURE 4: The mechanical properties [7, 30] (a) and microhardness (b) of the AC and MH alloys.

(a)

(b)
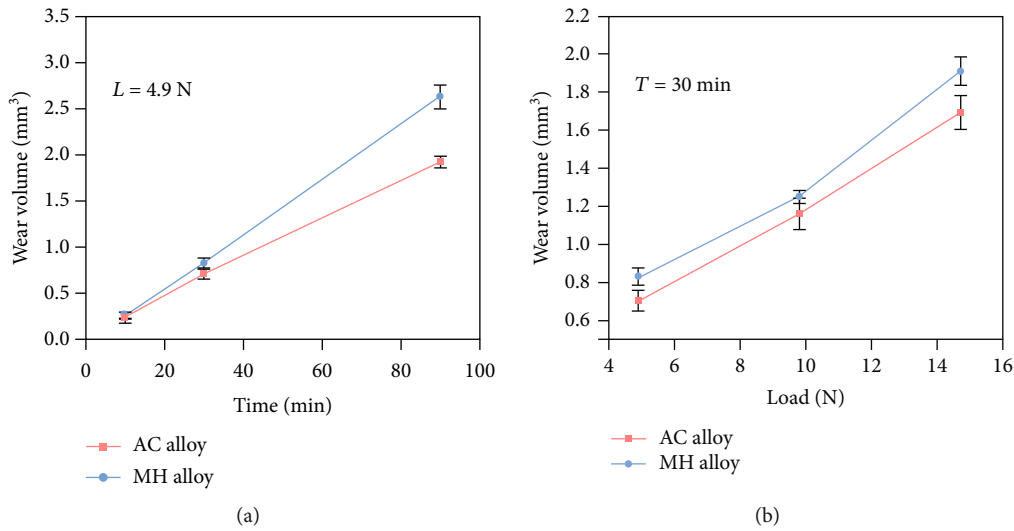
FIGURE 5: Wear volume of the AC and MH alloys as the function of the duration time T (a) and the applied load L (b).

results demonstrate that the MH alloy exhibits a poorer wear resistance than the AC alloy, although it has better mechanical properties.

Figure 6 shows the wear track cross-section profiles of the AC and MH alloys. Under short duration time or small applied load, the wear track of two alloys is similar, while it is slightly deeper for the MH alloy, as shown in Figures 6(a) and 6(c). Increasing duration time, both the wear track depth and width of the MH alloy are growing faster than that of the AC alloy, as shown in Figure 6(b), indicating rapidly increased wear volume. Increasing the applied load, the discrepancy of the wear track depth between the AC alloy and the MH alloy dramatically grows, but the wear track widths of two alloys are similar.

Figure 7 shows the evolution of the COF for the AC and MH alloys under the applied load of 4.9 N and 14.7 N. After a rapid increase, the COF tends to be steady for all the samples, although the fluctuation is still visible. It is evident that the AC alloy shows more drastic COF fluctuation than the MH alloy. Furthermore, the COF fluctuation is influenced by the applied load, as shown in Figure 7. To be specific, the lower applied load, the more fluctuant COF.

The average COF of the AC and MH alloys during the steady wear stage was calculated, and the result is shown in Figure 8. As the duration time increases, the COF of these two alloys increases first and then decreases. The COF of the AC alloy is higher than that of the MH alloy under different duration times (Figure 8(a)). The highest COF is 0.341 for
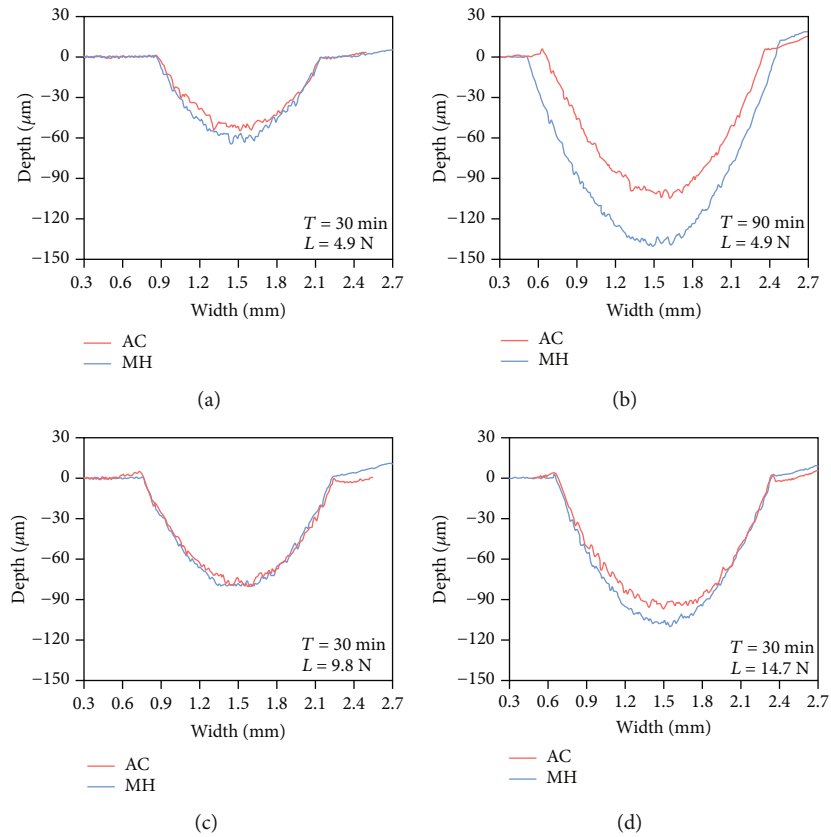
FIGURE 6: The wear track cross-section profiles of the AC and MH alloys under the applied load L of 4.9 N (a, b) and the duration time T of 30 min (c, d).
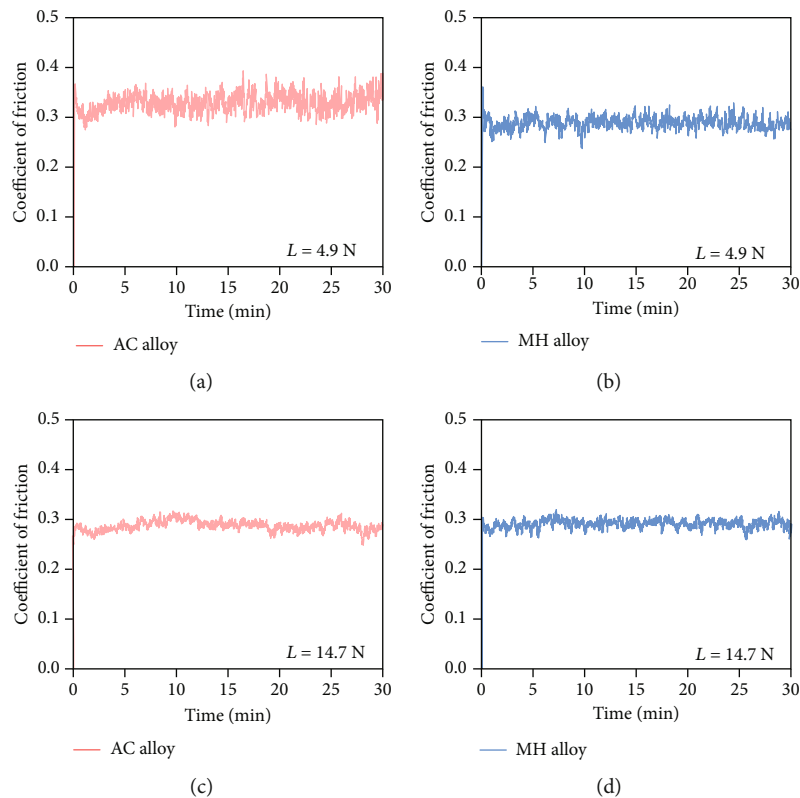
FIGURE 7: The fluctuation of the COF values of the AC (a, c) and MH (b, d) alloys under the applied load L of 4.9 N (a, b) and 14.7 N (c, d).

(a)   (b)
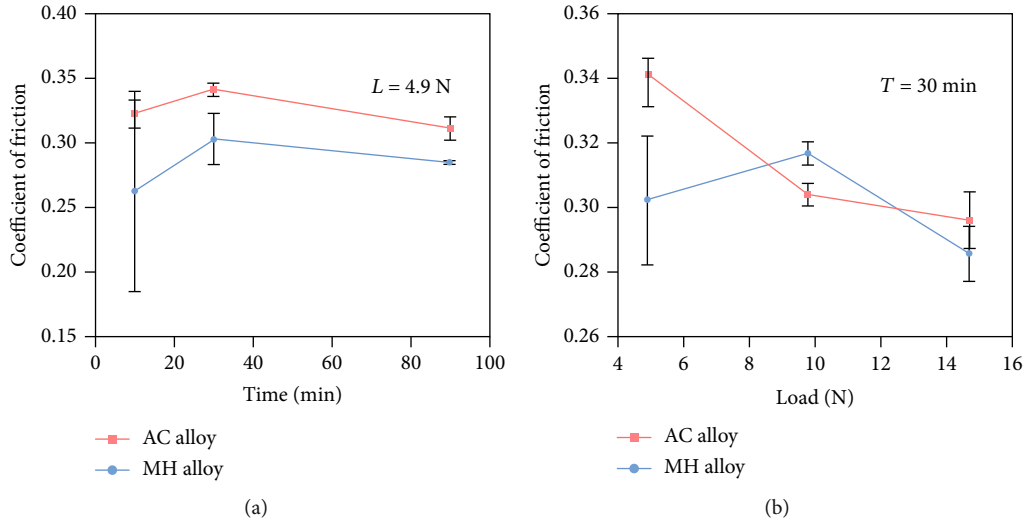
FIGURE 8: The average COF of the AC and MH alloys versus the different duration times T (a) and applied loads L (b).
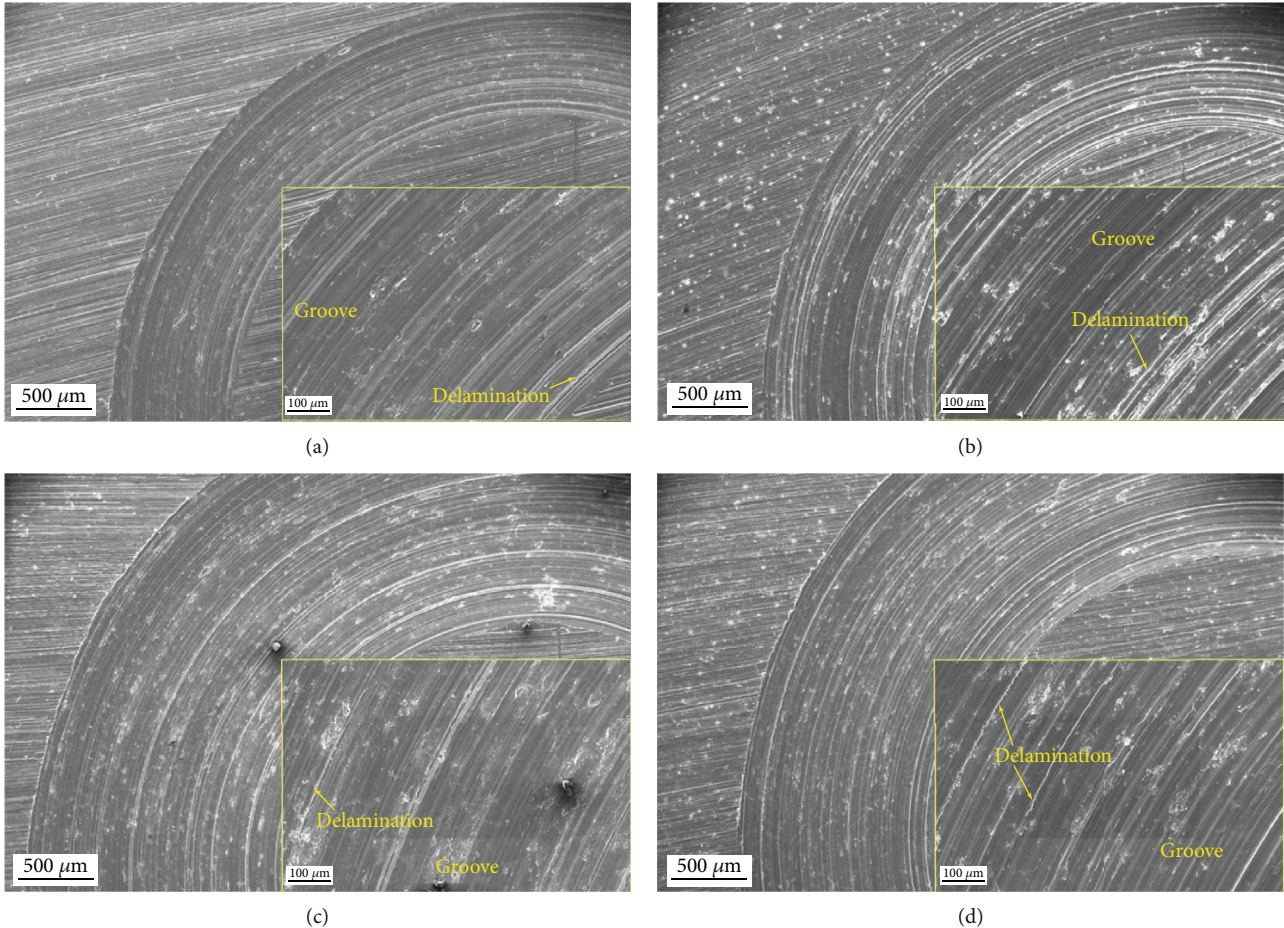
FIGURE 9: The SEM images of the typical wear surfaces of the AC alloy: (a) $T = 10$ min, $L = 4.9$ N; (b) $T = 30$ min, $L = 4.9$ N; (c) $T = 90$ min, $L = 4.9$ N; (d) $T = 30$ min, $L = 9.8$ N.

the AC alloy, while it is decreased to 0.302 for the MH alloy. Nevertheless, under different applied loads, the variation trend of COF of the AC and MH alloys is quite different, as shown in Figure 8(b). The COF of the AC alloy (from 0.341

to 0.296) rapidly decreases, followed by a relatively gentle descent. In contrast, the COF of the MH alloy first increases and then decreases with increasing the applied load. Therefore, the MH alloy exhibits a low COF at an applied load of

(a)

(b)

(c)

(d)
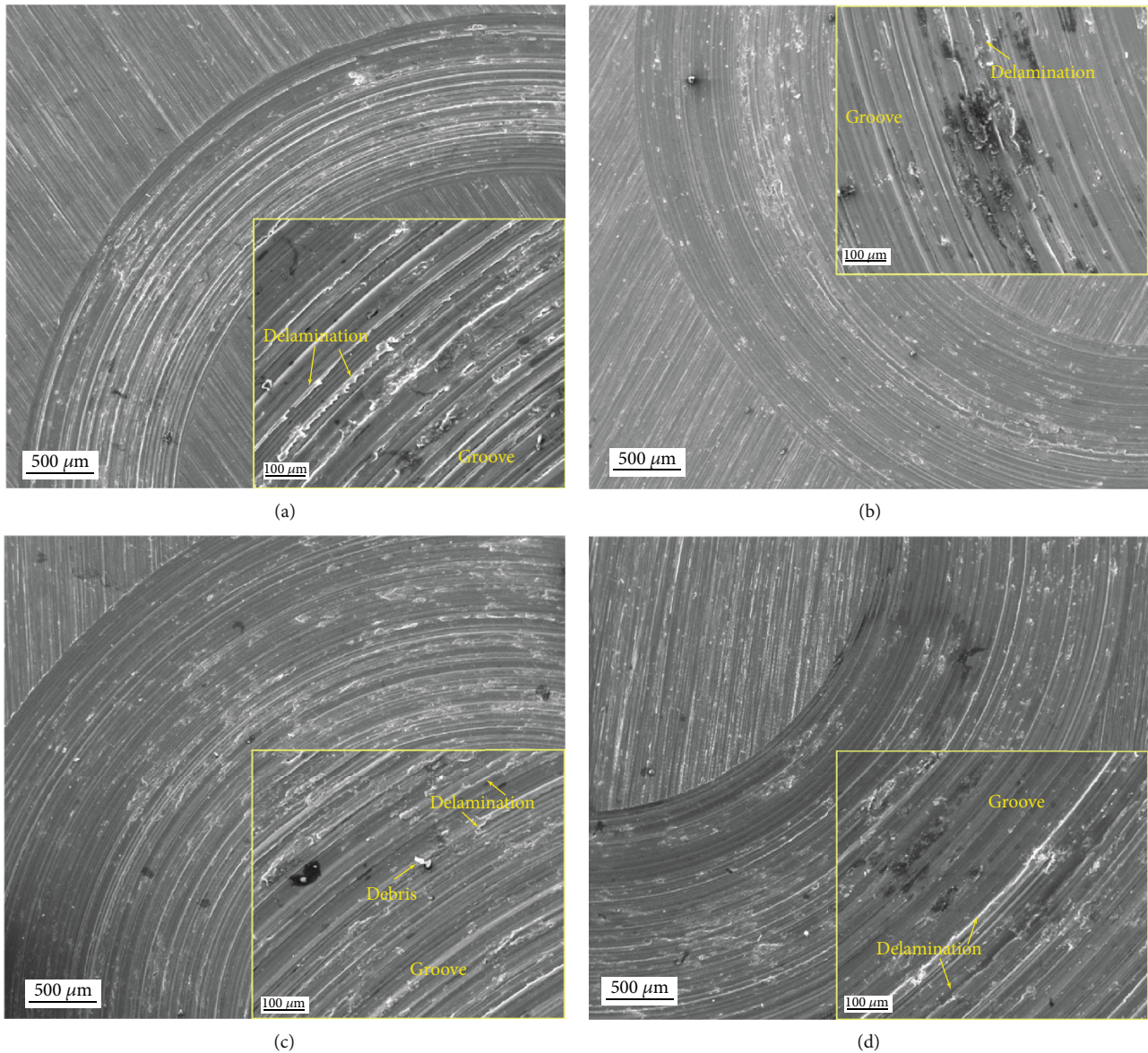
FIGURE 10: The SEM images of the typical wear surfaces of the MH alloy: (a) $T = 10$ min, $L = 4.9$ N; (b) $T = 30$ min, $L = 4.9$ N; (c) $T = 90$ min, $L = 4.9$ N; (d) $T = 30$ min, $L = 9.8$ N.

4.9 N (0.262) and 14.7 N (0.286). As a whole, the MH alloy shows the relatively lower COF compared to the AC alloy under different duration times and applied loads.

3.3. Wear Mechanism. The morphologies of the wear surface were further characterized using SEM combined with EDS to reveal wear mechanism. Figures 9 and 10 present the SEM images of the typical wear surfaces of the AC and MH alloys. Along the sliding direction, numerous grooves, ridges, and debris can be observed on the wear surface of both alloys at all conditions, representing the typical morphologies of abrasive wear. Therefore, the abrasive wear is the primary wear mechanism for both alloys. Besides, some adhesion marks and delamination are visible for both alloys, indicating the occurrence of adhesion wear and delamination wear. Some black stains can be found in

both alloys. The EDS analysis demonstrates that these stains contain high-concentration O element, giving rise to the occurrence of oxidation wear, as shown in Figure 11. In comparison, the MH alloy shows relatively severer adhesion, delamination, and oxidation. As the duration time and applied load increase, the wear track width of both alloys increase, but it is hard to tell the difference in the wear mechanism. The present result is consistent with these previous researches that the dominant wear mechanism of the AZ91 alloy at low load and sliding is abrasive wear [33, 34], and confirms that the MH alloy has almost same wear mechanism to the AC alloy.

The MH alloy exhibits finer grains compared to the AC alloy. The fine grains benefit to the improvement in strength and ductility due to the well-known Hall-Petch law. In contrast, fine grain is a sword with double blades for the wear
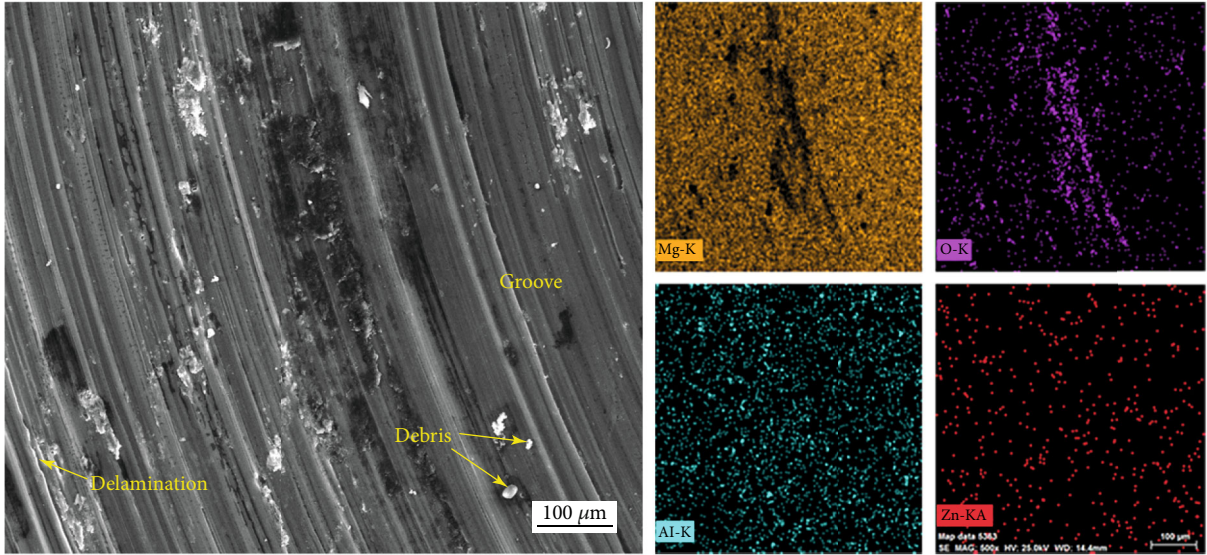
Figure 11: Large-magnification SEM images and EDS elemental mappings of the typical worn surfaces of the MH alloy under the applied load L of 4.9 N and the duration time T of 30 min.

behavior, which not only can hinder wear due to the improved hardness but also can accelerate wear due to the abundant unstable grain boundaries. During the dry sliding wear process, the high friction heat will deteriorate the instability of the grain boundaries, which is confirmed by the observed relatively severe oxidation. Also, the modification of the precipitate microstructure impacts the wear behavior. The fine lamellar γ-phase precipitates in the MH alloy may be obstructive to improve wear resistance, because the small precipitates are easy to be dug out when the abrasive wear prevails. Therefore, the MH alloy exhibits larger wear volume than the AC alloy during the present dry sliding wear condition, although it has significantly improved strength, ductility, and hardness. Indeed, the decreased and improved wear resistance are both frequently reported for the ECAP metals in literature. For example, Patil et al. [35] indicated that the ECAP processed samples displayed a poorer wear resistance as compared to the as-cast sample at 20 N and 30 N loads, but a decreased wear resistance at 10 N. On contrast, Xu et al. [36] reported that the wear volume of ECAP-processed AZ31 is smaller than for the as-received unprocessed alloy. Therefore, the wear resistance of the MH alloy prepared by ECAP is not only related to its physical properties but also significantly related to the wear condition. One should reasonably use the MH alloy considering the service conditions to seek advantages and avoid disadvantages.

4. Conclusion

In this work, the dry sliding wear behavior of the MH AZ91 alloy with multiheterostructure was investigated, which was prepared *via* the combined processing route of industrial-scale ECAP and aging. Although the MH AZ91 alloy exhibits high-desirable strength-ductility synergy due to its special multiheterostructure, it shows a poorer wear resistance compared to the AC alloy at the present condition. As a whole,

the MH alloy shows the relatively lower COF compared to the AC alloy. The difference in wear volume between two alloys is hard to be perceived under a short duration time, while the MH alloy has a much larger wear volume than the AC alloy under a long duration time. The wear volume of both alloys is almost linearly increased with the increase in the applied load. The wear mechanism of both alloys mainly involves abrasive wear, as well as mild adhesion, delamination, and oxidation. In comparison, the MH alloy shows relatively severer adhesion, delamination, and oxidation. The poor wear resistance of the MH alloy at the present dry sliding wear condition is linked to the abundant grain boundaries and small and fine precipitates.

Data Availability

The data used to support the findings of this study are available from the corresponding author upon request.

Conflicts of Interest

The authors declare that they have no competing interests.

Acknowledgments

References

[1] J. Song, J. She, D. Chen, and F. Pan, "Latest Research Advances on Magnesium and Magnesium Alloys Worldwide," *Journal of Magnesium and Alloys*, vol. 8, no. 1, pp. 1–41, 2020.

[2] H. Wu, Z. Shi, X. Zhang et al., "Achieving an acid resistant surface on magnesium alloy via bio-inspired design," *Applied Surface Science*, vol. 478, pp. 150–161, 2019.

[3] G. Wu, Y. Zhao, X. Zhang, J. M. Ibrahim, and P. K. Chu, "Self-protection against corrosion of aged magnesium alloy in simulated physiological environment," *Corrosion Science*, vol. 68, pp. 279–285, 2013.

[4] C. Liu, Z. Ren, Y. Xu, S. Pang, X. Zhao, and Y. Zhao, "Biodegradable magnesium alloys developed as bone repair materials: a review," *Scanning*, vol. 2018, Article ID 9216314, 15 pages, 2018.

[5] G. Wu, H. Wu, X. Zhang, S. Xiao, Z. Wu, and P. K. Chu, "Electrochemical degradation and extraction capability of magnesium wastes in sewage treatment," *Materials and Design*, vol. 111, pp. 537–540, 2016.

[6] G. Wu, K. Chan, L. Zhu, L. Sun, and J. Lu, "Dual-phase nanostructuring as a route to high-strength magnesium alloys," *Nature*, vol. 545, no. 7652, pp. 80–83, 2017.

[7] J. Sun, B. Xu, Z. Yang et al., "Achieving excellent ductility in high-strength Mg-10.6Gd-2 Ag alloy *via* equal channel angular pressing," *Journal of Alloys and Compounds*, vol. 817, 2020.

[8] X. Ma, Q. Jiao, L. J. Kecskes, J. A. el-Awady, and T. P. Weihs, "Effect of basal precipitates on extension twinning and pyramidal slip: a micro-mechanical and electron microscopy study of a Mg-Al binary alloy," *Acta Materialia*, vol. 189, pp. 35–46, 2020.

[9] J. Zheng and B. Chen, "Atomic-scale characterization of the equilibrium β phase in Mg-Nd-Y alloy by means of HAADF-STEM," *Scanning*, vol. 38, no. 6, pp. 743–746, 2016.

[10] S. Tang, T. Xin, W. Xu et al., "Precipitation strengthening in an ultralight magnesium alloy," *Nature Communications*, vol. 10, no. 1, p. 1003, 2019.

[11] J. Zhang, S. Liu, R. Wu, L. Hou, and M. Zhang, "Recent developments in high-strength Mg-RE-based alloys: focusing on Mg-Gd and Mg-Y systems," *Journal of Magnesium and Alloys*, vol. 6, no. 3, pp. 277–291, 2018.

[12] S. You, Y. Huang, K. U. Kainer, and N. Hort, "Recent research and developments on wrought magnesium alloys," *Journal of Magnesium and Alloys*, vol. 5, no. 3, pp. 239–253, 2017.

[13] F. Zhao, T. Suo, B. Chen, and Y. L. Li, "Strength-ductility combination of fine-grained magnesium alloy with high deformation twin density," *Journal of Alloys and Compounds*, vol. 798, pp. 350–359, 2019.

[14] B. Xu, J. Sun, Z. Yang et al., "Microstructure and anisotropic mechanical behavior of the high-strength and ductility AZ91 Mg alloy processed by hot extrusion and multi-pass RD-ECAP," *Materials Science and Engineering A*, vol. 780, p. 139191, 2020.

[15] S.-J. Meng, H. Yu, S.-D. Fan et al., "Recent Progress and development in extrusion of rare earth free Mg alloys: a review," *Acta Metallurgica Sinica (English Letters)*, vol. 32, no. 2, pp. 145–168, 2019.

[16] H. Yu, Y. Xin, M. Wang, and Q. Liu, "Hall-Petch relationship in Mg alloys: a review," *Journal of Materials Science and Technology*, vol. 34, no. 2, pp. 248–256, 2018.

[17] L. R. Xiao, X. F. Chen, Y. Cao et al., "Solute segregation assisted nanocrystallization of a cold-rolled Mg-Ag alloy during annealing," *Scripta Materialia*, vol. 177, pp. 69–73, 2020.

[18] Y. Fu, J. Sun, Z. Yang et al., "Aging behavior of a fine-grained Mg-10.6Gd-2Ag alloy processed by ECAP," *Materials Characterization*, vol. 165, p. 110398, 2020.

[19] W. Wang, P. Han, P. Peng et al., "Friction stir processing of magnesium alloys: a review," *Acta Metallurgica Sinica (English Letters)*, vol. 33, no. 1, pp. 43–57, 2020.

[20] Y. Hu and X. Wu, "Perspective on hetero-deformation induced (HDI) hardening and back stress," *Materials Research Letters*, vol. 7, no. 10, pp. 393–398, 2019.

[21] I. A. Ovid'Ko, R. Z. Valiev, and Y. T. Zhu, "Review on superior strength and enhanced ductility of metallic nanomaterials," *Progress in Materials Science*, vol. 94, pp. 462–540, 2018.

[22] Y.-F. Jia, Y.-X. Liu, J. Huang et al., "Fatigue-induced evolution of nanograins and residual stress in the nanostructured surface layer of Ti-6Al-4V," *Materials Science and Engineering A*, vol. 764, 2019.

[23] Y.-F. Jia, R.-J. Pan, P.-Y. Zhang et al., "Enhanced surface strengthening of titanium treated by combined surface deep-rolling and oxygen boost diffusion technique," *Corrosion Science*, vol. 157, pp. 256–267, 2019.

[24] B. Wang, D. Xu, L. Sheng, E. Han, and J. Sun, "Deformation and fracture mechanisms of an annealing-tailored "bimodal" grain-structured Mg alloy," *Journal of Materials Science and Technology*, vol. 35, no. 11, pp. 2423–2429, 2019.

[25] M. Zha, H. M. Zhang, Z. Y. Yu et al., "Bimodal microstructure - a feasible strategy for high-strength and ductile metallic materials," *Journal of Materials Science and Technology*, vol. 34, no. 2, pp. 257–264, 2018.

[26] S. M. Ramezani, A. Zarei-Hanzaki, H. R. Abedi, A. Salandari-Rabori, and P. Minarik, "Achievement of fine-grained bimodal microstructures and superior mechanical properties in a multi-axially forged GWZ magnesium alloy containing LPSO structures," *Journal of Alloys and Compounds*, vol. 793, pp. 134–145, 2019.

[27] S. Liu, J. Zhang, X. Chen et al., "Improving mechanical properties of heterogeneous mg-Gd alloy laminate via accumulated extrusion bonding," *Materials Science and Engineering A*, vol. 785, p. 139324, 2020.

[28] W. Rong, Y. Zhang, Y. Wu et al., "The role of bimodal-grained structure in strengthening tensile strength and decreasing yield asymmetry of Mg-Gd-Zn-Zr alloys," *Materials Science and Engineering A*, vol. 740-741, pp. 262–273, 2019.

[29] C. Xu, G. H. Fan, T. Nakata et al., "Deformation behavior of ultra-strong and ductile Mg-Gd-Y-Zn-Zr alloy with bimodal microstructure," *Metallurgical and Materials Transactions A: Physical Metallurgy and Materials Science*, vol. 49, no. 5, pp. 1931–1947, 2018.

[30] J. Sun, B. Xu, Z. Yang et al., "Developing an industrial-scale ECAP Mg-Al-Zn alloy with multi-heterostructure for synchronously high strength and good ductility," *Materials Characterization*, vol. 164, p. 110341, 2020.

[31] J. Sun, Z. Yang, H. Liu et al., "Tension-compression asymmetry of the AZ91 magnesium alloy with multi-heterogenous microstructure," *Materials Science and Engineering A*, vol. 759, pp. 703–707, 2019.

[32] J. Sun, Z. Yang, J. Han et al., "High strength and ductility AZ91 magnesium alloy with multi-heterogenous microstructures prepared by high-temperature ECAP and short-time aging," *Materials Science and Engineering A*, vol. 734, pp. 485–490, 2018.

[33] B. N. Sahoo and S. K. Panigrahi, "Development of wear maps of in-situ TiC+TiB2 reinforced AZ91 Mg matrix composite with varying microstructural conditions," *Tribology International*, vol. 135, pp. 463–477, 2019.

[34] S. García-Rodríguez, B. Torres, A. Maroto, A. J. López, E. Otero, and J. Rams, "Dry sliding wear behavior of globular AZ91 magnesium alloy and AZ91/SiCp composites," *Wear*, vol. 390-391, pp. 1–10, 2017.

[35] A. Patil, S. Bontha, and M. R. Ramesh, "Effect of ECAP on sliding wear behaviour of Mg-Zn-Gd-Zr alloy," *Materials Today: Proceedings*, vol. 20, pp. 97–102, 2020.

[36] J. Xu, X. Wang, X. Zhu et al., "Dry sliding wear of an AZ31 magnesium alloy processed by equal-channel angular pressing," *Journal of Materials Science*, vol. 48, no. 11, pp. 4117–4127, 2013.

Research Article

Parametric Optimization of Laser Additive Manufacturing of Inconel 625 Using Taguchi Method and Grey Relational Analysis

Bo Yang [iD],[1] **Youbin Lai** [iD],[1] **Xiang Yue,**[1] **Dongyang Wang,**[1] **and Yuhui Zhao**[2]

[1]*College of Engineering, Shenyang Agricultural University, Shenyang 110866, China*
[2]*Shenyang Institute of Automation Chinese Academy of Sciences, Shenyang 110016, China*

Correspondence should be addressed to Youbin Lai; yblai@syau.edu.cn

In order to improve the forming quality of the Inconel 625 cladding layer and make it to be more widely used. This paper addresses an experimental investigation on the influence of major process parameters like laser power, scanning speed, powder feed rate, and overlapping rate along with their interactions on surface roughness and width error of laser additive manufacturing process for forming Inconel 625 samples. Taguchi method and grey relational analysis were used to optimize the selected parameters, and the verification tests were carried out. The change of microhardness and microstructure in the overlapping zone and nonoverlapping zone of the cladding layer were studied by microhardness tester and scanning electron microscopy (SEM). The results show that the most significant effect in processing parameters on surface roughness and width error are both overlapping rate, and the optimal levels of laser power, scanning speed, powder feeder rate, and overlapping rate are 1800 W, 8 mm/s, 10 g/min, and 30%, respectively. Analysis of microstructure and composition showed that the content of Cr was high both in the Laves phase and matrix, the content of Nb in the Laves phase increased significantly and reached up to 24.48 wt%, and the Laves in the nonoverlapping zone was more compact than the overlapping zone.

1. Introduction

Inconel 625 is a solid-solution strengthened Ni-Cr-Mo alloy with a face-centered cubic structure [1]. Because of its excellent mechanical strength and resistance to creep and corrosion in harsh environments, Inconel 625 has been widely used in aerospace, chemical, petrochemical, and marine applications. However, many of the Inconel 625 components are highly complex shapes that are very expensive to produce due to extensive machining [2–6].

Laser additive manufacturing (LAM) is a new technology, which is widely used in aerospace, medical, military, and many other fields [7]. It integrates the latest achievements in the field of mechanical engineering, CAD/CAM, CNC or robot technology, laser technology, and materials science. And it can quickly transform the design idea into a prototype with a certain structure and function or manufacture parts directly, reducing the processing costs significantly [8–10]. In the LAM process, lots of different parameters such as laser power, scanning speed, and powder feed rate can be coupled together to influence the quality of the parts. Hence, optimizing the process parameters to obtain a quality part becomes a focus problem for many experts [11–18].

Nevertheless, most scholars only study the influence of multiple parameters on a single response target. Few experts have studied the influence of multiple parameters on multiple response targets in laser additive manufacturing of Inconel 625 alloy. In addition, the overlapping rate is a parameter that has an important influence on forming quality. The area of the overlapping zone will be increased when the overlapping rate is too high, the microstructure and microhardness of the cladding layer will be affected. However, the surface of the cladding layer will be uneven when the overlapping rate is too small. But many scholars often neglect its influence when they study the optimization of process parameters. In this paper, the comprehensive influence of parameters of laser power, scanning speed, power feed rate, and overlapping rate on the surface roughness and width error of the LAM process of Inconel 625 has been studied. And the microstructure and microhardness
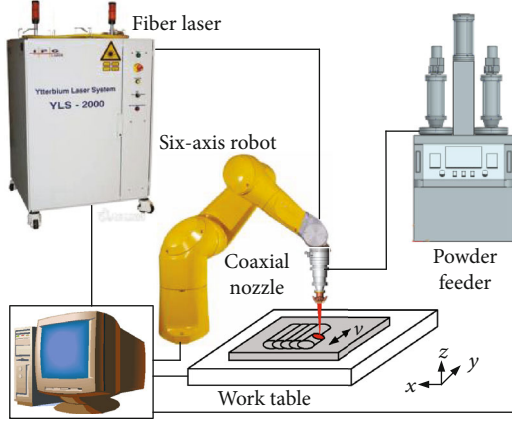
FIGURE 1: Schematic diagram of LAM.

TABLE 1: Powder composition of Inconel 625.

Cr	Mo	Nb	Fe	Si	C	Al	Ti	Mn	Co	Ni
21.3	8.58	3.73	0.11	0.09	0.053	0.18	0.16	0.04	0.025	Bal.

of overlapping zone and nonoverlapping zone have been explored. The Taguchi method and grey relational analysis have been used to analyse the influence of multiple parameters on multiple response targets, and the LAM parameters have been optimized.

2. Experimental Method

2.1. Experimental Equipment and Material. The experiments were carried out with the LAM setup shown in Figure 1. The setup system includes a fiber laser with a 2000 W maximum output power, a robot with six-axis, a powder feeder system, and other auxiliary equipment. The base material used in the experiment was Inconel 625 alloy, and the Inconel 625 alloy was selected as alloy powder; the chemical composition of the powder was shown in Table 1. Before the experiment, the substrate was polished to remove the surface oxidation layer and improve its surface finish. Then, the substrate was cleaned with acetone to remove the oil on the surface. The Inconel 625 alloy powder was placed at 120°C vacuum environment for drying treatment.

2.2. The Taguchi Method. The Taguchi method is an optimized design technology founded by Genichi Taguchi PhD, a Japanese quality engineer. The method is mainly used for technology development, product development, and process development. The Taguchi method is divided into three procedures [19]: (1) Select factors and their levels according to experimental analysis; in this paper, laser power, scanning speed, powder feeding speed, and overlapping speed are selected as experimental factors, each of which are three levels. Factors and levels are shown in Table 2. Other factors are kept at their fixed level as mentioned in Table 2. (2) Select orthogonal array (OA) to conduct the experiments, the $L_9 3^4$ Taguchi OA is selected to perform experiments. (3) Calculate the signal to noise (S/N) ratio and statistical analysis of

variance (ANOVA), and then obtain the optimal process parameters.

2.3. DLF Experiments and Measurements. In the LAM experiment, the overlapping rate (OR) was computed by the following equation [20]:

$$\mu = \frac{w - \lambda}{w}, \tag{1}$$

where w is the width of a single-track formation as shown in Figure 2, and λ is the offset distance between adjacent tracks as shown in Figure 3.

In the experiment, the overlapping rate is decided by the offset distance between adjacent tracks. According to Eq. (1), the distance between adjacent tracks can be expressed as follows:

$$\lambda = (1 - \mu) \cdot w. \tag{2}$$

It is obvious that in addition to the overlapping rate, the value of λ is decided by the width of one single track. Therefore, the single-track experiment needs to be made at first, measure the width of the single-track, and calculate the offset distance between adjacent tracks. Using $L_9 3^4$ Taguchi OA to perform the single-track single layer LAM experiments, 9 samples with a length of 50 mm were formed (Figure 4). The width of each sample was measured, three different locations have been selected, and their averages were considered. The measured results are shown in Table 3.

Calculate the offset distance between adjacent tracks according to the results of single-track formation, and then using the $L_9 3^4$ Taguchi OA to perform the multitrack single layer LAM experiments; the number of the track is 10; the length of every track is 50 mm; three experimental replicates were performed for better accuracy, thence the total number of samples was 27, Figure 5 shows a group of samples among them.

The quality characteristics LAM is determined by measuring surface roughness (δ) (Figure 3) and the width error (w_e). The surface roughness refers to the difference height of the highest and lowest points of the sample surface. The width error refers to the difference between the theoretical calculation width (Eq. (3)) and the actual measurement width (Eq. (4)).

$$w_c = w + (t - 1) \cdot \lambda, \tag{3}$$

$$w_e = |w_m - w_c|, \tag{4}$$

where t is the number of tracks (in our case $t = 10$), w_c is the calculated value of the sample width, and w_m is the measured value of the sample width. The measurement and calculation results of samples in each group were given in Table 4.

2.4. Microhardness and Microstructure Experiments. The microstructure of the overlapping zone and the nonoverlapping zone of the cladding layer were analyzed by SEM. Microhardness tester was used to measure the transverse

TABLE 2: Factors and levels used in Taguchi design.

Fixed factors	Value	Unit	Control factors	Symbol	Level			Unit
					1	2	3	
Standoff distance	17	mm	Laser power	LP	1600	1800	2000	W
Laser spot diameter	3	mm	Scanning speed	SS	4	6	8	mm/s
Carrier gas flow rate	450	ml/h	Powder feed rate	PFR	10	20	30	g/min
Shielding gas flow rate	300	ml/min	Overlapping rate	OR	30	35	40	%

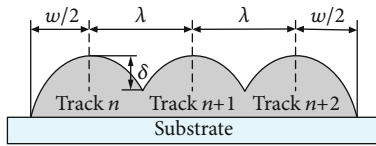FIGURE 2: Geometry of section of single-track formation.

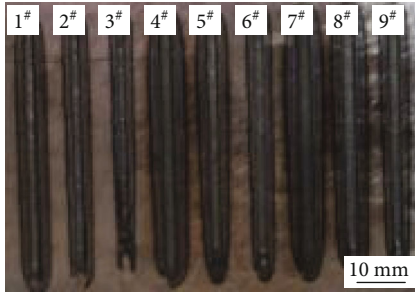FIGURE 3: Schematic diagram of cross section of multitrack formation.

FIGURE 4: Single track samples.

TABLE 3: The results of single-track formation.

Expt. No.	Factors and levels			Measured values (mm)			
	LP	SS	PFR	1	2	3	Average
1	1	1	1	2.56	2.60	2.46	2.54
2	1	2	2	2.22	2.26	2.12	2.20
3	1	3	3	1.78	1.58	1.58	1.65
4	2	1	2	3.12	2.98	3.10	3.07
5	2	2	3	2.66	2.56	2.46	2.56
6	2	3	1	2.28	2.12	2.02	2.14
7	3	1	3	3.22	3.32	3.20	3.25
8	3	2	1	2.76	2.88	2.78	2.81
9	3	3	2	2.78	2.52	2.44	2.58

microhardness of the section of the cladding layer. Under the load of 4.903 N, the load was maintained for 10s, the microhardness was measured from 0.1 mm to the left of the coating, and the measured interval was about 0.1 mm, and the microhardness variation law of the overlapping zone and nonoverlapping zone of the cladding layer was obtained. The indentation morphology of measurement points was shown in Figure 6.

3. Results and Discussion

3.1. Microhardness and Microstructure Analysis. Through the analysis of the transverse microhardness of the cross section of the cladding layer under different process parameters, the change rule of the microhardness between overlapping zone and nonoverlapping zone was basically the same. The sample of S_6 was taken as an example; SEM and EDS analysis were carried out on the overlapping zone and nonoverlapping zone. The transverse microhardness of cross section of the substrate and cladding layer is shown in Figure 7. The figure showed that the microhardness of the overlapping zone was lower than that of the nonoverlapping zone.

The SEM images were shown in Figure 8, and the energy spectrum analysis results of A, B, A′, B′ were shown in Table 5. The SEM image of the nonoverlapping zone of the simple was shown in Figure 8(a), while the SEM image of the overlapping zone was shown in Figure 8(b). The figure shows that the coating was mainly composed of light grey matrix A and Laves phase B, and the Laves in the nonoverlapping region is dense, while Laves in the overlapping region is dispersed. This is because part of the heat input into the lap zone is absorbed by the remelting zone of the cladding layer, and the Laves phase in the lap zone is not completely precipitated due to the insufficient heat absorbed by the alloy powder, so the Laves phase content in the lap zone is lower. According to the results of energy spectrum analysis, the light gray matrix A is the solid solution of the first precipitated nickel, which is mainly composed of Ni, Cr, Mo, Nb, Fe, Si, Al, Mn, Co, and other elements. Its mass fraction is similar to that of nickel base alloy powder, which can be seen that the dilution ratio of the coating near the surface was relatively low. Both Laves phase B and matrix have high Cr content, but compared with the matrix, the content of Nb in the Laves phase significantly increased, in which Nb content was up to 24.48 wt%, and the content of Ni decreased significantly. It follows that, at this time, the Laves phase in the coating is enriched with the Nb element, and the formation of the Ni element is limited at the same time. This is because that the niobium intergranular segregation produces the Laves phase.

The SEM and partial enlarged images of the overlapping zone and nonoverlapping zone were shown in Figure 9. Figure 9(a) shows that there are many fine cracks in the substrate of the overlapping zone compared with the substrate of
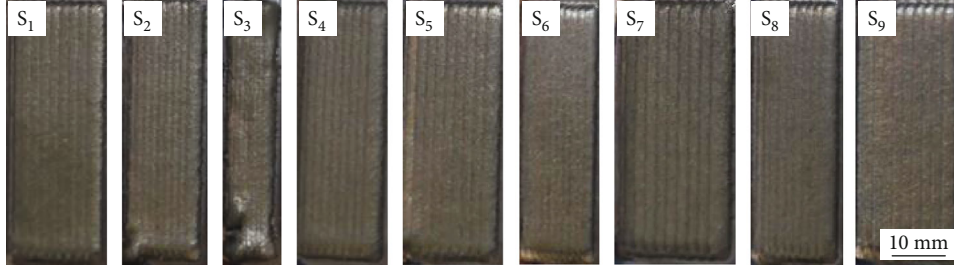
FIGURE 5: Multitrack samples.

TABLE 4: Mean of three replicates and the S/N ratio.

Expt. No.	Factors and levels				Mean of three replicates		S/N ratio	
	LP	SS	PFR	OR	δ (mm)	w_e (mm)	δ	w_e
1	1	1	1	1	0.157	0.036	16.097	28.256
2	1	2	2	2	0.223	0.164	13.146	13.948
3	1	3	3	3	0.280	0.122	11.053	17.988
4	2	1	2	3	0.241	0.130	12.391	15.872
5	2	2	3	1	0.110	0.058	19.148	22.298
6	2	3	1	2	0.120	0.083	18.396	19.900
7	3	1	3	2	0.167	0.137	15.539	15.421
8	3	2	1	3	0.210	0.214	13.549	11.658
9	3	3	2	1	0.153	0.033	16.283	26.446

FIGURE 7: Variation of microhardness in overlapping zone and nonoverlapping zone of the cladding layer.
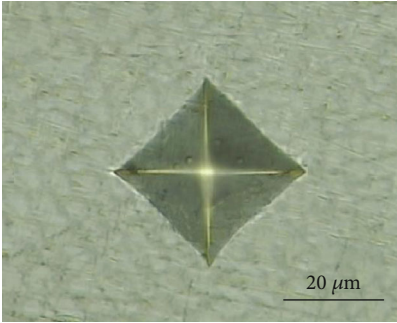

FIGURE 6: Indentation morphology.

the nonoverlapping zone (Figure 9(b)). It is because that the overlapping zone is subjected to the action of the double high-energy laser beam, which results in the increase of heat accumulation and temperature gradient of the substrate, the cooling shrinkage of the substrate results in a larger tensile stress, which leads to more micro cracks.

3.2. Signal to Noise Ratio. The change in the quality characteristics of a product under investigation, in response to the factor introduced in the experimental design, is the "signal" of the desired effect. However, when an experiment is conducted, there are numerous external factors not designed into the experiment which influence the outcome. These external factors are called the noise factors, and their effect on the outcome of the quality characteristic under test is termed "the noise". The signal to noise ratio (S/N ratio) measures the sen-

sitivity of the quality characteristic being investigated in a controlled manner, to those external influencing factors (noise factors) not under control. The aim of any experiment is always to determine the highest possible S/N ratio for the result. A high value of S/N implies that the signal is much higher than the random effects of the noise factors. Product design or process operation consistent with the highest S/N always yields the optimum quality with minimum variance. From the quality point of view, there are three possible categories of quality characteristics. They are (1) smaller is better, (2) nominal is best, and (3) bigger is better. The conversion of a set of observations into the S/N ratio is performed in two steps. First, the Mean Squared Deviation (MSD) of the set is calculated. Second, the S/N ratio is computed from the MSD by the equation [21, 22]:

$$\eta = -10 \log_{10}(\text{MSD}). \tag{5}$$

The smaller is better quality characteristic:

$$\text{MSD} = \frac{1}{n} \sum_{i=1}^{n} y_i^2. \tag{6}$$

(a)

(b)
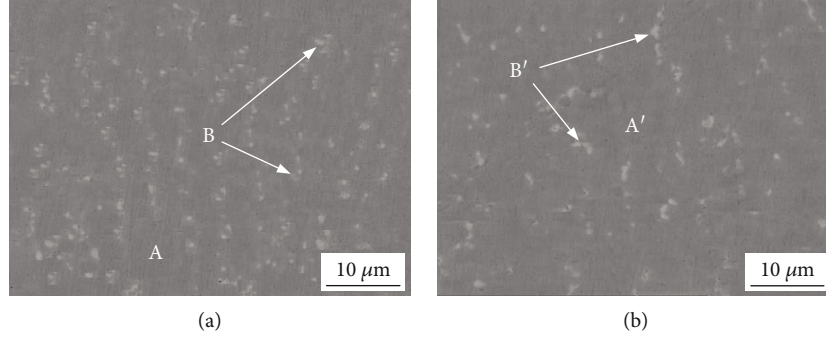
FIGURE 8: SEM images of non-overlapping zone (a) and overlapping zone (b) of coating.

TABLE 5: Results of energy dispersive spectrometer (%).

Marked location	Ni	Cr	Mo	Nb	Fe	Si	Al	Mn	Co
A	38.14	16.29	15.59	24.48	2.21	2.26	0.11	0.55	0.36
B	65.33	21.75	7.86	2.26	0.89	0.57	0.00	0.84	0.09
A′	41.71	16.47	12.03	19.46	0.71	2.30	0.00	0.54	0.21
B′	62.07	21.24	5.57	1.28	4.61	0.49	0.11	0.18	0.00

The nominal is the best quality characteristic:

$$\text{MSD} = \frac{1}{n}\sum_{i=1}^{n}(y_i - y_0)^2. \tag{7}$$

The bigger is better quality characteristic:

$$\text{MSD} = \frac{1}{n}\sum_{i=1}^{n}\frac{1}{y_i^2}, \tag{8}$$

where n is number of observations, y_0 is nominal or target value.

In our case, S/N ratio was calculated for both δ and we considering smaller is a better criterion for both the responses by using Eq. (6). The calculated S/N ratio is shown in Table 4.

Table 6 shows the significance of parameters for surface roughness and width error. According to rang analysis, the affect order of each factor on surface roughness and width error are OR > LP > PFR > SS and OR > SS > LP > PFR, respectively.

3.3. *Influences of Factors on Responses.* Figure 10 shows the effect of factors and their levels on the mean S/N ratio of surface roughness and width error. The highest values of S/N ratios show the levels of the factors which correspond to minimum surface roughness and width error. Figure 10(a) shows that minimum surface roughness can be achieved at 1800 W laser power, 6 mm/s scanning speed, 10 g/min powder feed rate, and 30% overlapping rate. Figure 10(b) shows that minimum width error can be achieved at 1600 W laser power, 8 mm/s scanning speed, 10 g/min powder feed rate, and 30% overlapping rate. Obviously, the effect of factors on surface roughness and width error is different.

3.4. *ANOVA Analysis.* Analysis of Variance (ANOVA) is routinely used to provide a measure of confidence. The technique does not directly analyze the data, but rather determines the variance of the data. By understanding the source and magnitude of variance, robust operating conditions can be predicted. Parameters used in ANOVA are calculated by the following equations [23, 24]:

$$S_M = \frac{\left(\sum_{i=1}^{9}\eta_i\right)^2}{9}, \tag{9}$$

$$S_A = \frac{\sum_{i=1}^{3}\eta_{Ai}^2}{N} - S_m, \tag{10}$$

$$S_T = \sum_{i=1}^{9}\eta_i^2 - S_m, \tag{11}$$

$$S_e = S_T - \sum S_A, \tag{12}$$

$$V_A = \frac{S_A}{f_A}, \tag{13}$$

$$F_A = \frac{V_A}{V_e}, \tag{14}$$

where S_M is the average of the squares of the sums, S_A is the sum of squares of the control factor A (laser power, scanning speed, powder feed rate, and overlapping rate), S_T is the sum of squares of the variance, S_e is the sum of squares of the errors, N is the number of samples in each group (here $N = 3$), V_A is the variance of the control factor A, f_A is the degree of freedom of factor A, and F_A is F-ratio of factor A.

Table 7 shows the ANOVA for S/N ratio for surface roughness and width error. Comparing the calculated F-values with standard F-values, which can be seen that laser power, powder feeder rate, and overlapping rate have a significant effect on surface roughness at 95%, 90%, and 95% confidence levels, respectively. And for width error, it is revealed that scanning speed and overlapping rate have a significant effect at 95% and 99% confidence levels, respectively.

3.5. *Grey Relation Analysis.* Taguchi method only can be used to perform single-objective optimization, but in the present
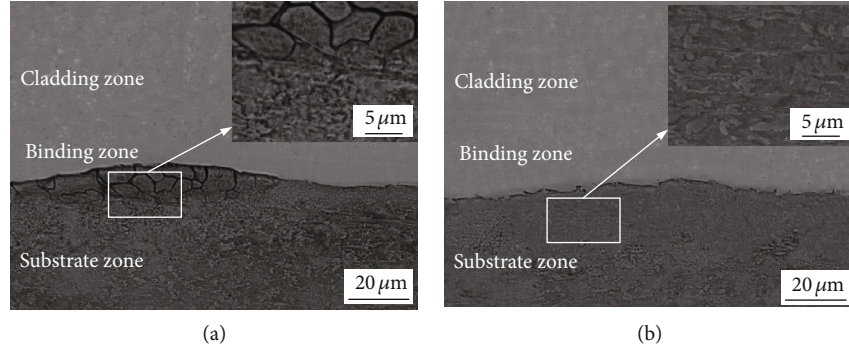
(a) (b)

FIGURE 9: SEM images of a substrate in the overlapping zone (a) and nonoverlapping zone (b).

TABLE 6: Significance of factors for surface roughness and width error.

Response factor	Factors	Mean S/N ratio			Range	Rank
		Level 1	Level 2	Level 3		
Surface roughness (δ)	LP	13.432	16.645	15.124	3.213	2
	SS	14.676	15.281	15.244	0.605	4
	PFR	16.014	13.940	15.247	2.074	3
	OR	17.176	15.694	12.331	4.845	1
Width error (w_e)	LP	20.064	19.357	17.842	2.222	3
	SS	19.850	15.968	21.445	5.477	2
	PFR	19.938	18.755	18.569	1.369	4
	OR	25.667	16.423	15.173	10.494	1

(a) (b)
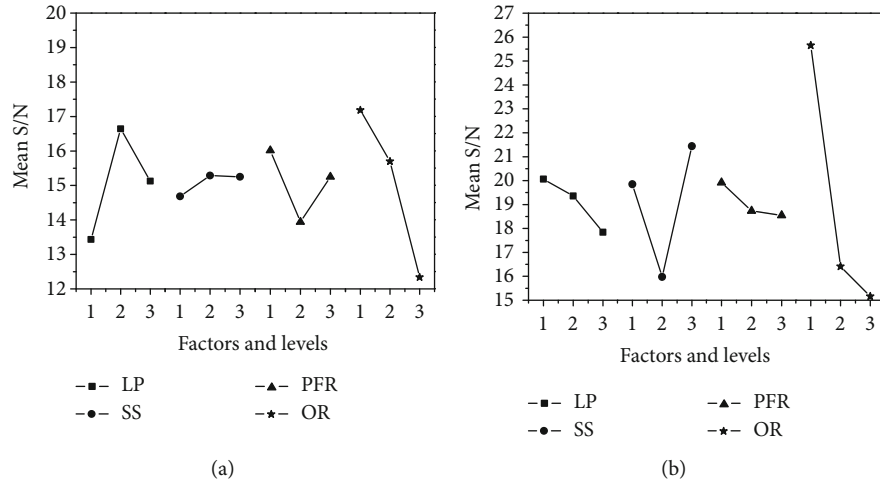
FIGURE 10: Effect of factors and their levels on mean S/N ratio of (a) surface roughness and (b) width error.

study, there are two response characteristics (surface roughness and width error) that should be considered. The present paper used Grey relation analysis (GRA) for carrying out multiobjective optimization [25, 26].

3.5.1. Grey Relational Generating. In the grey relation analysis, the first step is called grey relational generating, which is to perform the normalization of measurement data to make the range between 0 and 1. According to the type of response, there are three expressions of the normalized value.

If the expectancy is higher-the-better, then the normalized value x_{ij} can be expressed as

$$x_{ij} = \frac{y_{ij} - \min y_{ij}}{\max y_{ij} - \min y_{ij}}. \tag{15}$$

If the expectancy is smaller-the-better, then the normalized value x_{ij} can be expressed as

Table 7: ANOVA for S/N ratio for surface roughness and width error.

Response	Factors	S_A	f_A	V_A	F_A	% contribution
Surface roughness (δ)	LP	15.5	2	7.75	22.464	25.934
	SS	0.69	2	Pooled	—	—
	PFR	6.597	2	3.299	9.562	11.038
	OR	36.98	2	18.49	53.594	61.874
	Error	(0.69)	(2)	(0.345)		(1.154)
	Total	59.767	8			100
Width error (w_e)	LP	7.735	2	Pooled	—	—
	SS	47.605	2	23.803	8.624	18.612
	PFR	3.308	2	Pooled	—	—
	OR	197.125	2	98.563	35.711	77.07
	Error	(11.043)	(4)	(2.76)		(4.318)
	Total	255.773	8			100

$F_{0.25}(2, 2) = 3.00$; $F_{0.10}(2, 2) = 9.00$; $F_{0.05}(2, 2) = 19.00$; $F_{0.01}(2, 2) = 99.00$; $F_{0.25}(2, 4) = 2.00$; $F_{0.10}(2, 4) = 4.32$; $F_{0.05}(2, 4) = 6.94$; $F_{0.01}(2, 4) = 18.00$.

Table 8: Grey relational generating, grey relational coefficient, grey relational grade, and rank for each experiment.

Expt. No.	Grey relational generating		Grey relational coefficient		Grey relational grade	Rank
	Surface roughness (δ)	Width error (w_e)	Surface roughness (δ)	Width error (w_e)		
1	0.724	0.983	0.644	0.967	0.789	3
2	0.335	0.276	0.429	0.408	0.420	7
3	0.000	0.508	0.333	0.504	0.410	8
4	0.229	0.464	0.393	0.485	0.434	6
5	1.000	0.862	1.000	0.784	0.903	1
6	0.941	0.724	0.894	0.644	0.782	4
7	0.665	0.425	0.599	0.465	0.539	5
8	0.412	0.000	0.460	0.333	0.403	9
9	0.747	1.000	0.664	1.000	0.815	2

Table 9: Influence of factors on grey relational grade.

Factors	Mean grey relational grade			Range	Rank
	Level 1	Level 2	Level 3		
LP	0.540	0.706*	0.586	0.166	2
SS	0.587	0.575	0.669*	0.094	4
PFR	0.658*	0.556	0.617	0.102	3
OR	0.836*	0.580	0.416	0.420	1

* Optimized level of parameters.

$$x_{ij} = \frac{\max y_{ij} - y_{ij}}{\max y_{ij} - \min y_{ij}}. \tag{16}$$

If the expectancy is nominal-the-better, then the normalized value x_{ij} can be expressed as

$$x_{ij} = 1 - \frac{\left| y_{ij} - y_0 \right|}{\max \left(\max y_{ij} - y_0, y_0 - \min y_{ij} \right)}. \tag{17}$$

In the present research, both the surface roughness and width error are smaller-the-better type. Thence, the data in
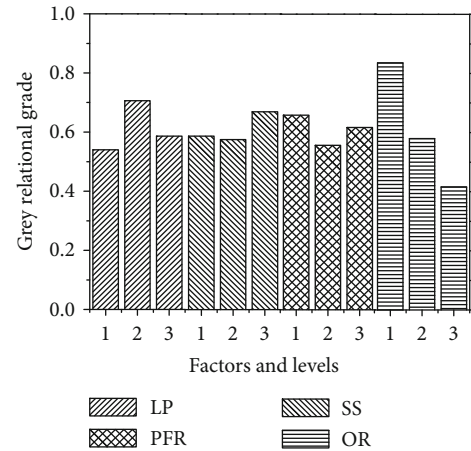

Figure 11: Effect of factors and their levels on grey relational grade.

Figure 12: Multitrack sample of predicted parameters.

TABLE 10: Comparison between initial parameters and optimal parametric combinations.

	Initial parameters	Optimal parametric combinations	
		Prediction	Experiment
Setting level	$LP_1SS_1PFR_1OR_1$	$LP_2SS_3PFR_1OR_1$	$LP_2SS_2PFR_3OR_1$
Surface roughness (δ/mm)	0.157	0.102	0.110
Width error (w_e/mm)	0.036	0.041	0.058
Grey relational grade	0.789		0.903

Table 4 are normalized using Eq. (16), and the normalized values are shown in Table 7.

3.5.2. Grey Relational Coefficient. The grey relational coefficient can be calculated as follows:

$$\gamma(x_{0j}, x_{ij}) = \frac{\Delta_{\min} + \xi\Delta_{\max}}{\Delta_{ij} + \xi\Delta_{\max}}, \tag{18}$$

for $i = 1, 2, 3, \cdots, m, j = 1, 2, 3, \cdots, n$.

where $\Delta_{ij} = |x_{oj} - x_{ij}|$, x_{0j} is the reference data or best data, here, $x_{0j} = 1.000$. $\Delta_{\min} = \min \Delta_{ij}$, $\Delta_{\max} = \max \Delta_{ij}$. ξ is the distinguishing coefficient, $\xi \in (0, 1)$.

The grey relational coefficient is calculated by Eq. (18), and the results are shown in Table 7. The distinguishing coefficient is assumed at 0.5.

3.5.3. Grey Relational Grade. After calculating the grey relational coefficient, the grey relational grade can be calculated by Eq. (19).

$$\Gamma(x_0, x_i) = \sum_{j=1}^{n} \omega_j \gamma(x_{0j}, x_{ij}), \tag{19}$$

for $i = 1, 2, 3, \cdots, m$. ω_j is the weight of attribute j and usually depends on the maker's judgment or the structure of the problem, and $\sum_{j=1}^{n} \omega_j = 1$. In the present study, the weights for the percentage change in surface roughness and width error are taken as 0.55 and 0.45, respectively. The calculated results are shown in Table 8.

3.5.4. Analysis of the Grey Relational Grade. According to Table 8, the best multiple performance is achieved by experiment no. 5. That is to say, the multiobjective optimum process parametric combination is 1800 W laser power, 6 mm/s scanning speed, 30 g/min powder feeder rate, and 30% overlapping rate. Table 9 shows the mean of grey relational grade, which indicates that the affect order of each factor on grey relational grade is OR > LP > PFR > SS.

Figure 11 shows the effect of factors and their levels on grey relational grade, it can be seen; the optimal levels of laser power, scanning speed, powder feeder rate, and overlapping rate are 1800 W, 8 mm/s, 10 g/min, and 30%, respectively. Figure 12 shows the multitrack sample with the optimum combination of parameters. The measurement results were shown in Table 10. Obviously, both the surface roughness and width error are smaller in the prediction levels than experiment no.5.
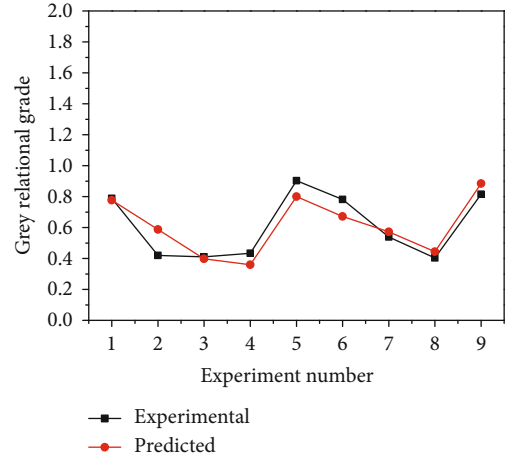

FIGURE 13: Comparison of experimental and predicted.

3.6. Regression Analysis. In the regression analysis, a mathematical model (Eq. (20)) was developed to predict the grey relational grade. Figure 13 shows the comparison of experimental and predicted, the trends of the two curves roughly consistent.

$$\begin{aligned} GRG = {}& 1.797122 + 0.000115LP + 0.020417SS - 0.00203PFR \\ & - 0.042OR \end{aligned} \tag{20}$$

4. Conclusions

In this paper, Inconel 625 cladding layer was prepared by LAM. The influence of major process parameters such as laser power, scanning speed, powder feed rate, and overlapping rate along with their interactions on surface roughness and width error were investigated. Taguchi method and grey relational analysis were used to optimize the selected parameters. In addition, the change of microhardness and microstructure in the overlapping zone and nonoverlapping zone of the cladding layer were explored. Through analysis, the conclusions of this study are as follows:

(1) The effect of factors on surface roughness and width error is different, whereas the Taguchi method is only suitable for the optimization of a single performance characteristic. The grey relational analysis combined the entire objectives into a single value that can be used as the single characteristic in optimization issues

(2) The content of Cr was high both in the Laves phase and matrix, the content of Nb in the Laves phase increases significantly and reaches up to 24.48 wt%, and the Laves in the nonoverlapping zone is more compact than overlapping zone. The microhardness of the overlapping zone of the cladding layer is lower than that of the nonoverlapping zone

(3) The most significant effect in processing parameters on surface roughness and width error are both overlapping rate. The optimal levels of laser power, scanning speed, powder feeder rate, and overlapping rate are 1800 W, 8 mm/s, 10 g/min, and 30%, respectively

Data Availability

The data used to support the findings of this study are included within the article.

Conflicts of Interest

The authors declare that there is no conflict of interest regarding the publication of this paper.

Acknowledgments

References

[1] J. A. Gonzalez, J. Mireles, S. W. Stafford, M. A. Perez, C. A. Terrazas, and R. B. Wicker, "Characterization of Inconel 625 fabricated using powder-bed-based additive manufacturing technologies," *Journal of Materials Processing Technology*, vol. 264, pp. 200–210, 2019.

[2] T. E. Abioye, D. G. McCartney, and A. T. Clare, "Laser cladding of Inconel 625 wire for corrosion protection," *Journal of Materials Processing Technology*, vol. 217, pp. 232–240, 2015.

[3] G. U. Jeong, C. K. Jin, H. Y. Seo, and C. G. Kang, "Experimental investigation on the deformation behavior of Inconel 625 superalloy at high temperatures," *Metals*, vol. 9, no. 7, p. 720, 2019.

[4] D. Verdi, M. A. Garrido, C. J. Múnez, and P. Poza, "Microscale evaluation of laser cladded Inconel 625 exposed at high temperature in air," *Materials & Design*, vol. 114, pp. 326–338, 2017.

[5] P. D. Enrique, E. Marzbanrad, Y. Mahmoodkhani, Z. Jiao, E. Toyserkani, and N. Y. Zhou, "Surface modification of binder-jet additive manufactured Inconel 625 via electrospark deposition," *Surface & Coatings Technology*, vol. 362, pp. 141–149, 2019.

[6] A. Mostafaei, P. Rodriguez de Vecchis, I. Nettleship, and M. Chmielus, "Effect of powder size distribution on densification and microstructural evolution of binder-jet 3D-printed alloy 625," *Materials & Design*, vol. 162, pp. 375–383, 2019.

[7] C. Cui, V. Uhlenwinkel, A. Schulz, and H. W. Zoch, "Austenitic stainless steel powders with increased nitrogen content for laser additive manufacturing," *Metals*, vol. 10, no. 1, p. 61, 2020.

[8] Y. B. Lai, W. J. Liu, Y. Kong, F. Y. Wang, and Y. H. Zhao, "Influencing factors of residual stress of Ti-6.5Al-1Mo-1V-2Zr alloy by laser rapid forming process," *Rare Metal Materials and Engineering*, vol. 42, pp. 1526–1530, 2013.

[9] F. Wang, W. Liu, Y. Zhao, Y. Lai, and W. Han, "Subarea simulation and distributed computing of direct laser fabrication," *International Journal of Advanced Manufacturing Technology*, vol. 71, no. 1-4, pp. 667–673, 2014.

[10] Y. Liu, C. Liu, W. Liu et al., "Optimization of parameters in laser powder deposition AlSi10Mg alloy using Taguchi method," *Optics & Laser Technology*, vol. 111, pp. 470–480, 2019.

[11] T. Yang, T. Liu, W. Liao et al., "The influence of process parameters on vertical surface roughness of the AlSi10Mg parts fabricated by selective laser melting," *Journal of Materials Processing Technology*, vol. 266, pp. 26–36, 2019.

[12] B. Liu, B. Q. Li, and Z. Li, "Selective laser remelting of an additive layer manufacturing process on AlSi10Mg," *Results in Physics*, vol. 12, pp. 982–988, 2019.

[13] T. Yu, L. Yang, Y. Zhao, J. Sun, and B. Li, "Experimental research and multi-response multi-parameter optimization of laser cladding Fe313," *Optics & Laser Technology*, vol. 108, pp. 321–332, 2018.

[14] T. Bhardwaj, M. Shukla, C. P. Paul, and K. S. Bindra, "Direct Energy Deposition - Laser Additive Manufacturing of Titanium-Molybdenum alloy: Parametric studies, microstructure and mechanical properties," *Journal of Alloys and Compounds*, vol. 787, pp. 1238–1248, 2019.

[15] Y. Li and D. Gu, "Parametric analysis of thermal behavior during selective laser melting additive manufacturing of aluminum alloy powder," *Materials & Design*, vol. 63, pp. 856–867, 2014.

[16] H. Hu, X. Ding, and L. Wang, "Numerical analysis of heat transfer during multi-layer selective laser melting of AlSi10Mg," *Optik*, vol. 127, no. 20, pp. 8883–8891, 2016.

[17] P. Conti, F. Cianetti, and P. Pilerci, "Parametric finite elements model of SLM additive manufacturing process," *Procedia Structural Integrity*, vol. 8, pp. 410–421, 2018.

[18] C. Pleass and S. Jothi, "Influence of powder characteristics and additive manufacturing process parameters on the microstructure and mechanical behaviour of Inconel 625 fabricated by selective laser melting," *Additive Manufacturing*, vol. 24, pp. 419–431, 2018.

[19] W. H. Yang and Y. S. Tarng, "Design optimization of cutting parameters for turning operations based on the Taguchi method," *Journal of Materials Processing Technology*, vol. 84, no. 1-3, pp. 122–129, 1998.

[20] Y. B. Lai, B. H. Zhang, J. B. Zhao, W. J. Liu, and Y. H. Zhao, "Calculation and experimental verification of optimal overlapping ratio in laser metal direct manufacturing," *Transactions of the China Welding Institution*, vol. 37, pp. 79–82+132-133, 2016.

[21] A. Balaram Naik and A. Chennakeshava Reddy, "Optimization of tensile strength in TIG welding using the Taguchi method and analysis of variance (ANOVA)," *Thermal Science and Engineering Progress*, vol. 8, pp. 327–339, 2018.

[22] A. H. Bademlioglu, A. S. Canbolat, N. Yamankaradeniz, and O. Kaynakli, "Investigation of parameters affecting Organic Rankine Cycle efficiency by using Taguchi and ANOVA methods," *Applied Thermal Engineering*, vol. 145, pp. 221–228, 2018.

[23] K. Viswanath Allamraju, "Voltage optimization of piezoelectric circular transducer by Taguchi and ANOVA approches," *Materials Today: Proceedings*, vol. 5, no. 2, pp. 5322–5327, 2018.

[24] Y. Dongxia, L. Xiaoyan, H. Dingyong, N. Zuoren, and H. Hui, "Optimization of weld bead geometry in laser welding with filler wire process using Taguchi's approach," *Optics and Laser Technology*, vol. 44, no. 7, pp. 2020–2025, 2012.

[25] J. Kanchana, V. Prasath, V. Krishnaraj, and B. Geetha Priyadharshini, "Multi response optimization of process parameters using grey relational analysis for milling of hardened custom 465 steel," *Procedia Manufacturing*, vol. 30, pp. 451–458, 2019.

[26] M. I. Equbal, R. kumar, M. Shamim, and R. K. Ohdar, "A grey-based Taguchi method to optimize hot forging process," *Procedia Materials Science*, vol. 6, pp. 1495–1504, 2014.